LBL-5458

CARBON AND DEUTERIUM NUCLEAR MAGNETIC RESONANCE IN SOLIDS

Thomas Wayne Shattuck
(Ph. D. thesis)

July 1976

Prepared for the U. S. Energy Research and
Development Administration under Contract W-7405-ENG-48

LBL-5458

Carbon and Deuterium Nuclear Magnetic Resonance in Solids

Thomas Wayne Shattuck

Abstract

In Chapter I we present the results on a study of cross polarization dynamics, between protons and carbon-13 in adamantane, by the direct observation of the dilute, carbon-13, spins. These dynamics are an important consideration in the efficiency of proton enhancement double-resonance techniques and they also provide good experimental models for statistical theories of cross relaxation. In order to test these theories we present a comparison of the experimental and theoretical proton dipolar fluctuation correlation time τ_c, which is experimentally 110 ± 15 μsec and theoretically 122 μsec for adamantane. These double resonance considerations provide the background for extensions to deuterium and double quantum effects discussed in Chapter II.

In Chapter II an approach to high resolution nmr of deuterium in solids is described. The $m = 1 \rightarrow -1$ transition is excited by a double quantum process and the decay of coherence $Q(\tau)$ is monitored. Fourier transformation yields a deuterium spectrum devoid of quadrupole splittings and broadening. If the deuterium nuclei are dilute and the protons are spin decoupled, the double-quantum spectrum is a high resolution one and yields information on the deuterium chemical shifts $\Delta\omega$. The relationship $Q(\tau) \sim \cos 2\Delta\omega\tau$ is checked and the technique is applied to a single crystal of oxalic acid dihydrate enriched to ∿ 10% in deuterium. The carboxyl and the water deuterium shifts are indeed resolved and the anisotropy of the

carboxyl shielding tensor is estimated to be $\Delta\sigma = 32 \pm 3$ ppm. A complete theoretical analysis is presented.

The extension of cross relaxation techniques, both direct and indirect, to proton-deuterium double resonance is also described. The $m = 1 \rightarrow -1$ double quantum transition and the $m = \pm 1 \rightarrow 0$ single quantum transitions may all be polarized and we present the derivation of the Hartmann-Hahn cross polarization conditions for each case. In addition the dynamics of the double quantum process, for monodeutero benzene are discussed, giving proton dipolar fluctuation correlation times, and spin heat capacities for the double quantum transition.

Dedication

To Mrs. Karen S. Day and Dr. Rufus S. Day III

Acknowledgments

I would like to thank Professor Alex Pines for his guidance and constant encouragement during this research. His physical insight and broad scientific knowledge were invaluable for the completion of this work. I would also like to express my deep gratitude to Dr. Shimon Vega whose patience, encouragement and broad theoretical understanding made this thesis possible.

I am grateful to David Wemmer, Art Gaylord, Jim Murdoch, Dr. James Chang and Dr. David Ruben for assistance with various aspects of the experimental and theoretical details of this thesis, along with their encouragement and friendship and many hours of helpful discussions. I would also like to thank Kevin Klotter for his support and friendship, and Professor George F. Jackson and Dr. Rufus S. Day for their scientific vision. I would also like to thank my family for the energy and courage that their confidence and support gave me.

I would like to thank the fifty technicians and service personnel who had a hand in the construction of the spectrometer. Finally, I would like to thank Carol Hacker for her patience and industry in preparing this manuscript.

This work was supported by the Materials and Molecular Research Division of the Lawrence Berkeley Laboratory. It was performed under the auspices of the U.S. Energy Research and Development Administration.

TABLE OF CONTENTS

Dedication i

Acknowledgments ii

Table of Contents iii

CHAPTER 1 1

I. Introduction 1

II. Cross Polarization: Background 6

III. Theory 11

A. Hamiltonians 11

B. Thermodynamics 15

C. Correlation Time 27

IV. Experimental 40

A. Sample 40

B. Spectrometer 40

C. Adamantane Dynamics 43

1. Relaxation Times 44

2. Cross Polarization 52

V. Discussion 61

Appendices 67

1.1 Lattice Sums for an FCC Lattice and the CaF_2 Lattice . . . 67

1.2 Averages for the Polycrystalline Cross Polarization Time . . 81

1.3 Computer Programs 87

References 102

CHAPTER 2 105

I. Introduction 105

II. Approach for High Resolution 108

III. Theory. 115

A. Quadrupole Satellite Spectroscopy 118

B. Fictitious Spin Operators 119

1. Single Quantum Transition Hamiltonian 127

2. Double Quantum Transition Hamiltonian 130

C. Observables 134

D. Previous Double Quantum Experiments 147

1. Double Quantum Spectroscopy 147

2. General Solution 158a

IV. Cross Relaxation. 163

A. Previous Quadrupole Cross Relaxation Experiments 163

B. Cross Polarization Theory 164

1. Single Quantum Cross Polarization 167

2. Double Quantum Cross Polarization 173

3. Magic Pulse 180

4. Destruction Spectra 183

V. Chemical Shielding Tensors 187

VI. Experimental. 191

A. Double Quantum Spectroscopy 191

1. Sample 191

2. Double Quantum Pulse 191

3. Double Quantum Decay 199

B. High Resolution 214

1. Sample 214

2. Quadrupole Satellite Spectroscopy 218

3. Double Quantum Spectroscopy 229

C. Cross Polarization. 247

1. Sample 247

2. Indirect Detection 247

3. Direct Detection 261

4. Double Quantum Cross Polarization Dynamics 270

VII. Discussion 283

A. Spectroscopy 283

B. Cross Polarization 285

C. Chemical Shielding Tensor 287

Appendices 289

2.1 Transformation Properties of the Fictitious Spin ½ . . . . Operators 289

2.2 Fictitious Spin ½ Operators and Group Theory 313

2.3 Derivation of the Cross Polarization Time 323

References 344

Chapter I

I. Introduction

New double-resonance techniques have been developed for high sensitivity and high resolution NMR of dilute spins in solids, and these techniques have become quite common laboratory tools.[1-5] The spectroscopic utility of these techniques comes about because the normally very large linewidths in solids are narrowed to the point that chemical shift information may be obtained. This narrowing is brought about by an isotopic dilution, which decreases the homonuclear interactions, combined with spin decoupling which decreases the heteronuclear interactions, giving rise to high resolution. However this dilution necessarily decreases the sensitivity so that double resonance techniques must be used. The basis of one set of these experiments is the transfer of nuclear magnetic polarization from one nuclear species (I), normally protons, to a dilute species (S), such as ^{13}C, under study, and the application of high power spin decoupling.[6-10] A prime candidate for application of the techniques is the determination of full ^{13}C chemical shielding tensors in organic single crystals.[11] An important consideration in the design and efficiency of such experiments is that of the dynamics of the polarization transfer from I to the S system, since this ultimately determines the sensitivity enhancement, the time scale accessible, and thus the range of possible systems that can be studied. In this chapter we present a study of cross-polarization dynamics by direct observation of the dilute nuclear spins, and an approach to "total cross-polarization." The direct detection method is termed

Proton Enhanced Nuclear Induction Spectroscopy.

To make the problem more concrete, Figure 1 shows a schematic of the general approach. Two extreme cases may be considered: "multiple cross-polarization" and "total cross-polarization." In the first, a small amount of I polarization is transferred to the S spins and the cycle is repeated many times as indicated, with the S signal being accumulated. In the second, all or a substantial amount of the I polarization is transferred "in one shot"[4] and the experiment and observation of the S spins are performed once per I repolarization. It is not clear that the second approach is advantageous, since the dynamics of the cross-polarization may render the process slow and technically difficult. However, for experiments that require long observation times of the S spins, such as long-lived spin echoes or very high resolution spectroscopy, the multiple cross-polarization is clearly not possible, since it requires the expenditure of rf power and the maintenance of I spin order for unrealistically long times. Thus it is clear that a quantitative understanding of the process is a mandatory prerequisite for the development of these experiments.

The present experiments were performed on a small sample of solid polycrystalline adamantane. Cross-polarization occurs from a proton system demagnetized in the rotating frame.[12,13] This approach is selected since the analysis is simple and the technical requirements for total cross-polarization are not too stringent. The mechanism for the cross-polarization derives from fluctuations in the I-S magnetic dipolar coupling due to mutual spin flips among the I spins.[14,15] That is, the proton-proton magnetic dipole interaction causes a modulation of the magnetic field at a particular ^{13}C nucleus. This fluctuating field

Figure 1. General schematic of cross polarization experiment: a) shows the abundant I and dilute S nuclear species coupled to each other and to the lattice with characteristic times T_{IS} (cross polarization times) and T_{1I}, T_{1S} (spin-lattice relaxation times); b) shows the general approach where repeating the cross polarization step characterizes the multiple contact procedure.

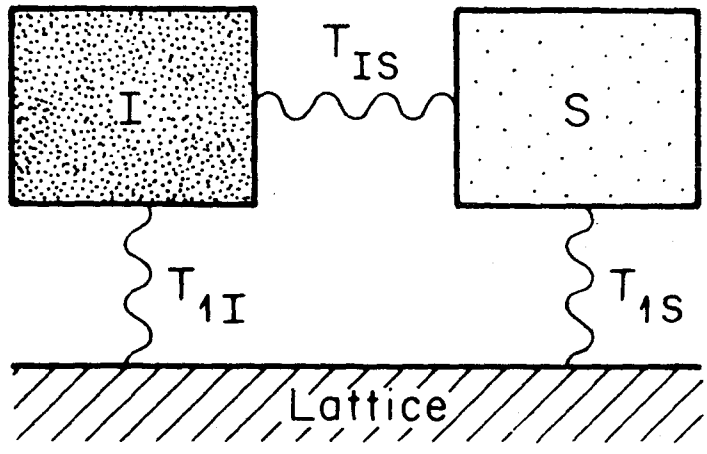

a

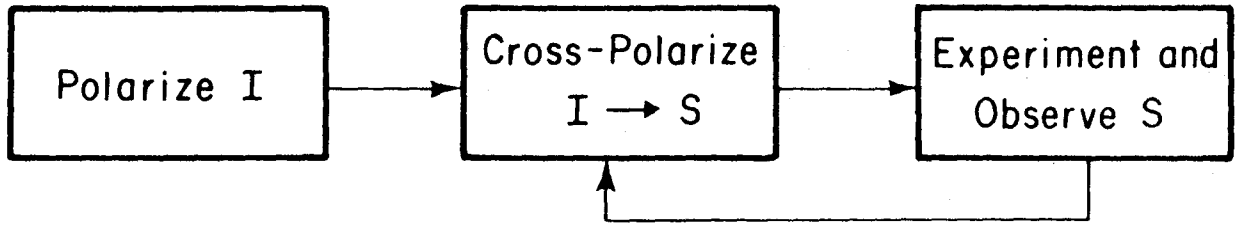

b

XBL 7312-7169

induces transitions between the ^{13}C Zeeman levels causing the energy transfer, and can be characterized by a correlation time τ_c. This can be thought of as the average time during which the magnetic field at a ^{13}C nucleus stays constant. The correlation time can be rigorously calculated knowing the structure of the solid of interest. These calculations are of great interest since (a) they are useful structural tools, (b) they will permit the design of optimal high sensitivity techniques for detection of rare isotopes, (c) they provide good models for statistical mechanical theories of spin behavior. We have carried out this calculation for an FCC lattice, and have found the correlation time, τ_c, for adamantane. The experimental τ_c and theoretical are in quite good agreement.

In the second chapter we present an entirely new approach to proton magnetic resonance in solids. It is analogous to the carbon-13 proton experiments above except now we choose to observe dilute deuterium nuclear spins (^2H). We show the development of two new spectroscopic techniques which allow the first high resolution determination of deuterium chemical shifts. We also show the application of double resonance cross-polarization techniques to the deuterium proton system.

II. Cross Polarization: Background

The cross polarization process takes place in three distinct steps. First we cool the I spins, we then effect a transfer of spin energy between the I and S spins and lastly we observe. We use two different ways of cooling the I spins reservoir, spin locking (SL) and adiabatic demagnetization in the rotating frame (ADRF). See Figure 8 for the pulse sequences used. Spin locking serves to rotate the quantization axis into the X-Y plane giving a net cooling of H_o/H_{1I} where H_{1I} is the intensity of the I spin radio frequency (r.f.) irradiation. ADRF produces a low temperature in the dipolar state. This temperature concept applied to the dipolar state is illustrated in Figure 2, where each of the Zeeman levels is broadened severely by the dipole-dipole interaction (numbers shown are for protons in adamantane). The populations of this quasi-continuous level scheme are given by two spin temperatures, T_Z the normal Zeeman spin temperature and T_D the dipolar temperature. In the dipolar state $T_Z = \infty$ while T_{1D} is finite. The energy of such a system is given purely in terms of the dipole-dipole Hamiltonian for like spins:

$$H_{II}^{(o)} = \sum_{i<j} - \frac{\gamma_I^2 \hbar}{r_{ij}^3} \frac{1}{2} (3 \cos^2\theta_{ij} - 1) \{3 I_{iZ} I_{jZ} - \underset{\sim}{I}_i \underset{\sim}{I}_j\} \qquad (1)$$

or thermodynamically in terms of the local field H_L,

$$E = \beta C_I H_L^2 \qquad (2)$$

where C_I is the normal Curie constant,

Figure 2. Level scheme for a spin ½ nuclei interacting with each other through the homonuclear dipole-dipole interaction. The representative frequencies given are for protons in adamantane in an external field of 25 Kgauss. The populations of the Zeeman levels are described by the Zeeman spin temperature T_Z or the inverse temperature $\beta_Z = 1/k\ T_Z$. The populations of the dipolar sublevels are given by the dipolar spin temperature T_D or its inverse β_D.

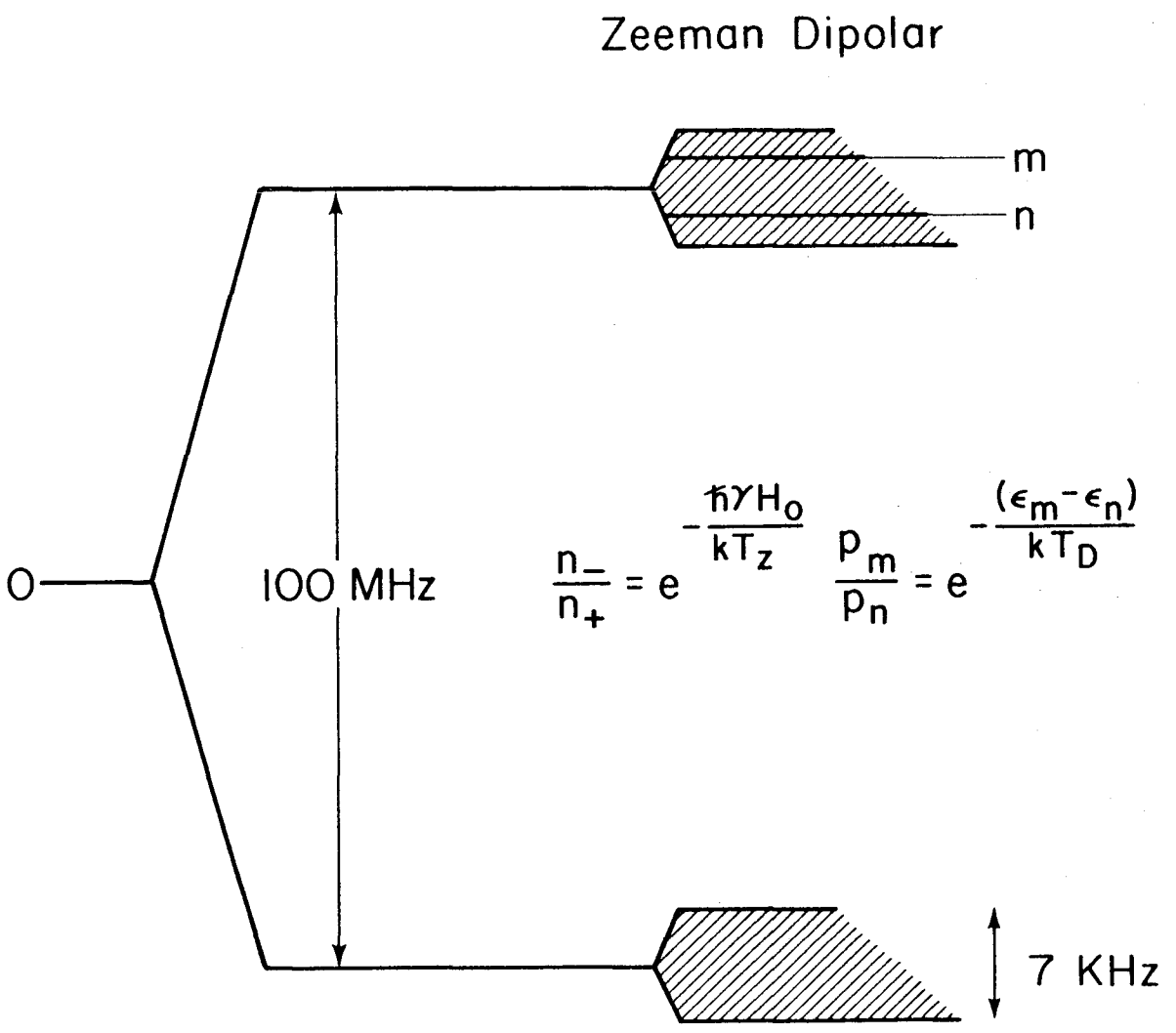
Zeeman Dipolar
m
n
0
100 MHz
$\frac{n_-}{n_+} = e^{-\frac{\hbar\gamma H_0}{kT_Z}}$
$\frac{p_m}{p_n} = e^{-\frac{(\epsilon_m - \epsilon_n)}{kT_D}}$
7 KHz

XBL 764-1515

$$C_I = \gamma_I^2 \hbar^2 N_I \otimes I(I+1)/3$$

β is the appropriate inverse spin temperature $\beta = \frac{1}{kT}$ and the local field is given by[12,29]

$$H_L^2 = \frac{tr\ (H_{II}^{(o)2})}{tr\ (M_Z^2)} \tag{3}$$

where M_Z is the magnetization operator $M_Z = \gamma_I \hbar \sum_i I_{iZ}$. H_L is effectively the net field a spin would experience due to its neighbors. ADRF gives rise to a net cooling of H_0/H_L.[12,13,31]

To effect an efficient transfer of polarization we must arrange that mutual I- and S-spin flips become energy conserving. This will be true in the rotating frame if the Hartmann-Hahn condition is satisfied,[16]

$$\gamma_I H_{1I} = \gamma_S H_{1S} \tag{4}$$

where we apply r.f. irradiation at the I and S Larmor frequencies of strength H_{1I} and H_{1S} respectively.

The observation may be carried out either by directly observing the S-spin or indirectly by observing the destruction of the I-spin order. The direct observation has the advantage that high resolution spectra may be obtained with the simultaneous application of spin decoupling and this is the method used in this chapter. In Chapter 2 the indirect methods are also described for deuterium indicating the greater sensitivity available. For reference purposes for the second chapter we present the complete equations for both ADRF and SL cases. These will be expanded but are presented now to introduce the notation.

The theory for these experiments is quite well established[3,13,14,16,17] and will only be briefly sketched here to define the notation and provide easy reference.

III. Theory

A. Hamiltonians

We consider the following system in a large external magnetic field, H_0: an abundant I spin system with a resonance frequency ω_{OI} is dipolar coupled to a rare S-spin system with resonance frequency ω_{OS}.

$$H = H_Z + H_{II} + H_{IS} + H_{rf}(t) \tag{5}$$

where $H_Z = H_{IZ} + H_{SZ} = -\omega_{OI} I_Z - \omega_{OS} S_Z$ and $\omega_{OI} = \gamma_I H_O$, $\omega_{OS} = \gamma_S H_O$, $I_Z = \sum_i I_{iZ}$, $S_Z = \sum_i S_{iZ}$ and γ_I and γ_S are the magnetogyric ratios of the I and S spin reservoirs. We have neglected the dipole-dipole term between S-spins, since we assume them to be sufficiently dilute that they are isolated from each other. The I-I dipolar coupling is taken in its high field truncated form as

$$H_{II}^{(o)} = \sum_{i<j} - \frac{\gamma_I^2 \hbar}{r_{ij}^3} \frac{1}{2} (3 \cos^2\theta_{ij} - 1) \{3 I_{iZ} I_{jZ} - \underset{\sim}{I}_i \underset{\sim}{I}_j\} \tag{6}$$

where θ_{ij} is the angle between the internuclear vector and the external field. The I-S dipolar coupling is also taken in its high field truncated form:

$$H_{IS}^{(o)} = \sum_i - \frac{2\gamma_I \gamma_S \hbar}{r_i^3} \frac{1}{2} (3 \cos^2\theta_i - 1) (I_{iZ} S_Z) \tag{7}$$

where only a single S spin is considered. For convenience we define the following coupling constants:

$$a_{ij} = -\frac{\gamma_I^2 \hbar}{r_{ij}^3} \frac{1}{2} (3 \cos^2\theta_{ij} - 1)$$

$$b_i = -\frac{2\gamma_I \gamma_S \hbar}{r_i^3} \frac{1}{2} (3 \cos^2\theta_i - 1) \tag{8}$$

These dipolar couplings are illustrated for 2 I-spins and one S in Figure 3. Two strong r.f. fields with rotating components H_{1I} and H_{1S} are applied at frequencies ω_{0I} and ω_{0S}.

$$H_{rf}(t) = -\gamma_I H_{1I} I_X \cos \omega_{0I} t - \gamma_S H_{1S} S_X \cos \omega_{0S} t \tag{9}$$

We remember that since

$$[H_{IZ}, H_{II}^{(o)}] = 0 \tag{10}$$

we must consider both terms as separate constants of the motion, during a time $t < T_1$ where T_1 is the spin lattice relaxation time. We now transform (5) into the double rotating frame using the transformation operator:

$$T = \exp\{- it (\omega_{0I} I_Z + \omega_{0S} S_Z)\} \tag{11}$$

yielding the transformed Hamiltonian

$$H^* = H_Z^* + H_{II}^{(o)} + H_{IS}^{(o)} \tag{12}$$

where

$$H_Z^* = H_{IZ}^* + H_{SZ}^* = - \omega_{1I} I_X - \omega_{1S} S_X$$

Figure 3. Lattice variables for interacting spins.

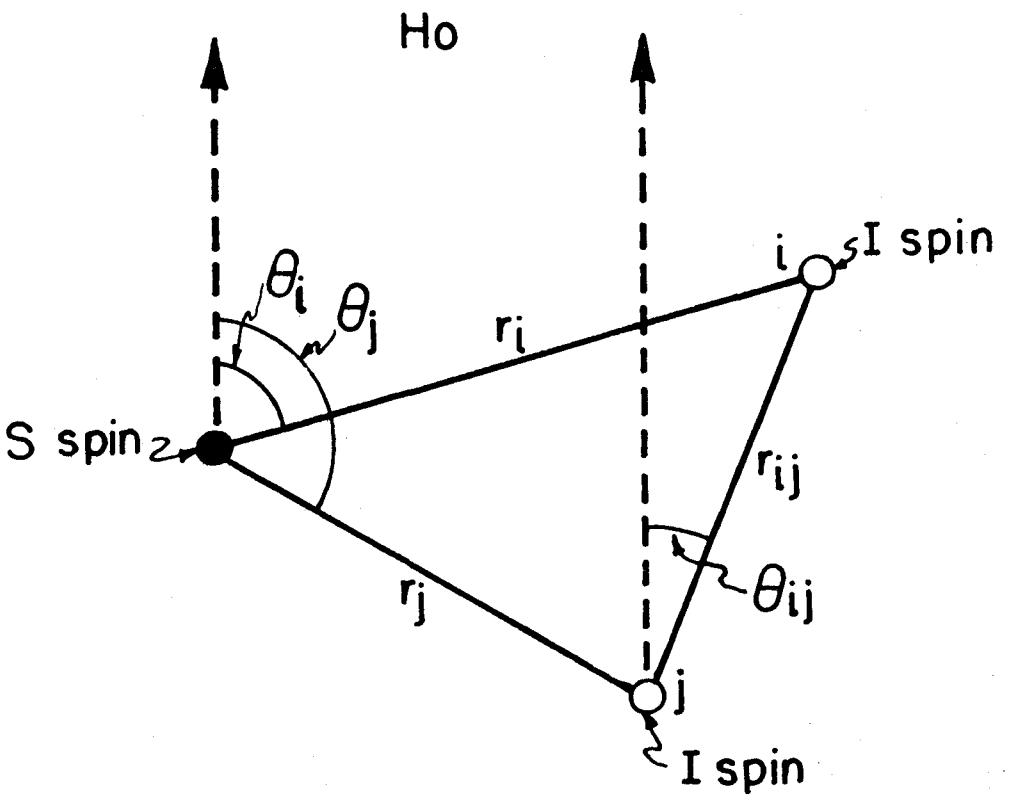

XBL752-5722

B. Thermodynamics

We now discuss the thermodynamic properties of the cross polarization, followed by a discussion on the dynamics of the energy exchange. We may use thermodynamics, following Redfield, since the Hamiltonian in the rotating frame is effectively time independent. The two terms H_{IZ} and H_{SZ} may then be considered as reservoirs of Zeeman energy, and because of the commutation relation, equation (10), we must also consider the term H_{II} as a reservoir of dipolar energy. The equilibrium density matrix in the rotating frame is

$$\rho^*_{eq} = \exp(-\beta H^*)/\mathrm{tr}\,\exp(-\beta H^*) \tag{13}$$

We now invoke the high temperature approximation giving:

$$\rho^*_{eq} = Z^{-1}\,(1 - \beta H^*) \tag{14}$$

for which we use the shorthand notation

$$\sigma^*_{eq} = \beta H^* \tag{15}$$

since the constant value, 1, will not enter into the expectation value of any observable. This is the reduced density matrix for the system. The density matrix for a system with a Hamiltonian given in equation (12) is for the quasi-equilibrium state for which the I and S spin system are not allowed to interact:

$$\sigma^*_{eq} = \beta_I H_{IZ} + \beta_S H_{SZ} + \beta_{Id} H_{II} \tag{16}$$

Here we will treat $H^{(o)}_{IS}$ as a perturbation, whose effect will be to

equalize β_I and β_S, but whose energy will be negligible in the thermodynamic sense, thus it's neglect in (16). The expectation value of any observable is given as

$$\langle Q \rangle = \mathrm{tr}\,\{\rho Q\} \tag{17}$$

giving for the energy of the spin system in equation (12)

$$E = \mathrm{tr}\,\{\sigma^*_{eq} H^*\} = \beta_I C_I H_{1I}^2 + \beta_{Id} C_I H_L^2 + \beta_S C_S H_{1S}^2 \tag{18}$$

where C_I and C_S are the Curie constants given by $C_I = \gamma_I^2 \hbar^2 N_I I(I + 1)/3$ and similarly for C_S, and H_L is the local field (equation 3). In the spin locked state (SL) for the protons $H_{1I} >> H_L$ so that the I spin energy is given as

$$E_I = \beta_I C_I H_{1I}^2 \tag{19}$$

and for the adiabatically demagnetized state $H_{1I} = 0$ giving

$$E_I = \beta_I C_I H_L^2 \tag{20}$$

The heat capacities will be, for the I and S spins

$$\frac{\partial E_I}{\partial \beta_I} = C_I H_L^2 \quad \text{or} \quad C_I H_{1I}^2 \qquad \frac{\partial E_S}{\partial \beta_S} = C_S H_{1S}^2 \tag{21}$$

and the I and S spin magnetizations, the actual observable quantities in these experiments,

$$M_I = \frac{E_{1I}}{H_{1I}}, \qquad M_I = \beta_I C_I H_{1I} \tag{22}$$

and similarly for S and for the ADRF experiment $M_I = 0$.

The initial magnetization for a normal free induction decay (FID) for both of these systems at equilibrium is given as

$$M_I^{(o)} = \beta_L C_I H_0 \quad \text{and} \quad M_S^{(o)} = \beta_L C_S H_0 \tag{23}$$

where β_L is the inverse lattice temperature. We may produce a lower spin temperature by spin locking, where the magnetization for the I-spins, equation (23), is locked along the x axis in the rotating frame giving

$$E_I = \beta_0 C_I H_{1I}^2 \ , \quad M_I(0) = \beta_0 C_I H_{1I}$$

$$\text{where} \quad \beta_0 = \beta_L H_0 / H_{1I} \tag{24}$$

If on the other hand we adiabatically demagnetize the I-spin system we obtain no magnetization but an enhanced internal dipolar order with energy:

$$E_I = \beta_0 C_I H_L^2$$

$$\text{where} \quad \beta_0 = \beta_L H_0 / H_L \tag{25}$$

Since $H_{1I} << H_0$ and $H_L << H_0$ both experiments correspond to a cooling of the I spin reservoir.

In the absence of any coupling between the I and S spins, each reservoir can be in equilibrium at a different spin temperature as indicated in equation (18). If the perturbation H_{1S} exists, however there will be a coupling between the reservoirs, and they will approach equilibrium. As pointed out before this rate will be slow unless the

Hartmann-Hahn conditions is close to being matched

$$\gamma_I H_{1I} \simeq \gamma_S H_{1S} \quad \text{for SL}$$

and

$$\gamma_I H_L \approx \gamma_S H_{1S} \quad \text{for ADRF} \tag{26}$$

Under such conditions the system will evolve from the initial conditions characterized by the temperature β_0 and β_S to the final equilibrium state given by the conservation of energy as

$$\beta_0 C_I H_{1I}^2 + \beta_S C_S H_{1S}^2 = \beta_1 C_I H_{1I}^2 + \beta_1 C_S H_{1S}^2$$

or

$$\beta_0 C_I H_L^2 + \beta_S C_S H_{1S}^2 = \beta_1 C_I H_L^2 + \beta_1 C_S H_{1S}^2 \tag{27}$$

Solving for the equilibrium spin temperature assuming $\beta_S \approx 0$ we obtain:

$$\beta_1 = \beta_0 \, (1 - \varepsilon\eta^2)^{-1} \tag{28}$$

where $\varepsilon\eta^2$ is the ratio of the S-spin and I-spin heat capacities and:

$$\varepsilon = \frac{N_S S(S + 1)}{N_I I(I + 1)}$$

with

$$\eta = \frac{\gamma_S H_{1S}}{\gamma_I H_L} \quad \text{for ADRF}$$

and

$$\frac{\gamma_S H_{1S}}{\gamma_I H_{1I}} \quad \text{for SL.} \tag{29}$$

The magnetization following this thermal mixing is:

$$M_S^{(1)} = \beta_1 C_S H_{1S}^2 = \beta_0 (1 + \varepsilon\eta^2)^{-1} \; C_S H_{1S}^2 \tag{30}$$

We now inquire by how much has the signal been enhanced from the normal FID, equation (23). This is for the S spin system,

$$\frac{M_S^{(1)}}{M_S^{(o)}} = \frac{\beta_1 C_S H_{1S}}{\beta_L C_S H_0} = \frac{H_{1S}}{H_{1I}} \quad (1 + \varepsilon\eta^2)^{-1} = \frac{\gamma_I}{\gamma_S} \eta (1 + \varepsilon\eta^2)^{-1} \tag{31}$$

If the Hartmann-Hahn condition is exactly matched $\eta = 1$ and

$$\frac{M_S^{(1)}}{M_S^{(o)}} = \frac{\gamma_I}{\gamma_S} \; \frac{1}{1 + \varepsilon} \tag{32}$$

for both S_L and ADRF. Then ε is usually small by virtue of experimental design, i.e., $N_S << N_I$ thus the maximum enhancement obeying $\eta = 1$ is γ_I/γ_S which is ≈ 4 for carbons and protons.

There are two ways of obtaining more of the polarization which is stored in the proton reservoir; one by performing multiple contacts and the other is to cross polarize such that $\eta >> 1$. This second case is what we term total cross polarization.

For the multiple contact case ($\eta = 1$) the signal enhancement after n contacts is, assuming ε is small,

$$\frac{M_S^{(n)}}{M_S^{(o)}} = \left(\frac{\gamma_I}{\gamma_S}\right) \; (1 - \varepsilon)^n \tag{33}$$

where we take the sum of all the n magnetizations for the final signal

obtained. This is a very time consuming process and in practice is restricted to 3-10 contacts for many systems. We wish instead to optimize the single contact cross polarization. These conditions are found by maximizing equation (29), obtaining

$$\eta = (\sqrt{\varepsilon})^{-1} \tag{34}$$

Experimentally this means we must increase H_{1S}, until the heat capacities of the I- and S-spins are equal. The maximum enhancement is then

$$\frac{M_S^{(1)}}{M_S^{(o)}} = \gamma_I/\gamma_S \quad \frac{1}{2\sqrt{\varepsilon}} \tag{35}$$

which is then one-half of the enhancement which would be obtained by a purely adiabatic transfer. However, we are no longer matched to the Hartmann-Hahn condition, which will severely slow the cross polarization process. If there are spin lattice relaxation mechanisms present whose characteristic relaxation times are of the same order as the cross polarization time we will not gain from this process. We must therefore consider the dynamics of the process before we can come to any conclusion about the relative merits of the SL and ADRF experiments.

C. Dynamics

The equations describing the dynamics of the cross relaxation are well known, and were first derived by Hahn and co-workers,[14,16] and later in more general form by Demco et al.[17] We will use the latter author's treatment of the Hamiltonian and sketch the former treatment of the dynamics. Beginning again with equation (5) we apply the r.f. irradiations

at frequencies ω_I and ω_S now no longer necessarily at resonance, and for the ADRF case we will take $\omega_{1I} = 0$. We now transform into the double rotating frame and tilt each frame so that the Z axis lies along the direction of quantization in each frame, which is defined by the effective field. The rotating frame transformation is defined by

$$R_I R_S = \exp(-\, i\omega_I I_Z t)\, \exp(-\, i\omega_S S_Z t) \tag{36a}$$

and the tilt by

$$T_I T_S = \exp(i\theta_I I_Y)\, \exp(i\theta_S S_Y) \tag{36b}$$

giving

$$H^* = -\, \omega_{eI}\, I_Z - \omega_{eS}\, S_Z + P_2(\cos\theta_I)\, H_{II}^{(o)} + H_{II}^{(ns)} + H_P \tag{37}$$

where the effective frequencies are $\omega_{eI} = [\omega_{1I}^2 + \Delta\omega_I^2]^{1/2}$ and $\omega_{eS} = [\omega_{1S}^2 + \Delta\omega_S^2]^{1/2}$ with $\Delta\omega_I = \omega_{0I} - \omega_I$ and $\Delta\omega_S = \omega_{0S} - \omega_S$.

The geometrical coefficient for $H_{II}^{(o)}$ indicates another truncation this time with respect to the effective field where $H_{II}^{(o)}$ has the same form as before, equation (1), but in the new axis system. $H_{II}^{(ns)}$ denotes the remaining nonsecular terms for the SL case. For the ADRF case $\omega_{1I} = 0$ and the effective field is the Zeeman field, so that $P_2(\cos\theta_I) = \frac{1}{2}(3\cos^2\theta_I - 1) = 1$. Thus for the SL case we drop $H_{II}^{(ns)}$ while it is kept for ADRF. The Hamiltonian H_P is the I-S dipolar coupling in the tilted axis system:

$$H_P = \cos\theta_I \cos\theta_S \sum_i b_i\, I_{iZ} S_Z + \sin\theta_I \sin\theta_S \sum_i b_i\, I_{iX} S_X$$

$$- \sin\theta_I \cos\theta_S \sum_i b_i\, I_{iX} S_Z - \cos\theta_I \sin\theta_S \sum_i b_i\, I_{iZ} S_X \quad . \tag{38}$$

To simplify matters we will choose to irradiate the protons on resonance (this will hold for Chapter 2 also) giving for SL

$$H_P = \sin\theta_S \sum_i b_i \, I_{iX} S_X - \cos\theta_S \sum_i b_i I_{iX} S_Z \tag{39a}$$

and for ADRF (where $\omega_{1I} = 0$):

$$H_P = \cos\theta_S \sum_i b_i \, I_{iZ} S_X - \sin\theta_S \sum_i b_i \, I_{iZ} S_X \tag{39b}$$

These equations point out the first real difference between the SL and ADRF case. For the ADRF case the I-spin Hamiltonian is the full rotating frame Hamiltonian, but for SL we truncate all of the interactions one step further, with respect to the effective field.

We must now solve the equation for the time evolution of the density matrix in the rotating frame

$$\frac{\partial \rho^*}{\partial t} = -i \, [H^*, \rho^*] \tag{40}$$

which we want to cast into the form of a differential equation for the macroscopic observables. (For a general discussion see Schumacher, ref. 30). These equations must also include the appropriate relaxation mechanisms which are indicated in Figure 1. For the I-spin system, in the SL state the process is spin lattice relaxation in the rotating frame characterized by $T_{1\rho I}$ and for ADRF the relaxation process occurs in the dipolar state with the time T_{1D}. The S-spin relaxation is also in the spin locked state with $T_{1\rho S}$. The differential equation for the time evolution of the inverse spin temperatures is then, for the ADRF state,

$$\frac{d\beta_S}{dt} = -(\beta_S - \beta_I)/T_{IS} - (\beta_S - \beta_L)/T_{1\rho}$$

$$\frac{d\beta_I}{dt} = -\varepsilon\eta^2(\beta_I - \beta_S)/T_{IS} - (\beta_I - \beta_L)/T_{1D} \tag{41}$$

where $\varepsilon\eta^2$ is the ratio of the heat capacities, equation (29), β_L is the laboratory inverse temperature, and T_{IS} is the characteristic time for cross polarization. T_{IS} may be calculated with the assumption of short correlation times from the master equation for the time rate of change of the density matrix.[18] This gives

$$\frac{1}{T_{IS}} = \frac{1}{\mathrm{tr}\, S_Z^2} \int_0^\infty d\tau\ \mathrm{tr}\{S_Z[H_P(0),\ [H_P(\tau),\ S_Z]]\} \tag{42}$$

where $H_P(\tau) = TH_PT^+$, $T = \exp[(H_{II} - \omega_{eS}\ S_Z)i\tau]$

or with a small rearrangement,

$$\frac{1}{T_{IS}} = \frac{1}{\mathrm{tr}\ S_Z^2} \int_0^\infty d\tau\ \mathrm{tr}\{[H_P, S_Z]\ T[H_P, S_Z]T^+\} \tag{43}$$

We evaluate the trace, tr_S (where $\mathrm{tr} \equiv \mathrm{tr}_I \mathrm{tr}_S$) in (43) giving:

$$T_{IS}^{-1} = \sin^2\theta_S\ M_{2IS} \int_0^\infty d\tau\ \cos(\omega_{eS}\tau)C(\tau)$$

$$C(\tau) = \frac{\mathrm{tr}_I\left(\sum_i b_i I_{iP}\ \exp(iH_{IP}\ \tau) \sum_i b_i I_{iP}\ \exp(-iH_{IP}\ \tau)\right)}{\mathrm{tr}_I\left(\sum_i b_i I_{iP}\right)^2} \tag{44}$$

where M_{2IS} is the Van Vleck second moment of the S magnetic resonance line:[19]

$$M_{2IS} = \frac{\mathrm{tr}\ [H_{IS},\ S_X]^2}{\mathrm{tr}\ S_X^{\ 2}} \tag{45}$$

and p = X for SL and p = Z for ADRF. $H_{II}^{(o)}$ is the normal high field truncated dipole-dipole Hamiltonian. For ADRF $\omega_{1I} = 0$ and then $\theta_I = 0°$, giving the effective I-I dipole interaction as

$$H_{IZ} = H_{II}^{eff} = P_2\ (\cos\theta_I)\ H_{II}^{(o)} = H_{II}^{(o)}$$

as we expect. But for the SL case $\omega_{1I} \neq 0$ and $\theta_I = 90°$ if we apply the r.f. irradiation at resonance. We must then truncate the dipole-dipole Hamiltonian one more time, in this case with respect to the rotating frame defined by the effective field then:

$$H_{IX} = -\ \omega_{1I}\ I_X + H_{II}^{eff}$$

$$H_{II}^{eff} = P_2\ (\cos\theta_I)\ H_{II}^{(o)} = -\ \frac{1}{2}\ H_{II}^{(o)} \quad .$$

$C(\tau)$ is the auto correlation function of the perturbation, the heteronuclear dipole-dipole interaction. Taking the integral in (44) gives the corresponding spectral density with the final result for ADRF

$$T_{IS}^{-1} = \sin^2\theta_S\ M_{2IS}\ \ J_Z(\omega_{eS}) \tag{46}$$

and for SL (see Appendix 2.3 and reference 17 for details)

$$T_{IS}^{-1} = \frac{1}{2}\ \sin^2\theta_S\ M_{2IS}\ J_X(\Delta\omega_e) \tag{47}$$

where $\Delta\omega_e = (\omega_{eS} - \omega_{eI})$. The spectral densities are given as

$$J_X(\omega) = \int_0^\infty d\tau \cos\omega\tau \; c_X(\tau)$$

$$J_Z(\omega) = \int_0^\infty d\tau \cos\omega\tau \; c_Z(\tau) \tag{48}$$

and the correlation functions are

$$c_X(\tau) = \frac{\mathrm{tr}\,\left(\sum_i b_i\, I_i \;\exp(i(-\frac{1}{2} H_{II}^{(o)}\tau))\; \sum_i b_i\, I_{iX} \exp(-i(-\frac{1}{2} H_{II}^{(o)}\tau))\right)}{\mathrm{tr}\,\left(\sum_i b_i\, I_{iX}\right)^2}$$

$$c_Z(\tau) = \frac{\mathrm{tr}\,\left(\sum_i b_i\, I_{iZ} \exp(iH_{II}^{(o)}\tau)\; \sum_i b_i\, I_{iZ} \exp(-iH_{II}^{(o)}\tau)\right)}{\mathrm{tr}\,\left(\sum_i b_i\, I_{iZ}\right)^2} \tag{49}$$

This, then, shows that the spin fluctuations due to the I-I dipolar coupling is communicated to the S-spins via the I-S dipolar interaction, these fluctuations induce flip-flop transitions between the I and S spins equalizing the energies of the two reservoirs. The rate of the process will be proportional to the intensity (spectral density) of the fluctuations at the difference of the precession frequencies of the S and I spins in their effective fields. If the precession frequencies are equal a flip-flop transition between an I and S spin will conserve energy and this then will be a very rapid process.

We now wish to combine the thermodynamics and the dynamics to describe the growth of the S-spin magnetization during the cross polarization process. The thermodynamics provide the limiting state for the S magnetization equation (31), and we wish to solve equation (41) for the evolution towards this limiting value. For the case at hand we may neglect the $T_{1\rho S}$ term simplifying matters considerably. The solution

of equation (41) with boundary conditions $\beta_S(o) = 0$ and $\beta_I(o) = \beta_I$ and assuming $\beta_L \approx 0$ gives

$$\beta_S(t) = \frac{\beta_I}{T_{IS}(\alpha_+ - \alpha_-)} (e^{-\alpha_- t} - e^{-\alpha_+ t}) \tag{50}$$

with

$$\alpha_\pm = \frac{1}{2}\left(\frac{1+\varepsilon\eta^2}{T_{IS}} + \frac{1}{T_{1D}}\right) \pm \frac{1}{2}\left[\left(\frac{1+\varepsilon\eta^2}{T_{IS}} + \frac{1}{T_{1D}}\right)^2 - \frac{4}{T_{IS}T_{1D}}\right]^{1/2}$$

The maximum inverse temperature will be for $t = \infty$ and $T_{1D} = \infty$. This gives:

$$\sigma^{(o)}(\infty) = \beta_I/1+\varepsilon\eta^2 \quad \text{and} \quad \beta_I = \beta_L \mu\, H_0/H_L \tag{51}$$

where the superscript o indicates the ideal case where $T_{1D} = \infty$.
We have also introduced the constant μ to account for the fact that the demagnetization is not perfect, some order is lost. Then μ is the efficiency of the demagnetization process in the rotating frame. Using equation (22) we derive

$$\frac{M_o(t)}{M_S^{(o)}} = \frac{\mu\eta}{T_{IS}(\alpha_+ - \alpha_-)} (e^{-\alpha_- t} - e^{-\alpha_+ t}) \tag{52}$$

where for $t = \infty$ and $T_{1D} = \infty$

$$\frac{M_S^{(o)}(\infty)}{M_S^{(o)}} = \mu \frac{\gamma_I}{\gamma_S} \left(\frac{\eta}{1+\varepsilon\eta^2}\right) \tag{53}$$

Note that T_{IS} is a function of η also.

Then, while the magnetization is increasing due to cross polarization it is being destroyed by spin lattice relaxation. The technique which

will be most successful for a particular η, will be the one which gives the shortest T_{IS}. From general considerations we expect the spectral density to be broader for the ADRF case, making it the likely choice if we wish to approach total cross polarization.

The complete solution of the dynamics is obtained by the maximization of equation (52) with respect to t and η, given the relaxation times, T_{1D} and $T_{1\rho}$ and the functional dependence of T_{IS} on η. This functional dependence is discussed in the next section for the ADRF case. The results for the SL case are also given for reference in the second chapter.

D. Correlation Time

We now wish to characterize the correlation functions in equation (49). The exact solution would, of course, involve solving the complete manybody problem. We must choose either an empirical form, or a form determined directly from experiment. In the experimental section that follows we show that the spectral density for the ADRF experiment is exponential over much of its range, giving upon Fourier transformation a Lorentzian correlation function. This agrees with the results of Mc Arthur et al.[14] for CaF_2, and the theoretical study by Demco et al.[17] using a memory function approach. This latter study also shows the spin locked state will give rise to an approximately Gaussian correlation function and spectral density. This is an important distinction since for the same value of the correlation time an exponential spectral density will give more intensity at high fluctuation frequencies then a Gaussian function.

Using the Lorentzian function for the ADRF correlation function

$$C_Z(\tau) = (1 + \tau^2/\tau_c^{\,2})^{-1}$$

giving

$$J_Z(\omega) = \frac{\pi}{2}\,\tau\, e^{-\omega\tau_c} \tag{54a}$$

Mc Arthur et al. calculate

$$T_{IS}^{-1} = \frac{\pi}{2}\sin^2\theta_S\, M_{2IS}\,\tau_c\,\exp(-\omega_{eS}\,\tau_c) \tag{55}$$

and expanding equations (49) and (54) in a power series and equating the coefficients of τ^2 gives

$$\tau_c^{-2} = -\frac{1}{2}\,\frac{\mathrm{tr}\,[H_{II}, \sum_i b_i\, I_{iZ}]^2}{\mathrm{tr}\,[\sum_i b_i\, I_{iZ}]^2} \tag{56}$$

The correlation time, for the rigid lattice, is seen to be a function purely of the lattice parameters through the coefficients a_{ij} and b_i.

For the SL case we choose a Gaussian correlation function

$$C_X(\tau) = e^{-\tau^2/\tau_i^2} \tag{54b}$$

from which,

$$J_X(\omega) = \sqrt{\frac{\pi}{2}}\,\tau_c\, e^{-\omega^2\tau_c^2/4} \tag{54c}$$

and

$$T_{IS}^{-1} = \sqrt{\frac{\pi}{2}}\,\frac{\sin^2\theta_S}{2}\, M_{IS}\,\tau_c\,\exp^{-\omega_e^2\tau_c^2/4} \tag{55b}$$

At this point we wish to be quite precise about our definitions, since there is much confusion in the literature. Even though the Hamiltonian in equations (1), (6), and (7) are the standard forms, in order to be consistent with the work of Canters and Johnson[20] and Demco et al.[17] we introduce new constants as they are defined in Van Vleck's work. Here:

$$H_{II}^{(o)} = \sum_{i<j} -3 \frac{\gamma_I^2 \hbar}{r_{ij}^3} \frac{1}{2} (3 \cos^2\theta_{ij} - 1) \{I_{iZ} I_{jZ} - \frac{1}{3} \underset{\sim}{I}_i \underset{\sim}{I}_j\}$$

and

$$A_{ij} = -3 \frac{\gamma_I^2 \hbar}{r_{ij}^3} \frac{1}{2} (3 \cos^2\theta_{ij} - 1) \tag{57}$$

$$H_{IS} = \sum_i -2 \frac{\gamma_I \gamma_S \hbar}{r_i^3} \frac{1}{2} (3 \cos^2\theta_i - 1) (I_{iZ} S_Z)$$

with

$$B_i = 2 \frac{\gamma_I \gamma_S \hbar}{r_i^3} \frac{1}{2} (3 \cos^2\theta_i - 1) \tag{58}$$

The correlation time is given by the second moment of the correlation function as (see equation (56))

$$\tau_c = (2/M_2)^{1/2} \tag{59}$$

carrying out the commutators and traces in equation (56) gives for the second moment of the correlation function:

$$M_2 = M_4^{ISII} / M_{2IS} = \frac{I(I+1)}{27} \frac{\sum_{i \neq j} A_{ij}^2 (B_i - B_j)^2}{\sum_i B_i^2} \tag{60}$$

where M_4^{ISII} is the standard fourth moment of the absorption line shape of an S spin due to surrounding abundant I-spins and M_{2IS} is the normal second moment of the S-spins due to the surrounding I-spins. This notation is that of Abragam.[18]

We may rewrite (60) in terms of the lattice sums normally used in moment calculations as

$$\frac{M_4^{ISII}}{M_{2IS}} = \frac{2I(I+1)}{27} \left(\frac{S_1 S_2 - 2S_4}{S_1}\right) \tag{61}$$

with

$$S_1 = \sum_i B_i^2$$

$$S_2 = \sum_i A_{ij}^2$$

$$S_4 = \sum_i A_{ij}^2 B_i B_j \tag{62}$$

or finally $\tau_c^{-2} = \frac{I(I+1)}{27} \left(\frac{S_1 S_2 - 2S_4}{S_1}\right)$ (63)

We note parenthetically that using the definitions (8)

$$\frac{M_4^{ISII}}{M_{2IS}} = \frac{2S(S+1)}{3} \left(\frac{Q_1 Q_2 - 2Q_4}{Q_1}\right)$$

where

$$Q_1 = \sum_i b_i^2$$

$$Q_2 = \sum_i a_{ij}^2$$

$$Q_4 = \sum_{i<j} a_{ij}^2 \; b_i b_j$$

To evaluate the traces we used[21]

$$\mathrm{tr}\; I_X^2 = \mathrm{tr}\; I_Y^2 = \frac{1}{3}\, I(I+1)\;(2I+1)^N$$

where

$$I_X = \sum_i I_{iX} \quad \text{for N spins.} \tag{64}$$

For the SL case the second moment of the fluctuation correlation function may also be obtained in the same manner[17] with:

$$M_2 = P_2(\cos\theta_I)^2\, \frac{2I(I+1)}{27}\, \left(\frac{5\; S_1 S_2 + 8\; S_4}{S_1}\right) \tag{61b}$$

Note that if the proton irradiation is applied at resonance

$$M_2 = \frac{1}{4}\, \frac{2I(I+1)}{27}\, \left(\frac{5\; S_1 S_2 + 8\; S_4}{S_1}\right) \tag{61c}$$

The correlation time is still given by equation (59). We can now calculate the ratio between the SL and ADRF correlation times,

$$\frac{\tau_{c\;SL}^2}{\tau_{c\;ADRF}^2} = \frac{4}{5}\, \frac{S_1 S_2 - 2\; S_4}{S_1 S_2 + \frac{8}{5}\, S_4}$$

If $S_4 << S_1S_2$ as we might be led to expect from calculations of the lattice sums (see Table 1) we find that:

$$\frac{\tau^2_{c\ SL}}{\tau^2_{c\ ADRF}} \approx \frac{4}{5} \text{ giving } \frac{\tau_{c\ SL}}{\tau_{c\ ADRF}} = 0.894$$

that is τ_c for SL is shorter than ADRF. Note that <u>if</u> the correlation functions for the two cases were the same this would imply that the SL case would have larger spectral density at higher frequency. But because the SL correlation function is Gaussian this is not true.

We wish to find the correlation time for a polycrystalline sample of adamantane which has an FCC structure.[27] Adamantane rotates rapidly in the solid at room temperature, so that initially we assume that each adamantane molecule can be approximated as 16 protons at each lattice point. We choose the origin as a single carbon-13 occupying one of the lattice sites, which will not interact with the protons in the same molecule because of the rapid orientational averaging.

The lattice sums have been computed by Canters and Johnson,[20] Mc Arthur <u>et al.</u>[14] and by Demco <u>et al.</u>[17] for a simple cubic lattice. We extend this to an FCC lattice and carry out the orientational averaging necessary for a powdered sample. The lattice sums for the CaF_2 structure (cubic for the F atoms with the Ca surrounded by a tetrahedron of F atoms) and for adamantane (FCC) are listed in Table 1 along with the results of Demco <u>et al.</u> for two orientations, a) for H_o along the 100 direction and b) along the 110 direction.

Table 1. Lattice sums for simple cubic and FCC lattices

Structure	Direction of H_o	S_1'	S_2'	S_4'	T_c (μsec)
CaF_2	100	1.564	30.03	9.179	42.76
	110	20.24	11.36	21.50	60.19
FCC	100	1.073	2.414	0.2514	149.4
	110	1.534	3.451	0.1994	116.6
CaF_2 [17]	100	1.554	30.01	9.985	44.16
	110	20.34	11.36	22.32	60.42

Here we list the sums as unitless quantities with

$$S_1 = \left(\frac{\gamma_I \gamma_S \hbar}{a^3}\right)^2 S_1' \; ; \; S_2 = \left(\frac{\gamma_I^2 \hbar}{a^3}\right)^2 S_2' \quad \text{and} \quad S_4 = \frac{(\gamma_I^2 \hbar)^2 \, (\gamma_I^+ \gamma_S^+ \hbar)^2}{a^{12}} S_4' \tag{65}$$

$$\text{and } M_2 = f\left(\frac{S_1' S_2' - 2 S_4'}{S_1'}\right) \tag{66}$$

$$\text{with } f = \frac{1}{18} \frac{\gamma_I^4 \hbar^2}{a^6} N_{site}$$

where a is the lattice spacing and N_{site} is the number of spins at each lattice site. For adamantane the unit cell size is 9.43 Å,[22] N site = 16 giving $f = 4.61 \times 10^7 \text{ sec}^{-2}$. See appendix 1.3 for the details of the computer program used to calculate the lattice sums. For CaF_2 the unit cell size is 5.46 Å, N site = 1, and $f = 5.98 \times 10^7 \text{ sec}^{-2}$.

Our lattice sums compare favorably with reference 17 even though we took only 1331 F atoms to calculate S_1 and S_2 and 125 for S_4. The FCC calculations used 343 molecules for S_1 and S_2 and 64 for S_4.

The sums did not change significantly upon increasing the number of molecules to 512 for S_1 or S_2 ($\sim$ 0.02% change) or upon decreasing the number to 27 for S_4 (2.5% change).

The lattice sums for θ = 0-90° and ϕ = 0-45° where θ and ϕ are the normal polar angles are compiled in appendix 1.1. The orientation dependence of τ_c is shown in Figures 4 and 5 for rotations of the lattice about the 100 (θ = 90°, ϕ = 0°) and the 110 (θ = 90°, ϕ = 45°) axis. The integration to find the powder average was carried out as

$$\bar{\tau}_c = \int_0^{\pi/4} d\phi \int_0^1 d \cos\theta \; \tau_c(\theta,\phi) \tag{67}$$

where ϕ and $\cos\theta$ were generated in equal steps to give intervals of equal area on the sphere and where we have taken advantage of the symmetry of the crystal by integrating only over θ = 0-90° and ϕ = 0-45°. Both integrations were done numerically by Simpson's integration over 121 different orientations, giving the final result

$$\bar{\tau}_c = 122 \ \mu\text{sec} \tag{68}$$

and the powder averaged 2nd moments

$$M_{2IS} = \frac{1}{3} I(I+1) \quad S_1 = 1.90 \times 10^7 \ \text{rad}^2\text{sec}^{-2} \tag{69}$$

We now inquire about the assumption that the spins sit exactly on the lattice points. We should actually find the averaged interaction,

$$\int \frac{P_2(\cos\theta)}{r^3} \; dS_1 \; dS_2$$

Figure 4. Orientation dependence of τ_c for adamantane as the crystal is rotated about the 100 axis.

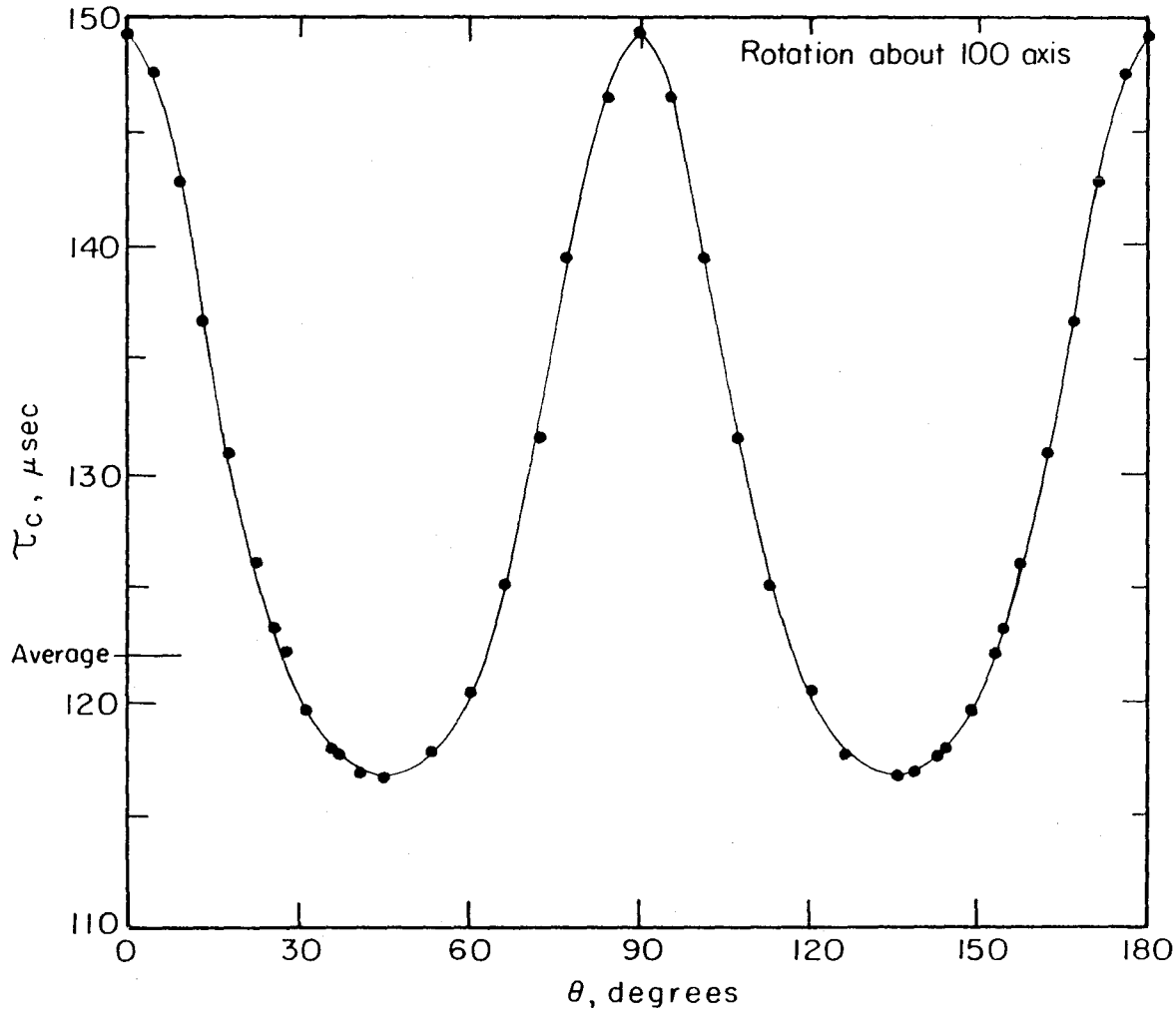
Rotation about 100 axis
150
140
130
Average
120
110
τ_c, μsec
0
30
60
90
120
150
180
θ, degrees

XBL 751-5608

Figure 5. Orientation dependence of τ_c for adamantane as the crystal is rotated about the 110 axis.

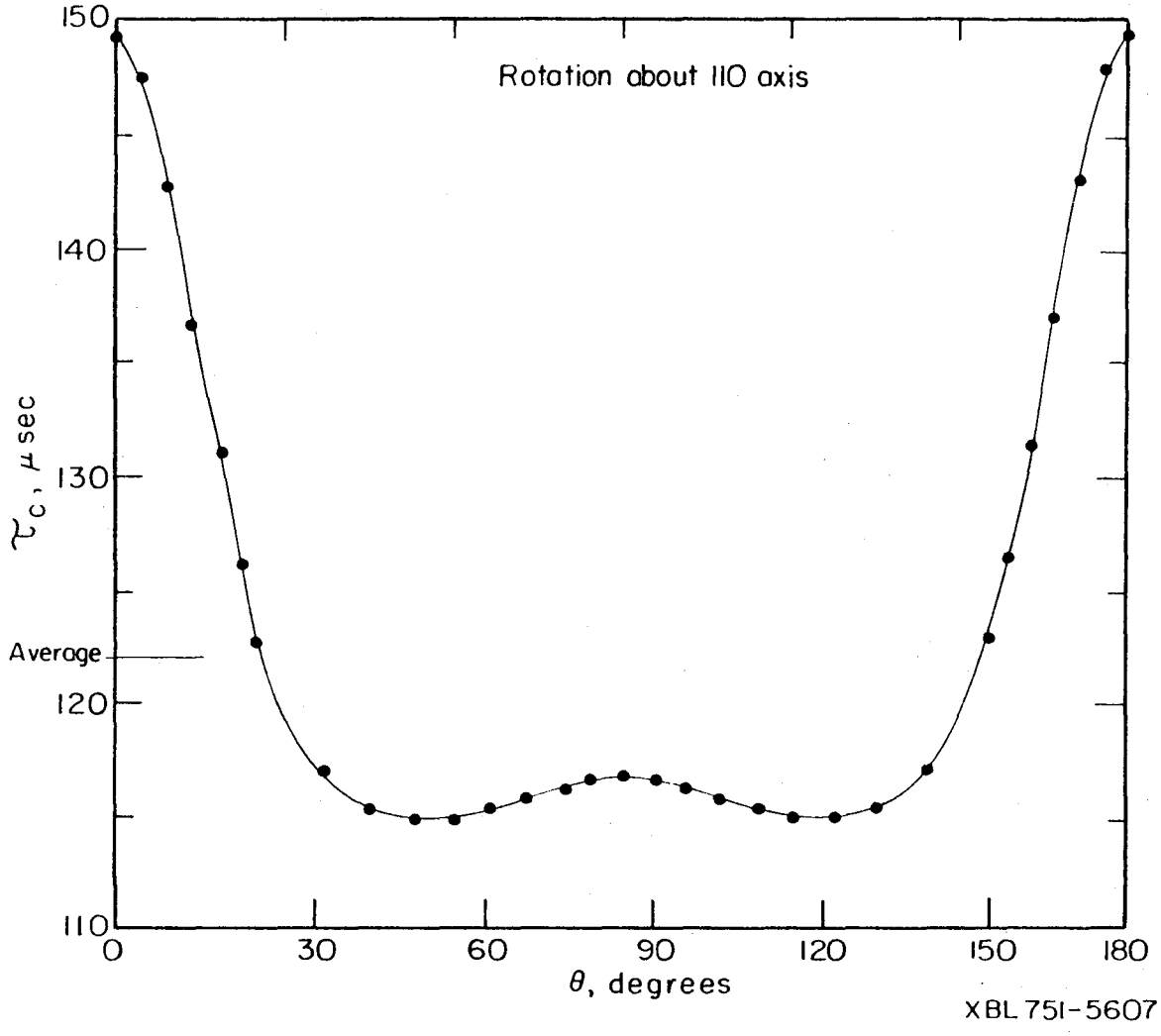
Rotation about 110 axis
150
140
130
120
110
Average
τ_c, μsec
0
30
60
90
120
150
180
θ, degrees
XBL 751-5607

where dS_1 dS_2 denote integration variables over two spheres with distance R between their centers. This integration shows that the above assumption is actually rigorous, as has been indicated by several authors.[32-37] That is, we can exactly calculate τ_c in the presence of isotropic motion over two non-overlapping spheres by placing the spins at the center of each of the spheres. This is discussed in more detail in appendix 1.2, along with a discussion of the polycrystalline averaging.

IV. Experimental

A. Sample

Adamantane was chosen for the cross polarization study for three reasons

1) Adamantane is essentially a rigid lattice solid. However the rapid rotation of the entire molecule shortens the relaxation times into a convenient range (≈ 1 sec.). T_1 is short enough to allow a fast repetition rate and T_{1D} is long enough compared to the cross polarization times ($T_{IS} \approx T_2$).

2) The molecular rotation narrows the lines, and averages the dipole-dipole interaction between directly bonded carbon proton pairs. The effect of these very strong dipolar interactions is the appearance of coherence oscillations in the cross polarization curves.[25]

3) There is a high density of carbons giving rise to very large signals, which are observed with a 30 to 1 signal to noise ratio for the optimum cross polarization conditions.

Adamantane (Aldrich 99+%) was used without further purification. Recrystallization followed by sublimation did not change any of the relaxation properties. The crystal structure is FCC with a lattice spacing of 9.43 Å.[22]

B. Spectrometer

The spectrometer was homebuilt, operating at ∿ 25 K gauss with a Westinghouse superconducting magnet. The proton resonance frequency was 106.3 Mhz and the carbon 26.7 Mhz. The schematic for the spectrometer and the probe are shown in Figure 6. Details are to be published separately.[26] The proton transmitter is a modified Millen radio amateurs transmitter

Figure 6. Schematic of the 106.34 MHz spectrometer and probe.

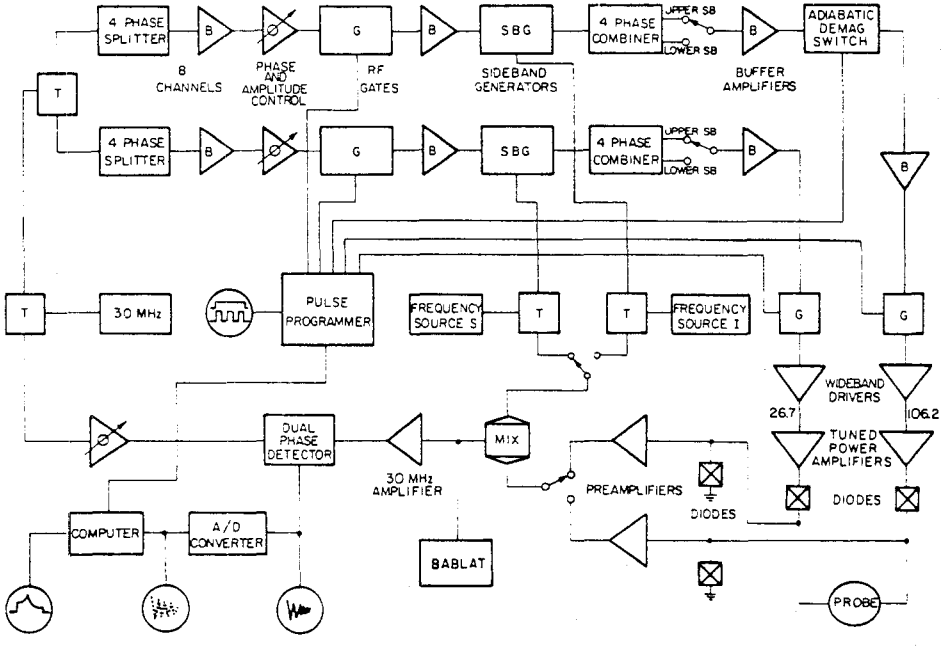

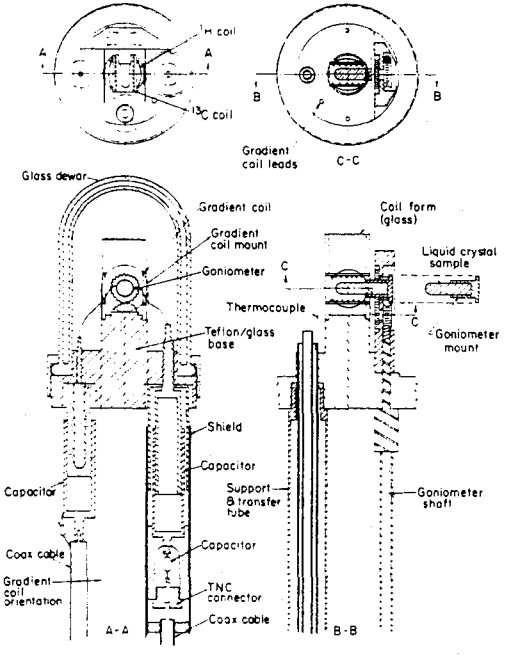

XBL 749-4022A

operatingat an output power of $\sim$ 200 watts. The Carbon-13 transmitter is an ENI 350 L operating at 50 watts. Repetitive spectra are averaged and Fourier transformed with an on-line PDP-8 computer. Only one channel of the phase detector can be observed at a time, this causes the complex Fourier transform spectrum to "fold over". That is, positive and negative frequencies with respect to the irradiation frequency cannot be distinguished.

One unique feature of the spectrometer is the adiabatic switch which is used to adiabatically demagnetize the protons in the following cross polarization experiments. A digital ramp is generated using a D-A converter (Zeltex ZD432) which is converted into a power law function (Z^m) with desired exponent positive or negative by a hybrid multifunction generator (Analog Devices 433).

Temperature control is achieved using a flow of nitrogen gas heated with a small tungsten wire coil. The gas is flowed in and out of the probe through an evacuated transfer line. The temperature is monitored with a copper-constantan thermocouple, which is tied into the feedback loop controlling the heater.

C. Adamantane dynamics

The cross polarization time can be easily extracted by monitoring the intensity after a cross polarization time τ. If one knows the relevant relaxation times the experimental curves can be fit by equation (52). The spectral density can be found by varying the carbon effective field and extracting the cross polarization time. A plot of T_{IS} versus ω_e then yields exactly the spectral density. This in turn may be Fourier transformed if desired to obtain the correlation function, whose second

moment will yield the correlation time τ_c. We have chosen the ADRF experiment from which to extract the dynamics for these reasons:

1) the analysis is simpler

2) the stability requirements for the r.f. power is much less stringent since there is only one r.f. field applied during cross polarization and

3) we expect the proton dipolar state to have a broader spectral density than the spin locked state allowing a greater mismatch in the Hartmann-Hahn condition and therefore a closer approach to total cross polarization.

The experiments were all carried out with simultaneous proton decoupling during the observation of the carbon signals. The decoupling field strength was $\nu_{1I} \approx 26$ khz $\equiv 6.1$ gauss. The adiabatic demagnetization times were varied from 1-10 msec, while the maximum signals occured at 2 msec, which is the value used for the following experiments. The carbon field strengths were calibrated using simple 180° pulse width measurements. The temperature in the probe was 10-13° C. The experiment repetition rate was 8 sec.

1. Relaxation times

The proton relaxation time T_{1D} was determined by the standard technique of an ADRF followed at time τ with a 45° pulse which probes the dipolar order. The results are shown in Figure 7. The deviations at short times are as yet unexplained, but are quite reproducible. The relaxation time extracted is

$$T_{1D} = 0.30 \pm .01 \text{ sec.} \tag{73}$$

Figure 7. Proton dipolar relaxation time in adamantane, T_{1D}. The temperature was 13 ± 3°C and the pulse sequence used was the standard ADRF (for 2 msec) followed at time τ by a 45° pulse. The solid line is the exponential least square fit, omitting times shorter than 50 msec. The amplitude of the normal pulse FID is also shown, and was obtained from a solid echo experiment. The zero time intercept of the T_{1D} curve can then be used to calculate the efficiency of the ADRF, μ.

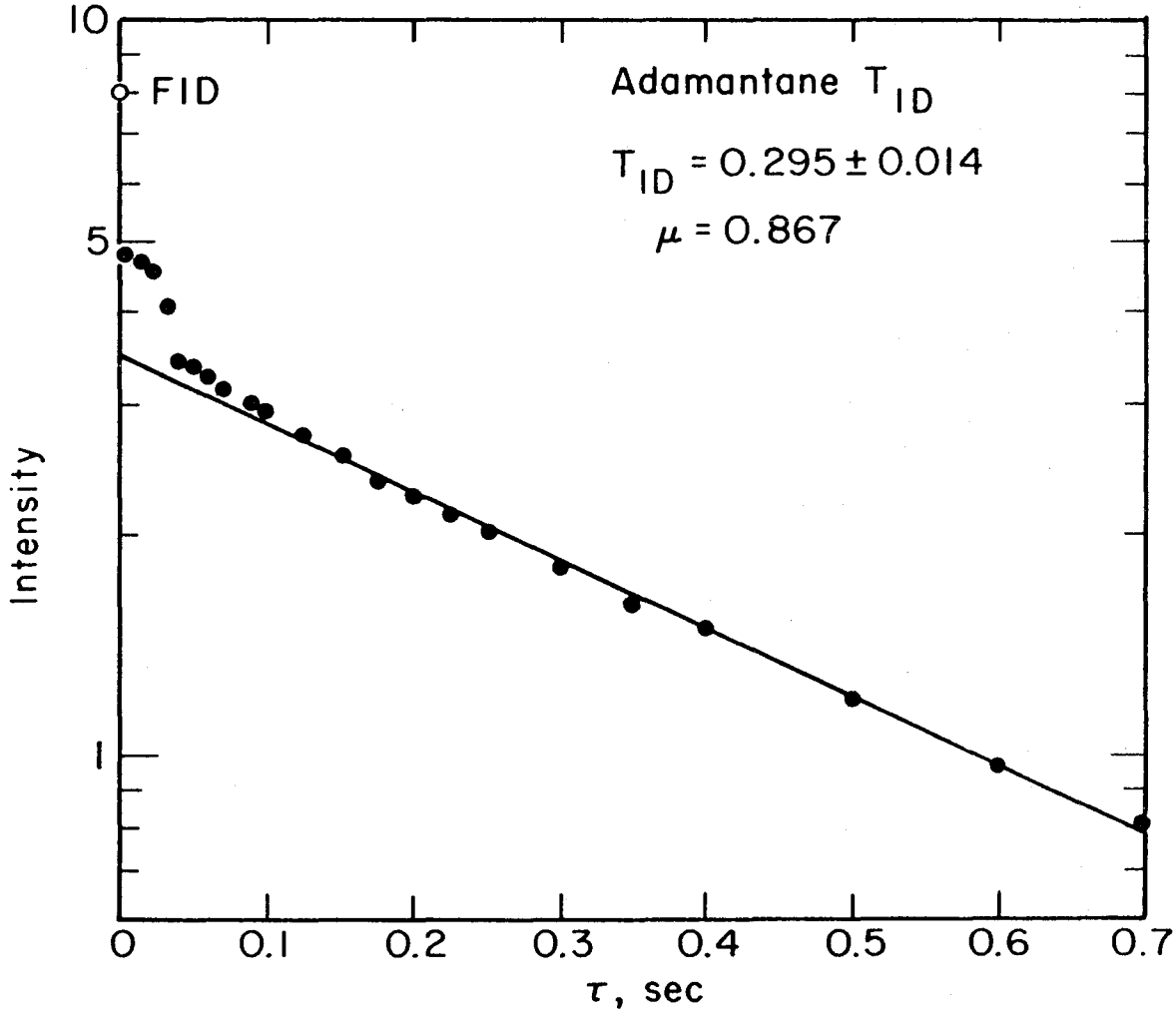
10
5
1
FID
Adamantane T_{1D}
T_{1D} = 0.295 ± 0.014
μ = 0.867
Intensity
0
0.1
0.2
0.3
0.4
0.5
0.6
0.7
τ, sec

XBL 765-1984

The $T_{1\rho}$ for the carbons was measured for H_{1S} = 6.6 kHz ≡ 6.18 gauss (see Figure 9) and found to be

$$T_{1\rho} = 3.39 \text{ sec} \tag{74}$$

The experiment consisted of a SL type cross polarization, after which the proton field was turned off allowing the carbon spin locked state evolve for a time τ, after which the signal was detected with simultaneous proton decoupling. The pulse sequence is shown in Figure 8. The relaxation times were found using exponential least mean squares. The details of all the fitting programs are to be found in appendix 1.3. Since $T_{1\rho}$ is approximately one or two orders of magnitude greater than the expected cross polarization times we can use equation (52) safely to fit the cross polarization curves.

We must also find the efficiency of the demagnetization. This was easily calculated knowing that the height of the derivative FID after the 45° pulse for t = 0 in the T_{1D} experiment should be 0.525 of the normal FID,[12] assuming a purely Gaussian proton lineshape. The initial height for the T_{1D} experiment was obtained by extrapolating the line in Figure 8 to $\tau = 0$. The height of the normal FID was obtained by extrapolating the height of a solid echo (90-τ-90) to $\tau = 0$. The ratio of the two divided by 0.525 gives

$$\mu = 0.87 \pm .03 \tag{75}$$

The extrapolation to $\tau = 0$ was accomplished by a linear least squares fit to a Gaussian function

$$I = a\ e^{-t^2/\omega^2}$$

Figure 8. Pulse sequences for direct detection of cross polarization. The pulse sequences used for an initial dipolar state (ADRF) and an initial spin locked state (SL) are shown in (a) and (b) respectively. $T_{1\rho}$ of the S spins is measured by polarization of the S spins for a time τ after which the I spin irradiation is turned off. The S-spins spin locked state is then allowed to evolve for time τ after which the polarization is monitored with simultaneous spin decoupling.

a) ADRF

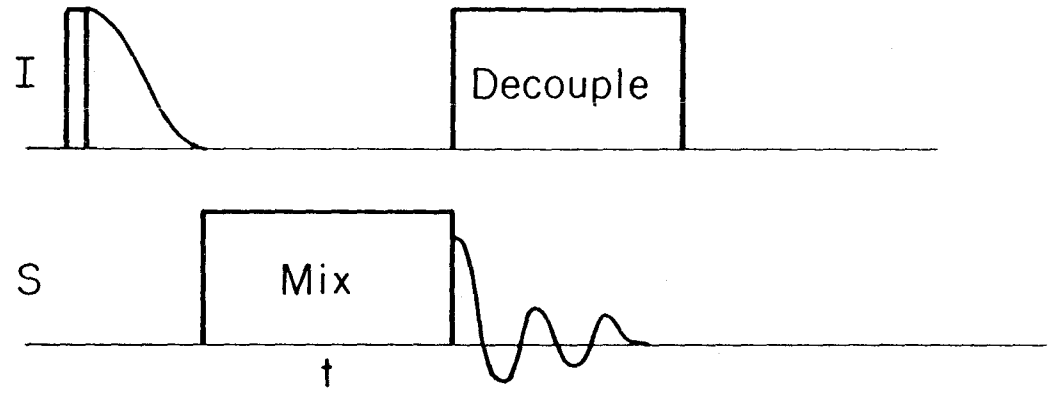

b) S. L.

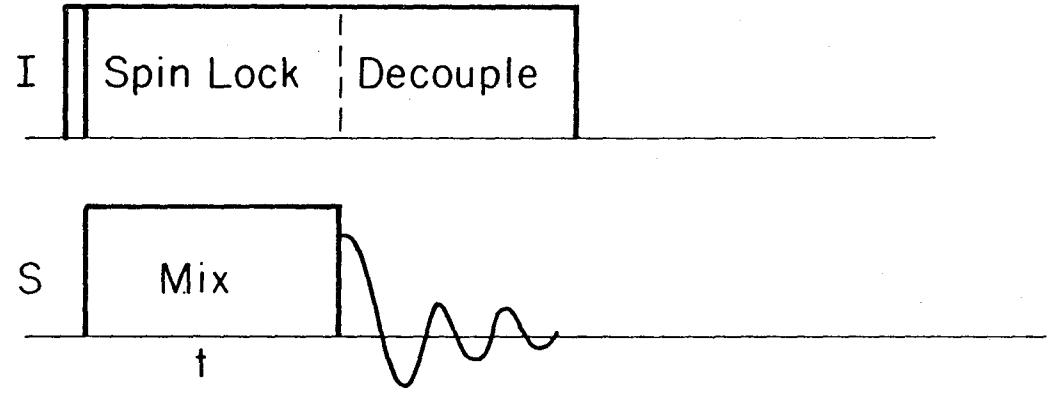

c) $T_{1\rho}$

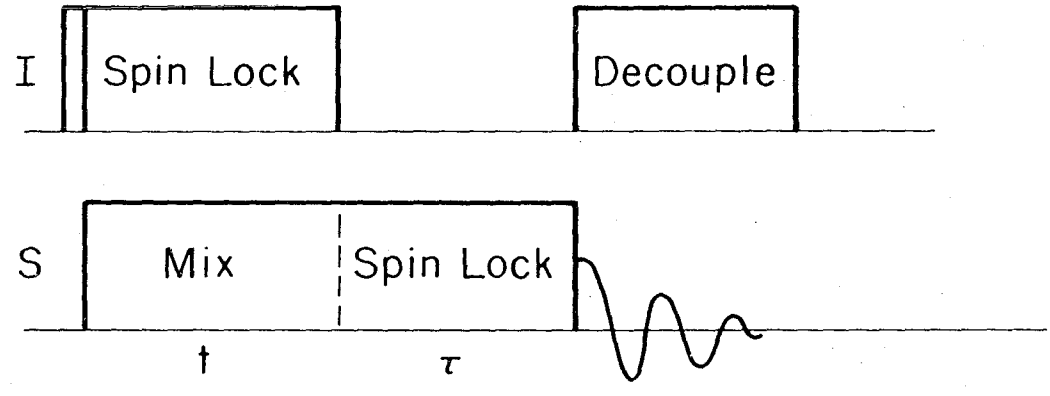

XBL 765-1985

Figure 9. Carbon rotating frame relaxation time, $T_{1\rho}$ for adamantane. The temperature was 13 ± 3°C and the carbon field strength was ν_{1S} = 6.6 kHz (H_{1S} = 6.18 gauss). The solid line is the exponential least squares fit to the data.

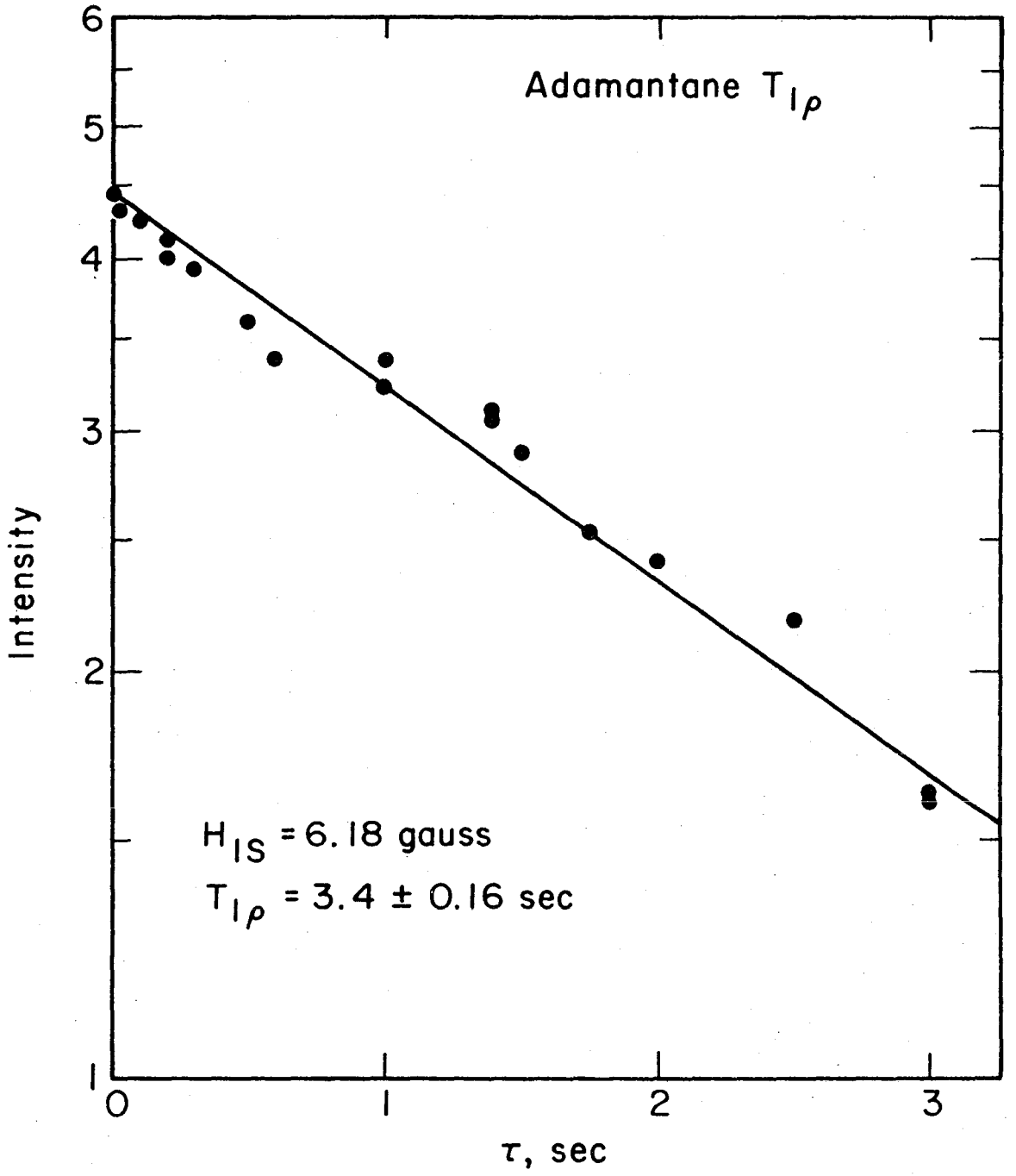
Adamantane $T_{1\rho}$
H_{1S} = 6.18 gauss
$T_{1\rho}$ = 3.4 ± 0.16 sec
Intensity
τ, sec
6
5
4
3
2
1
0
1
2
3

XBL 765-1983

2. Cross polarization

A typical cross polarization curve is shown in Figure 10. The maximum enhancement over the normal FID we obtained was x 15. This was obtained after eliminating the Overhauser effect from the normal FID by turning the proton transmitter off during the time between experiments. Knowing the relaxation parameters and the efficiency we can now carry out a least squares fitting procedure, the results are given in Table 2, and in Figure 11. The fitting was carried out by varying the two parameters T_{IS} and H_L. The average H_L found from these data was $H_L = 0.37$ gauss whereas the value expected from Resing's work was 0.544 gauss.[23]

The spectral density function, Figure 11, see equation (46), is seen to be exponential over most of the range we studied. The flattening for small ω appears to be real and this feature had been reproduced by the memory function theory of Demco et al.[17] This occurs because of the breakdown of the short correlation time assumption that was used to extend the range of integration in equation (42) to infinity. The long tail for large ω on the other hand is an artifact caused by the neglect of the carbon $T_{1\rho}$. The cross polarization times are of the same order of magnitude as the $T_{1\rho}$ for these data points.

The cross polarization times were fitted to an exponential function. The experimental points obtained while on resonance, Figure 12, are the most accurate for this purpose since they provide better signal to noise over a larger range of ω_e. We choose to omit the points 1 and 2 (large ω) for the above reason. The correlation time is then found to be

$$\tau_c = 108 \pm 5 \ \mu\text{sec} \tag{76}$$

Figure 10. Typical cross polarization curve for adamantane, from the dipolar state (ADRF). Demagnetization time was 2 msec, the temperature was 13 ± 3°C, the frequency offset for the carbons was $\frac{\delta\nu}{2\pi}$ = +5.24 kHz, the effective field was H_e = 10.6 gauss. The cross polarization time was 1.07 sec.

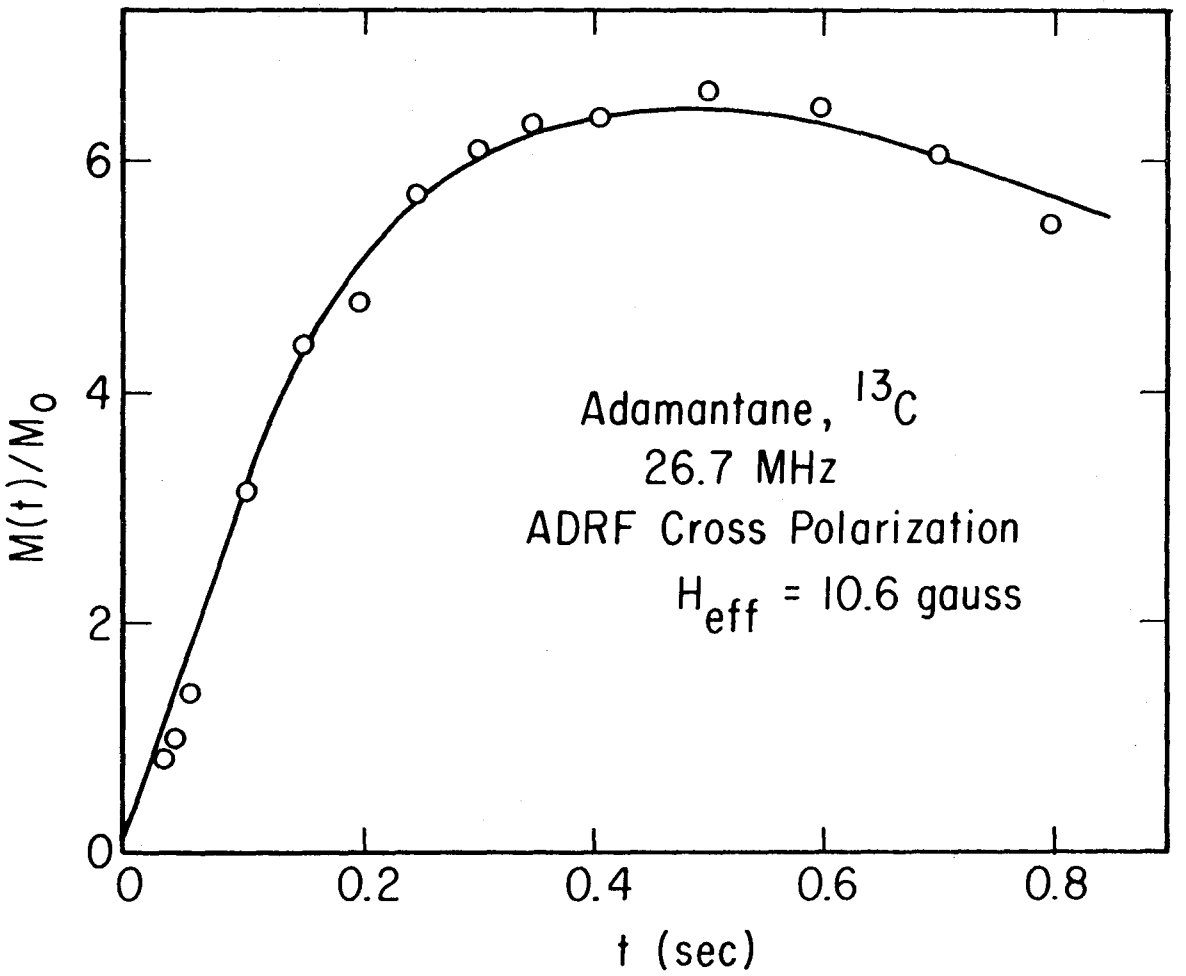
Adamantane, ^{13}C
26.7 MHz
ADRF Cross Polarization
H_{eff} = 10.6 gauss
M(t)/M$_0$
t (sec)
0
2
4
6
0
0.2
0.4
0.6
0.8

XBL 765-1847

Figure 11. Dependence of the cross polarization time T_{IS} on rotating ^{13}C H_1 field and frequency offset, in adamantane. The frequency offsets are ⊖, $\delta\omega = 0$; ▲, $\frac{\delta\nu}{2\pi} = +2.74$ kHz; ⊡, $\frac{\delta\nu}{2\pi} = +5.24$ kHz.

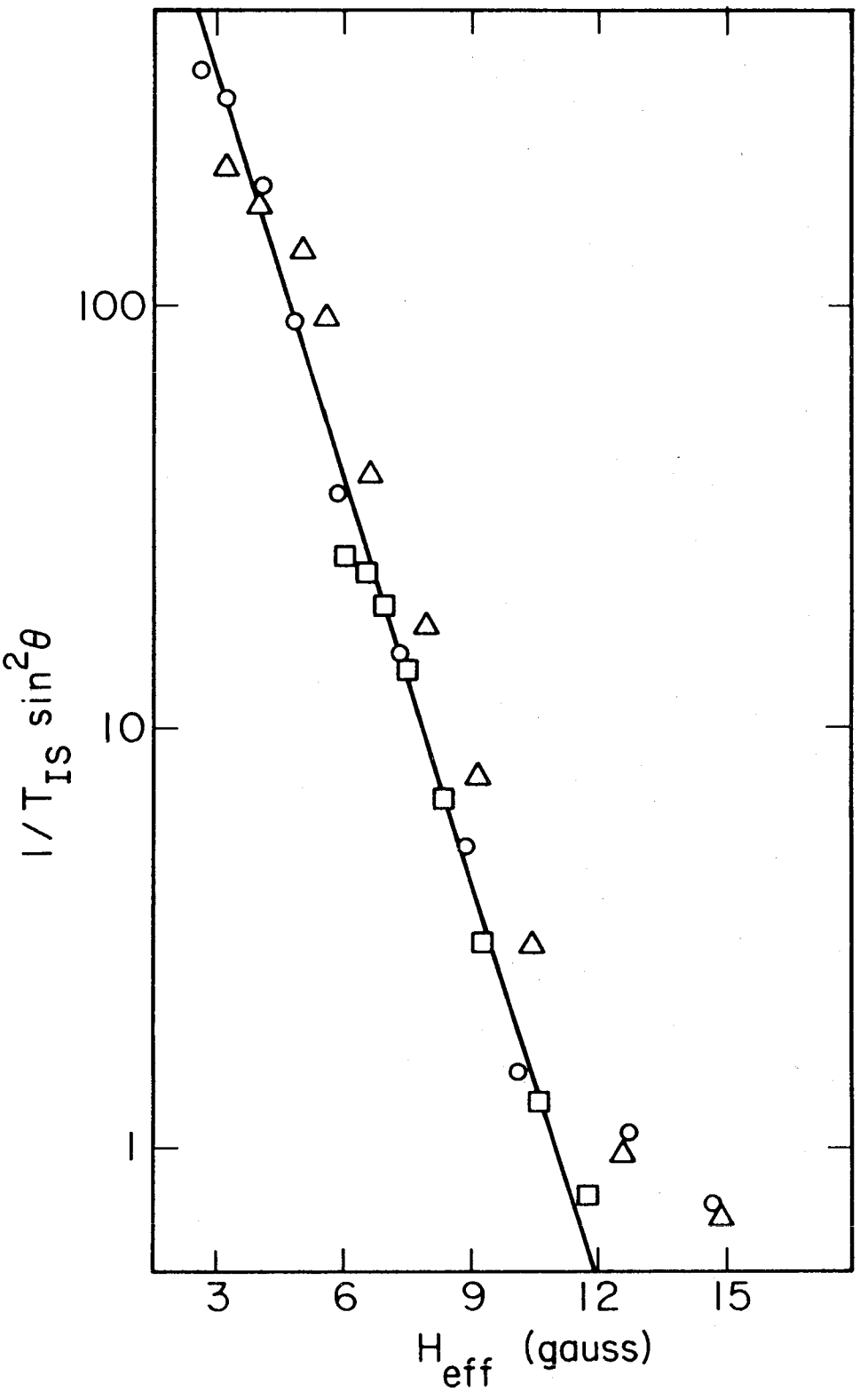

XBL 764-1524

Figure 12. Dependence of the cross polarization time on the carbon r.f. field strength for the ^{13}C field applied at resonance. Only those points used in the curve fitting (exponential least mean squares) are shown. The T_{IS} found is 110 ± 15 μsec.

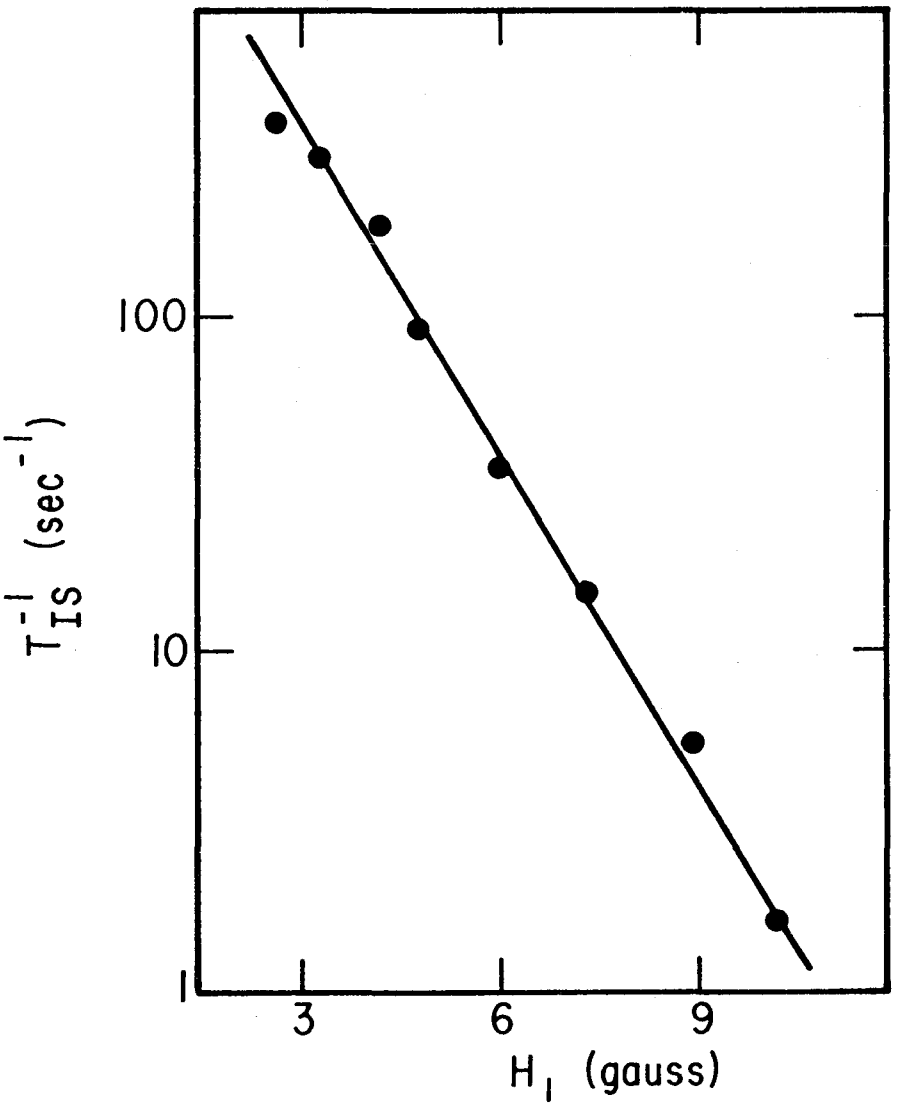

XBL 742-5579

Table 2. Cross polarization times

	Freq. offset	H_{1e} gauss	ω_e(kHz)	θ	T_{IS} msec
1	0	14.7	15.7		1374
2	0	12.5	13.4		947.6
3		10.3	11.0		678.9
4		8.99	9.63		192.8
5		7.54	8.08		69.22
6		6.18	6.62		29.27
7		5.02	5.38		12.35
8		4.34	4.65		5.501
9		3.62	3.88		3.303
10		2.60	2.78		3.098
11	+ 2.74 kHz	14.94	16.0	11.3	1508
12		12.8	13.7	13.2	1108
13		10.7	11.5	15.9	1139
14		9.46	10.1	18.0	361.6
15		8.09	8.66	21.2	150.1
16		6.84	7.33	25.4	71.97
17		5.81	6.22	30.3	33.73
18		5.24	5.61	34.0	15.90
19		4.66	4.99	39.0	12.47
20		3.92	4.20	48.4	13.26
21		3.49	3.74	57.4	16.72
22	+ 5.24 kHz	11.72	12.5	28.6	1705
23		10.6	11.4	32.0	1071
24		9.40	10.1	36.6	491.3
25		8.35	8.94	42.2	267.5
26		7.53	8.06	48.2	162.8
27		7.09	7.59	52.3	138.1
28		6.68	7.15	57.2	150.0
29		6.18	6.62	66.1	232.0

For small ω_e we have noted the flattening of the spectral density. We should also omit this point (point #10) since its inclusion would not be consistent with the exponential form for the spectral density which is obtained from the short correlation time assumption. This omission is quite justified on this basis because we wish to compare our theoretical results with a theory which is only valid in a specific region, large ω. We do not expect to reproduce the behavior at small ω. The correlation time with this omission is found to be

$$\tau_c = 115 \ \mu\text{sec} \tag{77}$$

If the data for the other two irradiation frequencies are included the correlation time is (omitting points 1, 2, 11, 10, 21)

$$\tau_c = 129 \ \mu\text{sec} \tag{78}$$

Taking into account all of the above fittings we then conclude that our uncertainty is rather large giving,

$$\tau_c = 110 \pm 15 \ \mu\text{sec} \tag{79}$$

V. Discussion

The correspondence of the experimental and theoretical values for the correlation time is quite satisfying.

τ_c (theory) = 122 μsec τ_c (experimental) = 110 ± 15 μsec

In the work of Mc Arthur et al. on Calcium Fluoride, theory and experiment were also in close agreement, indicating that for rigid lattices, of which both CaF_2 and adamantane are examples, the cross polarization dynamics are indeed very well characterized.

The effects of relaxation are shown to be of considerable importance for adamantane. The effect of relaxation is shown in Figure 13. The solid circles are the experimental data from Figure 10. Superimposed on this is the polarization expected, curve b, if there were no proton relaxation. The inclusion of proton relaxation, which is shown as curve a, combines to give curve c. As can be seen the proton relaxation strongly limits the final polarization.

On the otherhand, the effects of relaxation for a multiple contact SL experiment is clearly seen from Figure 14. Experimentally for 5 contacts we obtain an enhancement 2.4 times larger than for a single shot, for 10 contacts 3.75 times, and for 20 contacts 6 times. Using equation (33) the theory predicts enhancements of 4.89, 9.63 and 18.61 times the single shot enhancement. So then for a factor of 15 enhancement single contact ADRF must cross polarize for 0.125 sec at the optimum η. For a 15 fold enhancement multiple contact SL must accumulate $\simeq$ 20 contacts each with a cross polarization time of 5 msec for a total time of 0.4 sec.

Figure 13. Growth of ^{13}C magnetization after coupling to ^{1}H spins. The circles are the experimental data from Figure 10. Curve (a) shows the loss of proton spin order due to spin-lattice relaxation of the dipolar reservoir. Curve (b) shows the predicted growth of the ^{13}C magnetization with no ^{1}H spin-lattice relaxation and curve (c) is the combined predicted behavior (also shown in Figure 10).

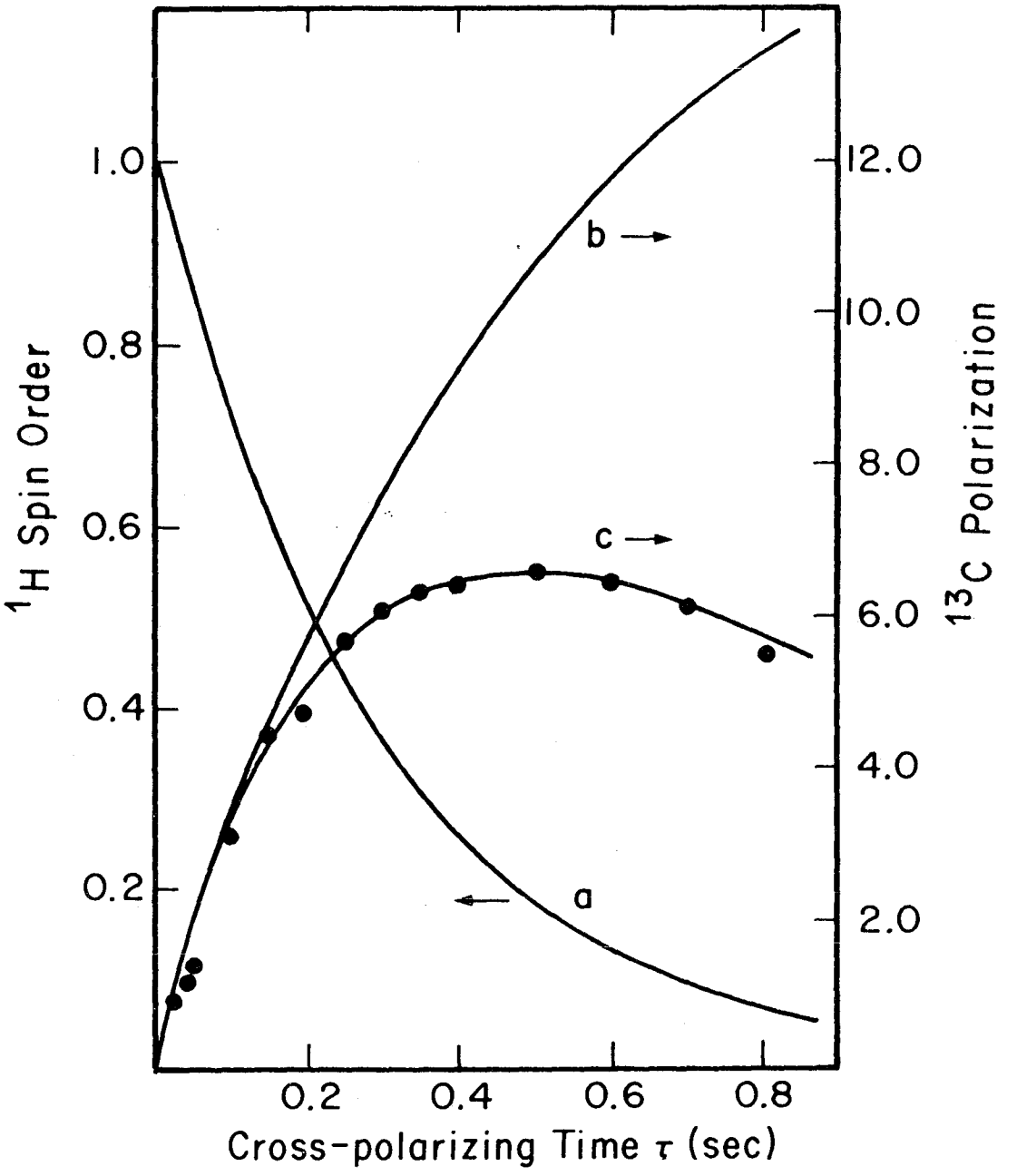

XBL 7312-7170

Figure 14. Multiple contact SL cross polarization, for n contacts. The oscilloscope traces show the actual signals obtained which are coadded to give the corresponding accumulated FID's. The total elapsed time is also given. The mixing time was 5 msec and the temperature was 13 ± 3°C.

PROTON-ENHANCED NMR OF ^{13}C IN ADAMANTANE

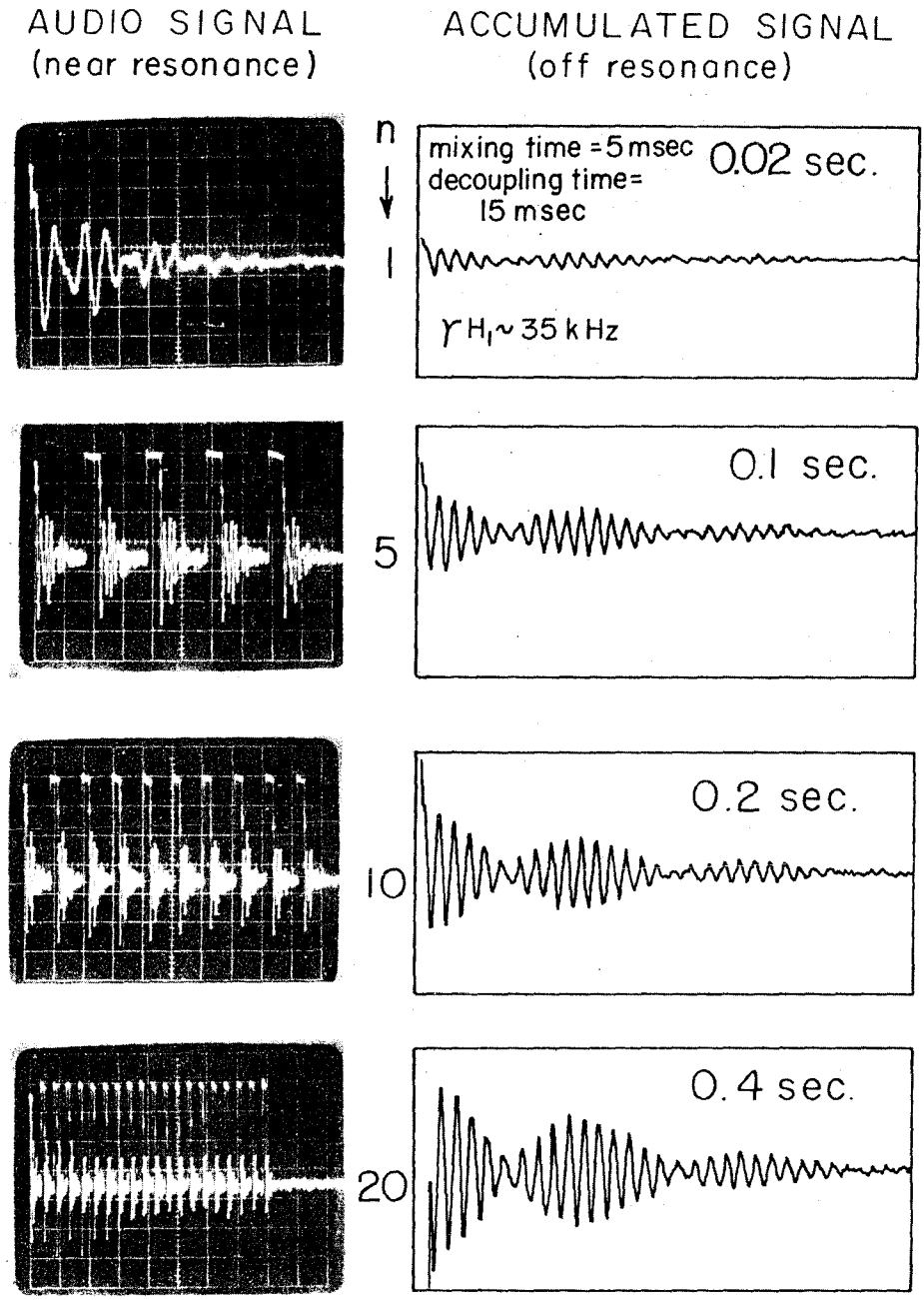

XBB 738-4786

The conclusion is that when the proton relaxation time is long ADRF is a superior method to SL multiple contact experiments. We note that if T_{1D} is very long multple contact ADRF experiments provide even more enhancement. However if the relaxation times are short $T_{1D} \leq T_{IS}$ we must choose $\eta = 1$ and then the SL experiment becomes preferable because it allows a shorter T_{IS}. The T_{IS} for $\eta = 1$ for SL is shorter because it samples the dipolar spectral density at $\omega_{1S}-\omega_{1I} = 0$ where it is a maximum rather than at ω_{1S} as for the ADRF case. τ_c is also generally shorter for SL, compare equations (61) and (61c) for small S_4.

The use of these enhancement schemes have grown rapidly since their inception. They allow the high sensitivity determination of chemical shifts as mentioned before, but also of relaxation parameters, for example the $T_{1\rho}$ experiment mentioned in this chapter and T_2 experiments which have also been carried out in our laboratory.[24] Quite recently we have also extended these methods to deuterium proton double resonance (see Chapter 2) which should expand the applications even more.

Appendix 1.1 Lattice Sums for an FCC Lattice and the CaF_2 Lattice

The details of the calculation are given in Section III D, and the computer program is given in A1.3. For the following tables the lattice sums and the second and forth moments are given in dimensionless form with

$$S_1' = \sum_i \left(\frac{P_2(\cos\theta_{ij})}{r_i^3} \right)^2$$

$$S_2' = \sum_i \left(\frac{P_2(\cos\theta_{ij})}{r_{ij}^3} \right)^2$$

$$S_4' = \sum_{i<j} \left(\frac{P_2(\cos\theta_{ij})}{r_{ij}^3} \right)^2 \left(\frac{P_2(\cos\theta_i)}{r_i^3} \right) \left(\frac{P_2(\cos\theta_j)}{r_j^3} \right) \qquad \text{(A1.1-1)}$$

for the angles as depicted in Figure 3 with r in units of the lattice cell size. For CaF_2 the lattice cell size (a) is the crystallographic unit cell dimension. For adamantane the lattice cell size is one half the crystallographic unit cell size, since the FCC lattice is constructed by omitting every other lattice point on a lattice cell grid. The unitless moments are

$$M_4^{ISII,} = 2S_1' \, S_2' - 4S_4'$$

$$M_{2IS}' = S_1' \qquad \text{(A1.1-2)}$$

The units are defined by:

$$S_1 = \left(\frac{\gamma_I \gamma_S \hbar}{a^3} \right)^2 S_1'$$

$$S_2 = \left(\frac{\gamma_I \hbar}{a^3}\right)^2 S_2'$$

$$S_4 = \frac{(\gamma_I^2 \hbar)^2 \; (\gamma_I \gamma_S \hbar)^2}{a^{12}} S_4' \qquad \text{(A1.1-3)}$$

and

$$M_4^{ISII} = \frac{\gamma_I^6 \gamma_S^2 \hbar^4}{a^{12}} \quad \left(\frac{S(S+1)}{3}\right)^2 \; \frac{1}{9} M_4^{ISII},$$

$$M_{2IS} = \frac{\gamma_I^2 \gamma_S^2 \hbar^2}{a^6} \; \frac{S(S+1)}{3} M_{2IS}' \qquad \text{(A1.1-4)}$$

and giving

$$\tau_c = \left(\frac{M_4^{ISII}}{2 \; M_2^{IS}}\right)^{-1/2} \qquad \text{(A1.1-5)}$$

The angles θ and ϕ are given as the polar angles of H_o, the external field, with respect to the crystal axis a, b, c, and for cubic lattices a, b, c are equivalent. The powder averages are discussed in appendix 1.2. The computer program used to calculate the table is given in appendix 1.3. Table 3 gives the results for the CaF_2 lattice and Table 4 for the FCC lattice with the τ_c's given for adamantane. The polycrystalline averaging is duscussed in appendix 1.2.

Table 3. CaF_2 lattice sums, fourth moments (M_4^{ISII}) and correlation times (τ_c). The values for the lattice sums are given in dimensionless units according to equation (65). The numerical value of f, equation 66, is 5.6776×10^7 sec^{-2}. The lattice size for S_1 for 11 atoms cubed, for S_2 it was 11 cubed and for S_4 it was 5 atoms cubed. The number of theta angles was 11 for θ = 0-90° and for phi again 11 with ϕ = 0-45°.

θ	ϕ	$S_1'(M_{2IS}')$	S_2'	S_4'	M_4^{ISII},	τ_c (μsec)
- 0.00	0.00	1.558	30.01	6.606	67.11	39.41
- 0.00	4.50	1.558	30.01	6.606	67.11	39.41
- 0.00	9.00	1.558	30.01	6.606	67.11	39.41
- 0.00	13.50	1.558	30.01	6.606	67.11	39.41
- 0.00	18.00	1.558	30.01	6.606	67.11	39.41
- 0.00	22.50	1.558	30.01	6.606	67.11	39.41
- 0.00	27.00	1.558	30.01	6.606	67.11	39.41
- 0.00	31.50	1.558	30.01	6.606	67.11	39.41
- 0.00	36.00	1.558	30.01	6.606	67.11	39.41
- 0.00	40.50	1.558	30.01	6.606	67.11	39.41
- 0.00	45.00	1.558	30.01	6.606	67.11	39.41
25.84	0.00	13.05	18.53	-3.973	499.8	41.81
25.84	4.50	13.07	18.51	-4.250	501.1	41.78
25.84	9.00	13.12	18.46	-5.052	504.8	41.70
25.84	13.50	13.19	18.39	-6.300	510.6	41.58
25.84	18.00	13.29	18.29	-7.869	517.8	41.44
25.84	22.50	13.39	18.19	-9.603	525.8	41.28
25.84	27.00	13.49	18.08	-11.33	533.7	41.13

Table 3 continued

θ	ϕ	$S_1'(M_{2IS}')$	S_2'	S_4'	$M_4^{ISII,}$	τ_c (μsec)
25.84	31.50	13.59	17.99	-12.88	540.8	41.01
25.84	36.00	13.66	17.92	-14.11	546.3	40.91
25.84	40.50	13.71	17.87	-14.90	549.9	40.85
25.84	45.00	13.73	17.85	-15.18	551.1	40.83
36.87	0.00	18.77	12.82	14.30	424.2	54.41
36.87	4.50	18.83	12.76	13.70	425.9	54.39
36.87	9.00	19.00	12.59	11.97	430.7	54.33
36.87	13.50	19.27	12.32	9.304	437.8	54.27
36.87	18.00	19.61	11.98	5.991	446.1	54.23
36.87	22.50	19.98	11.61	2.381	454.6	54.23
36.87	27.00	20.35	11.24	- 1.161	462.3	54.28
36.87	31.50	20.69	10.90	- 4.300	468.5	54.36
36.87	36.00	20.96	10.63	- 6.752	472.9	54.46
36.87	40.50	21.13	10.46	- 8.308	475.5	54.53
36.87	45.00	21.19	10.40	- 8.841	476.4	54.56
45.57	0.00	20.23	11.36	21.46	374.0	60.15
45.57	4.50	20.35	11.24	20.75	374.8	60.27
45.57	9.00	20.69	10.90	18.73	376.3	60.65
45.57	13.50	21.23	10.36	15.69	377.4	61.35
45.57	18.00	21.90	9.690	12.07	376.3	62.41
45.57	22.50	22.66	8.941	8.309	371.9	63.84
45.57	27.00	23.41	8.191	4.815	364.2	65.57
45.57	31.50	24.08	7.515	1.894	354.4	67.43

Table 3 continued

θ	ϕ	$S_1'(M_{2IS}')$	S_2'	S_4'	$M_4^{ISII,}$	τ_c (μsec)
45.57	36.00	24.62	6.978	-26.74	344.7	69.13
45.57	40.50	24.97	6.633	- 1.582	337.6	70.34
45.57	45.00	25.08	6.515	- 2.022	335.0	70.79
53.13	0.00	18.77	12.82	14.30	424.2	54.41
53.13	4.50	18.96	12.63	13.61	424.6	54.65
53.13	9.00	19.50	12.09	11.72	424.8	55.42
53.13	13.50	20.35	11.24	9.054	421.5	56.83
53.13	18.00	21.41	10.18	6.178	411.4	59.01
53.13	22.50	22.59	9.001	3.626	392.3	62.08
53.13	27.00	23.78	7.821	1.742	365.0	66.02
53.13	31.50	24.84	6.756	.6173	333.2	70.63
53.13	36.00	25.69	5.911	.1115	303.3	75.28
53.13	40.50	26.23	5.368	- .3254	281.8	78.92
53.13	45.00	26.42	5.181	- .4946	274.0	80.32
60.00	0.00	15.56	16.02	2.129	490.4	46.09
60.00	4.50	15.82	15.76	1.447	493.2	46.33
60.00	9.00	16.57	15.02	.3514	499.2	47.12
60.00	13.50	17.73	13.86	- 2.623	502.1	48.61
60.00	18.00	19.19	12.39	- 4.565	494.3	50.97
60.00	22.50	20.82	10.77	- 5.519	470.8	54.39
60.00	27.00	22.44	9.155	- 5.212	431.8	58.97
60.00	31.50	23.91	7.693	- 3.852	383.2	64.60
60.00	36.00	25.07	6.532	- 2.043	335.7	70.69
60.00	40.50	25.81	5.787	- .5412	300.9	75.76

Table 3 continued

θ	ϕ	$S_1'(M_{2IS}')$	S_2'	S_4'	$M_4^{ISII,}$	τ_c (μsec)
60.00	45.00	26.07	5.530	.3814	288.2	77.80
66.42	0.00	11.60	19.98	- 6.132	488.2	39.87
66.42	4.50	11.92	19.66	- 6.927	496.6	40.08
66.42	9.00	12.85	18.72	- 8.953	517.5	40.77
66.42	13.50	14.31	17.27	- 11.27	539.7	42.13
66.42	18.00	16.15	15.43	- 12.75	549.8	44.34
66.42	22.50	18.19	13.40	- 12.50	537.6	47.58
66.42	27.00	20.22	11.37	- 10.26	501.0	51.97
66.42	31.50	22.06	9.535	- 6.549	447.0	57.47
66.42	36.00	23.52	8.079	- 2.449	389.9	63.53
66.42	40.50	24.45	7.145	.7191	346.6	68.71
66.42	45.00	24.78	6.823	1.908	330.5	70.83
72.54	0.00	7.677	23.90	- 6.896	394.6	36.08
72.54	4.50	8.056	23.52	- 7.925	410.7	36.22
72.54	9.00	9.155	22.42	- 10.52	452.7	36.78
72.54	13.50	10.86	20.71	- 13.42	503.9	37.98
72.54	18.00	13.02	18.56	- 15.08	543.9	40.02
72.54	22.50	15.41	16.17	- 14.33	556.0	43.06
72.54	27.00	17.80	13.79	- 10.84	534.4	47.21
72.54	31.50	19.95	11.63	- 5.346	485.9	52.42
72.54	36.00	21.66	9.930	.5972	427.9	58.20
72.54	40.50	22.76	8.833	5.151	381.6	63.18
72.54	45.00	23.14	8.455	6.854	364.0	65.23
78.46	0.00	4.427	27.14	- 1.953	248.2	34.54
78.46	4.50	4.848	26.72	- 3.264	272.2	34.52

Table 3 continued

θ	ϕ	$S_1'(M_{2IS}')$	S_2'	S_4'	$M_4^{ISII,}$	τ_c (μsec)
78.46	9.00	6.071	25.50	- 6.594	336.1	34.76
78.46	13.50	7.975	23.60	-10.35	417.9	35.73
78.46	18.00	10.37	21.20	-12.62	490.6	37.61
78.46	22.50	13.03	18.55	-11.92	531.3	40.51
78.46	27.00	15.69	15.89	- 7.837	530.3	44.50
78.46	31.50	18.09	13.50	- 1.245	493.5	49.53
78.46	36.00	19.99	11.59	5.946	440.1	55.14
78.46	40.50	21.22	10.37	11.47	394.5	59.99
78.46	45.00	21.64	9.957	13.55	376.8	61.99
84.26	0.00	2.298	29.27	4.024	118.4	36.03
84.26	4.50	2.746	28.82	2.485	148.3	35.19
84.26	9.00	4.046	27.52	- 1.442	228.5	34.41
84.26	13.50	6.071	25.50	- 5.950	333.5	34.90
84.26	18.00	8.623	22.95	- 8.838	431.3	36.57
84.26	22.50	11.45	20.13	- 8.398	494.7	39.35
84.26	27.00	14.28	17.30	- 4.129	510.9	43.24
84.26	31.50	16.83	14.76	3.005	484.9	48.19
84.26	36.00	18.85	12.73	10.88	436.9	53.74
84.26	40.50	20.15	11.43	16.97	393.3	58.56
84.26	45.00	20.60	10.99	19.26	375.9	60.56
90.00	0.00	1.558	30.01	6.606	67.11	39.41
90.00	4.50	2.015	29.55	4.981	99.22	36.86
90.00	9.00	3.342	28.23	.8231	185.4	34.72
90.00	13.50	5.408	26.16	- 3.977	298.9	34.79
90.00	18.00	8.012	23.56	- 7.118	406.1	36.33

Table 3 continued

θ	ϕ	$S_1'(M_{2IS}')$	S_2'	S_4'	$M_4^{ISII,}$	τ_c (μsec)
90.00	22.50	10.89	20.68	- 6.810	478.1	39.05
90.00	27.00	13.78	17.80	- 2.517	500.9	42.91
90.00	31.50	16.38	15.20	4.775	479.2	47.83
90.00	36.00	18.45	13.14	12.87	433.5	53.37
90.00	40.50	19.78	11.81	19.14	390.9	58.19
90.00	45.00	20.23	11.35	21.50	373.8	60.19

Table 4. FCC Lattice Sums and correlation times (τ_c - see equation (63)). The values for the lattice sums are given in dimensionless form according to equation (65). The numerical value of f for adamantane is 4.6083×10^7 sec^{-2}. The lattice size for S_1 was 7 molecules cubed, for S_2 it was 7 cubed and for S_4 it was 4 cubed. The number of theta angles was 11 for θ = 0-90° and 11 for ϕ = 0-45°.

θ	ϕ	S_1'	S_2'	S_4'	τ_c(μsec)
- 0.00	0.00	1.072	2.413	.2514	14.93
- 0.00	4.50	1.072	2.413	.2514	14.93
- 0.00	9.00	1.072	2.413	.2514	14.93
- 0.00	13.50	1.072	2.413	.2514	14.93
- 0.00	18.00	1.072	2.413	.2514	14.93
- 0.00	22.50	1.072	2.413	.2514	14.93
- 0.00	27.00	1.072	2.413	.2514	14.93
- 0.00	31.50	1.072	2.413	.2514	14.93
- 0.00	36.00	1.072	2.413	.2514	14.93
- 0.00	40.50	1.072	2.413	.2514	14.93
- 0.00	45.00	1.072	2.413	.2514	14.93
25.84	0.00	1.356	3.052	.1286	12.31
25.84	4.50	1.357	3.053	.1290	12.31
25.84	9.00	1.358	3.056	.1301	12.30
25.84	13.50	1.360	3.060	.1318	12.30
25.84	18.00	1.362	3.065	.1340	12.29
25.84	22.50	1.365	3.071	.1364	12.29
25.84	27.00	1.367	3.077	.1388	12.28

Table 4 continued

θ	ϕ	S_1'	S_2'	S_4'	τ_c (μsec)
25.84	31.50	1.369	3.082	.1410	12.28
25.84	36.00	1.371	3.086	.1428	12.27
25.84	40.50	1.372	3.089	.1440	12.27
25.84	45.00	1.373	3.090	.1444	12.27
36.87	0.00	1.497	3.370	.1757	11.76
36.87	4.50	1.499	3.373	.1776	11.76
36.87	9.00	1.503	3.383	.1829	11.75
36.87	13.50	1.510	3.397	.1914	11.74
36.87	18.00	1.518	3.416	.2023	11.73
36.87	22.50	1.527	3.437	.2146	11.72
36.87	27.00	1.536	3.458	.2273	11.71
36.87	31.50	1.545	3.476	.2390	11.70
36.87	36.00	1.551	3.491	.2484	11.69
36.87	40.50	1.556	3.501	.2546	11.69
36.87	45.00	1.557	3.504	.2567	11.69
45.57	0.00	1.533	3.451	.1992	11.66
45.57	4.50	1.536	3.457	.2028	11.65
45.57	9.00	1.545	3.476	.2134	11.64
45.57	13.50	1.558	3.506	.2305	11.62
45.57	18.00	1.575	3.544	.2530	11.60
45.57	22.50	1.593	3.586	.2790	11.58
45.57	27.00	1.612	3.627	.3063	11.55
45.57	31.50	1.629	3.665	.3320	11.54
45.57	36.00	1.642	3.695	.3531	11.52

Table 4 continued

θ	ϕ	S_1'	S_2'	S_4'	τ_c (μsec)
45.57	40.50	1.650	3.714	.3670	11.52
45.57	45.00	1.653	3.720	.3718	11.51
53.13	0.00	1.497	3.370	.1757	11.76
53.13	4.50	1.502	3.380	.1802	11.75
53.13	9.00	1.515	3.410	.1936	11.72
53.13	13.50	1.536	3.457	.2158	11.68
53.13	18.00	1.563	3.517	.2460	11.64
53.13	22.50	1.592	3.582	.2824	11.59
53.13	27.00	1.621	3.648	.3218	11.55
35.13	31.50	1.647	3.707	.3601	11.51
53.13	36.00	1.668	3.754	.3922	11.49
53.13	40.50	1.682	3.784	.4137	11.48
53.13	45.00	1.686	3.795	.4212	11.47
60.00	0.00	1.418	3.192	.1405	12.03
60.00	4.50	1.425	3.206	.1441	12.01
60.00	9.00	1.443	3.247	.1555	11.96
60.00	13.50	1.472	3.312	.1756	11.88
60.00	18.00	1.508	3.393	.2052	11.79
60.00	22.50	1.548	3.483	.2435	11.70
60.00	27.00	1.588	3.574	.2876	11.62
60.00	31.50	1.624	3.655	.3323	11.56
60.00	36.00	1.653	3.720	.3712	11.51
60.00	40.50	1.671	3.761	.3977	11.49
60.00	45.00	1.678	3.775	.4071	11.48
66.42	0.00	1.320	2.971	.1281	12.49

Table 4 continued

θ	ϕ	S_1'	S_2'	S_4'	τ_c (μsec)
66.42	4.50	1.328	2.989	.1291	12.46
66.42	9.00	1.351	3.041	.1334	12.35
66.42	13.50	1.387	3.122	.1439	12.20
66.42	18.00	1.433	3.224	.1638	12.03
66.42	22.50	1.483	3.337	.1945	11.87
66.42	27.00	1.533	3.450	.2343	11.74
66.42	31.50	1.579	3.552	.2780	11.64
66.42	36.00	1.615	3.633	.3180	11.57
66.42	40.50	1.638	3.685	.3461	11.53
66.42	45.00	1.646	3.703	.3562	11.51
72.54	0.00	1.223	2.753	.1499	13.15
72.54	4.50	1.233	2.774	.1472	13.08
72.54	9.00	1.260	2.835	.1369	12.89
72.54	13.50	1.302	2.930	.1369	12.63
72.54	18.00	1.355	3.050	.1408	12.35
72.54	22.50	1.414	3.183	.1571	12.10
72.54	27.00	1.473	3.316	.1858	11.90
72.54	31.50	1.527	3.435	.2226	11.74
72.54	36.00	1.569	3.531	.2590	11.64
72.54	40.50	1.596	3.592	.2858	11.58
72.54	45.00	1.605	3.613	.2956	11.56
78.46	0.00	1.143	2.573	.1936	13.93
78.46	4.50	1.154	2.596	.1870	13.81

Table 4 continued

θ	ϕ	S_1'	S_2'	S_4'	τ_c (μsec)
78.46	9.00	1.184	2.664	.1703	13.51
78.46	13.50	1.231	2.770	.1507	13.10
78.46	18.00	1.290	2.903	.1374	12.70
78.46	22.50	1.356	3.051	.1374	12.34
78.46	27.00	1.421	3.199	.1529	12.05
78.46	31.50	1.481	3.332	.1803	11.85
78.46	36.00	1.528	3.438	.2110	11.71
78.46	40.50	1.558	3.506	.2349	11.63
78.46	45.00	1.568	3.529	.2439	11.61
84.26	0.00	1.091	2.455	.2348	14.64
84.26	4.50	1.102	2.479	.2254	14.47
84.26	9.00	1.134	2.552	.2007	14.05
84.26	13.50	1.184	2.664	.1695	13.50
84.26	18.00	1.247	2.806	.1432	12.97
84.26	22.50	1.317	2.963	.1307	12.52
84.26	27.00	1.386	3.120	.1357	12.18
84.26	31.50	1.449	3.262	.1554	11.93
84.26	36.00	1.499	3.374	.1812	11.76
84.26	40.50	1.532	3.447	.2025	11.67
84.26	45.00	1.543	3.471	.2107	11.64
90.00	0.00	1.072	2.413	.2514	14.93
90.00	4.50	1.084	2.439	.2510	14.75
90.00	9.00	1.116	2.513	.2133	14.27
90.00	13.50	1.167	2.627	.1779	13.66

Table 4 continued

θ	ϕ	S_1'	S_2'	S_4'	τ_c (μsec)
90.00	18.00	1.232	2.772	.1467	13.08
90.00	22.50	1.303	2.932	.1295	12.59
90.00	27.00	1.374	3.093	.1306	12.22
90.00	31.50	1.438	3.237	.1473	11.96
90.00	36.00	1.489	3.352	.1712	11.78
90.00	40.50	1.522	3.426	.1915	11.69
90.00	45.00	1.534	3.451	.1993	11.66

Appendix 1.2 Averages for the Polycrystalline Cross Polarization Time

In the calculation of T_{IS} for adamantane there are two separate averages to be performed. We must first average the dipolar interaction between spins on two molecules over the rapid isotropic motion that occurs at room temperature. From this averaged interaction the second moment of the autocorrelation function is calculated, for a specific orientation of the lattice in the external field. The desired polycrystalline moment is then calculated by averaging the individual second moments over many orientations. We present in this appendix a discussion of how this first average is calculated and then a discussion of the manner in which the orientational average should be carried out. Lastly we present the results of the averages for the moments of the correlation function and a listing of the proper conversion factors.

As mentioned in Chapter One the averaged interaction between spins on two different molecules is found by evaluating the following integral, over the isotropic motion of the two spins on two spheres:

$$\int \frac{P_2(\cos\gamma)}{r^3} \quad dS_1 dS_2 \tag{A1.2-1}$$

where γ and r are the instantaneous angle and distance between the two spins; the angle is between the external field direction and the vector between the two spins. Also S_1 and S_2 are the variables appropriate to two nontouching spheres whose centers are separated by the distance R of radius r_1 and r_2 respectively. The result of this integration has been reported and used many times in the literature,[32-37] but the specific details have never been presented.

If we average r^{-3} itself we find, following Dimetrieva et al.[32] that:

$$\left\langle \frac{1}{r^3} \right\rangle_{S_1 S_2} = \frac{1}{4Rr_1r_2} \ \ell n \ \frac{R^2-(r_1-r_2)^2}{R^2-(r_1+r_2)^2} \tag{A1.2-2}$$

However if we average the full interaction the average becomes

$$\left\langle \frac{P_2(\cos\gamma)}{r^3} \right\rangle_{S_1 S_2} = \frac{P_2 \ B(\cos\theta)}{R^3} \tag{A1.2-3}$$

where θ is the angle between the external field direction and the line between the centers of the two spheres.

To show this we will first calculate the integral of the interaction between a point and a sphere with a uniform spin density. We take the Z axis $(\vec{H}_o || \vec{Z})$ to be the line between the point and the center of the sphere. The radius of the sphere is r_2. Then $\gamma = \theta$ in equation (A1.2-3) and we find

$$\left\langle \frac{P_2(\cos\gamma)}{r^3} \right\rangle_{S_2} = \int_0^{\pi} \frac{3/2 \ \cos^2 \gamma - \frac{1}{2}}{r^3} \ 2\pi r^2 \ \sin\alpha \ d\alpha \tag{A1.2-4}$$

where r is the distance between the spin at the point and the spin on the sphere and α is the angle between the Z axis and the vectors from the center of the sphere and the spin on its surface. Then:

$$r = \sqrt{R^2 + r_2^2 - 2Rr_2 \cos\alpha} \quad \text{and} \quad \cos^2\gamma = \frac{1-r_2^2 \sin^2\alpha}{r^2} \tag{A1.2-5}$$

This integral gives

$$\left\langle \frac{P_2(\cos\theta)}{r^3} \right\rangle_{S_2} = \frac{1}{R^3} \tag{A1.2-6}$$

If we now choose an arbitrary direction for the Z axis we must transform the coordinates in A1.2-4. Note that

$$P_2(\cos\gamma) = \left(\frac{4\pi}{5}\right)^{\frac{1}{2}} Y_{20}(\gamma,\beta) \tag{A1.2-7}$$

The transformation to a new Z axis is given by the addition rule for spherical harmonics with a rotation defined by $D^2_{m,m'}(0,\theta,0)$ where θ is the angle between the new Z axis and the old which is the line between the point and the center of the sphere. This gives:

$$\begin{aligned}\langle R(0,\theta,0)\,\frac{P_2(\cos\gamma)}{r^3}\,R^+(0,\theta,0)\rangle_{S_2} &= P_2(\cos\theta)\left\langle\frac{P_2(\cos\gamma)}{r^3}\right\rangle_{S_2} \\ &+ \frac{3}{8}\sin^2\theta\left(\left\langle\frac{Y_{2,-2}(\gamma,\beta)}{r^3}\right\rangle_{S_2} + \left\langle\frac{Y_{2,+2}(\gamma,\beta)}{r^3}\right\rangle_{S_2}\right) \\ &+ \frac{3}{2}\sin\theta\cos\theta\left(\left\langle\frac{Y_{2,1}(\gamma,\beta)}{r^3}\right\rangle_{S_2} - \left\langle\frac{Y_{2,-1}(\gamma,\beta)}{r^3}\right\rangle_{S_2}\right)\end{aligned} \tag{A1.2-8}$$

where β is the azimuthal angle about the vector between the point and the center of the sphere. However we know that the cylinderical symmetry of the system will average the terms with an β dependence to zero. For example (see A1.2-4)

$$\left\langle\frac{Y_{2,2}(\gamma,\beta)}{r^3}\right\rangle_{S_1} = \left(\frac{5}{4\pi}\right)^{\frac{1}{2}}\left(\frac{3}{8}\right)^{\frac{1}{2}}\int_0^{\pi}\int_0^{2\pi}\frac{\sin^2\gamma\;\theta^{\pm 2i\beta}}{r^3}\,r^2\,\sin\alpha\,d\alpha\,d\phi \tag{A1.2-9}$$

where we retain the old integration variable α and ϕ is the azimuthal angle of the vector from the spin on the sphere and the sphere's center. By this definition $\beta = \phi$ and we have:

$$\left\langle \frac{Y_{2,2}(\gamma,\beta)}{r^3} \right\rangle_{S_2} = C \int_0^{\infty} \frac{\sin^2\gamma}{r^3} \sin\alpha \, d\alpha \int_0^{2\pi} e^{\pm i2\phi} \, d\phi = 0 \qquad \text{(A1.2-10)}$$

since we note that γ and r are functions of α only, because of the spherical symmetry. This leaves only

$$\left\langle R(0,\theta,0) \frac{P_2(\cos\gamma)}{r^3} R^+(0,\theta,0) \right\rangle_{S_2} = P_2(\cos\theta) \left\langle \frac{P_2(\cos\gamma)}{r^3} \right\rangle_{S_2} \qquad \text{(A1.2-11)}$$

which we have shown reduces to (see equation A1.2-6)

$$\left\langle R \frac{P_2(\cos\gamma)}{r^3} R^+ \right\rangle = \frac{P_2(\cos\theta)}{R^3} \qquad \text{(A1.2-12)}$$

To calculate the interaction of two spheres we note that we may break the integral into two parts. First perform the average between a fixed spin on S_1 and the entire sphere S_2. Then average this result over the variables of S_1. The first average is of the form we have just completed. But because of the simple form of this first average (A1.2-7) the second integration is again the same integral yielding:

$$\left\langle \frac{P_2(\cos\gamma)}{r^3} \right\rangle_{S_1 S_2} = \frac{P_2(\cos\theta)}{R^3} \qquad \text{(A1.2-13)}$$

which is much different than we found for $\langle \frac{1}{r^3} \rangle$ itself (A1.2-2). In words then, the spins on two adamantane molecules behave as if they are placed at the center of the two spheres, giving the average distance as R.

Using the distance R as indicated above we calculated the second moment at many orientations of the lattice (See A1.1). The polycrystalline average is then the average of these moments over a sphere. However, we must prove that the average of the second moments is actually the second

moment of the polycrystalline correlation function which we obtain from experiment. To prove we are correct in our approach remember that the second moment of a function is,[18]

$$M_2 = \frac{-\frac{d^2}{dt^2} G(t)\Big|_{t=0}}{G(0)} \tag{A1.2-14}$$

Here we take G(t) to be the autocorrelation function. For a polycrystalline sample we must add up the functions G(t) for each crystallite giving the overall correlation function

$$\bar{G}(t) = \int_{\text{Sphere}} G(t,\Omega)\, d\Omega \tag{A1.2-15}$$

where the variables Ω determine the orientation of the crystallite and the integral is taken over a sphere. We find that polycrystalline moment $\bar{M}_2$ is given by

$$\bar{M}_2 = \frac{-\frac{d^2}{dt^2} \bar{G}(t)\Big|_{t=0}}{\bar{G}(o)} = \frac{\int_{\text{Sphere}} d\Omega \; -\frac{d^2}{dt^2} G(t,\Omega)\Big|_{t=0}}{\int_{\text{Sphere}} d\Omega \; G(0,\Omega)} \tag{A1.2-16}$$

$$= \frac{\int d\Omega \; M_2(\Omega) \; G(0,\Omega)}{\int d\Omega \; G(0,\Omega)} \tag{A1.2-17}$$

Since the correlation function is normalized so that $G(0,\Omega) = 1$ (see equation (1.49)) we have finally

$$\bar{M}_2 = \frac{\int_{\text{Sphere}} d\Omega \; M_2(\Omega)}{\int_{\text{Sphere}} d\Omega} \tag{A1.2-18}$$

which is the simple average of the individual moments. With this motivation we find that

$$\overline{M'_{2IS}} = 1.4508 = S'_1$$

$$\overline{M'^{ISII}_4} = 8.6061 = 2S'_1S'_2 - 4S'_4 \qquad \text{(A1.2-19)}$$

for an FCC lattice. For adamantane then

$$\overline{M_{2IS}} = \left(\frac{\gamma_I\gamma_S\hbar}{a^3}\right)^2 \frac{I(I+1)}{3} N_{site} \overline{M'_{2IS}} \qquad \text{(A1.2-20)}$$

$$= 3.278 \times 10^6 \left(\frac{1}{4}\right) (16) \quad 1.4508 = 1.90 \times 10^7 \text{ rad}^2\text{sec}^2$$

$$\overline{M_4^{ISII}} = \left(\frac{\gamma_I^2\hbar}{a^3}\right)^2 \left(\frac{\gamma_I\gamma_S\hbar}{a^3}\right)^2 \left(\frac{I(I+1)}{3}\right)^2 \left(\frac{1}{9}\right) N_{site} \overline{M_4^{ISII}} \qquad \text{(A1.2-21)}$$

$$= 3.278 \times 10^6 \cdot 5.184 \times 10^7 \left(\frac{1}{16}\right) \frac{1}{9}\, 16\; 8.6061$$

$$= 1.62 \times 10^{14} \text{ rad}^4\text{sec}^{-4}$$

which gives

$$\tau_c = \left(\frac{2}{\overline{M_2}}\right)^{1/2} = 122 \ \mu\text{sec, for } M_2 = \frac{M_4^{ISII}}{M_{2IS}} \qquad \text{(A1.2-22)}$$

Appendix 1.3 Computer Programs

The relaxation times, T_{1D} and $T_{1\rho}$, the cross polarization times, T_{IS}, and the correlation time, τ_c, were fit using the standard matrix form of non-linear least mean squares. The program was a standard Oak Ridge version called ORGELS. The voltage ranges on the Biomation were found not to be accurate, giving a 5% error when changing from 50 mv to 100 mv scale. This was corrected by using the ORGELS subroutine PRELIM (not listed here), which scaled the 100 mv data properly before curve fitting. This is in general not necessary, however. The only necessary user supplied subroutine is the routine to calculate the relaxation function, and its derivatives with respect to all of the parameters to be varied. For T_{IS} the equation 1-50 was used and the parameters to be varied are β_I, $\varepsilon\eta^2$ and T_{IS}. This subroutine for T_{IS} is given in Table I. (Note $\beta_{AI} = \beta_I$, TAU = T_{IS}, EPS = $\varepsilon\eta^2$, $T_{1A} = T_{1D}$, α_+ = ALPP, α_- = ALPM, $\frac{\partial}{\partial\beta_I}$ = DBB, $\frac{\partial}{\partial T_{IS}}$ = DBT and $\frac{\partial}{\partial\varepsilon\eta^2}$ = DBE). It should be noted that equation (1-52) is in a particularly poor form for a least squares analysis, since the parameters are all highly correlated. We use instead equation (1-50) to aid in achieving convergence. It is even better to use (1-41) directly; this will be done in Chapter 2.

The program for calculating lattice sums is given in Table 5 for the CaF_2 lattice. The CaF_2 lattice is easily generated by first forming a cubic lattice with the displacements

X = LA

Y = MA for L, M, N integers

Z = NA and A the lattice cell size (A1.3-1)

and then displacing the lattice by $\frac{1}{2}$ A in each direction in order to place the origin at the tetrahedral calcium site.

$$X = LA + \frac{1}{2} A$$

$$Y = MA + \frac{1}{2} A$$

$$Z = NA + \frac{1}{2} A \qquad \text{(A1.3-2)}$$

An FCC lattice is formed by excluding every lattice point for which L + M + N is odd in equation (1). For the FCC lattice the origin displacement is not needed. The subroutine for the formation of an FCC lattice, COORD, is shown in Table III.

To calculate $P_2(\cos\theta)$ the dot product formula was used

$$\vec{H}\cdot\vec{r} = |H| \quad |r| \cos\theta$$

for the coordinates as directly generated from the lattice. This was much faster than conventional methods, as suggested by McCall and Hamming, for example.[25] The lattice size for the sum S_4' was smaller than for S_1' and S_2' because of time limitations. Fortunately, S_4' converges much faster than S_1' or S_2' (see Section III iv).

Simpsons integration was found to be more accurate than Gauss' method for integrations over a sphere. This was tested by integrating the function f(x) = 1 over a sphere. This is included as a subroutine.

Table 5. Derivative subroutine for T_{IS} curve fitting. CALC calculates the value of the function and its derivatives for the current values of the trial fitting parameters for the least squares fitting program ORGELS. (See the text for the definitions of the important variables).

```
CALC
                SUBROUTINE CALC(XI,Y,P,D)
                DIMENSION P(4),D(3)
                BAI=P(1)
          6     TAU=P(2)
         10     EPS=P(3)
         11     T1A=P(4)
         13     T=XI
         14     APA=(1.+EPS)/TAU +1./T1A
         50     AMA=SQRT(APA*APA-1./(TAU*T1A))
         56     ALPP=.5*APA+.5*AMA
         30     ALPM=.5*APA-.5*AMA
         32     EALPP=EXP(-ALPP*T)
         36     EALPM=EXP(-ALPM*T)
         40     DBS=(EALPM-EALPP)/(TAU*AMA)
         43     ETA=APA/AMA
         45     DBE1=-BAI/(TAU*TAU*AMA)
         47     DBE2=(EALPM*(1-ETA)-EALPP*(1+ETA))*T/2.+(EALPM-EALPP)*ETA/AMA
        103     DBE=DBE1*DBE2
        104      DTT1=-(1./(2.*T1A)-AMA*(1.+EPS))/(TAU*AMA)**3
        111      DTT2=-1./(AMA*TAU*TAU)
        113     DTT=DTT1+DTT2
        114     DALTP=-(1.+EPS)/(2.*TAU*TAU)+(1./(2.*T1A)-APA*(1.+EPS))/(2*TAU
               1 *TAU*AMA)
        122     DALTM=-(1.+EPS)/(2.*TAU*TAU)-(1./(2.*T1A)-APA*(1.+EPS))/(2.*TAU
               1 *TAU*AMA)
        127     DEME=-T*EALPM*DALTM+T*EALPP*DALTP
        134     DBT=BAI*DEME/(TAU*AMA)+BAI*(EALPM-EALPP)*DTT
        140     Y=BAI*(EALPM-EALPP)/(TAU*AMA)
        144     D(1)=DBS
        146     D(2)=DBT
        147     D(3)=DBE
        151     RETURN
        151     END
```

SUBPROGRAM LENGTH

05301

FUNCTION ASSIGNMENTS

STATEMENT ASSIGNMENTS

BLOCK NAMES AND LENGTHS

VARIABLE ASSIGNMENTS

ALPM	= 000262	ALPP	= 000261	AMA	= 000260	APA	= 000257	BAI	= 000252	DALTM	= 000276		
DALTP	= 000275	DBS	= 000265	DBE	= 000271	DBE1	= 000267	DBE2	= 000270	DBT	= 000300		
DEME	= 000277	DTT	= 000274	DTT1	= 000272	DTT2	= 000273	EALPM	= 000264	EALPP	= 000263		
EPS	= 000254	ETA	= 000266	T	= 000256	TAU	= 000253	T1A	= 000255				

START OF CONSTANTS=000154 TEMPS=000161 INDIRECTS=000243

7600 COMPILATION -- RUN76 LEVEL 731 73/11/08.

Table 6. Program to calculate lattice sums, the second and fourth moments and the correlation time for a rigid lattice. The subroutine COORD forms the CaF_2 lattice (see Table IV for an FCC lattice).

```
PDR
                PROGRAM PDR(INPUT,OUTPUT,TAPE11=INPUT,TAPE10=OUTPUT)
          C     CALCULATES POWDER AVERAGE OF SPIN CORRELATION TIME
          C     AVERAGE IS TAKEN OVER HALF OF ONE OCTANT
          C     SIMPSON INTEGRATION USED
          C
                DIMENSION LSIZE(3),ARRAY(50,50),SUM(50)
          C
                NTMIN=3
      3         NTMAX=50
      4         NPMIN=3
      4         NPMAX=50
          C     READ PARAMETERS
      6   10    READ(11,11) FACTOR
          11    FORMAT(E10.0)
     14         IF (FACTOR .EQ. 0) GO TO 100
     15         WRITE(10,12) FACTOR
          12    FORMAT(1H1,*FACTOR=*,E15.8)
     23         READ(11,13) (LSIZE(I),I=1,3)
          13    FORMAT(3I3)
     31         DO 14 I=1,3
     33         IF (MOD(LSIZE(I),2) .EQ. 0) LSIZE(I)=LSIZE(I)-1
     42         IF (LSIZE(I) .LT. 3) LSIZE(I)=3
     47   14    CONTINUE
     51         WRITE(10,15) (LSIZE(I),I=1,3)
          15    FORMAT(1X,*S1 LATTICE SIZE=*,I2/1X,*S2 LATTICE SIZE=*,I2/
                1X,*S4 LATTICE SIZE=*,I2)
     57         READ(11,16) NTHETA,NPHI
          16    FORMAT(2I3)
     67         IF (MOD(NTHETA,2) .EQ. 0) NTHETA=NTHETA-1
     73         IF (NTHETA .LT. NTMIN) NTHETA=NTMIN
     76         IF (NTHETA .GT. NTMAX) NTHETA=NTMAX
    101         IF (MOD(NPHI,2) .EQ. 0) NPHI=NPHI-1
    105         IF (NPHI .LT. NPMIN) NPHI=NPMIN
    110         IF (NPHI .GT. NPMAX) NPHI=NPMAX
    113         WRITE(10,17) NTHETA,NPHI
          17    FORMAT(1X,*NTHETA=*,I2/1X,*NPHI=*,I2/)
          C
          C     CALCULATE DELTAS
    123         PI=4.0*ATAN(1.0)
    127         DTHETA=1.0/(NTHETA-1)
    132         DPHI=(PI/4.0)/(NPHI-1)
          C
          C     GET TAUS
    137         DO 23 I=1,NTHETA
    141         COST=1.0-(I-1)*DTHETA
    145         SINT=SQRT(1.0-COST*COST)
    150         THETA=ATAN2(SINT,COST)
    153         TDEG=THETA*(180.0/PI)
    156         DO 22 J=1,NPHI
    160         PHI=(J-1)*DPHI
    163         PDEG=PHI*(180.0/PI)
    166         ARRAY(I,J)=TAU(THETA,PHI,FACTOR,LSIZE)
    176         WRITE(10,21) TDEG,PDEG,ARRAY(I,J)
          21    FORMAT(1X,*THETA=*,F6.2,1X,*PHI=*,F6.2,1X,*TAU=*,E15.8)
   212    22    CONTINUE
   215    23    CONTINUE
```

```
PDR
          C
          C      DO AVE OVER THETA
    217          DO 31 J=1,NPHI
    221          SUM(J)=SIMP(ARRAY(1,J),NTHETA)/(NTHETA-1)
    232    31    CONTINUE
          C      DO AVE OVER PHI
    234          TAUAVE=SIMP(SUM,NPHI)/(NPHI-1)
    242          WRITE(10,32) TAUAVE
           32    FORMAT(/*AVERAGE CORRELATION TIME=*,E15.8)
    250          GO TO 10
    251   100    STOP
    253          END


PROGRAM LENGTH INCLUDING I/O BUFFERS

06442

FUNCTION ASSIGNMENTS

STATEMENT ASSIGNMENTS
10      - 000007     11      - 000267     12      - 000272     13      - 000276     14      - 000050     15      - 000400
16      - 000312     17      - 000314     21      - 000324     32      - 000333     100     - 000252

BLOCK NAMES AND LENGTHS

VARIABLE ASSIGNMENTS
ARRAY   - 000363     COST    - 005364     DPHI    - 005363     DTHETA  - 005362     FACTOR  - 005355     I       - 005356
J       - 005370     LSIZE   - 000362     NPHI    - 005360     NPMAX   - 005354     NPMIN   - 005353     NTHETA  - 005357
NTMAX   - 005352     NTMIN   - 005351     PDEG    - 005372     PHI     - 005371     PI      - 005361     SINT    - 005365
SUM     - 005267     TAUAVE  - 005373     TDEG    - 005367     THETA   - 005366

START OF CONSTANTS-000256       TEMPS--000341    INDIRECTS-000354

7600 COMPILATION -- RUN76 LEVEL 98       05 JAN 75

ROUTINE COMPILED IN 044400
```

```
TAU
            FUNCTION TAU(THETA,PHI,FACTOR,LSIZE)
      C
      C     CALCULATES SPIN CORRELATION TIME GIVEN FIELD DIRECTION
      C
            DIMENSION LSIZE(3),FIELD(3),ATOM1(3),ATOM2(3)
            INTEGER SIZE
            REAL M2
            LOGICAL OCC
      C
      C     CALCULATE FIELD
            FIELD(1)=SIN(THETA)*COS(PHI)
 14         FIELD(2)=SIN(THETA)*SIN(PHI)
 26         FIELD(3)=COS(THETA)
      C
      C     CALCULATE S1
 35         SIZE=LSIZE(1)
 36         IMAX=SIZE**3
 40         S1=0.0
 41         DO 11 I=1,IMAX
 43         CALL COORD(OCC,ATOM1,I,SIZE)
 46         IF (.NOT. OCC) GO TO 11
 52         S1=S1+BI(ATOM1,FIELD)**2
 61   11    CONTINUE
      C
      C     CALCULATE S2
 64         SIZE=LSIZE(2)
 65         IMAX=SIZE**3
      C     FIND INDX OF CENTER POINT
 67         CALL COORD(OCC,ATOM1,1,SIZE)
 72         RE2MIN=ATOM1(1)**2+ATOM1(2)**2+ATOM1(3)**2
 76         INDXC=1
 77         DO 21 I=2,IMAX
103         CALL COORD(OCC,ATOM1,I,SIZE)
106         IF (.NOT. OCC) GO TO 21
112         RE2=ATOM1(1)**2+ATOM1(2)**2+ATOM1(3)**2
116         IF (RE2 .GE. RE2MIN) GO TO 21
120         RE2MIN=RE2
121         INDXC=I
123   21    CONTINUE
126         CALL COORD(OCC,ATOM1,INDXC,SIZE)
131         S2=0.0
132         DO 22 I=1,IMAX
136         CALL COORD(OCC,ATOM2,I,SIZE)
141         IF (.NOT. OCC) GO TO 22
145         S2=S2+BI(ATOM1,ATOM2,FIELD)**2
155   22    CONTINUE
      C
      C     CALCULATE S4
160         SIZE=LSIZE(3)
161         IMAX=SIZE**3
162         S4=0.0
163         DO 32 J=2,IMAX
165         CALL COORD(OCC,ATOM2,J,SIZE)
170         IF (.NOT. OCC) GO TO 32
174         BI2=BI(ATOM2,FIELD)
176         JM1=J-1
```

```
TAU
 201          DO 31 I=1,JM1
 205          CALL COORD(CCC,ATOM1,I,SIZE)
 210          IF (.NOT. OCC) GO TO 31
 214          S4=S4+BIJ(ATOM1,ATOM2,FIELD)**2*BI(ATOM1,FIELD)*BI2
 227    31    CONTINUE
 232    32    CONTINUE
        C
        C     CALCULATE M2
 235          WRITE(10,41) S1,S2,S4
        41    FORMAT(1A,*S1=*,E15.8,1X,*S2=*,E15.8,1X,*S4=*,E15.8)
 251          M2=FACTOR*(S1*S2-2.0*S4)/S1
        C     CALCULATE TAU
 255          TAU=SQRT(2.0/M2)
 261          RETURN
 261          END
```

```
SUBPROGRAM LENGTH

00344

FUNCTION ASSIGNMENTS

STATEMENT ASSIGNMENTS
11      - 000062     21      - 000124     22      - 000156     31      - 000230     32      - 000233     41      - 000267

BLOCK NAMES AND LENGTHS

VARIABLE ASSIGNMENTS
ATOM1   - 000320     ATOM2   - 000329     BI2     - 000342     FIELD   - 000315     I       - 000333     IMAX    - 000331
INDXC   - 000335     J       - 000341     JM1     - 000343     M2      - 000327     OCC     - 000330     RE2     - 000336
RE2MIN  - 000334     SIZE    - 000328     S1      - 000332     S2      - 000337     S4      - 000340     TAU     - 000314

START OF CONSTANTS-000264        TEMPS--000276    INDIRECTS-000313

7600 COMPILATION -- RUN76 LEVEL 98       05 JAN 75

ROUTINE COMPILED IN 044300
```

```
BI
                FUNCTION BI(ATOM,FIELD)
          C
          C     CALCULATES BI GIVEN ATOM COORDS AND FIELD DIR COSINES
          C
                DIMENSION ATOM(3),FIELD(3)
          C
          C     CALC R,R**2,R**3
                X=ATOM(1)
        6       Y=ATOM(2)
        7       Z=ATOM(3)
       10       RE2=X*X+Y*Y+Z*Z
       13       RE1=SQRT(RE2)
       15       RE3=RE1*RE2
          C     CHECK FOR ZERO VECTOR
       17       IF (RE1 .NE. 0.0) GO TO 20
       21       BI=0.0
       22       GO TO 100
          C     CALC DIRECTION COSINES OF ATOM
       22  20   DCX=X/RE1
       24       DCY=Y/RE1
       25       DCZ=Z/RE1
          C     CALC COS THETA
       27       COST=DCX*FIELD(1)+DCY*FIELD(2)+DCZ*FIELD(3)
          C     CALC P2(COS THETA)
       34       P2CT=1.5*COST*COST-0.5
          C     CALC BI
       36       BI=-2.0*P2CT/RE3
       41  100  RETURN
       43       END
```

```
SUBPROGRAM LENGTH

00100

FUNCTION ASSIGNMENTS

STATEMENT ASSIGNMENTS
20      - 000023      100     - 000042

BLOCK NAMES AND LENGTHS

VARIABLE ASSIGNMENTS
BI      - 000064      COST    - 000076      DCX     - 000073      DCY     - 000074      DCZ     - 000075      P2CT    - 000077
RE1     - 000071      RE2     - 000078      RE3     - 000072      X       - 000065      Y       - 000066      Z       - 000067

START OF CONSTANTS-000046        TEMPS--000052     INDIRECTS-000056

7600 COMPILATION -- RUN76 LEVEL 98       05 JAN 75

ROUTINE COMPILES IN 044000
```

COORD

```
      SUBROUTINE COORD(OCC,ATOM,INDX,SIZE)
C
C     CALCULATES COORDINATES OF ATOM IN FCC LATTICE GIVEN INDEX
C     COORDS=(L,M,N), L,M,N=-(SIZE-1)/2,...,0,1,...(SIZE-1)/2
C     INDX=(L+SMIH)+(M+SMIH)*SIZE+(N+SMIH)*SIZE**2+1
C        SMIH=(SIZE-1)/2
C
      DIMENSION ATOM(3)
      INTEGER SIZE,SIZESQ,SMIH
      LOGICAL OCC
C
      SIZESQ=SIZE*SIZE
      ITEMP=INDX-1
      N=ITEMP/SIZESQ
      ITEMP=ITEMP-N*SIZESQ
      M=ITEMP/SIZE
      L=ITEMP-M*SIZE
      SMIH=(SIZE-1)/2
      L=L-SMIH
      M=M-SMIH
      N=N-SMIH
   10 OCC=.TRUE.
      ATOM(1)=L+0.5
      ATOM(2)=M+0.5
      ATOM(3)=N+0.5
  100 RETURN
      END
```

SUBPROGRAM LENGTH

00063

FUNCTION ASSIGNMENTS

STATEMENT ASSIGNMENTS

11 - 000031 100 - 000041

BLOCK NAMES AND LENGTHS

VARIABLE ASSIGNMENTS

ITEMP - 000057 L - 000062 M - 000061 N - 000060 SIZESQ - 000055 SMIH - 000056

START OF CONSTANTS-000044 TEMPS--000046 INDIRECTS-000052

7600 COMPILATION -- RUN76 LEVEL 11E 07 JUN 75

ROUTINE COMPILES IN 044000

```
BIJ
                FUNCTION BIJ(ATOM1,ATOM2,FIELD)
          C
          C     CALCULATES BIJ GIVEN ATOM COORDS AND FIELD DIR COSINES
          C
                DIMENSION ATOM1(3),ATOM2(3),FIELD(3)
          C
          C     CALC R,R**2,R**3
                X=ATOM2(1)-ATOM1(1)
     10         Y=ATOM2(2)-ATOM1(2)
     12         Z=ATOM2(3)-ATOM1(3)
     14         RE2=X*X+Y*Y+Z*Z
     17         RE1=SQRT(RE2)
     21         RE3=RE1*RE2
          C     CHECK FOR ZERO VECTOR
     23         IF (RE1 .NE. 0.0) GO TO 20
     26         BIJ=0.0
     27         GO TO 100
          C     CALC DIRECTION COSINES OF VECTOR
     27   20    DCX=X/RE1
     31         DCY=Y/RE1
     32         DCZ=Z/RE1
          C     CALC COS THETA
     34         COST=DCX*FIELD(1)+DCY*FIELD(2)+DCZ*FIELD(3)
          C     CALC P2(COS THETA)
     41         P2CT=1.5*COST*COST-0.5
          C     CALC BIJ
     43         BIJ=-3.0*P2CT/RE3
     46   100   RETURN
     50         END


SUBPROGRAM LENGTH

00110

FUNCTION ASSIGNMENTS

STATEMENT ASSIGNMENTS
20      = 000030      100     = 000047

BLOCK NAMES AND LENGTHS

VARIABLE ASSIGNMENTS
BIJ     = 000074      COST    = 000106      DCX     = 000103      DCY     = 000104      DCZ     = 000105      P2CT    = 000107
RE1     = 000101      RE2     = 000108      RE3     = 000102      X       = 000075      Y       = 000076      Z       = 000077

START OF CONSTANTS-000053        TEMPS--000057    INDIRECTS-000063

7600 COMPILATION -- RUN76 LEVEL 98       05 JAN 75

ROUTINE COMPILES IN 044000
```

```
SIMP
                FUNCTION SIMP(ARRAY,N)
          C
          C     PERFORMS SIMPSON INTEGRATION
          C     N MUST BE ODD AND .GE. 3
          C
                DIMENSION ARRAY(N)
                SIMP=ARRAY(1)+4.0*ARRAY(2)
      6         NPAIR=(N-3)/2
     10         IF (NPAIR .LE. 0) GO TO 12
     12         DO 11 I=1,NPAIR
     22         SIMP=SIMP+2.0*ARRAY(2*I+1)+4.0*ARRAY(2*I+2)
     25   11    CONTINUE
     30   12    SIMP=(SIMP+ARRAY(N))/3.0
     33         RETURN
     34         END


SUBPROGRAM LENGTH

00055

FUNCTION ASSIGNMENTS

STATEMENT ASSIGNMENTS
12      = 000031

BLOCK NAMES AND LENGTHS

VARIABLE ASSIGNMENTS
I       = 000054      NPAIR   = 000053      SIMP    = 000052

START OF CONSTANTS=000037       TEMPS--000043    INDIRECTS=000047

7600 COMPILATION -- RUN76 LEVEL 98       05 JAN 75

ROUTINE COMPILES IN 044000
```

Table 7. Subroutine COORD used to form an FCC lattice for the program PDR. See Table 6 for the main program.

```
COORD
            SUBROUTINE COORD(OCC,ATOM,INDX,SIZE)
      C
      C     CALCULATES COORDINATES OF ATOM IN FCC LATTICE GIVEN INDEX
      C     COORDS=(L,M,N) L,M,N=-(SIZE-1)/2,...,0,1,...,(SIZE-1)/2
      C     INDX=(L+SM1H)+(M+SM1H)*SIZE+(N+SM1H)*SIZE**2+1
      C        SM1H=(SIZE-1)/2
      C
            DIMENSION ATOM(3)
            INTEGER SIZE,SIZESQ,SM1H
            LOGICAL OCC
      C
            SIZESQ=SIZE*SIZE
   10       ITEMP=INDX-1
   11       N=ITEMP/SIZESQ
   14       ITEMP=ITEMP-N*SIZESQ
   16       M=ITEMP/SIZE
   20       L=ITEMP-M*SIZE
   23       SM1H=(SIZE-1)/2
   24       L=L-SM1H
   25       M=M-SM1H
   26       N=N-SM1H
   27       IF (MOD(L+M+N,2) .EQ. 0) GO TO 11
   34       OCC=.FALSE.
   35       GO TO 100
   35  11   OCC=.TRUE.
   36       ATOM(1)=L
   37       ATOM(2)=M
   41       ATOM(3)=N
   43  100  RETURN
   44       END


SUBPROGRAM LENGTH

00070

FUNCTION ASSIGNMENTS

STATEMENT ASSIGNMENTS
11      - 000036      100     - 000044

BLOCK NAMES AND LENGTHS

VARIABLE ASSIGNMENTS
ITEMP   - 000064      L       - 000067      M       - 000066      N       - 000065      SIZESQ - 000062      SM1H    - 000063

START OF CONSTANTS-000047        TEMPS--000050     INDIRECTS-000057

7600 COMPILATION -- RUN76 LEVEL 98       05 JAN 75

ROUTINE COMPILES IN 044000
```

Chapter One References

1. H. E. Bleich and A. G. Redfield, J. Chem. Phys. 55, 5405 (1971); C. S. Yannoni and H. E. Bleich, ibid. 55, 5406 (1971).
2. P. Mansfield and P. K. Grannell, J. Phys. C 4, L197 (1971).
3. A. Pines, M. G. Gibby, and J. S. Waugh, J. Chem. Phys. 59, 569 (1973).
4. A. Pines, Proceedings of the First Specialized Colloque Ampere, Krakow, Poland, August 1973 (to be published).
5. J. S. Waugh, Proceedings of the First Specialized Colloque Ampere, Krakow, Poland, August 1973 (to be published).
6. L. R. Sarles and R. M. Cotts, Phys. Rev. 111, 853 (1958).
7. M. Mehring, A. Pines, W-K. Rhim, and J. S. Waugh, J. Chem. Phys. 54, 3239 (1971).
8. A. Pines and J. D. Ellett, Jr., J. Am. Chem. Soc. 95, 4437 (1973).
9. M. Mehring, G. Sinning and A. Pines, Z. Phys., in press; Lawrence Berkeley Laboratory Annual Report No. 4550, 1975.
10. A. Pines, D. J. Ruben, S. Vega, and M. Mehring, Phys. Rev. Lett., published; Lawrence Berkeley Laboratory Annual Report No. 4550, 1975.
11. For example, a) S. Pausak, A. Pines, and J. S. Waugh, J. Chem. Phys. 59, 591 (1973), b) J. J. Chang, R. G. Griffin, and A. Pines, J. Chem. Phys. 60, 2561 (1974), c) A. Pines and E. Abramson, J. Chem. Phys. 61, 1021 (1974).
12. M. Goldman, Spin Temperatures and Nuclear Magnetic Resonance in Solids (Oxford University Press, London 1970).
13. J. Jeener and P. Broekaert, Phys. Rev. 157 (2) 232 (1967).
14. D. A. Mc Arthur, E. L. Hahn, and R. Walstedt, Phys. Rev. 188, 609 (1969).

15. A preliminary report has been published on this study. There was an error in the experimental τ_c reported: A. Pines and T. W. Shattuck, J. Chem. Phys. 61 (3) 1255 (1974).

16. S. R. Hartmann and E. L. Hahn, Phys. Rev. 128, 2042 (1962).

17. D. E. Demco, J. Tegenfeld and J. S. Waugh, Phys. Rev. B. 11 (11) 4134 (1974)

18. A. Abragam, The Principles of Nuclear Magnetism (Oxford University Press, Oxford, 1961).

19. J. H. Van Vleck, Phys. Rev. 74 (9) 1168 (1948).

20. G. W. Canters and C. S. Johnson, J. Mag. Res. 6, 1 (1972).

21. C. P. Slichter, Principles of Magnetic Resonance (Harper and Row, New York, 1963); E. Ambler, J. C. Eisenstein and J. F. Schooley, J. Math. Phys. 3 (18) 118 (1962).

22. a) N. Nowacki, Hevl. Chim. Acta 28, 1233 (1945).

b) G. Giacomello and G. Illuminati, Gazz. Chim. Ital. 75, 246 (1945) and Ric. Sci. 15, 559 (1945).

c) C. E. Nordman and D. L. Schmitkons, Acta. Cryst. 18, 764 (1965).

d) J. Donohue and S. H. Goodman, Acta. Cryst. 22, 352 (1967).

23. H. A. Resing, Mol. Cryst. Liquid. Crst. 9, 101 (1969).

24. A. Pines and T. W. Shattuck, Chem. Phys. Lett. 23 (4) 614, (1973).

25. L. Müller, A. Kumar, T. Baumann, and R. R. Ernst, Phys. Rev. Lett. 32 (25) 1402 (1974).

26. T. W. Shattuck, Lawrence Berkeley Laboratory report, University of California, 1976.

27. D. W. McCall and R. W. Hamming, Acta. Cryst. 12, 81 (1959).

28. F. R. Lurie and C. P. Slichter, Phys. Rev. 133 (4) 1108 (1964).

29. C. P. Slichter and W. C. Holton, Phys. Rev. 122, 1701 (1961).

30. R. T. Schumacher, Phys. Rev. 112 (3), 837 (1958).

31. A. G. Anderson and S. R. Hartman, Phys. Rev. 128 (5), 2023 (1962).

32. L. V. Dmitrieva and V. V. Moskalev, Fizika Tverdogo Tela, 5 (8), 2230-2231 (1963), [Sov. Phys. Solid State, 5 (8), 1623 (1964)].

33. D. M. McCall and D. C. Douglass, J. Chem. Phys. 33 (3), 777 (1960).

34. G. W. Smith, J. Chem. Phys. 36, 2081 (1962).

35. D. J. Kroon, Philips Res. Reports, 15, 501 (1960).

36. G. W. Smith, J. Chem. Phys. 35, 1134 (1961).

37. J. D. Graham and J. K. Choi, J. Chem. Phys. 62 (6), 2509 (1975).

Chapter 2

I. Introduction

Solid state NMR is rapidly being developed into a powerful means of probing electronic structure, molecular conformation and molecular dynamics. Although these techniques have been applied to many different nuclei of spin ½ (^{1}H, ^{13}C, ^{31}P, ^{109}Ag, ^{43}Ca, ^{19}F, ^{15}N) the most ubiquitous spin species, protons, have remained the most difficult to deal with experimentally. We present here a new method to circumvent the problems posed by solid state proton nmr. Instead of observing the proton magnetic resonance we choose to observe deuterium nuclei (spin -1) which have been substituted into the molecule of interest. This isotopic dilution serves to decrease the strong dipole-dipole interactions which might obscure chemical shift information,[1] as we have seen in Chapter 1.

On the other hand, the ability to extract information from deuterium resonance is severely hampered by the extreme broadening caused by the interaction of the nuclear quadrupole moment with electric field gradients. For deuterium, the quadrupolar splittings are typically of the order of $\sim$ 200 kHz, whereas the chemical shifts are expected to span a range of $\sim$ 500 Hz. We have developed two different techniques for dealing with this problem. The first which we call Quadrupole Satellite Spectroscopy (QSS) takes advantage of the very sharp lines which are available from a single crystal to measure the small chemical shifts. If these satellites are too broad, due either to crystal imperfections, chemical exchange or complex due to many inequivalent spins or polycrystalline samples, the second technique, Fourier Transform Double Quantum (FTDQ) Spectroscopy

is used to effectively eliminate the quadrupole interaction, leaving the chemical shift, dipolar and scalar interactions. Both of these methods greatly expand the number of systems for which high resolution spectra may be obtained. As an example we report the first measurement of the chemical shift of deuterium in a solid. This includes the resolution of chemical shifts for different deuterium nuclei in a crystal and a measure of the anisotropy of the chemical shifts as the crystal is rotated.

Cross polarization techniques have proven quite useful for carbon-13-proton double resonance (see Chapter 1). Since deuterium can now be used as a high resolution probe we have extended these enhancement techniques to the realm of deuterium-proton double resonance. The experiments involve a cross polarization of the deuterium double-quantum transition. This completes the correspondence of established solid state techniques to the deuterium case.

Apart from its practical significance the coherence properties of multilevel systems is of great interest for many types of systems including microwave double resonance, pulsed optical studies and optically detected magnetic resonance.[2] Deuterium NMR is a useful tool in studying coherence phenomena since it is a tractable three level system. We present here an approach for the exact treatment of the coherence properties of this system for both single and double resonance experiments.

We report the results of what we believe to be the first cross polarization experiments, of the thermal mixing type at high field, between deuterium and protons. The detection is achieved both indirectly and directly, from which we have extracted cross polarization times, correlation times and spin heat capacities, including the novel case of

the double-quantum processes.

As an approach to high resolution spectroscopy we must deal with interactions on three levels; first the very large electric quadrupole interactions, second the dipolar interactions and third the chemical shift. In the second section we deal with the problems caused by each of these interactions in turn. Having presented the general philosophy, the third section will give the necessary theory. The treatment of double resonance is presented in the fourth section.

II. Approach for High Resolution

Part of the deuterium spectrum of a powder of dimethylsulfoxide (DMSO) is shown in Figure 1. The pattern is much too broad to extract any fine structure. The spectrum of a single crystal however would contain two sharp lines split by the electric field gradient along the external magnetic field direction. High field spectra of this type have been used for example to extract information on hydrogen bonding and the reorientation and structure of water of hydration in solids.[3-5] The above work is based on the determination of the electric field gradient (EFG) tensor and the observation of dipolar fine structure of the quadrupole spectrum. We note that since the EFG tensor is traceless the spectrum will be centered at a frequency determined solely by the chemical shift and small second-order quadrupolar effects. Following the center of mass of the two lines as the crystal is rotated then essentially maps out the chemical shift tensor. If there are dipole-dipole interactions in the crystal, the results will show up as line broadening and/or fine structures on the satellites themselves. The main disadvantages of this method are

1) that it is difficult to strike a compromise between the high resolution necessary to observe the small effects of the chemical shift and the wide bandwidth required to observe the entire quadrupole splitting and

2) the satellites may be so broad due to crystal imperfections, etc., that it is impossible to obtain the resolution needed.

These difficulties can be resolved if a way is found of cancelling out the quadrupole coupling while retaining the other interactions. The level diagram for deuterium (S = 1) is shown in Figure 2. The normal

Figure 1. Deuterium spectrum of polycrystalline perdeutero Dimethyl sulfoxide (99.5%). Note that the entire breadth is 88 kHz since only the middle portion of the powder pattern is shown. The temperature is -75°C.

DMSO - d_6 (~99.5 %)

T~-75 °C

^{2}D Fourier Transform, 16.3 MHz

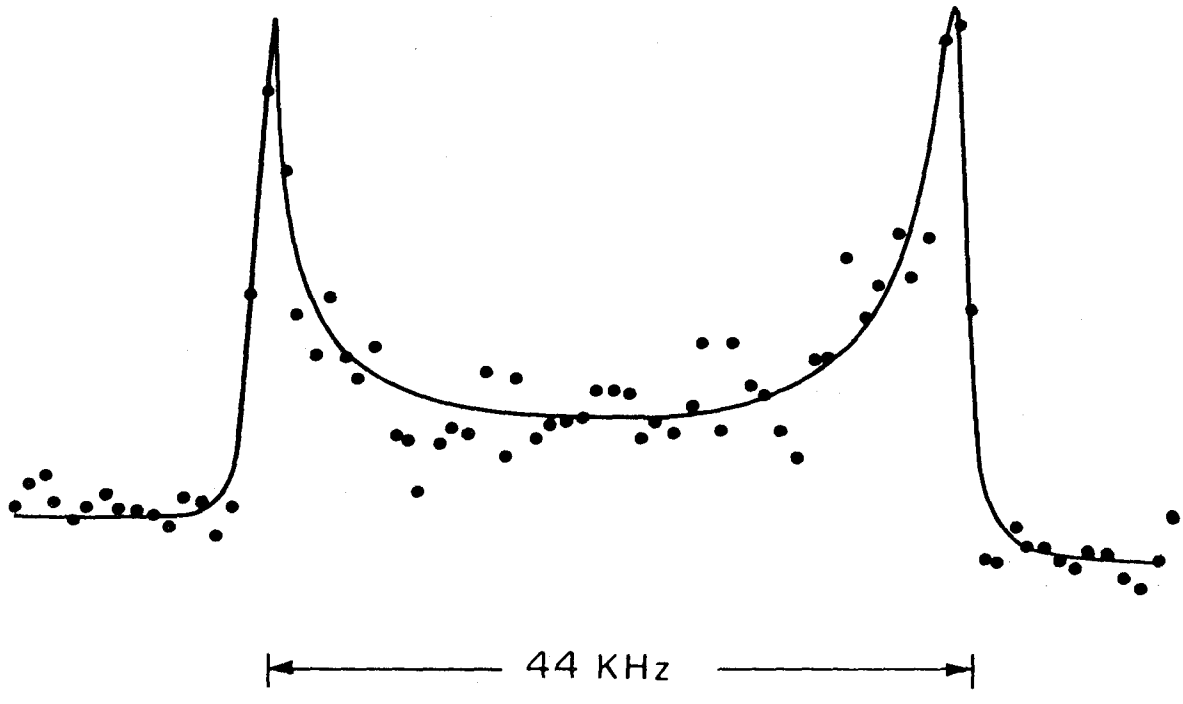

XBL 756-6464

Figure 2. Zeeman and Quadrupole energy levels for spin = 1. The double quantum transition occurs at ω_0 since the m = ± 1 levels are shifted by the same amount (to first order).

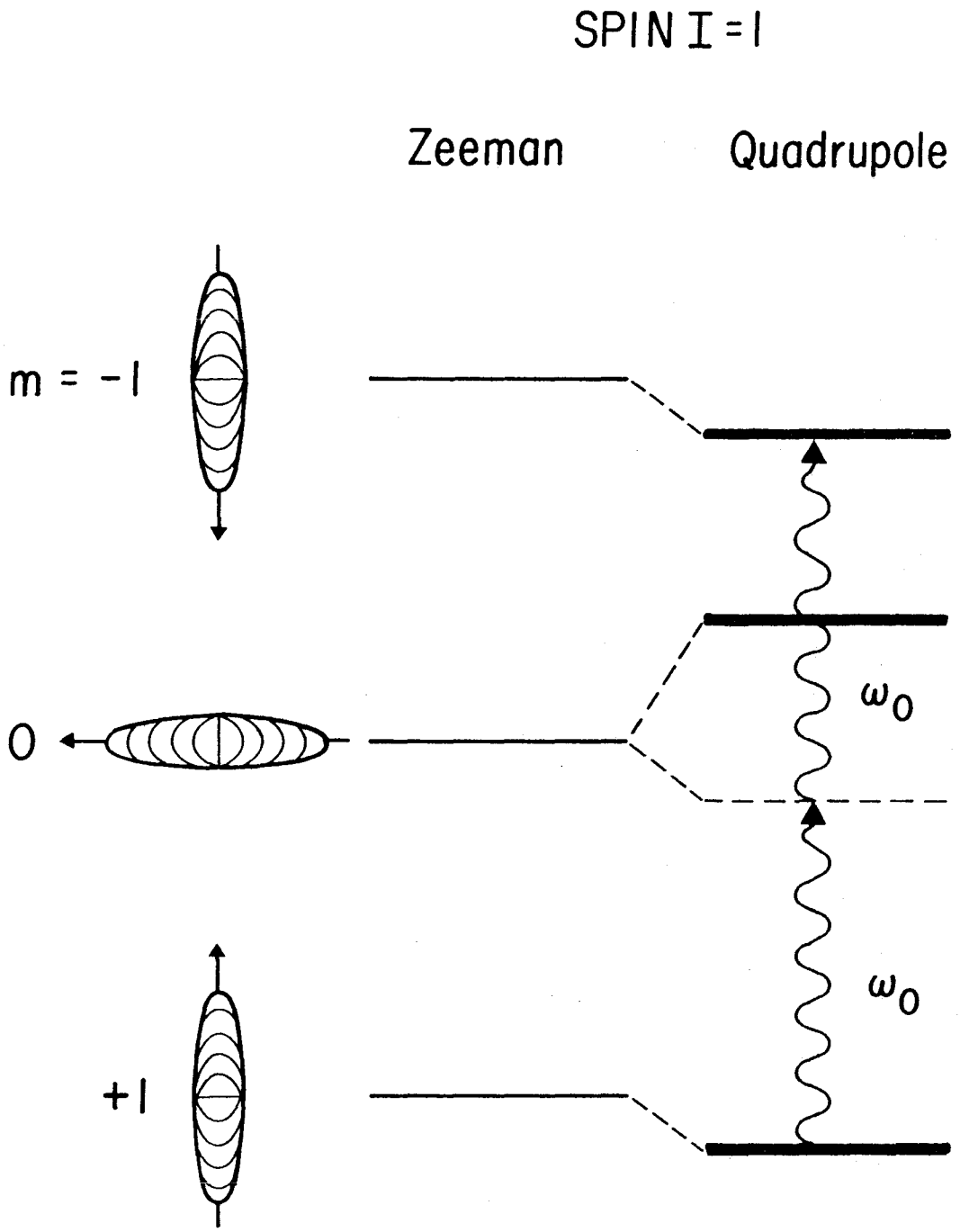

XBL 763-629

allowed transitions for the spin-1 are $m = 1 \rightarrow 0$ and $m = 0 \rightarrow -1$ which are shifted by the quadrupolar interaction, ω_Q. To first order, the $m = 1 \rightarrow -1$ splitting is not shifted, however, The splitting remains at $2\,\omega_0$ no matter what the quadrupole interaction is, and of course this splitting contains the chemical shift. We induce the transition $m = 1 \rightarrow -1$ with a radio frequency field of intensity ω_1 at the unshifted frequency, ω_0, placing the levels ± 1 in coherent superposition. This coherence, which we label tentatively $Q(\tau)$, now evolves as

$$Q(\tau) \sim a(\tau) \cos 2\Delta\omega\tau \qquad (1)$$

where $\Delta\omega$ is the resonance offset or chemical shift and $a(\tau)$ is the decay due to relaxation by deuterium-deuterium, deuterium-proton or deuterium lattice coupling. We shall see that $Q(\tau)$ does not contain ω_Q and thus we have effectively removed the quadrupole broadening.

If we wish to observe only the chemical shift the dipolar coupling must be reduced. This is conveniently handled by isotopic dilution,[1] as mentioned before. The more conventional choice for protons has been to use multiple-pulse line narrowing techniques,[7] to reduce homonuclear dipole-dipole couplings. These techniques are difficult and our hope was to replace them with something more generally applicable. For isotopic dilution the homonuclear dipole-dipole coupling is reduced through its distance dependence, leaving only the heteronuclear dipole-dipole coupling which is easily averaged to zero by spin decoupling.

Lastly we must extract the full chemical shielding tensor. This can be done either by rotating a single crystal about its axes or by observing the polycrystalline lineshape (powder lineshape). As mentioned above, direct observation of the quadrupole spectrum, QSS, is only amenable to the former method. While the double quantum approach may

have the advantage of better resolution, its applicability is truly demonstrated by it's ability to handle powder samples.

Isotopic dilution, however, decreases the signal to noise drastically just as in the case of carbon-13. The cross polarization experiments discussed will undoubtably aid in dealing with the problem. For a spin 1 we have the additional possiblity of being able to cross polarize any one of the three different transitions. Cross polarizing either of the satellites is the direct extension of the carbon-13 work in Chapter 1. Cross polarization of the double quantum transition will be seen to produce a fundamentally different kind of deuterium polarization, a tensor polarization. In addition the dynamics of the process help to confirm the theory we have formulated.

III. Theory

The total Hamiltonian for the deuterium spin system (S) neglecting other spin species can be written (in angular frequency units):

$$H_S = H_{SZ} + H_{SQ} + H_{SS} + H_{rf}(t) \tag{2}$$

The Zeeman term

$$H_{SZ} = -\omega_0 \ (1-\sigma_{ZZ})S_Z \text{ where } S_Z = \Sigma_i \ S_{iZ}$$

$$\omega_0 = \gamma_S H_o \tag{3}$$

takes into account the projection of the chemical shielding tensor $\underset{\approx}{\sigma}$ along the direction of the external field H_o, σ_{ZZ}. The deuterium magnetogyric ratio is γ_S.

The quadrupole term is:

$$H_{SQ} = \frac{3e^2qQ}{8\ \hbar} \ [(3 \cos^2 \theta_Q - 1) + \eta(\sin^2 \theta_Q \cos^2 \phi_Q)] \ .$$

$$[S_Z^2 - \frac{1}{3} S \ (S + 1)] \tag{4}$$

and we define further $\omega_Q = \frac{3e^2qQ}{8\ \hbar} \ ((3 \cos^2\theta_Q - 1) + \eta(\sin^2\theta_Q(\cos 2\phi_Q))$ which is the actual splitting observed between the satellite and zero frequency, see Figures 2 and 3. Q is the nuclear quadrupole moment, q is the largest element of the electric field gradient (EFG) tensor and η is the asymmetry parameter:

$$q = q_{33}, \ \eta = \frac{(q_{11}-q_{22})}{q_{33}} \quad \text{with} \quad |q_{33}| \geq |q_{22}| \geq |q_{11}| \tag{5}$$

Figure 3. a) Quadrupole energy level scheme for a chemical shift of σ. The allowed quadrupole aatellite transitions are indicated in b). The effect of fold over is indicated, for the case that the irradiation frequency is exactly ω_0 in c).

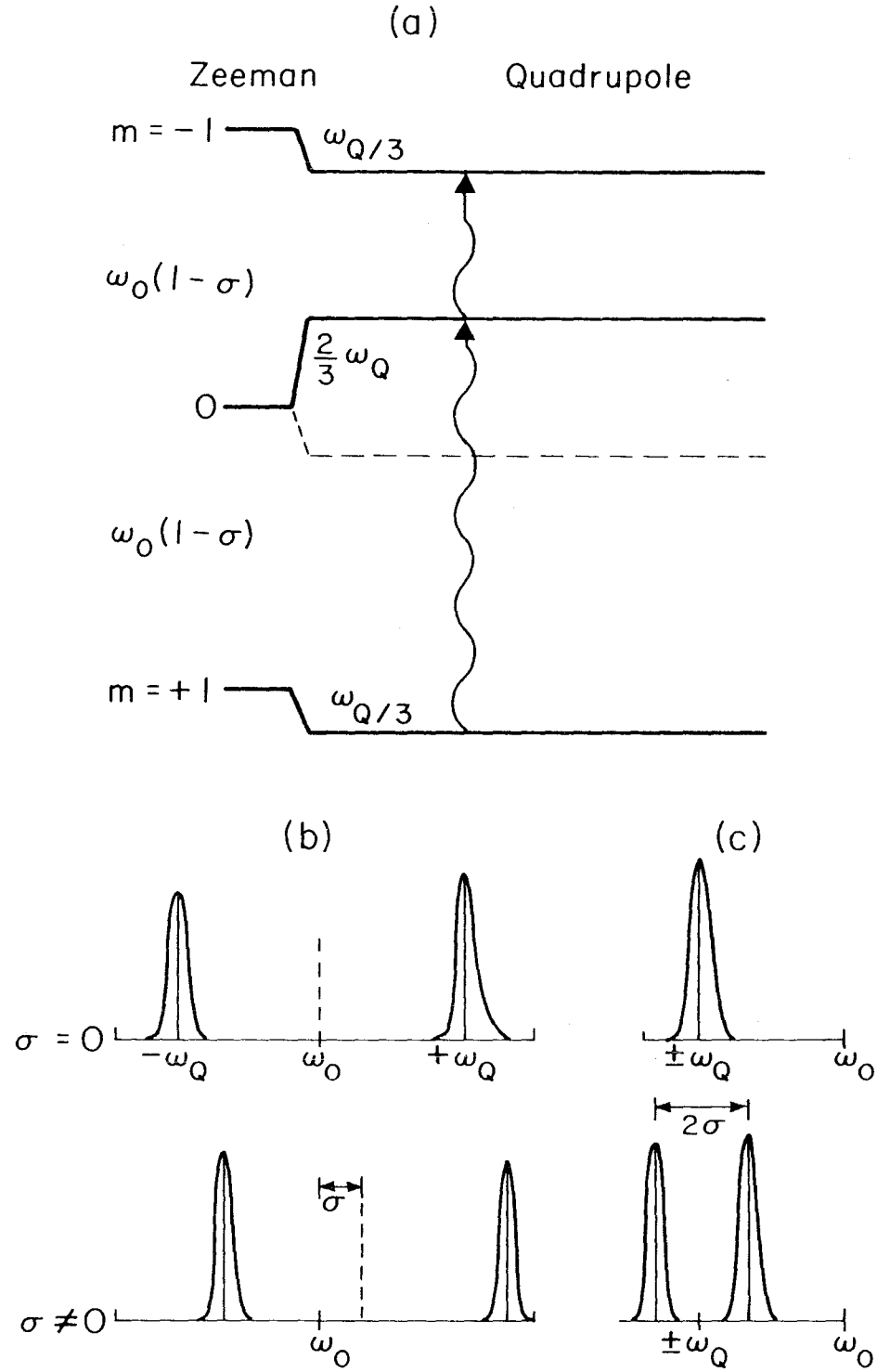
(a)
Zeeman
Quadrupole
m = −1
$\omega_{Q/3}$
$\omega_0(1-\sigma)$
$\frac{2}{3}\omega_Q$
0
$\omega_0(1-\sigma)$
m = +1
$\omega_{Q/3}$
(b)
(c)
σ = 0
$-\omega_Q$
ω_0
$+\omega_Q$
$\pm\omega_Q$
ω_0
2σ
σ
σ ≠ 0
ω_0
$\pm\omega_Q$
ω_0

XBL 765-1982

where q_{ii} are the principal values of the EFG tensor. The angles θ_Q and ϕ_Q are taken between the laboratory axes as defined by H_o and the principal axes of the EFG.

The homonuclear dipole-dipole term

$$H_{II}^{(o)} = \sum_{i<j} \frac{-\gamma_I^2 \hbar}{r_{ij}^3} \frac{1}{2}(3 \cos^2\theta_{ij} - 1) \{3I_{iZ}I_{jZ} - \underset{\sim}{I}_i \cdot \underset{\sim}{I}_j\} \tag{6}$$

is taken in the truncated high field form, as is the quadrupole Hamiltonian. The angle θ_{ij} is taken between the internuclear vector and the external field.

The radio frequency irradiation is given as

$$H_{rf}(t) = -2\omega_1 S_X \cos \omega t$$

where

$$\omega_1 = \gamma_S H_1 \tag{7}$$

and H_1 is the strength of the applied rf field.

A. Quadrupole Satellite Spectroscopy

Let us first concentrate on the first two terms of equation (2); in order to explain QSS. The Zeeman interaction generates three non-degenerate levels characterized by m = +1, 0, -1, the quadrupole interaction then lifts the degeneracy of the +1 → 0 and the 0 → -1 transition to give a two-line spectrum, as in Figure 3. The experiments were performed with a single phase detector so that positive and negative frequency with respect to the carrier frequency are indistinguishable. This causes the spectrum to "fold over", and the splitting between the two satellites is then:

$$\Delta\nu = 2\,\nu_{offset} + 2\,\nu_{chemical\ shift}\,;\ \nu_{offset} = \nu - \nu_0 \qquad (8)$$

where ν_{offset} is the spectrometer offset frequency and $\nu_{chemical\ shift}$ is the desired chemical shift.

The inclusion of the dipole-dipole term has been handled previously,[3] so it will not be discussed further, except to notice that the effect of isotopic dilution will be a corresponding narrowing of the satellites which will allow the high resolution determination of the peak positions.

B. Fictitious Spin Operators

We wish to develop a theory for our system which is not based on a perturbation approach. This is easy for two level systems. Since their operators have a formal correspondence to angular momentum operators, spin operators can be used as generators for rotations. This, then, is the formal basis for viewing spin ½ systems as precessing and nutating magnetizations. This correspondence breaks down for bilinear operators, operating on a three-level system, such as the quadrupole interaction, so closed form operator expressions are more difficult to obtain.

This difficulty can be somewhat alleviated by using fictitious spin ½ operators.[8] Their usefulness has been demonstrated in work on pure NQR systems.[9] If any two levels are coupled by a nearly resonant interaction, we can in some sense ignore any other levels. The resulting system then corresponds to a normal spin ½ system, that is,it has two eigenfunctions and energy levels, and its operators can be expressed as 2 x 2 matrices.[8] We choose these matrices to be the Pauli spin matrices, whose correspondence to angular momentum operators allows the transformation properties to be considered as rotations.

The operators are defined by the commutation relationships given in Table 1. Choosing a basis set which will be convenient for our present calculations determines the matrix form of the operators as follows:

$$|X\rangle = \frac{-1}{\sqrt{2}}\,(|+1\rangle - |-1\rangle)$$

$$|Y\rangle = \frac{i}{\sqrt{2}}\,(|+1\rangle + |-1\rangle)$$

$$|Z\rangle = |0\rangle \tag{9}$$

where $|+1\rangle$, $|-1\rangle$ and $|0\rangle$ are the eigenfunctions of S_Z for $S = 1$.

$$S_{Z,1} = \frac{1}{2}\,S_Z = \frac{1}{2}\begin{pmatrix} 0 & i & 0 \\ -i & 0 & 0 \\ 0 & 0 & 0 \end{pmatrix} \qquad S_{Z,2} = \frac{1}{2}\begin{pmatrix} 0 & 1 & 0 \\ 1 & 0 & 0 \\ 0 & 0 & 0 \end{pmatrix} \qquad S_{Z,3} = \frac{1}{2}\begin{pmatrix} 1 & 0 & 0 \\ 0 & -1 & 0 \\ 0 & 0 & 0 \end{pmatrix}$$

$$S_{Y,1} = \frac{1}{2}\,S_Y = \frac{1}{2}\begin{pmatrix} 0 & 0 & 1 \\ 0 & 0 & 0 \\ 1 & 0 & 0 \end{pmatrix} \qquad S_{Y,2} = \frac{1}{2}\begin{pmatrix} 0 & 0 & i \\ 0 & 0 & 0 \\ -i & 0 & 0 \end{pmatrix} \qquad S_{Y,3} = \frac{1}{2}\begin{pmatrix} -1 & 0 & 0 \\ 0 & 0 & 0 \\ 0 & 0 & 1 \end{pmatrix}$$

$$S_{X,1} = \frac{1}{2}\,S_X = \frac{1}{2}\begin{pmatrix} 0 & 0 & 0 \\ 0 & 0 & 1 \\ 0 & 1 & 0 \end{pmatrix} \qquad S_{X,2} = \frac{1}{2}\begin{pmatrix} 0 & 0 & 0 \\ 0 & 0 & -i \\ 0 & i & 0 \end{pmatrix} \qquad S_{X,3} = \frac{1}{2}\begin{pmatrix} 0 & 0 & 0 \\ 0 & 1 & 0 \\ 0 & 0 & -1 \end{pmatrix}$$

Here instead of the three linearly independent operators S_X, S_Y, and S_Z the set has been replaced by a set of nine operators, in such a way that each corresponds to a spin ½ operator for one of the transitions in the three level system. Only 8 of these are linearly independent and this dependence is expressed by

$$S_{X,3} + S_{Y,3} + S_{Z,3} = 0 \tag{10}$$

Table 1. Commutation Relations

	B								
	$S_{X,1}$	$S_{X,2}$	$S_{X,3}$	$S_{Y,1}$	$S_{Y,2}$	$S_{Y,3}$	$S_{Z,1}$	$S_{Z,2}$	$S_{Z,3}$
$S_{X,1}$	0	$S_{X,3}$	$-S_{X,2}$	$\frac{1}{2}S_{Z,1}$	$-\frac{1}{2}S_{Z,2}$	$\frac{1}{2}S_{X,2}$	$-\frac{1}{2}S_{Y,1}$	$\frac{1}{2}S_{Y,2}$	$\frac{1}{2}S_{X,2}$
$S_{X,2}$	$-S_{X,3}$	0	$S_{X,1}$	$-\frac{1}{2}S_{Z,2}$	$-\frac{1}{2}S_{Z,1}$	$-\frac{1}{2}S_{X,1}$	$\frac{1}{2}S_{Y,2}$	$\frac{1}{2}S_{Y,1}$	$-\frac{1}{2}S_{X,1}$
$S_{X,3}$	$S_{X,2}$	$-S_{X,1}$	0	$-\frac{1}{2}S_{Y,2}$	$\frac{1}{2}S_{Y,1}$	0	$-\frac{1}{2}S_{Z,2}$	$\frac{1}{2}S_{Z,1}$	0
$S_{Y,1}$	$-\frac{1}{2}S_{Z,1}$	$\frac{1}{2}S_{Z,2}$	$\frac{1}{2}S_{Y,2}$	0	$S_{Y,3}$	$-S_{Y,2}$	$+\frac{1}{2}S_{X,1}$	$-\frac{1}{2}S_{X,2}$	$\frac{1}{2}S_{Y,2}$
$S_{Y,2}$	$\frac{1}{2}S_{Z,2}$	$\frac{1}{2}S_{Z,1}$	$-\frac{1}{2}S_{Y,1}$	$-S_{Y,3}$	0	$S_{Y,1}$	$-\frac{1}{2}S_{X,2}$	$-\frac{1}{2}S_{X,1}$	$-\frac{1}{2}S_{Y,1}$
$S_{Y,3}$	$-\frac{1}{2}S_{X,2}$	$\frac{1}{2}S_{X,1}$	0	$S_{Y,2}$	$-S_{Y,1}$	0	$-\frac{1}{2}S_{Z,2}$	$\frac{1}{2}S_{Z,1}$	0
$S_{Z,1}$	$\frac{1}{2}S_{Y,1}$	$-\frac{1}{2}S_{Y,2}$	$\frac{1}{2}S_{Z,2}$	$-\frac{1}{2}S_{X,1}$	$\frac{1}{2}S_{X,2}$	$\frac{1}{2}S_{Z,2}$	0	$S_{Z,3}$	$-S_{Z,2}$
$S_{Z,2}$	$-\frac{1}{2}S_{Y,2}$	$-\frac{1}{2}S_{Y,1}$	$-\frac{1}{2}S_{Z,1}$	$\frac{1}{2}S_{X,2}$	$\frac{1}{2}S_{X,1}$	$-\frac{1}{2}S_{Z,1}$	$-S_{Z,3}$	0	$S_{Z,1}$
$S_{Z,3}$	$-\frac{1}{2}S_{X,2}$	$\frac{1}{2}S_{X,1}$	0	$-\frac{1}{2}S_{Y,2}$	$\frac{1}{2}S_{Y,1}$	0	$S_{Z,2}$	$-S_{Z,1}$	0

$[A,B] = iC$

The significance of these operators to other problems and their relationship to standard spherical tensor operators is given in Appendix 2.1.

The similarity of these operators to the normal spin ½ operators is seen through the commutation relations;

$$[S_{p,i}, S_{p,j}] = i\, S_{p,k} \tag{11}$$

with

$p = X$, Y, or Z and $i,j,k = 1,2,3$ or cyclic permutations

$$[S_{p,3},\ S_{q,3}] = 0 \qquad p,q = X,Y,Z$$

$$[S_{p,3}-S_{q,3},\ S_{r,i}] = 0 \qquad p \neq q \neq r \ \text{ and } i = 1,2,3 \tag{12}$$

These show that $S_{p,1}$, $S_{p,2}$ and $S_{p,3}$ behave like Pauli matrices σ_X, σ_Y, σ_Z for the transition p. The Quadrupole Hamiltonian is given as:

$$H_S = -\omega_0\, S_Z + \omega_Q\, (S_Z^2 - \frac{1}{3}\, S(S+1)) - 2\omega_1\, S_X \cos\omega t \tag{13}$$

Transformation to a frame rotating at the frequency of the applied rf field gives

$$H_S^* = -\Delta\omega S_Z - \omega_1 S_X + \omega_Q (S_Z^2 - \frac{1}{3}\, S(S+1)) \tag{14}$$

with $\Delta\omega = \omega_0 - \omega$.

The functions $|X\rangle$, $|Y\rangle$ and $|Z\rangle$ were chosen to form the basis set because they are the eigenfunctions of the rotating frame Quadrupole Hamiltonian without the rf interaction:

$$H_S^* = -\Delta\omega\ S_Z + \omega_Q(S_Z^2 - \frac{1}{3}\ (S(S+1)) \tag{14a}$$

The level scheme for this Hamiltonian is shown in Figure 4.

We rewrite (14) in terms of our fictious spin half angular momentum operators:

$$H_S^* = -2\Delta\omega\ S_{Z,1} - 2\omega_1\ S_{X,1} + \omega_r\ S_{r,3} - E_r(S_{p,3}-S_{q,3}) \tag{15}$$

with p,q,r = X,Y,Z or cyclic permutations and where

$$\omega_X = -\omega_Y = \omega_Q \quad ; \quad \omega_Z = 0$$

$$E_X = E_Y = \frac{1}{3}\ \omega_Q \ ; \quad E_Z = -\ \frac{2}{3}\ \omega_Q$$

The level scheme for this Hamiltonian is the same as for equation (14), and Figure 4, where levels $|X\rangle$ and $|Y\rangle$ are degenerate in the absence of the rf irradiation. (Here we note the correspondence to both pure NQR and Raman Spectroscopy). The operators $S_{X,i}$ for example, correspond to transitions between levels $|Y\rangle$ and $|Z\rangle$ where the elements 1,2,3 are the Pauli spin operators between the two levels. The picture then corresponds to three separate coordinate systems X, Y and Z each corresponding to a different transition and each having axis 1, 2 and 3.

As a consequence of the basis set we have chosen the operators $S_{X,i}$ and $S_{Y,i}$ which do not correspond to the normal transition $|0\rangle \leftrightarrow |+1\rangle$ and $|0\rangle \leftrightarrow |-1\rangle$. Instead, to find the operators which couple these transitions we must take linear combinations of the operators. The $|+1\rangle$ and $|-1\rangle$ levels are given by

Figure 4. Quadrupole energy level scheme in the rotating frame. The allowed transitions are indicated. Note the analogy with Raman spectroscopy.

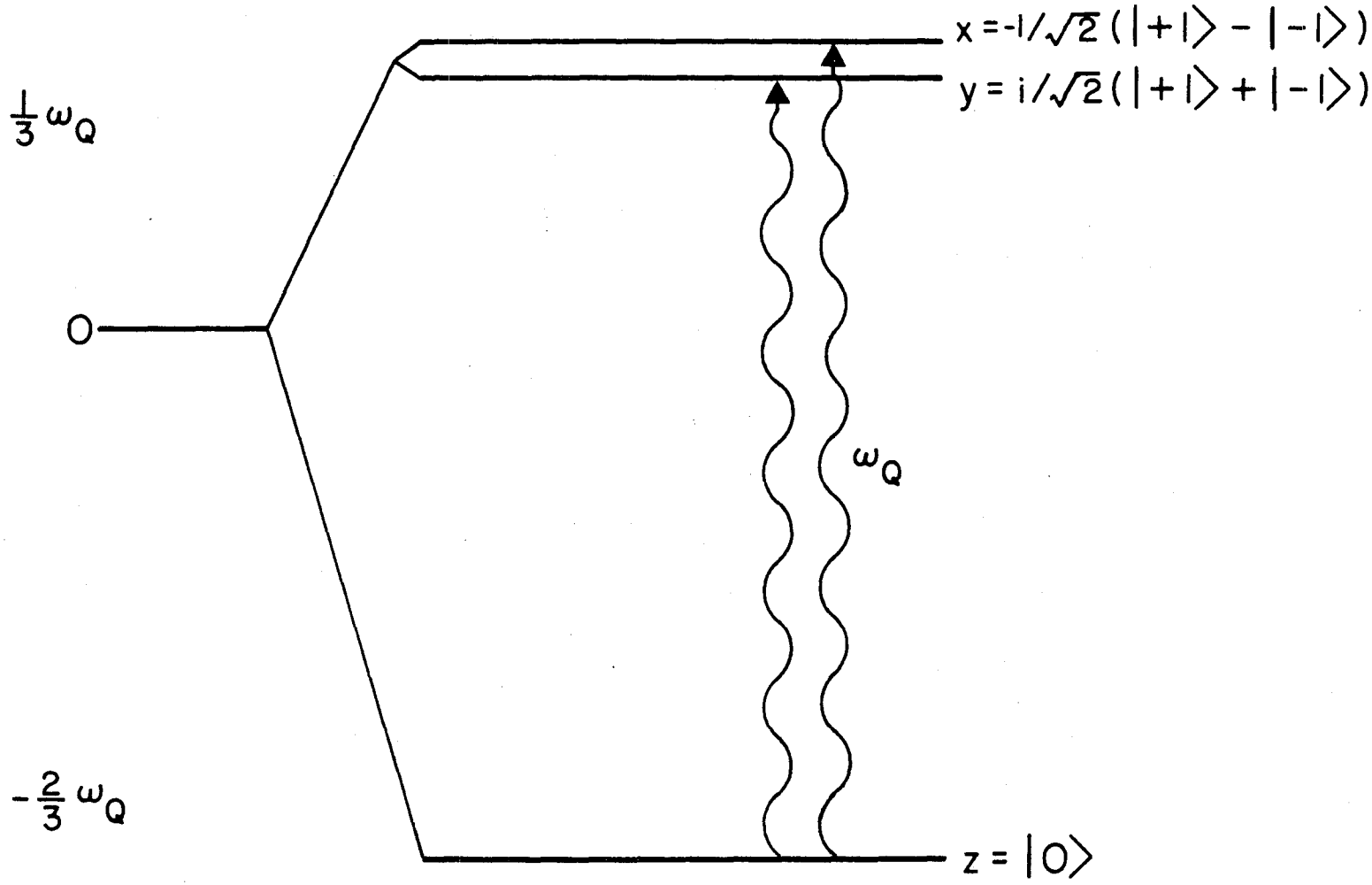
$x = -1/\sqrt{2}\,(|+1\rangle - |-1\rangle)$
$y = i/\sqrt{2}\,(|+1\rangle + |-1\rangle)$
$\frac{1}{3}\omega_Q$
0
ω_Q
$-\frac{2}{3}\omega_Q$
$z = |0\rangle$

XBL 765-1981

$$|+1\rangle = \frac{-1}{\sqrt{2}} (|X\rangle + i|Y\rangle)$$
$$|-1\rangle = \frac{1}{\sqrt{2}} (|X\rangle - i|Y\rangle) \quad .$$

Simple algebra then gives the $S_{Y(+)}$ operator for the $|+1\rangle \leftrightarrow |0\rangle$ transition as $-(S_{Y,1} - S_{X,2})$ and $S_{X(+)}$ operator for the $|+1\rangle \leftrightarrow |0\rangle$ transition as $-(S_{X,1} - S_{Y,2})$. This can easily be verified by allowing each to operate on the spin function $|0\rangle$ ($= \begin{pmatrix}0\\0\\1\end{pmatrix}$). These operators will occur in the cross polarization section. For the other satellite we find the $S_{X(-)}$ operator to be $S_{Y,2} + S_{X,1}$ and for the $S_{Y(-)}$ operator $S_{X,2} + S_{Y,1}$. Note that these operators are the fictitious spin ½ operators for the satellites and not S_X and S_Y, the full spin operators.

We now discuss the transformation properties of these operators under rotations. For example an ε degree rotation about the 2 axis in the X coordinate system ($R_X(\varepsilon,2)$) will result in

$$S'_{X,1} = e^{-i\varepsilon S_{X,2}} \; S_{X,1} \; e^{+i\varepsilon S_{X,2}} = \cos\varepsilon \; S_{X,1} - \sin\varepsilon \; S_{X,3}$$

$$S'_{X,2} = S_{X,2}$$

$$S'_{X,3} = \sin\varepsilon \; S_{X,1} + \cos\varepsilon \; S_{X,3}$$

$$S'_{Y,1} = \cos\frac{\varepsilon}{2} S_{Y,1} - \sin\frac{\varepsilon}{2} S_{Z,2}$$

$$S'_{Z,1} = \sin\frac{\varepsilon}{2} S_{Y,2} + \cos\frac{\varepsilon}{2} S_{Z,1}$$

$$S'_{Y,3} - S'_{Z,3} = S_{Y,3} - S_{Z,3} \qquad (16)$$

As is seen the rotation properties are straight-forward, except for a rotation of one of the $S_{p,3}$ operators whose linear dependence on the other 3 operators makes matters somewhat complex. A summary of all possible rotations is given in Appendix 2.2. In a similar way it is shown that

$$e^{-i\alpha S_{X,1}t} S_{X,3} e^{+i\alpha S_{X,1}t} = S_{X,3} \cos\alpha t - S_{X,2} \sin\alpha t$$

$$e^{-i\alpha S_{X,1}t} S_{Y,1} e^{+i\alpha S_{X,1}t} = S_{Y,1} \cos \frac{\alpha}{2}t + S_{Z,1} \sin \frac{\alpha}{2}t \qquad (17)$$

where the first equation shows a rotation in the X-coordinate system and the second equation corresponds to a regular Cartesian-coordinate system rotation induced by the normal angular momentum operators S_X, S_Y, S_Z.

The success of our approach in using these operators is dependent upon our ability to write the Hamiltonian in two parts, the first must have the form of a spin ½ Hamiltonian and the second, which contains the rest of the system, must commute with the first. As we shall see, this second part may then be "ignored" in so far as the dynamics of the system are concerned.

1. Single Quantum Transition Hamiltonian

There are two important limiting cases for the experiments that follow, and the Hamiltonians for these are derived below. If we irradiate near the frequency ($\delta\omega$ away) of one of the satellites we will excite single quantum transitions and the Hamiltonian, equation (15), can be rewritten in a form particularly convenient for that case which fulfills the above conditions of commutativity of the two parts. The second case to be considered is when the frequency of the irradiation is near the center of the spectrum. Double quantum transitions can then be induced with a high probability, and we rewrite the Hamiltonian to emphasize this transition.

The Hamiltonian for the first case, where

$$\Delta\omega = \omega_Q + \delta\omega$$

becomes

$$H_S^* = -2(\delta\omega + \omega_Q)\ S_{Z,1} + \frac{2}{3}\ \omega_Q(S_{X,3} - S_{Y,3}) - 2\omega_1\ S_{X,1}$$

We now rotate the Z-coordinate system 90° around the 2-axis ($R_Z(90,2)$) and we get,

$$H_S^* = 2(\delta\omega + \omega_Q)S'_{Z,3} + \frac{2}{3}\ \omega_Q(S'_{X,3} - S'_{Y,3}) - \sqrt{2}\omega_1\ (S'_{X,1} - S'_{Y,2}) \quad (18)$$

Using equations (15) and (10) <u>and assuming $\omega_1 << \omega_Q$</u> we can ignore $\sqrt{2}\omega_1\ S'_{Y,2}$ with respect to $\frac{4}{3}\ \omega_1\ S'_{Y,3}$ so that the Hamiltonian becomes

$$H_S^{*\prime} = -\delta\omega\ S'_{X,3} - \sqrt{2}\ \omega_1\ S'_{X,1} - \frac{4}{3}\ \omega_Q\ (S'_{Y,3} - S'_{Z,3}) \quad (19)$$

In a similar way we get for irradiation near the other satellite where

$$\Delta\omega = -\omega_Q + \delta\omega$$

$$H_S^{*\prime} = -S\omega\ S'_{Y,3} + \sqrt{2}\ \omega_1\ S'_{Y,2} + \frac{4}{3}\ \omega_Q(S'_{Z,3} - S'_{X,3}) \quad (20)$$

There is a more pictorial way of deriving (19) and (20). By inspecting equation (18) we see that the energy associated with the transition between levels X and Y, which corresponds to the $S'_{Z,3}$ operator, must be $2(\delta\omega+\omega_Q)$. Also since the Zeeman term is given as proportional to $S'_{Z,3}$ the Z level must not be shifted, that is the $S'_{Z,3}$ operator has a vanishing matrix element $\langle Z|S'_{Z,3}|Z\rangle$. The energy of the Z level must then be $-\frac{2}{3}\ \omega_Q$. Using the fact that

$$E_X + E_Y + E_Z = 0 \tag{21}$$

where E denotes the energy of a level, we can generate the level diagram as shown in Figure 5b. We wish to write the Zeeman term so that it corresponds to the $Y \rightarrow Z$ $(+\omega_Q)$ transition, so it must be given as

$$(E_Y - E_Z)S_{X,3} \tag{22}$$

the energy of the rest of the system must then be proportional to $(S_{Y,3} - S_{Z,3})$ and we can calculate the proportionality constant by noting that if the system is in the state $|X\rangle$ its energy must be

$$E_X = \frac{4}{3}\,\omega_Q + \delta\omega \tag{23}$$

Including the r.f. irradiation term gives finally

$$H_S^{*\prime} = -\delta\omega\; S'_{Z,3} - \sqrt{2}\omega_1\; S'_{X,1} - (\frac{4}{3}\,\omega_Q + \delta\omega)(S'_{Y,3} - S'_{Z,3}) \tag{24}$$

Invoking the assumption that $\delta\omega \ll \omega_Q$ gives equation (19).

The equations (19) and (20) now have the form that we required; the first two terms correspond to a fictitious spin half Hamiltonian and the last commutes with them. The effective gyromagnetic ratio along the irradiation field for this fictitious spin is

$$\sqrt{2}\;\gamma_S = \gamma_{eS}$$

In this way we are motivated to consider one satellite as a spin half system with its effective gyromagnetic ratio γ_{eS}. This is of course only so if the r.f. field strength is much smaller than the distance between

the satellites of the S-spin system, i.e., $\omega_1 << \omega_Q$.

2. Double Quantum Transition Hamiltonian

We now consider the case in which the rf irradiation frequency is near the center of the S-spin spectrum, i.e.,:

$$\Delta\omega = \delta\omega << \omega_Q$$

After applying a $R_X(\theta_X, 2)$ rotation and using equation(16), we find:

$$H_S^{*'} = \sqrt{\omega_Q^2 + (2\omega_1)^2} \quad S'_{X,3} - \frac{1}{3}\omega_Q(S'_{Y,3} - S'_{Z,3})$$
$$- 2\delta\omega(S'_{Z,1}\cos\frac{\varepsilon}{2} + S'_{Y,2}\sin\frac{\varepsilon}{2})$$

where

$$\tan\theta_X = \frac{2\omega_1}{\omega_Q} \qquad \text{and } \omega_{eS} = \sqrt{\omega_Q^2 + (2\omega_1)^2} \tag{25}$$

This rotation is analogous to the rotations used to find the effective field for a normal spin ½ system irradiated near resonance. Assuming again that $\omega_1 << \omega_Q$ and $\delta\omega << \omega_Q$, ignoring the coefficient of $S_{Y,2}$ with respect to the coefficient of $S'_{Y,3}$ and considering only first order terms in ω_1 we get

$$H_S^{*'} = -\frac{1}{2}\left(\omega_Q^2 + (2\omega_1)^2 - \omega_Q\right) S'_{Z,3} + \frac{2}{3}\omega_Q(S'_{X,3} - S'_{Y,3}) - 2\delta\omega\, S_{Z,1} \tag{26a}$$

$$= -\frac{\omega_1^2}{\omega_Q} S'_{Z,3} - 2\delta\omega\, S'_{Z,1} + \frac{2}{3}\omega_Q(S'_{X,3} - S'_{Y,3}) \tag{26b}$$

Here again the easiest way to visualize the rewriting is to construct the level diagram. The energy of the transition $Y \rightarrow Z$ must be the coefficient of $S'_{X,3}$ since $S'_{X,3}$ couples the Y and Z levels.

$$E_Y - E_Z = \sqrt{\omega_Q^2 + (2\omega_1)^2} \tag{27}$$

and the X level must remain unchanged since $S'_{X,3}$ has no matrix element for the X level:

$$E_X = \frac{1}{3}\,\omega_Q \tag{28}$$

Using equation (21) allows us to complete the level diagram; Figure 5c. We wish to focus attention on the double quantum transition $X \rightarrow Y$ so the Zeeman term will be proportional to $S_{Z,3}$, this we call the "double quantum" frame. We may then complete the Hamiltonian as before yielding

$$H_S^{*\prime} = -\frac{1}{2}\left(\sqrt{\omega_Q^2 + (2\omega_1)^2} - \omega_Q\right)S_{Z,3} - \frac{1}{2}\left(\sqrt{\omega_Q^2 + (2\omega_1)^2} + \frac{1}{3}\,\omega_Q\right)$$
$$(S'_{X,3} - S'_{Y,3}) - 2\delta\omega\, S_{Z,1} \tag{29}$$

Invoking the condition $\omega_1 << \omega_Q$ gives the final result, equation (26a).

Again we obtain a Hamiltonian in which the first two terms in (26b) are a spin ½ Hamiltonian, which corresponds to the double quantum transition measured in a continuous wave (CW) experiment. The effective gyromagnetic ratio for this case is

$$\frac{\omega_1}{\omega_Q}\,\gamma_S = \gamma_{eS} \quad , \tag{30}$$

Figure 5. Quadrupole energy level scheme in the rotating frame with and without rf irradiation. A single quantum "reference frame" is indicated in (b), and the double quantum in (c). See equations 21-24 for the single quantum frame and equations 27-29 for the double quantum frame.

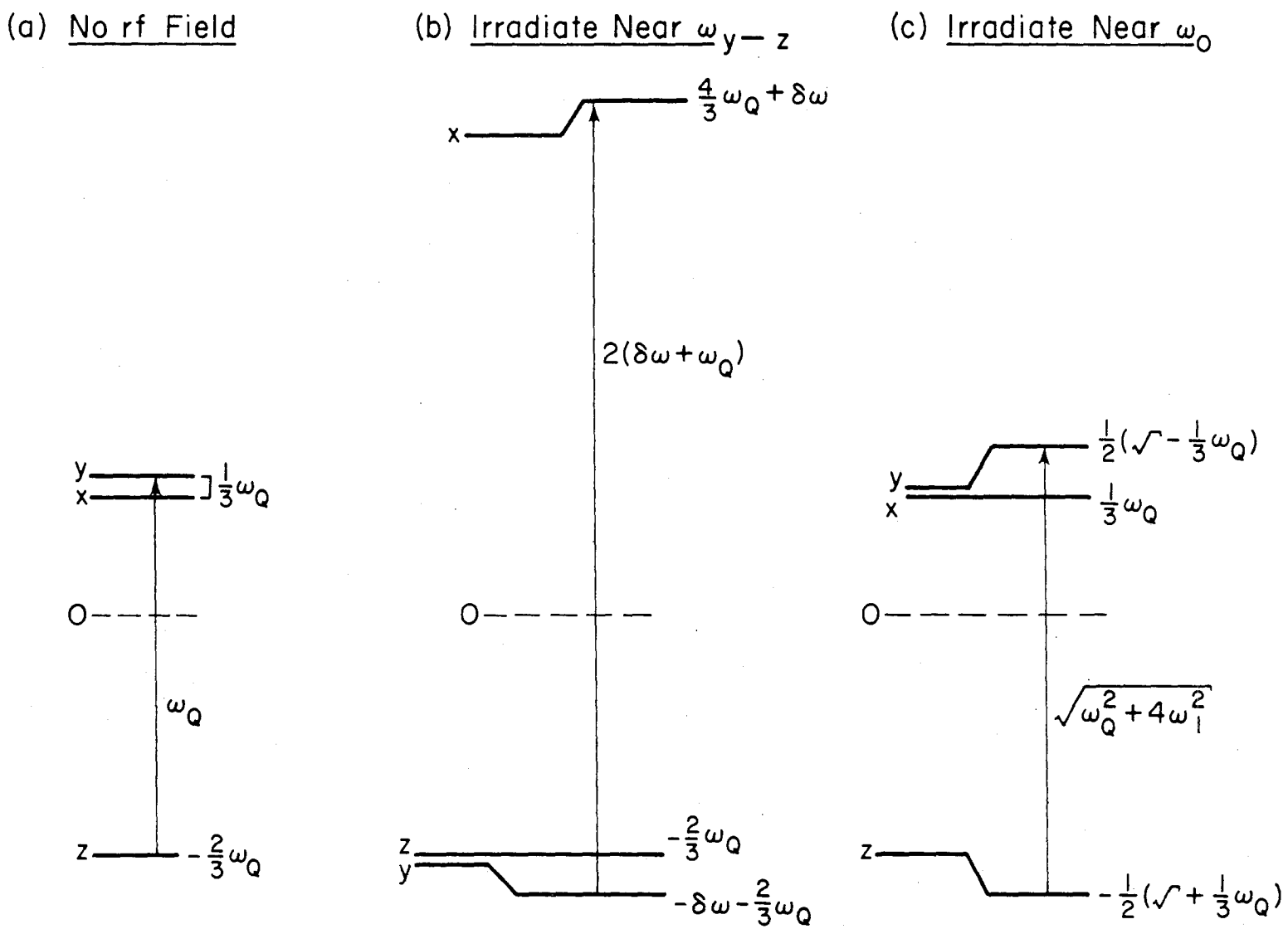
(a) No rf Field
y
x
$\frac{1}{3}\omega_Q$
0
ω_Q
z
$-\frac{2}{3}\omega_Q$
(b) Irradiate Near ω_{y-z}
x
$\frac{4}{3}\omega_Q + \delta\omega$
$2(\delta\omega + \omega_Q)$
0
z
y
$-\frac{2}{3}\omega_Q$
$-\delta\omega - \frac{2}{3}\omega_Q$
(c) Irradiate Near ω_0
$\frac{1}{2}(\sqrt{\ } - \frac{1}{3}\omega_Q)$
y
x
$\frac{1}{3}\omega_Q$
0
$\sqrt{\omega_Q^2 + 4\omega_1^2}$
z
$-\frac{1}{2}(\sqrt{\ } + \frac{1}{3}\omega_Q)$

XBL 765-1977

if $\delta\omega = 0$. Thus the effective magnetogyric ratio here is $2\gamma_S$ for the resonance offset and $\frac{\omega_1}{\omega_Q}\gamma_S$ for the effective irradiation field.

C. Observables

It is necessary at this point to ascertain which spin ½ operators correspond to physical observables. The best way of doing this is to find those operators whose expectation values correspond to signals measured in a pulsed NMR experiment. Here we detect the expectation values of S_X or S_Y which have been transformed into a frame rotating at the irradiation frequency. This frame corresponds experimentally to the phase detector whose axis we label $\underline{\bar{X}}$, $\underline{\bar{Y}}$ and $\underline{\bar{Z}}$. Signals whose initial amplitudes lie along the $\underline{\bar{X}}$ axis are termed in phase and those whose initial amplitude lie along the $\underline{\bar{Y}}$ axis are out of phase. The signal from the phase detector is then Fourier transformed giving a complex spectrum, ψ. In phase signals give rise to absorption shaped signals in Reψ and dispersion in Imψ. Out of phase signals give rise to absorption signals in Imψ and dispersion in Reψ. We choose this description because unlike the spin ½ case, we shall see that the expectation values of S_X and S_Y can behave quite independently.

Let us define the reduced density matrix of the S-spin system $\sigma_S^*(0)$ at the beginning of the free induction decay (FID) in the rotating frame using the high temperature approximation. First the high temperature approximation gives the full density matrix as

$$\rho_S^*(0) = \frac{1 - \beta H_S^*}{\mathrm{tr}\,(1)}$$

the reduced density matrix is given as

$$\sigma_S^*(0) = \beta H_X^* \tag{31}$$

This we may expand in terms of the nine operators giving:

$$\sigma_S^*(0) = \sum_{p=X,Y,Z;i=1,2,3} a_{pi}\, S_{p,i} \tag{32}$$

From the solution of the Schrödinger equation

$$\frac{\partial}{\partial t}\, \rho_S^*(t) = i\, [\rho_S^*(t),\, H_S^*] \tag{33}$$

with the Hamiltonian excluding the r.f. irradiation:

$$H_S^* = -2\Delta\omega\, S_{Z,1} + \frac{2}{3}\, \omega_Q (S_{X,3} - S_{Y,3}) \tag{33b}$$

we obtain

$$\sigma_S^*(t) = \sum_{p,i} a_{p,i} \exp(-i\, H_S^*\, t)\, S_{p,i} \exp(+i\, H_S^*\, t) \tag{34}$$

<u>As a simple example, let us first apply this to a standard spin ½ problem</u> in order to make more explicit the above comments about the phase relationships. We use the simplest Hamiltonian

$$H_S = \Delta\omega\, S_Z \tag{35}$$

the general density matrix is for this case expanded in three operators:

$$\sigma^*(0) = \sum_{p=X,Y,Z} a_p S_p \tag{35b}$$

finding the time evolution with the Hamiltonian gives

$$\sigma^*(t) = a_X(S_X \cos\Delta\omega t + S_Y \sin\Delta\omega t) + a_Y(S_Y \cos\Delta\omega t - S_X \sin\Delta\omega t) + a_Z S_Z \tag{36}$$

We then observe,

$$\langle S_X \rangle = \mathrm{tr}(\sigma\, S_X) = \frac{a_X}{2}\cos\Delta\omega t - \frac{a_Y}{2}\sin\Delta\omega t$$

$$\langle S_Y \rangle = \mathrm{tr}(\sigma\, S_Y) = \frac{a_Y}{2}\cos\Delta\omega t + \frac{a_X}{2}\sin\Delta\omega t \quad . \tag{37}$$

where $\mathrm{tr}(S_X^2) = \frac{1}{2}$

To relate (37) to what is experimentally observed in our spectrometer we must be somewhat careful about the phase relationships. Remember that the X,Y,Z spin axes are determined by the rotating frame transformation with respect to the r.f. irradiation, both in frequency and phase. The phase detector in general will not be in phase with the irradiation, that is the $\underline{\bar{X}}$ phase detector axis and the X-spin axis are not necessarily aligned. We assume for now that they are aligned since by doing so we loose no real generality. We will discuss below the adjustments to be made if they are not. The actual signals observed under these assumptions are simply,

$$g_{\underline{\bar{X}}}(t) = \langle S_X(t) \rangle \quad \text{and} \quad g_{\underline{\bar{Y}}}(t) = \langle S_Y(t) \rangle \tag{37a}$$

in the two channels of the phase detector.

The complex Fourier transform is defined by:

$$\psi(\omega) = f_{\underline{\bar{X}}}(\omega) + i f_{\underline{\bar{Y}}}(\omega) = \int_0^\infty dt\, e^{i\omega t}\, (g_{\underline{\bar{X}}}(t) + i g_{\underline{\bar{Y}}}(t)) \tag{37b}$$

The complex Fourier transform of equation (37b) is then a delta function at frequency $\Delta\omega$ in $\mathrm{Re}\psi$ of intensity a_X and a delta function at frequency $\Delta\omega$ in $\mathrm{Im}\psi$ of intensity a_Y. This is shown graphically in Figure 6a. The horizontal axis of the diagram is the frequency axis, ω. The vertical axis is the $\mathrm{Re}\psi$ axis and that axis projecting into the

Figure 6. a) Schematic representation of a spin ½ Fourier transform experiment, for a line of frequency $\Delta\omega$. b) The change of coordinates accomplished by the Fourier transform phase correction. The x and y axis are the spin axis which are transformed into a new axis system x' and y' which is aligned with the phase detector.

a) Spin 1/2 Fourier Transform

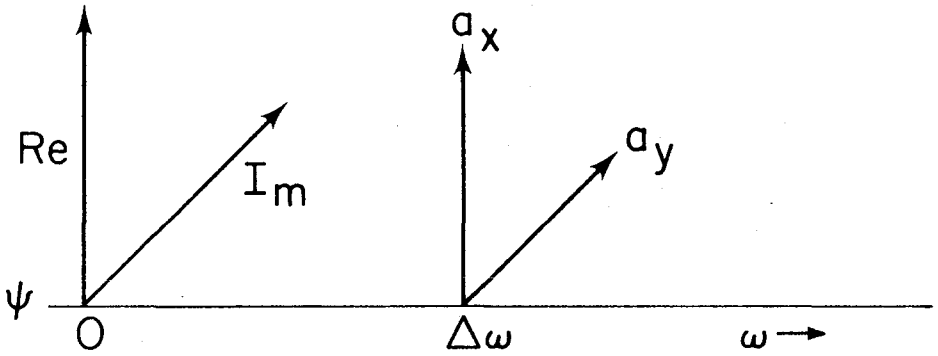

b) Phasing

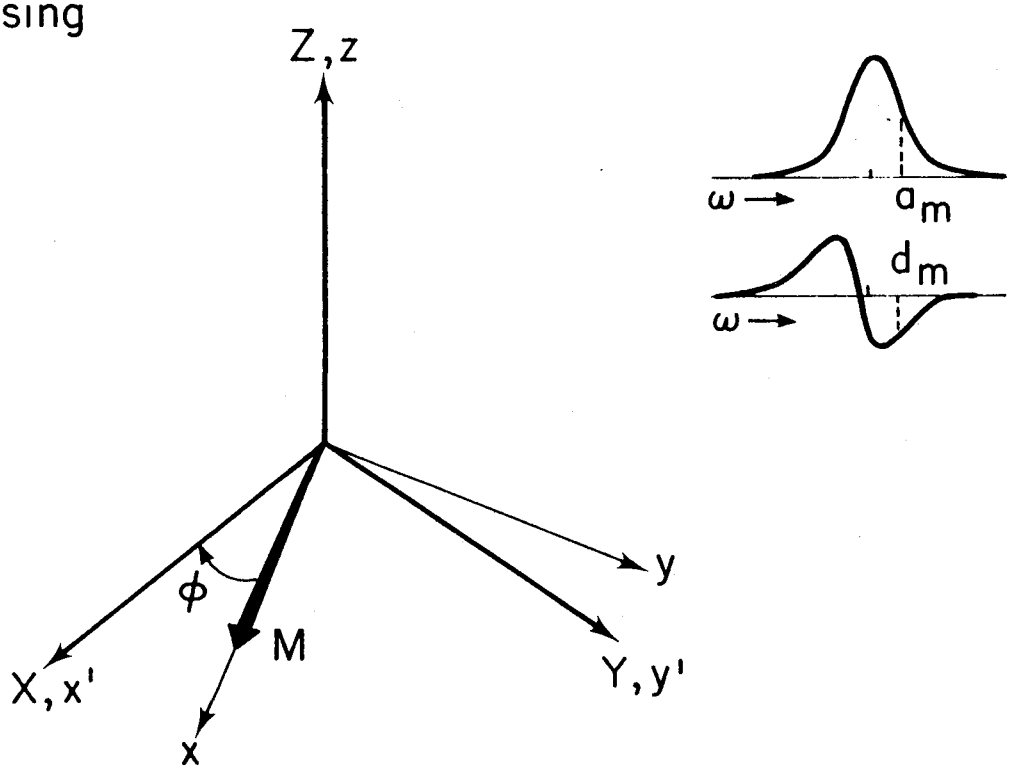

XBL 766 8062

page is the Imψ axis. The intensities, a_X, a_Y are shown plotted along their respective axis.

If we take into account relaxation processes, the absorption line shape will no longer be a delta function. We then introduce the free precession shape function or relaxation function a(t), (normalized to 1, see Abragam, ref. 8, for more details) whose cosine Fourier transform yields the absorptive line shape,

$$g(\omega) = \int_0^\infty a(t) \cos\omega t \, dt \quad . \tag{37c}$$

Equation (37) then becomes,

$$g_{\underline{\bar{X}}}(t) = \langle S_X \rangle = a_X \, a(t) \cos\Delta\omega t - a_Y \, a(t) \sin \Delta\omega t$$

$$g_{\underline{\bar{Y}}}(t) = \langle S_Y \rangle = a_Y \, a(t) \cos\Delta\omega t - a_X \, a(t) \sin\Delta\omega t \tag{37d}$$

and corresponding after Fourier transformation,

$$\psi(\omega) = f_{\underline{\bar{X}}}(\omega) + i \, f_{\underline{\bar{X}}}(\omega) = \int_0^\infty dt e^{i\omega t} \, (g_{\underline{\bar{X}}}(t) + i \, g_{\underline{\bar{Y}}}(t))$$

yields both absorption and dispersion in Reψ and Imψ. The term proportional to a_X yields an absorptive line in Reψ and a dispersive lineshape in Imψ and vice versa for a_Y. We obtain both absorption and dispersion automatically due to the complex Fourier transform. We will schematically represent this more realistic case in exactly the same way as before, Figure 6a.

The above assumed that the X spin axis in the rotating frame was aligned along the $\underline{\bar{X}}$ phase detector axis. This will always be assumed

for if it is not a trivial phase adjustment of the spectrometer (the spectrometer phase) or a phase transformation after the Fourier transformation, correct the misalignment. To illustrate the Fourier transform phase correction assume that the X spin axis and the $\bar{X}$ phase detector axis are misaligned by an angle ϕ, Figure 6b. The observed signal is then obtained from the time evolution of the density matrix after it has been transformed into a new frame X', Y'; in which the X' axis now lies along the $\bar{X}$ phase detector axis. The Fourier transform of this signal will give some mixture of absorption and dispersion in both Reψ and Imψ. If we wish to obtain the Fourier transform with respect to the old coordinate system (the original rotating frame) we must apply a phase transformation with phase $-\phi$. As an example we choose the density matrix of a single spin species after a 90° pulse has been applied (see Figure 6b).

$$\sigma(0) = \beta\omega_0 \, S_X \tag{38}$$

where β is the laboratory inverse temperature. Transforming to the new axes gives

$$\sigma(0) = \beta\omega_0 \cos\phi \, S_x' + \beta\omega_0 \sin\phi \, S_Y' \tag{39}$$

The Fourier transform will give

$$\psi(\omega) = a_\mu(\omega) \cos\phi - d_\mu(\omega) \sin\phi + i(a_\mu(\omega) \sin\phi + d_\mu(\omega) \cos\phi) \tag{39a}$$

where $a_\mu(\omega)$ and $d_\mu(\omega)$ are the intensities of the absorptive and dispersive lineshapes at the frequency of interest, ω, see Figure 6c. Had the X and $\bar{X}$ axis been aligned the Fourier transform would have given only

absorption in Reψ and the dispersion in Imψ. The effect of the misalignment is then to mix some dispersion into the absorption in Reψ and some absorption into the dispersion in Imψ. To obtain the purely absorptive lineshape in Reψ we must phase the Fourier transform by $(-\phi)$ giving

$$e^{-i\phi}\,\psi_{(\omega)} = (\cos\phi + i\,\sin\phi)\,\psi = a_{\mu}(\omega) + i\,d_{\mu}(\omega) \tag{40}$$

this must be computed for each value of ω.

In order to find the observables for the fictitious spin operators we carry out, now, the analogous analysis as we have sketched for the spin ½ case. The appropriate Hamiltonian for a system of quadrupolar spins is given in equation (33b). We rotate this with $R_Z(90,2)$ to give

$$H_S^{*\prime} = 2\Delta\omega\; S'_{Z,3} + \frac{2}{3}\,\omega_Q(S'_{X,3} - S'_{Y,3})$$

and

$$R_Z^{+}\,S_{X,1}\,R_Z = \frac{1}{2}\,(S'_{X,1} - S'_{Y,2})$$

$$R_Z^{+}\,S_{Y,1}\,R_Z = \frac{1}{2}\,(S'_{Y,1} + S'_{X,2}) \tag{41}$$

We take the initial density matrix as (see equation 32)

$$\sigma_S^{*}\,(0) = \sum_{\substack{p=X,Y,Z\\ i=1,2,3}} a_{p,i}S_{p,i} \tag{32}$$

From equations (34) and (16) we obtain

$$\sigma^{*\prime}(t) = \sum_p a'_{p3}\, S'_{p,3} + (a'_{X,1}\, S'_{X,1} + a'_{X,2}\, S'_{X,2}) \cos(\omega_Q - \Delta\omega)t$$
$$+ (a'_{X,1}\, S'_{X,2} - a'_{X,2}\, S'_{X,1}) \sin(\omega_Q - \Delta\omega)t$$
$$+ (a'_{Y,1}\, S'_{Y,1} + a'_{Y,2}\, S'_{Y,2}) \cos(-\Delta\omega - \omega_Q)t$$
$$+ (a'_{Y,1}\, S'_{Y,2} - a'_{Y,2}\, S'_{Y,1}) \sin(-\Delta\omega - \omega_Q)t \quad (42)$$

We must now rotate back with $R_Z(-90,2)$ giving $\sigma^*(t)$. Only the projections of $\sigma^*(t)$ on the X,1 and the Y,1 axis are observables which give the signal in the phase detector as,

$$2\langle S_{X,1}\rangle = \frac{1}{2}(a_{X,1} + a_{Y,2}) \cos(\omega_Q - \Delta\omega)t - \frac{1}{2}(a_{X,2} + a_{Y,1}) \sin(\omega_Q - \Delta\omega)t$$
$$- \frac{1}{2}(a_{Y,2} - a_{X,1}) \cos(\omega_Q - \Delta\omega)t - \frac{1}{2}(a_{Y,1} - a_{X,2}) \sin(-\omega_Q - \Delta\omega)t$$

$$2\langle S_{Y,1}\rangle = \frac{1}{2}(a_{Y,1} - a_{X,2}) \cos(-\omega_Q - \Delta\omega)t - \frac{1}{2}(a_{Y,2} - a_{X,1}) \sin(-\Delta\omega - \omega_Q)t$$
$$+ \frac{1}{2}(a_{X,2} + a_{Y,1}) \cos(\omega_Q - \Delta\omega)t - \frac{1}{2}(a_{Y,2} - a_{X,1}) \sin(-\Delta\omega - \omega_Q)t$$
$$(43)$$

It is clear that all initial $S_{p,i}$ with p = X, Y and i = 1, 2 can be detected. A summary of the results of Fourier transformation is given in Table II.

Table II. Fourier Transform for an arbitrary initial density matrix

Reψ			Imψ		
intensity of	frequency	shape	intensity of	frequency	shape
$a_{X,1}+a_{Y,2}$	$\omega_Q-\Delta\omega$	abs.(0°)	$a_{Y,1}+a_{X,2}$	$\omega_Q-\Delta\omega$	abs.(0°)
$a_{X,2}+a_{Y,1}$	$\omega_Q-\Delta\omega$	-disp.(-90°)	$a_{X,1}+a_{Y,2}$	$\omega_Q-\Delta\omega$	disp.(90°)
$a_{X,1}-a_{Y,2}$	$-\omega_Q-\Delta\omega$	abs.(0°)	$a_{Y,1}-a_{X,2}$	$-\omega_Q-\Delta\omega$	abs.(0°)
$a_{Y,1}-a_{Y.2}$	$-\omega_Q-\Delta\omega$	-disp.(-90°)	$a_{X,1}-a_{Y,2}$	$-\omega_Q-\Delta\omega$	disp.(90°)

A simple example may help to clarify the above relationships. Let us start with an initial density matrix aligned along the X,1 axis.

$$\sigma^*(0) = a_{X,1}\ S_{X,1} \tag{44}$$

The time evolution is described by equations (34) and yields at time t

$$\sigma(t) = \frac{a_{X,1}}{2}\ (S_{X,1}\ \cos(\omega_Q-\Delta\omega) + S_{X,2}\ \sin(\omega_Q-\Delta\omega) \tag{45a}$$

$$+\ S_{Y,2}\ \cos(\omega_Q-\Delta\omega) + S_{Y,1}\ \sin(\omega_Q-\Delta\omega) \tag{45b}$$

$$-\ S_{Y,2}\ \cos(-\omega_Q-\Delta\omega) + S_{Y,1}\ \sin(-\omega_Q-\Delta\omega) \tag{45c}$$

$$+\ S_{X,1}\ \cos(-\omega_Q-\Delta\omega) - S_{X,2}\ \sin(-\omega_Q-\Delta\omega) \tag{45d}$$

each of the terms above corresponds to a precessing magnetization as diagramed in Figure (7a).

Note the following,

1) the precession direction in the Y space is opposite to the X space.

2) if $\Delta\omega = 0$ all the magnetizations precess at the same rate.

3) for $\Delta\omega \neq 0$ d and c precess faster $(\omega_Q+\Delta\omega)$ than a and c $(\omega_Q-\Delta\omega)$.

We now find the expectation values of $S_{X,1}$ and $S_{Y,1}$ to find the signals actually detected. This is easily done by inspection of Figure (7a).

$$\bar{\underline{X}}:\ 2\langle S_{X,1}\rangle = a_{X,1}\ \cos(\omega_Q-\Delta\omega) + a_{X,1}\ \cos(-\omega_Q-\Delta\omega)$$

$$\bar{\underline{Y}}:\ 2\langle S_{Y,1}\rangle = a_{X,1}\ \sin(\omega_Q-\Delta\omega) + a_{X,1}\ \sin(-\omega_Q-\Delta\omega) \tag{46}$$

Note the following

1) if $\Delta\omega = 0$ there never appears a signal in the $\bar{\underline{Y}}$ channel, that

Figure 7. The time development of an initial density matrix $\sigma(0) = C\ S_{X,1}$. (a) Its schematic representation of the Fourier transform, and (b) the observed signals from the phase detector. In (a) the magnetizations a, b, c and d are from terms in equation (45) which show the free evolution governed by the Hamiltonian (equation 41). Terms a and b give the component of the Fourier transform at $\omega_Q - \Delta\omega$ and c and d give the component at $-\omega_Q - \delta\omega$. In (b) we add a and d in the x-spin space and b and c in the y space to derive the observed signal from the phase detector channel ($\underline{\bar{X}}$) and the 90° phase detector channel($\underline{\bar{Y}}$).

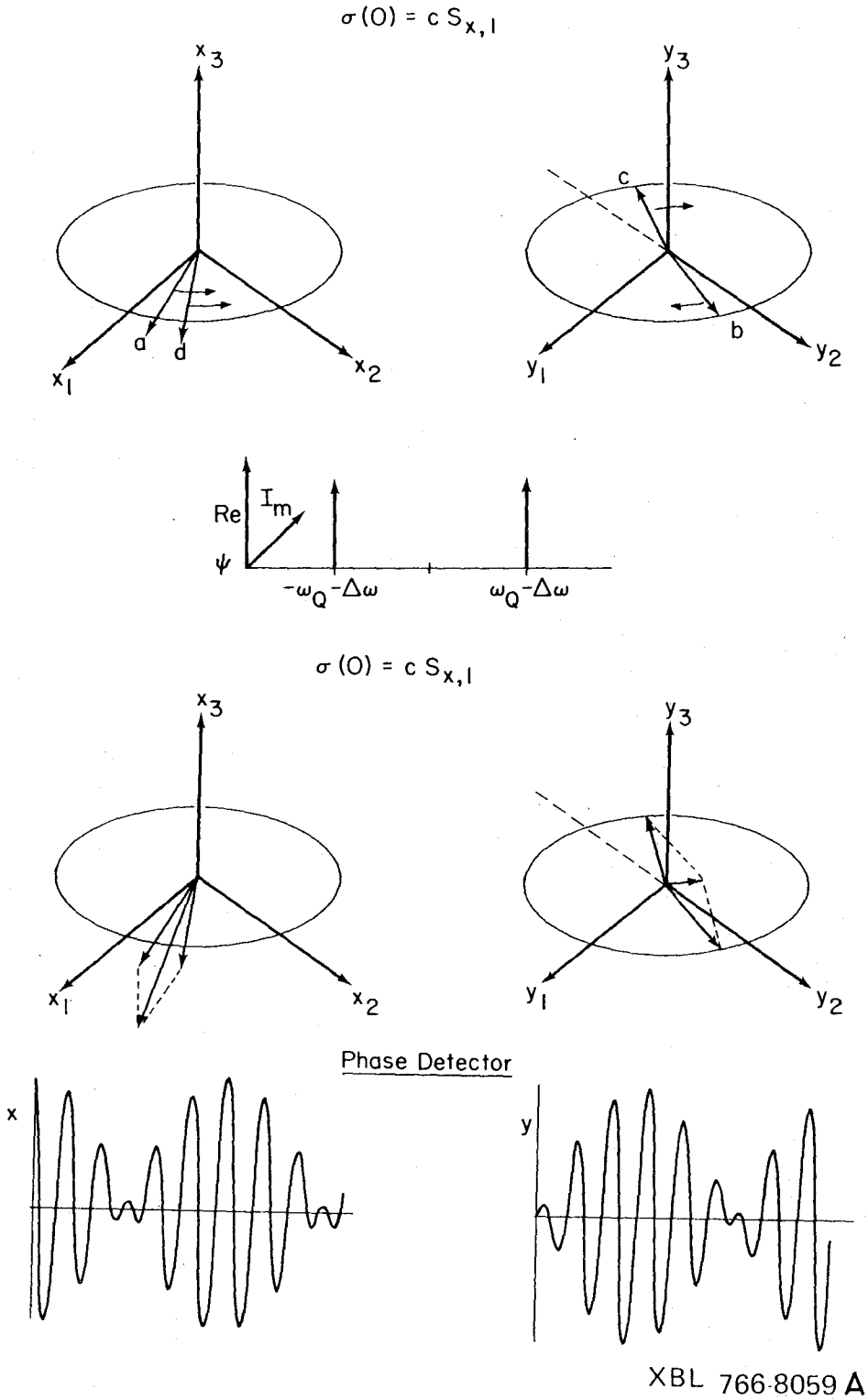

XBL 766-8059 A

is, the signal is linearly polarized along the X,1 direction.

2) if $\Delta\omega \neq 0$ the initial signal in the $\bar{Y}$ channel is still zero, but grows and decays at the frequency of the offset.

The Fourier transform of these signals is also given schematically in Figure (7a). The density matrix may also be viewed by finding the total magnetization in each space. This is diagramed in Figure (7b) for a finite offset frequency, $\Delta\omega$. Note the following,

1) At t = 0 the magnetization in the X spin space is $a_{X,1}$ and in the Y is zero.

2) the magnetization in each space precesses at ω_Q.

3) the magnetization in the X space shrinks as $\cos\Delta\omega$ and the magnetization in the Y grows as $\sin\Delta\omega$. The signals from the phase detector are now easily derived, see Figure (7b).

One thing remains, we must indicate what happens if we only detect one of $\langle S_X \rangle$ or $\langle S_y \rangle$, that is if we only have one phase detector. The Fourier transform will no longer distinguish between positive and negative frequency and we get "fold over". The results of this are easily generated from our diagrams by folding the diagram about the real axis at zero frequency, this operation produces the <u>correct phase relationships between peaks of different frequency</u>. For example fold over for a Fourier Transform as indicated in Figure (7a) for the initial density matrix $\sigma^*(0) = C\ S_{X,1}$ would generate a peak of twice the intensity at frequency $-\omega_Q-\Delta\omega$. However if the components were along the same direction in the imaginary plane fold over would produce cancellation of the two signals, since the transform as folded about the Re axis gives the original component along the Im axis but the folded over component along the -Im axis.

D. Previous Double Quantum Experiments

The history of double quantum processes in NMR is quite long. The first observations were on proton systems where there were spin-spin splittings, for example the work of Anderson[10] and Kaplan and Meiboom[11] in the late 50's. The complete theory for double quantum transitions in continuous wave (CW) NMR was worked out by Yatsiv in 1959.[12] Deuterium double quantum transitions were first detected by Yves Ayant et al. in 1961 in CW-NMR,[13] from D_2O in zeolites. Deuterium double quantum transitions were later detected in deuterated liquid crystals by Pirsson, Wennerström, and Lindman,[14a] Charvolin and Rigny,[14b] and Lawson and Flautt.[14c] The ease of deuterium decoupling in liquid crystals was also ascribed to deuterium double quantum transitions by Meiboom et al.[15]

Pulsed NMR observation of double quantum transitions was not carried out until this past year by Hatanaka and Hashi[16] and ourselves. Hatanaka et al. carried out their experiments on ^{27}Al using the technique of "transfer of coherence".[16a] The method that we have developed for deuterium is very closely related, although somewhat simpler to carry out experimentally.

1. Double quantum spectroscopy

We must now determine how to create coherence between the $m = \pm 1$ levels. Once this coherence has been created we must find the best way to detect its decay. This is done through the two pulse sequence shown in Figure (8). Starting with the equilibrium reduced density matrix:

$$\sigma_0 = \beta\omega_0 S_{Z,1} \tag{47}$$

we apply a pulse of strength ω_1 for a time τ at resonance, ω_0.

Figure 8. Double quantum pulse sequence with simultaneous proton decoupling. P_1 is the coherence pulse or double quantum pulse and P_2 is the probing pulse.

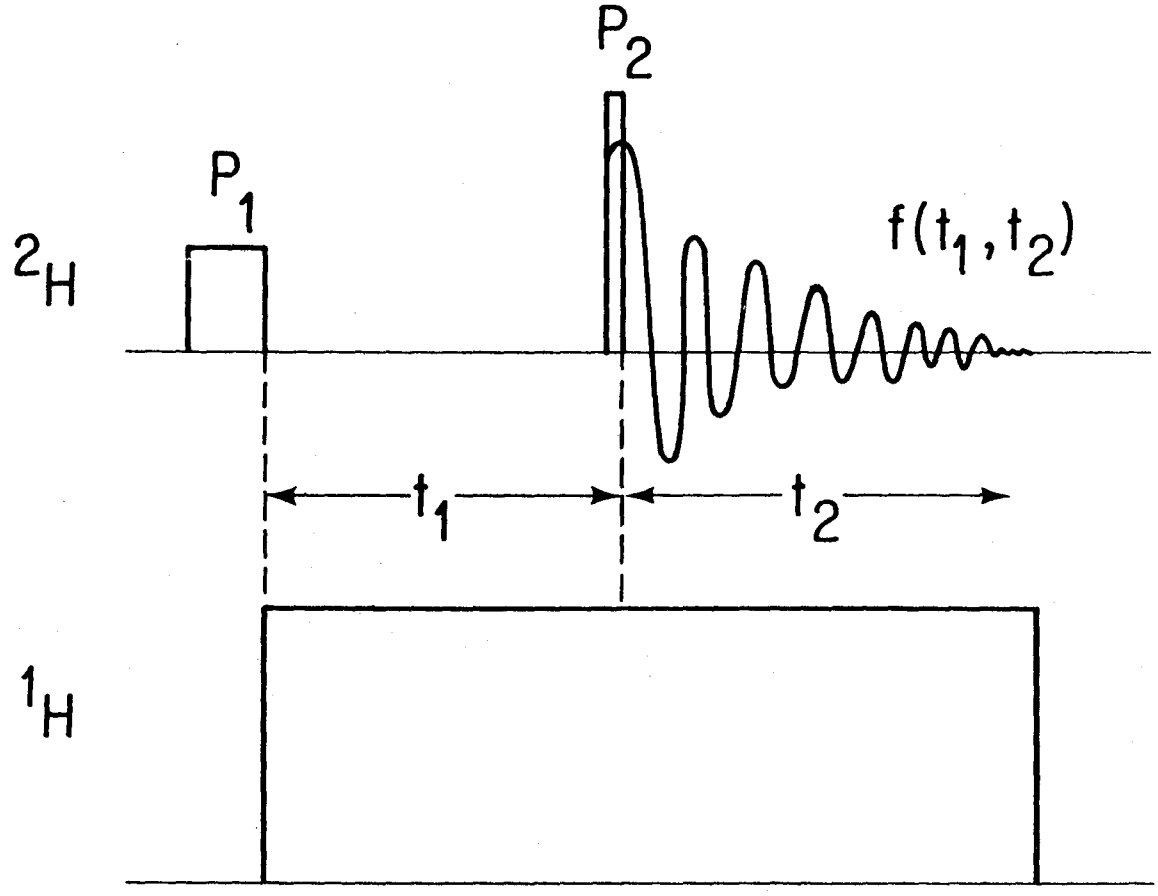

XBL 761-42

This corresponds to a time evolution generated by the Hamiltonian (equation (26a)): with $\Delta\omega = 0$

$$H_S^{*\prime} = -\omega_Z S'_{Z,3} + \frac{2}{3}\omega_Q (S'_{Y,3} - S'_{Y,3}) \tag{48}$$

with

$$\omega_Z = \frac{1}{2}\left(\sqrt{\omega_Q^2 + (2\omega_1)^2} - \omega_Q\right) \tag{49}$$

Giving for the new density matrix

$$\begin{aligned}\sigma(0) = \beta\omega_0 \{&\cos^2\frac{\varepsilon}{2}(S_{Z,1}\cos\omega_Z t - S_{Z,2}\sin\omega_Z\tau) \\ &+ \sin^2\frac{\varepsilon}{2}(S_{Z,1}\cos\omega_Y t + S_{Z,2}\sin\omega_Y t) + \sin\frac{\varepsilon}{2}[S_{Y,1}(\sin\omega_Z\tau \\ &+ \sin\omega_Y\tau) - S_{Y,2}(\cos\omega_Z t - \cos\omega_Y\tau)]\}\end{aligned} \tag{50}$$

where

$$\varepsilon = \tan^{-1}\frac{2\omega_1}{\omega_Q}$$

and

$$|\omega_Y| = |\omega_Q| + |\omega_Z|$$

The term in $S_{Z,2}$ corresponds to double quantum coherence, and we wish to isolate its effect from the other less interesting terms. We do so by placing the proper constraints on the pulse strength and width.

For the coefficients of $S_{Y,1}$ and $S_{Y,2}$ to be zero we must have

$$\omega_Z\tau + \omega_Y\tau = 2\pi k \quad k = 1,2,\ldots \tag{51}$$

and for the $S_{Z,1}$ coefficient to be zero, using equation (51)

$$\omega_Z \tau = \frac{\pi}{2} (2n + 1) \qquad n = 0,1,\ldots \tag{52}$$

Solving equation (5) and equation (51) gives

$$\tau = \frac{2m-1}{\omega_Q} \pi \qquad k,m = 1,2,\ldots \tag{53}$$

and with the definitions of ω_Z and ω_Y

$$\frac{\omega_1}{\omega_Q} = \frac{1}{2} \left(\left(\frac{2k}{2m-1} \right)^2 - 1 \right)^{1/2} \qquad \begin{array}{l} k,m = 1,2,\ldots \\ k \geq m \end{array} \tag{54}$$

Some selected values are given in Table 3.

Table 3. Allowed values of ω_1/ω_Q

k \ m	1	2	3	4	5
1	.84				
2	1.94	.44			
3		.84	.33		
4		1.24	.62	.28	
5			.87	.51	.24

By using an ω_1 which is allowed by equation (54) and a pulse length corresponding to equation (53) we can produce a density matrix after the pulse of

$$\sigma(0) = \beta\omega_0 \, S_{Z,2} \tag{55}$$

This indicates that the pulse has created a coherence superposition of the $|X\rangle$ and $|Y\rangle$ levels, without affecting the other transitions. There will be no signal after such a pulse.

The time dependence of this coherent superposition is governed by the Hamiltonian (equation 15):

$$H^* = -2\delta\omega\ S_{Z,1} + \frac{2}{3}\ \omega_Q\ (S_{X,3} - S_{Y,3}) \tag{56}$$

yielding,

$$\sigma(t_1) = a(t_1)\ (S_{Z,2}\ \cos 2\delta\omega t_1 - S_{Z,3}\ \sin 2\delta\omega t_1) \tag{57}$$

<u>So as expected the "precession frequency" for this double quantum transition is twice the offset frequency.</u> The details of the lineshape are contained in the constant which with the inclusion of spin relaxation will be time dependent.

This coherence cannot be observed directly since it remains entirely in the Z space, i.e.,

$$Tr(S_{X,j}\ S_{Z,k}) = Tr(S_{Y,j}\ S_{Z,k}) = 0 \quad j,k = 1,2,3$$

We must apply a second pulse to transfer this coherence to one of the observable transitions. This second pulse P_2 is also applied at resonance, ω_o, but now we investigate what happens if we use an applied field strength ω_1 as large as possible. Therefore we assume

$$\omega_1 >> \omega_Q \tag{58}$$

so that the effect of the pulse is a simple rotation about the X,1 axis

giving for a pulse length of time τ_p; a rotation of $R_X(-2\omega_1\tau_p)$ with:

$$\sigma(t_1,\tau_p) = C(S_{Z,2}\cos\omega_1\tau_p - S_{Y,2}\sin\omega_1\tau_p)\cdot\cos 2\delta\omega t + \frac{1}{2}C(S_{X,3}\cos 2\omega_1\tau_p + S_{X,2}\sin 2\omega_1\tau_p + (S_{Y,3} - S_{Z,3}))\sin 2\delta\omega t, \tag{59}$$

the observable coefficients are

$$a_{Y,2} = C\sin\omega_1\tau_p\cos 2\delta\omega t_1$$

$$a_{X,2} = C\frac{1}{2}\sin 2\omega_1\tau_p\sin 2\delta\omega t_1 \tag{60}$$

The signals obtained can then be determined from equation (42), giving a Fourier transform which corresponds to Figure (9a). We then repeat this for a range of t_1 values to determine the full time evolution of the double quantum state. This is an example of two dimensional Fourier transform spectroscopy introduced by Jeener[6c] and by Ernst et al.[2d] integrated over one axis. That is, the response after P_2 is double Fourier transformed giving the double quantum spectrum for each value of ω_Q:

$$f(t_1,t_2) \rightarrow \psi(\omega,\omega_Q) \tag{61}$$

where we have absorption for ω_Q and dispersion for ω.

When there are several lines in the spectrum, or if the sample is polycrystalline, then P_1 cannot be matched to all ω_Q simultaneously. Equation (52) then holds with a distribution of ω_Z and the resulting double-quantum spectra will be distorted. This can be accounted for in a straightforward manner and is the subject of further research.

Figure 9. a) Schematic representation of the Fourier transform obtained from the two pulse experiment for ideal pulses: P_1 producing only double quantum coherence and P_2 obeying $\omega_1 >> \omega_Q$. b) General results for the two pulse sequence. P_1 is assumed to satisfy the condition $\omega_Y \cong \omega_Z$, in equation , but with an error in the pulse length, thus giving an extra term in the density matrix $S_{Z,1}$. This term does not oscillate for varying t_1 thus it will give a constant intensity after the probe pulse P_2 for different values of t_1. The probe pulse transforms the $S_{Z,1}$ term to the $S_{Y,1}$ term shown in the schematic Fourier transform (see equation (71)). The term $a_{X,1}$ is the first approximation to the effects of a finite probe pulse P_2. It oscillates at the double quantum frequency, and thus introduces a phase shift as shown in the D.Q. FID, see equations (70) and (72).

Double Quantum: Ideal

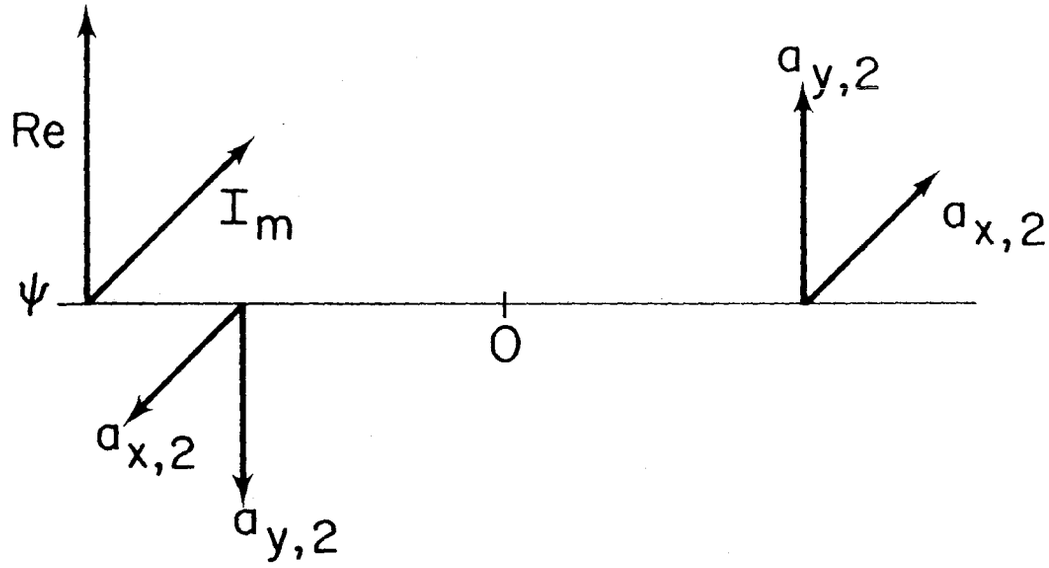

General

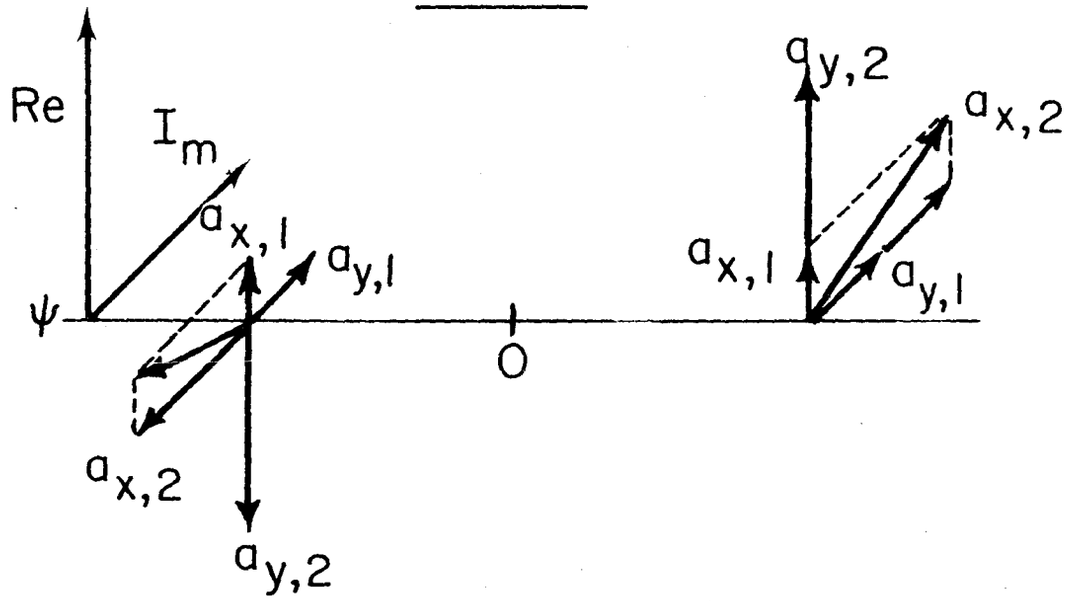

XBL 765-1978

We must now ascertain by what factor the observed dipole-dipole couplings are scaled in the double quantum frame. In high field the dipole-dipole (SS) coupling is given for all pairs of spins by:

$$H_{SS} = \sum_{ij} a_{ij} \, (12 \, S_{iZ,1} \, S_{iZ,1} - \underset{\sim}{S}_i \underset{\sim}{S}_j)$$

$$= \quad {}_{ij} \; 4 \, a_{ij} \{2 \, S_{iZ,1} \, S_{jZ,1} - S_{iX,1} \, S_{jX,1} - S_{iY,1} \, S_{jY,1}\} \quad (62a)$$

and the quadrupole Hamiltonian is given by:

$$H_S = \sum_{ij} \frac{2}{3} \, \omega_Q (I_{iX,3} - I_{iY,3}) \quad (62b)$$

the effective dipole-dipole Hamiltonian will be that part of equation (62a) which is secular with respect to H_S, i.e., commutes with it. We calculate this in the following way. First we find the time dependence of H_{SS} generated by H_S:

$$e^{-iH_S t} \, H_{SS} \, e^{iH_S t} = \sum_{ij} 4 \, a_{ij} \{2 \, S_{iZ,1} \, S_{jZ,1} - S_{iX,1} \, S_{jX,1}$$

$$\cos^2 \omega_Q t - S_{iX,2} \, S_{jX,2} \, \sin^2 - \omega_{QT} - S_{iY,1} \, S_{jY,1} \, \cos^2 \omega_Q t -$$

$$S_{iY,2} \, S_{jY,2} \, \sin^2 \omega_Q t + \frac{1}{2} \, (S_{iY,1} \, S_{jY,2} + S_{iY,2} \, S_{jY,2}) \sin 2\omega_Q t\}. \quad (63a)$$

We now extract the time independent parts giving:

$$\bar{H}^0_{SS} = \sum_{ij} 4 \, a_{ij} \, (2 \, S_{iZ,1} \, S_{jZ,1} - \frac{1}{2} \, (S_{iX,1} \, S_{jX,1} + S_{iX,2} \, S_{jX,2})$$

$$- \frac{1}{2} \, (S_{iY,1} \, S_{jY,1} + S_{iY,2} \, S_{jY,2})) \quad (63b)$$

The secular part of H_{SS} is commutative with $2\Delta\omega\ S_Z$ and therefore the effective dipolar interaction if independent of the single or double quantum transition.

To find the difference of the dipole-dipole coupling between the single and double quantum frames we calculate the second moment of transition involved in each of the frames:

$$M_2^S = \frac{tr[\bar{H}_{SS}^{(0)},\ (S_{X,1} - S_{Y,2})]^2}{tr[S_{X,1} - S_{Y,2}]^2} \tag{64a}$$

for single quantum transitions and

$$M_2^D = \frac{tr[\bar{H}_{SS}^{(0)},\ S_{Z,2}]^2}{tr[S_{Z,2}]^2}$$

where

$$S_{Z,2} = S_{iZ,2} + S_{jZ,2} \tag{64b}$$

for double quantum transitions. On the other hand we may rotate the dipole-dipole Hamiltonian into the proper frame and calculate the second moment:

$$M_2^T = \frac{tr[\bar{H}_{SS}^{(0)T},\ S_{X,1}]^2}{tr[S_{X,1}]^2}$$

where

$$S_{X,1} = S_{iX,1} + S_{jX,1} \tag{64c}$$

Tilting the effective dipolar Hamiltonian into the single quantum frame with the rotation $R_Z(90,2)$ (see equation (18)) we obtain

$$\bar{H}_{SS}^{(0)T} = \sum_{ij} 4\, a_{ij}\, (2\, S_{iZ,3}\, S_{jZ,3} - \frac{1}{2}\, (S_{iX,1}\, S_{jX,1} + S_{iX,2}\, S_{jX,2}) - \frac{1}{2}\, (S_{iY,1}\, S_{jY,1} + S_{iY,2}\, S_{jY,2}))\quad . \tag{64d}$$

We must now evaluate the following traces for the double quantum case:

$$\begin{aligned} \mathrm{tr}[\bar{H}_{SS}^{(0)},\, S_{Z,2}]^2 &= \mathrm{tr}\{ \sum_{ij} 8\, a_{ij}\, (S_{iZ,3}\, S_{jZ,1} + S_{iZ,1}\, S_{jZ,3})\}^2 \\ &= \sum_{ij} 64\, a_{ij}^2\, [\mathrm{tr}(S_{iZ,3})^2\, \mathrm{tr}(S_{jZ,1})^2 + \mathrm{tr}(S_{iZ,1})^2\, \mathrm{tr}(S_{jZ,3})^2] \\ &= \sum_{ij} 64\, a_{ij}^2\, [2\, \mathrm{tr}(S_{iX,1})^2\, \mathrm{tr}(S_{jX,1})^2] \end{aligned} \tag{65a}$$

and for the single quantum case:

$$\begin{aligned} \mathrm{tr}[\bar{H}_{SS}^{(0)T},\, S_{X,1}]^2 &= \mathrm{tr}\{ \sum_{ij} 4\, a_{ij}\, [-(S_{iZ,3}\, S_{jX,2} + S_{iX,2}\, S_{jX,3}) \\ &\quad + \frac{1}{2}\, (S_{iX,2}\, S_{jX,3} + S_{iX,3}\, S_{jX,2}) + \frac{1}{4}\, (S_{iY,1}\, S_{jZ,1} + S_{iZ,1}\, S_{jY,1}) \\ &\quad - \frac{1}{4}\, (S_{iY,2}\, S_{jZ,2} + S_{iZ,2}\, S_{jY,2})]\} \\ &= \sum_{ij} 16\, a_{ij}^2\, [\mathrm{tr}(S_{iZ,3})^2\, \mathrm{tr}(X_{jX,2})^2 + \mathrm{tr}(S_{iX,2})^2\, \mathrm{tr}(S_{iZ,3})^2 \\ &\quad + \frac{1}{4}\, \mathrm{tr}(S_{iX,2})^2\, \mathrm{tr}(S_{jX,3})^2 + \frac{1}{4}\, \mathrm{tr}(S_{iX,3})^2\, \mathrm{tr}(S_{jX,2})^2 + \frac{1}{16}\, \mathrm{tr}(S_{iY,1})^2 \\ &\quad \mathrm{tr}(S_{jZ,1})^2 + \frac{1}{16}\, \mathrm{tr}(S_{iZ,1})^2\, \mathrm{tr}(S_{jY,1})^2 + \frac{1}{16}\, \mathrm{tr}(S_{iY,2})^2\, \mathrm{tr}(S_{jZ,2})^2 \\ &\quad + \frac{1}{16}\, \mathrm{tr}(S_{iZ,2})^2\, \mathrm{tr}(S_{jY,2})^2] \\ &= \sum_{ij} 16\, a_{ij}^2\, [3\, \mathrm{tr}(S_{iX,1})^2\, \mathrm{tr}(S_{jX,1})^2] \end{aligned} \tag{65b}$$

We may now calculate the ratio of the double quantum and single quantum second moments, it is:

$$\frac{M_2^D}{M_2^S} = \frac{64.2}{16.3} = 4 \cdot \frac{2}{3} \tag{65c}$$

This shows that the dipole-dipole coupling scales by a factor of $\sqrt{\frac{8}{3}}$ = 1.6 for the double quantum transition whereas the frequency offset terms (chemical shift and frequency offset) scale by a factor of 2.

2. General solution

A more complete solution of the problem is needed in order to conduct the experiments. Incomplete supression of unwanted terms in the initial density matrix and the finiteness of the probing pulse, P_2, are factors which complicate the picture presented above; we will discuss both in turn.

The most common problem is a slight misadjustment in the pulse length of the first pulse, P_1, producing a term in the density matrix at t = 0 proportional to $S_{Z,1}$,

$$\sigma(0) = \beta\omega_o(\cos\omega_Z\tau\ S_{Z,1} - \sin\omega_Z\tau\ S_{Z,2}) \tag{66}$$

Note that the term in $S_{Z,1}$ is time independent during the subsequent evolution.

$$\sigma(t_1) = \beta\omega_o \{\cos\omega_Z\tau\ S_{Z,1} + \sin\omega_Z\tau(S_{Z,2}\ \cos 2\delta\omega t_1 + S_{Z,3}\ \sin 2\delta\omega t_1)\} \tag{67}$$

The probing pulse transforms this constant term to $S_{Y,1}$, as will soon be shown. If we choose to observe only the $S_{Y,2}$ term in equation (60) we have effectively canceled out this constant term since in the Fourier transform they are 90° out of phase ($a_{Y,2}$ is absorption along Reψ and $a_{Y,1}$ is dispersion along Reψ).

If the condition of equation (51) is not met, the terms in $S_{Y,1}$ and $S_{Y,2}$ appear in the density matrix, equation (66). Their time dependence will be an oscillation at the frequency $\delta\omega$, not $2\delta\omega$ as for the double quantum coherence, as seen in the synthesized FID, obtained from the first Fourier transform. These terms, then, will produce peaks in the double quantum Fourier transform which should not interfere with the double quantum lines. Experimentally, it is much easier to avoid this type (54), of imperfection than the constant $S_{Z,1}$ term, in equation (66) since $S_{Y,1}$ and $S_{Y,2}$ give signals after P_1, making pulse adjustment very easy.

The effect of the finiteness of the probing pulse is very complicated, and we only show the solution for the case that the field strength, ω_1, is finite but still obeys $\omega_1 >> \omega_Q$. The Hamiltonian during this pulse is (equation 25).

$$H_S^{*\prime} = \omega_e\ S'_{X,3} - \frac{1}{3}\ \omega_Q\ (S'_{Y,3} - S'_{Z,3}) - 2\delta\omega\ S'_{Z,1}$$

where

$$\omega_e = \omega_Q^2 + (2\omega_1)^2, \qquad \theta_X = \tan^{-1}\frac{2\omega_1}{\omega_Q} \tag{25}$$

The density matrix (equation 57) must be rotated by $R_X(\theta_X, 2)$ into this effective field frame giving

$$\sigma'(t_1) = \cos 2\delta\omega t_1 (S'_{Z,2} \cos\frac{\varepsilon}{2} + S'_{Y,1} \sin\frac{\varepsilon}{2}) + \sin 2\delta\omega t_1 [+ \frac{1}{2}(S'_{X,1} \sin\varepsilon + S'_{X,3} \cos\varepsilon + \frac{1}{2}(S'_{Y,3} - S'_{Z,3})] \tag{68}$$

and the result of the time dependence due to the pulse must then be rotated back.

In particular we wish to explain some imperfections (see experimental section and Figure 31) which can only come about by terms in the final density matrix after P_2 proportional to $S_{X,2}$ and $S_{Y,1}$. The term $\omega_e S_{X,3}$ will generate $S_{X,2}$ from $S_{X,1}$ in the density matrix but it will not generate $S_{Y,1}$. The quadrupolar term will generate $S_{X,2}$ from $S_{Y,1}$ in the density matrix along with $S_{Y,1}$. But the quadrupole term commutes with $S_{X,1}$ and $S_{X,3}$ so this term in the density matrix is not affected. It is rather complicated to calculate the effect of the quadrupole term, so at this level of approximation we wish to drop it. This still allows us to calculate exactly the effects of the $S_{X,1}$ and $S_{X,3}$ terms in the density matrix due to the effective Zeeman Hamiltonian which will give us a good starting point for understanding the origins of the experimental imperfections. With the above comments in mind we approximate the Hamiltonian equation (25) as

$$H_S^{*\prime} = \omega_e S'_{X,3} \tag{69}$$

realizing that we are neglecting important contributions from other terms in the density matrix. The final result of the time evolution during the pulse P_2 of length τ_P is:

$$\begin{aligned}\sigma(t_1,\tau_P) = \beta\{ & S_{Z,2} \cos 2\delta\omega t_1 \cos \frac{\omega_e}{2} \tau_P \\ & + S_{Z,1} \cos 2\delta\omega t_1 \sin \frac{\omega_e}{2} \tau_P \cos\varepsilon \\ & - S_{Y,2} \cos 2\delta\omega t_1 \sin \frac{\omega_e}{2} \tau_P \sin\varepsilon \\ & + S_{X,1} \sin 2\delta\omega t_1 (1 - \cos\omega_e\tau_P) (\frac{1}{4} \sin 2\varepsilon) \\ & + S_{X,2} \sin 2\delta\omega t_1 \sin\omega_e\tau_P (+ \frac{1}{2} \sin\varepsilon) \\ & + S_{X,3} \sin 2\delta\omega t_1 \frac{1}{2}(\cos^2\varepsilon + \cos\omega_e\tau_P \sin^2\varepsilon) (-\cos \frac{\varepsilon}{2}) \\ & + \frac{1}{2} \sin 2\delta\omega t_1 (S_{Y,3} - S_{Z,3}) \}\end{aligned} \tag{70}$$

The observable terms are

$$a_{Y,2} = \beta \cos 2\delta\omega t_1 \sin \frac{\omega_e}{s} \tau_P (-\sin\varepsilon)$$

$$a_{X,1} = \beta \sin 2\delta\omega t_1 (1 + \cos\omega_e\tau_P) (\frac{1}{4} \sin 2\varepsilon)$$

$$a_{X,2} = \beta \sin 2\delta\omega t_1 \sin\omega_e\tau_P (+ \frac{1}{2} \sin\varepsilon)$$

This is diagramed in Figure 9b.

The constant term in the density matrix, $S_{Z,1}$, is transformed by the same pulse as

$$S_{Z,1} \rightarrow S_{Z,1} \cos \frac{\omega_e}{2} \tau_P - S_{Z,2} \sin \frac{\omega_e}{2} \tau_P \cos\varepsilon + S_{Y,1} \cos \frac{\omega_e}{2} \tau_P \sin\varepsilon \tag{71}$$

The observable term is

$$a_{Y,1} = \beta \cos \frac{\omega_e}{2} \tau_P \sin\varepsilon \tag{72}$$

which is also diagramed in Figure 9b. If we align the phase detector with $a_{Y,1}$ as the reference phase and observe 90° out of phase with that we find for a delay between the pulses of t_1 and time after P_2 of t, an FID given as $S^{90}(t_1,t)$. For simplicity we restrict our attention to the high frequency satellite only giving:

$$S^{90}(t_1,t) = \frac{1}{2}\,[C_{Y,2} \cos 2\delta\omega t_1 + C_{X,1} \sin 2\delta\omega t_1] \cos(\omega_Q - \delta\omega)t$$

$$- \frac{1}{2}\,[C_{X,2} \sin 2\delta\omega r_1 + C_{Y,1}] \sin(\omega_Q - \delta\omega)t$$

with

$$C_{Y,2} = \frac{a_{Y,2}}{\cos 2\delta\omega t} \qquad C_{X,1} = \frac{a_{X,1}}{\sin 2\delta\omega t} \qquad \text{etc.} \tag{73}$$

First, let us assume $C_{X,2} = 0$. Then the Fourier transform of (73) will give a mixture of absorption and dispersion in Reψ. Upon synthesizing the double quantum FID (D.Q. FID) for different values of t_1 we would find signals for both the D.Q.FID synthesized from Reψ and the D.Q.FID synthesized from Imψ. However we can phase this FID taken as a whole so that the intensity is shifted completely into the Reψ D.Q.FID. With the inclusion of the term in $S_{X,2}$ this can no longer be done, so that no matter what phase corrections are performed on the FID there will always be intensity in the part from Imψ. This will be shown to occur for the experiments that follow.

We can now use equation (72) to ascertain which new terms are the most important in our experiments, the final signals from $a_{X,2}$ or from $a_{Y,1}$.

IV. Cross Relaxation

A. Previous Quadrupole Cross Relaxation Experiments

A number of cross relaxation experiments have been performed which involve quadrupolar species. They can be classified by the a) field strength at which the cross polarization takes place, zero or low field (<1 Kgauss) or high $\approx$ 25 Kgauss) and b) by the mechanism for the cross polarization. The mechanism used will either be related to continuous off resonance irradiation or thermal mixing from quasiequilibrium states (e.g., spin locked or ADRF). One of the early cross polarization experiments by thermal mixing was between quadrupolar species, by Anderson and Hartman, but the experiment was at zero field. Schwab and Hahn[19] extended this method to cross polarization between a quadrupolar species (chlorine or deuterium) and a spin ½ species (protons) also at zero field. Goldman and Landesman[20] achieved cross polarization between a quadrupolar species and a spin ½ species by off resonance irradiation of the quadrupolar spins also at low field. A level crossing approach at low field has also been used by Demco, Kaplan, Pausak and Waugh.[38] The level crossing occurs between chlorine and protons which preceeds a normal high field $^{13}C-^{1}H$ cross polarization experiment. Hahn *et al.*[48] have in addition, detected cross polarization to the double quantum transition for deuterium in $CaSO_4 \cdot 2H_2O$ (gypsum). This was again a low field experiment.

There have been two previous methods for cross polarization in high fields. Off resonance irradiation of protons was used by de Boer[21] (and references therein) to polarize deuterium. And Veeman and Yannoni[22] used a slow frequency sweep across the chlorine resonance to polarize

protons, which they postulate to be similar to a thermal mixing experiment.

The approach of de Boer *et al.* is most similar to our approach in that the goal of the cross polarization is to cool the quadrupolar reservoir (i.e., deuteriums). He has made a careful distinction between

the types of polarization, which is defined as

$$P = \frac{\langle I_P \rangle}{I} \quad , \quad P = X,Y,Z \tag{74}$$

is the normal type of polarization produced in spin -½ PENIS experiments. Another type of polarization is also possible, the tensor polarization or alignment:

$$A = \frac{\langle 3I_Z^2 - I(I+1) \rangle}{I(2I-1)} \tag{75}$$

This is the type of polarization produced in the experiments of de Boer et al. and in adiabatic demagnetization. The alignment is not directly observable, but must be probed either with a pulse, adiabatic remagnetization or continuous wave fast passage.

The density matrix that is produced after the first pulse in the two pulse sequence in Double Quantum Spectroscopy is also a type of alignment, with coherence in the X-Y plane. That is

$$\sigma(0) = \beta\omega_0 \, S_{Z,2} = \beta\omega_0 \, \frac{1}{2}(I_X \, I_Y + I_Y \, I_X) \tag{76}$$

is related to the spherical tensor components $T_{2,\pm 2}$ while the alignment of de Boer et al. is related to $T_{2,0}$ (see Appendix 2). It will be seen that our double-quantum cross polarization experiments, which are of the high field thermal mixing type, can also produce a tensor polarization.

B. Cross Polarization Theory

We have shown that it is possible to write the deuterium Hamiltonian in terms of a spin ½ Zeeman type interaction. We may now apply the theory of cross polarization used in Chapter 1 to the case in hand, the thermal contact of the abundant proton spins with an isolated deuterium which we

now consider to be a spin ½ system.

The total Hamiltonian for this case is

$$H = H_I + H_S + H_{IS} \tag{77}$$

with the proton Hamiltonian the same as before

$$H_I = -\omega_{0I} I_Z - 2\omega_{1I} I_X \cos\omega_{0I} t + H_{II}$$

$$\omega_{0I} = \gamma_I H_0, \quad \omega_{1I} = \gamma_I H_{1I} \quad \text{and} \quad I_P = \sum_i I_{ip} \tag{78}$$

H_0 is the external magnetic field, H_{1I} is the field strength of the radio frequency irradiation at resonance with the I spin system and H_{II} represents the homonuclear dipole-dipole interaction. H_S is given in equations (15, 19, 20, and 26b), where we neglect the interaction between the S-spins. H_{IS} is the heteronuclear dipole-dipole interaction between the I and S spin, and is responsible for the energy exchange. In the double rotating frame obtained by the transformation:

$$T = \exp(i\,\omega_{0I}\, I_Z + i\,\omega_{eS} S_Z)t \tag{79}$$

the Hamiltonian becomes:

$$H^* = -\omega_{1I}\, I_X + H_{II}^{(0)} + H_{S,1}^* + H_{S,2}^* + H_{IS}^{(0)}$$

with

$$H_{II}^{(0)} = \sum_{i<j} a_{ij}\, (3I_{iZ}\, I_{jZ} - \underset{\sim}{I}_i \cdot \underset{\sim}{I}_j)$$

$$H_{IS}^{(0)} = a \sum_i b_i\, S_{Z,1}\, I_{iZ} \tag{80}$$

The interaction coefficients a_{ij} and b_i are defined in Chapter 1 equation (8); these are the secular parts of the dipolar interactions $H^*_{S,1}$ equals the first two terms in equations 19, 20, and 26 depending on the S irradiation frequency ω_S and $H^*_{S,2}$ is the last term in each. We derived these equations so that:

$$[H^*_{S,1}, H^*_{S,2}] = 0 \tag{81}$$

and therefore we must consider $H^*_{S,1}$ and $H^*_{S,2}$ as separate constants of the motion.

The density matrix of the two spin systems in equilibrium is, in the rotating frame, given to a good approximation by:

$$\sigma^* = \sigma^*_S + \sigma_I = \beta_{S,1} H^*_{S,1} + \beta_{S,2} H^*_{S,2} + \beta_I H^*_I \tag{82}$$

where H^*_I is given by the first two terms in equation (80). There are two choices for the initial state (quasi-equilibrium) of the proton system, either spin locked (SL) or adiabatically demagnetized (ADRF). There are also three choices for the levels to be cross polarized; either one of the satellites (single quantum) for which the deuterium irradiation frequency is near one of the satellites or the double quantum transition for which the deuterium frequency is near the center of the spectrum.

1. Single Quantum Cross Polarization

If the r.f. field on the S-spins is applied near one of the side bands the relevant equations for this case are taken from equation (19), assuming $\omega_Q >> \delta\omega$

$$H^*_{S,1} = -\delta\omega\ S'_{X,3} - \sqrt{2}\ \ \omega_{1S} S'_{X,1} = -\omega_{eS}\ S''_{X,1} \tag{83}$$

$$H^*_{S,2} = -\frac{4}{3}\omega_Q\ (S'_{Y,3} - S'_{Z,3}) = -\frac{4}{3}\omega_Q (S''_{Y,3} - S''_{Z,3})$$

where we applied a $R_X(\theta_{X,2})$ rotation to obtain the double primed operators, where

$$\tan\ \theta_X = \frac{\delta\omega}{2\omega_{1S}}$$

$$\omega_{eS} = \sqrt{\delta\omega^2 + 2\omega_{1S}^2}$$

To describe the cross polarization thermodynamics, we apply the approach outlined by Pines et al.[1] with an effective S-spin ½ Hamiltonian given by $H^*_{S,1}$. The I-spin Hamiltonian can be written as

$$H^*_I = -\omega_{1I}\ I_X + P_X(\cos\theta_I)\ H^{(o)}_{II} \equiv \omega_{1I}\ I_X - \frac{1}{2}\sum_{i<j} a_{ij}\ (3I_{iX}\ I_{jX} - \underset{\sim}{I}_i \cdot \underset{\sim}{I}_j) \tag{84a}$$

for the SL case and

$$H^*_I = H^{(o)}_{II} = \sum_{i<j} a_{ij}\ (3I_{iZ}\ I_{jZ} - \underset{\sim}{I}_i \cdot \underset{\sim}{I}_j) \tag{84b}$$

for the ADRF case. The SL dipolar interaction is obtained by taking the secular part of $H^{(o)}_{II}$ with respect to $\omega_{1I}\ I_X$. The Hartmann-Hahn condition for this case is

$$(2\,\omega_{1S}^2 + \delta\omega^2)^{1/2} = \omega_I \tag{85}$$

where $\omega_I = \gamma_I H_{1I}$ for SL and $\omega_I = \gamma_I H_{LI}$ for ADRF with H_{LI} the I spin local field (see Chapter 1). Bringing the two spin reservoirs to thermal equilibrium (but disregarding spin-lattice relaxation) gives, from equation (82), the density matrix:

$$\sigma_S^* = \beta_1\, H_{S,1}^* + \beta_L\, H_{S,2}^* \tag{86}$$

with $\beta_L = \frac{1}{kT_L}$ and T_L is the lattice temperature. We wish to find the final equilibrium inverse spin temperature β_1. This is done by solving the equation for conservation of energy:

$$(\beta_L \frac{H_0}{H_{1I}})\, C_I\, H_{1I}^2 = \beta_1 C_I H_{1I}^2 + \beta_1\, C_{eS}\, (\frac{\omega_{eS}}{\gamma_{eS}})^2 \tag{87}$$

where $\gamma_{eS} = \sqrt{2}\,\gamma_S$ and $C_{eS} = \sqrt{2}\,C_S$

This gives:

$$\beta_1 = \beta_L \frac{H_0}{H_{1I}} \frac{1}{1+\varepsilon\eta^2} \tag{88}$$

where:

$$\eta = \frac{\omega_{eS}}{\omega_{1I}}$$

$$\text{and } \varepsilon = \frac{N_S(2I+1)}{N_I(2S+1)} = \frac{2N_S}{3N_I} \tag{88a}$$

The Curie constants in equations (87), (88a) were found by calculating the energy:

$$E = tr(\sigma H)$$

using for the density operators σ_I^* and $\sigma_{S,1}^*$ from equations (82) and for the Hamiltonians:

$$H_I = -\omega_{1I} I_X$$

$$H_{S,1} = -\omega_{eS} S_{X,1}$$

The equilibrium density matrices are

$$\sigma_I = \beta_I H_I$$

$$\sigma_S = \beta_S H_{S,1}$$

then

$$E_S = \mathrm{tr}(\beta_S H_S^2) = \beta_S \omega_{eS}^2 \frac{\mathrm{tr}\, S_{X,1}^2}{Z}$$

$$E_I = \mathrm{tr}(\beta_I H_I^2) = \beta_I \omega_{1I}^2 \frac{\mathrm{tr}\, I_X^2}{Z}$$

remembering that these spin operators are many spin operators:

$$S_{X,1} = \sum_i S_{iX,1} \qquad I_X = \sum_i I_{iX}$$

We reduce the trace to a trace of single spin operators and we note that $Z = (2S + 1)^N$ giving:

$$E_S = \beta_S \omega_{eS}^2 N_S \frac{(2S+1)^{N-1}}{(2S+1)^N} \mathrm{tr}\, S_{iX,1}^2$$

$$E_I = \beta_I \omega_{1I}^2 N_I \frac{(2I+1)^{N-1}}{(2I+1)^N} \mathrm{tr}\, I_{iX}^2$$

Reference to equations (9) indicates that

$$\mathrm{tr}\, S_{iX,1}^2 = \mathrm{tr}\, I_{iX}^2 = \frac{I(I+1)(2I+1)}{3} = \frac{1}{2}$$

since both $S_{iX,1}$ and I_{iX} are spin ½ operators (see reference 47 for the explicit evaluation of the traces). Finally we have:

$$I_S = \beta_S \, C_{eS} \, H_{1S}^2 \qquad C_{eS} = \gamma_{eS}^2 \, N_S \, \frac{\frac{1}{2}}{(2S+1)}$$

$$E_I = \beta_I \, C_I \, H_{1I}^2 \qquad C_I = \gamma_I^2 \, N_I \, \frac{\frac{1}{2}}{(2I+1)} \tag{89}$$

Note that C_{eS} and C_I differ only in the normalization. C_{eS} is normalized to a three state single spin manifold and C_I to a two state manifold:

$$(2S+1) = 3 \qquad \text{but } (2I+1) = 2$$

Other than the normalization the fictitious spin heat capacity is exactly the same as presented in Chapter 1. To obtain the intensity of the FID signal after the single quantum cross polarization, we write σ_S^* explicitly using equations (86) and (83),

$$\sigma_S^* = - \beta_1 (\delta\omega \, S'_{X,3} + \sqrt{2} \, \omega_{1S} \, S'_{X,1}) - \beta_L \, \frac{4}{3} \, \omega_Q (S'_{Y,3} - S'_{Z,3})$$

We now need to transform this back to the normal rotating frame where the signal is detected. This is done with a rotation by $R_Z(-90,2)$ to invert the $R_Z(90,2)$ transformation to equations (18) and (19). This yields

$$\sigma_S^* = (2\omega_Q \, \beta_L + \frac{1}{2} \, \delta\omega \, \beta_1) S_{Z,1} + (\frac{2}{3} \, \omega_Q \, \beta_L - \frac{1}{2} \, \delta\omega \, \beta_1) \cdot$$

$$(S_{X,3} - S_{Y,3}) - \beta_1 \;\; 2 \, \omega_1 \;\; \frac{1}{2} \, (S_{X,1} + S_{Y,2}) \tag{90}$$

From Table 2, page 142, we find the results after Fourier transformation of the FID obtained from the initial density matrix, equation (90),

$$M_X = 2 \langle \gamma_S \, S_{X,1} \rangle = - \frac{\gamma_S}{\gamma_{eS}} \beta_1 \, C_{eS} \, H_{1S} \quad \text{at} \; - \omega_Q - \delta\omega$$

$$M_Y = 2 \langle \gamma_S \, S_{Y,1} \rangle = 0$$

with

$$C_{eS} = \frac{N_S \, \gamma_{eS}^2 \, \frac{1}{2}}{2S+1} \tag{91}$$

The unenhanced FID gives two peaks, but after cross polarization we obtain only one peak, that which is near the irradiation frequency. Comparing this result with the FID signal, $M^{(0)}$, after a single intense 90° pulse with $\omega_1 >> \omega_Q$ gives

$$\left| \frac{M_X}{M^{(0)}} \right| = \frac{\gamma_S \, \beta_1 \, C_{eS} \, H_{1S}}{\gamma_{eS} \, \beta_L \, C_S \, H_0} = \frac{H_{1S}}{H_{1I}} \, \frac{1}{1+\varepsilon\eta^2} \tag{92}$$

and with $\eta = 1$ for exact matching of the Hartman-Hahn condition and $\delta\omega = 0$

$$\left| \frac{M_X}{M^{(0)}} \right| = \frac{\gamma_I}{\gamma_S} \, \frac{1}{1+\varepsilon} \tag{93}$$

The cross polarization time T_{IS} may also be easily derived using that the levels we irradiate behave as a spin ½ system. Using the same theory as in Chapter 1 of McArthur et al.[23]:

$$\frac{1}{T_{IS}} = \frac{1}{tr\{H^*_{S,1}\}^2} \int_0^\infty d\tau \; tr\{[H^{(o)}_{IS}, H^*_{S,1}] \; e^{-i(H^*_{S,1}+H^*_I)\tau}$$

$$[H^{(o)}_{IS}, H^*_{S,1}] \; e^{i(H^*_{S,1}+H^*_I)\tau} \tag{94}$$

where $H^*_{S,1}$ is given in equation (83). The form of the heteronuclear dipole-dipole interaction in the same frame (double primed) where $H^*_{S,1}$ is defined, is obtained by rotating with $R_Z(90,2)$ and $R_X(\theta_X,2)$ giving,

$$H^{(o)}_{IS} = \sum_i 2 \, I_{iZ} \, (S''_{X,3} \cos\theta_X + S''_{X,1} \sin\theta_X)$$

$$+ \sum_i 2b_i \, I_{iZ} \, (S''_{Y,3} - S''_{Z,3}) \tag{95}$$

This is now in the single quantum frame. Carrying out the details, which are given in Appendix 3 we find for the SL case,

$$T^{-1}_{IS} = \frac{1}{2} \cos^2 \theta_X \, M_{2,IS} \, J_X(\omega_{eS} - \omega_{1I}) \tag{96}$$

and for ADRF:

$$T^{-1}_{IS} = \cos^2 \theta_S \, M_{2,IS} \, J_Z(\omega_{eS}) \tag{97}$$

with the following definitions:

$$M_{2,IS} = \frac{tr[\sum_i 2b_i \, I_{iZ} \, S_{Z,1}, \; S_{X,1} - S_{Y,2}]^2}{tr[S_{X,1} - S_{Y,2}]^2}$$

$$J_p(\omega) = \int_0^\infty d\tau \; \cos\omega\tau \; C_p(\tau)$$

$$C_p(\tau) = \frac{\mathrm{tr}\{\sum_i b_i\, I_{ip}\, e^{-iP_2(\cos\theta_I)H_{II}^{(o)}} (\sum_i b_i\, I_{ip}\, e^{iP_2(\cos\theta_I)H_{II}^{(o)}}\}}{\mathrm{tr}\{\sum_i b_i\, I_{ip}\}^2}$$

$M_{2,IS}$ is the second moment of the satellite we irradiate during cross polarization; the linear combinations $S_{X,1}-S_{Y,2}$ corresponds to the satellite at $-(\omega_Q+\delta\omega)$, see Section IIIB. $C_p(\tau)$ is the autocorrelation function of the dipolar fluctuations and $J_p^{(\omega)}$ is its spectral density. As we expected, we get exactly the same result as for the spin ½ case, taking into account the effective magnetogyric ratio for the single quantum transition $\sqrt{2}\,\gamma_S$.

2. Double Quantum Cross Polarization

If we irradiate near the center of the S-spin spectrum and take the S-spin Hamiltonian to be (equation 26b)

$$H^*_{S,1} = -\,2\delta\omega\, S^1_{Z,1} - \frac{\omega_{1S}^2}{\omega_Q} S'_{Z,3} = -\omega_{eS}\, S''_{Z,3} \tag{98a}$$

$$H^*_{X,2} = \frac{2}{3}\,\omega_Q\,(S'_{X,3}-S'_{Y,3}) = \frac{2}{3}\,\omega_Q\,(S''_{X,3}-S''_{Y,3}) \tag{98b}$$

where the double primed operators are obtained by a $R_Z(\theta_{Z,2})$ rotation with

$$\omega_{eS} = \left(\frac{\omega_{1S}^4}{\omega_Q^2} + 4\delta\omega^2\right)^{1/2} \quad ;$$

$$\tan\theta_Z = \frac{2\delta\omega\,\omega_Q}{\omega_{1S}^2}$$

This frame we term loosely the double quantum frame. The H_I^* Hamiltonian is exactly the same as the single quantum case. The Hartman-Hahn condition for the double quantum transition is

$$\omega_{eS} = \left(\frac{\omega_{1S}^4}{\omega_Q^2} + 4\delta\omega^2\right)^{1/2} = \omega_I \ ;$$

$$\text{if } \delta\omega = 0 \quad \frac{\omega_{1S}^2}{\omega_Q} \quad \Rightarrow \omega_{eS} = \frac{\omega_{1S}^2}{\omega_Q} \quad \text{if } \delta\omega = 0 \tag{99}$$

This is shown schematically in figure 10 for $\delta\omega = 0$.

After a mixing pulse the result for the final equilibrium temperature β_1 is the same as in equation (88) except for the definition of γ_{eS},

$$\beta_1 = \beta_L \frac{H_0}{H_{1I}} \frac{1}{1+\varepsilon\eta^2}$$

$$\gamma_{eS} = \frac{\omega_1}{\omega_Q} \gamma_S \tag{100}$$

for $\delta\omega = 0$.

The S spin density matrix after cross polarization again ignoring relaxation effects is,

$$\sigma_S^{*\prime} = -\beta_1\left(2\delta\omega\, S'_{Z,1} + \frac{\omega_{1S}^2}{\omega_Q} S'_{Z,3}\right) + \beta_L \frac{2}{3}\omega_Q\left(S'_{X,3} - S'_{Y,3}\right) \tag{101}$$

We must now transform the density matrix which is in the double quantum frame back into the normal laboratory rotating frame to find the observable effects of the cross polarization. Rearranging equation (101) and using

Figure 10. Double quantum SL (spin locking) cross polarization for indirect detection. a) The Hartmann Hahn condition is indicated for a proton field strength of ω_{1I} and a deuterium field strength of ω_{1S} and $\delta\omega_S = 0$, and $\delta\omega_I = 0$. For $\delta\omega = 0$ the matching condition is

$$\frac{\omega_{1S}^2}{\omega_Q} = \omega_{1I}$$

and for $\delta\omega \neq 0$

$$\left(\frac{\omega_{1S}^4}{\omega_Q^2} + 4\ \delta\omega^2\right)^{1/2} = \omega_{1I} \quad ,$$

see equation (99). b) The SL sequence for indirect detection is shown for the deuterium r.f. field strength ω_{1S} and the proton r.f. field strength ω_{1I}. Cross polarization is detected as a decrease in the proton FID.

Cross Polarization

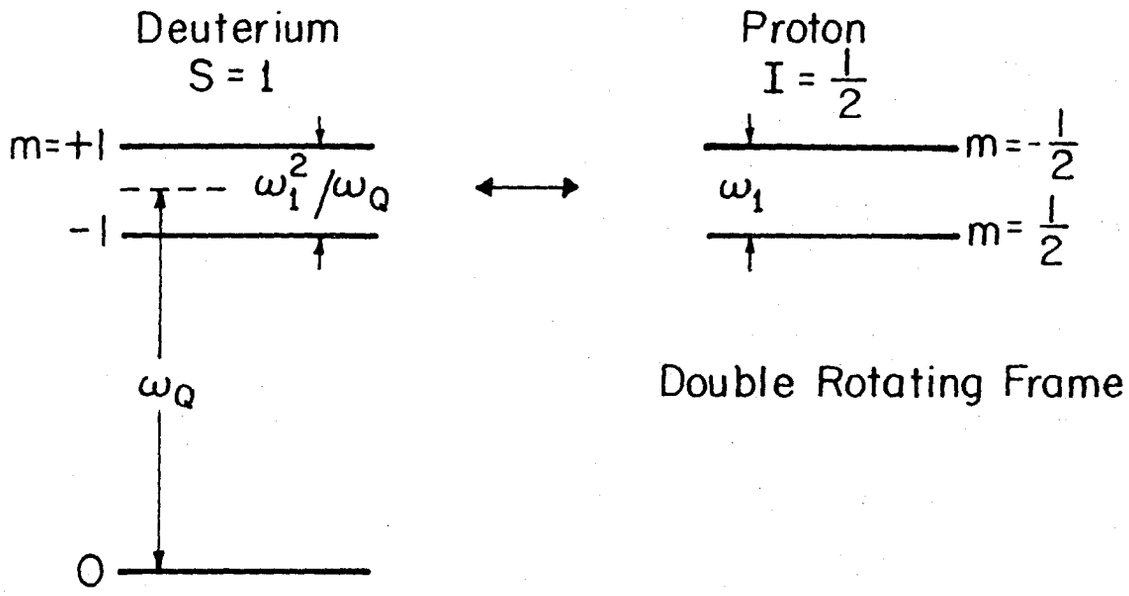

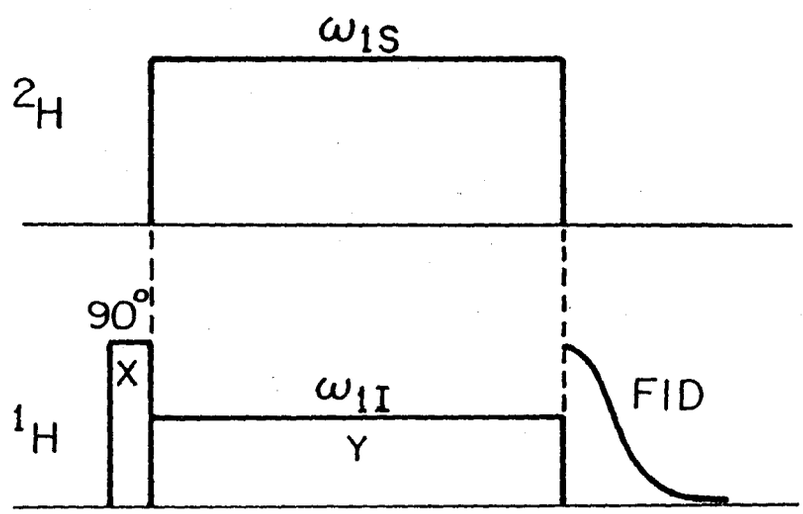

Pulse Sequence

XBL 762-6499a

the linear dependence of the $S_{p,3}$ operators we obtain:

$$\sigma_S^{*\prime} = (\beta_1 \frac{1}{2} \frac{\omega_1^2}{\omega_Q} - \beta_L\omega_Q)S'_{X,3} - (\frac{1}{3} \beta_L\omega_Q + \beta_1 \frac{1}{2} \frac{\omega_1^2}{\omega_Q})(S'_{Y,3}-S'_{Z,3})$$

$$+ 2\beta_1 \delta\omega \, S'_{Z,1}$$

We now apply a $R_X(-\varepsilon,2)$ rotation to return to the rotating frame (see equation (25)) and we assume that $\beta_L \approx 0$ such that $\beta_L\omega_Q << \beta_1 \frac{\omega_1^2}{\omega_Q}\}$ yielding:

$$\sigma_S^* = \beta_1 \frac{1}{2} \frac{\omega_1^2}{\omega_Q} (S_{X,3} \cos\varepsilon - S_{X,1} \sin\varepsilon) - \beta_1 \frac{1}{2} \frac{\omega_1^2}{\omega_Q}$$

$$(S_{Y,3}-S_{Z,3}) + 2\beta_1\delta\omega \, (S_{Z,1} \cos \frac{\varepsilon}{2} - S_{Y,2} \sin \frac{\varepsilon}{2}) \qquad (102)$$

It is clear that the FID signal after the cross polarization is very small due to the $\sin\varepsilon \approx 2\omega_1/\omega_Q$ factor in the coefficient of $S_{X,1}$. In order to measure the total polarization we must apply an additional pulse either 90° or 180° out of phase with the mixing pulse; this will be discussed shortly. <u>The maximum FID signal intensity after the proper pulse is</u>

$$M_X = \beta_1 \, C_{eS} \, H_{1S} \frac{\gamma_S}{\gamma_{eS}}$$

with

$$\gamma_{eS} = \frac{\omega_1}{\omega_Q} \gamma_S \qquad (103)$$

for $\delta\omega = 0$

with C_{eS} defined in equation (91). Comparing this with the maximum signal from the double quantum transition which could be obtained, if

we could detect the signal directly, $M^{(o)}$, we get

$$\frac{M_X}{M^{(o)}} = \frac{\gamma_S}{\gamma_{eS}} \frac{\beta_1 C_{eS} H_{1S}}{\beta_L C_S H_0} = \frac{\gamma_I}{\gamma_S} \frac{1}{1+\varepsilon} \tag{104}$$

In a cross polarization experiment we can also extract the ratio of the heat capacities of the S and I spins. We may then use this experiment to provide a direct measure of the effective magnetogyric ratio for the double quantum state. We must then explicitly calculate the heat capacities of the two systems. For the experiments that follow we take $\delta\omega = 0$. We can then ignore the offset term in equation (101). We also assume that $\beta_1 >> \beta_L$. The heat capacity is then given by

$$H_S = \frac{\partial\, tr(\sigma_S^{*'} H_{S1}^{*'})}{\partial \beta} = \left(\frac{\omega_{1S}^2}{\omega_Q}\right)^2 \frac{tr(S_{Z,3}^{'\,2})}{Z} = N_S \frac{\omega_{1S}^4}{\omega_Q^2} \frac{(2S+1)^{N-1}}{(2S+1)^N} tr(S_{iZ,3}^2)$$

Here we have included the normalization Z again, as was also done in equation (83). And likewise,

$$H_I = N_I \omega_1^2 \frac{(2I+1)^{N-1}}{(2I+1)^N} tr\{I_{iZ}^2\}$$

We remember that

$$tr\{S_{iZ,3}^2\} = tr\{I_{iZ}^2\} = \frac{1}{2}$$

since $S_{iZ,3}$ is a fictitious spin operator. This trace is easily evaluated explicitly from equation (9). Finally:

$$\frac{H_S}{H_I} = \varepsilon\eta^2 = \frac{N_S}{N_I} \frac{\gamma_{eS}^2}{\gamma_I^2} \frac{H_{1S}^2}{H_L^2} \frac{(2I+1)}{(2S+1)} \tag{104a}$$

We will now derive the cross polarization time for this case. Using equation (98), and its effective spin ½ form, allows us to derive the details of the cross polarization.

We must first rotate the perturbation $H_{IS}^{(o)}$ into the double quantum frame. Following the derivation of (98) with the rotations $R_X(\theta_{X,2})$ and $R_Z(\theta_{Z,2})$ with

$$\theta_X = \varepsilon = \tan^{-1} \frac{2\omega_1}{\omega_Q} \tag{105}$$

$$\theta_Z = \tan^{-1} \frac{2\delta\omega}{\frac{\omega_{1S}^2}{\omega_Q}} \tag{106}$$

we find

$$H_{IS}^{(o)''} = \sum_i 2b_i \left(S''_{Z,1} \cos\frac{\theta_X}{2} \cos\theta_Z - S''_{Z,3} \cos\frac{\theta_X}{2} \sin\theta_Z - S''_{Y,2} \sin\frac{\theta_X}{2} \cos\frac{\theta_Z}{2} - S''_{X,1} \sin\frac{\theta_X}{2} \sin\frac{\theta_Z}{2}\right) I_{iZ} \tag{107}$$

Assuming $\omega_1 \ll \omega_Q$ and $\delta\omega \ll \omega_{eS}$ gives:

$$H_{IS}^{(o)} = \sum_i 2b_i \cos\frac{\theta_X}{2} S_{Z,1} I_{iZ} \tag{108}$$

To calculate T_{IS} we now insert equations (98a), for $H^*_{S,1}$, and (108), for the perturbation H^*_p, into equation (94) and by a similar procedure as for the single quantum case we obtain for the SL cross polarization:

$$T_{IS}^{-1} = \frac{1}{2} \cos^2\frac{\theta_X}{2} \quad M_{2,IS} \; J_X(\omega_{eS}-\omega_{1I}) \tag{109}$$

and for ADRF

$$T_{IS}^{-1} = \cos^2 \frac{\theta_X}{2} \; M_{2,IS} \; J_Z(\omega_{eS}) \tag{110}$$

and $M_{2,IS}$ is the second moment of the double quantum transition due to the dipolar interaction between the I and the S spins,

$$M_{2,IS} = \mathrm{tr}\,[H_{IS}^{(o)}, S_{Z,3}]^2 / \mathrm{tr}\,[S_{Z,3}]^2$$

Once again we have obtained the same result we would have for a spin ½ case, but with an effective magnetogyric ratio of $(\omega_1/\omega_Q)\gamma_S$.

3. Magic Pulse

In order to recover all of the magnetization obtained after double quantum cross polarization an extra pulse must be applied. We shall dub this pulse a "magic" pulse and it must be either 90°, -90°, or 180° out of phase with the mixing pulse. This is shown schematically in figure (11a). If the cross polarization is performed at resonance for deuterium and the magic pulse obeys

$$\omega_1 >> \omega_Q$$

the effect of the pulse is to cause a precession of the magnetization in the X spin space. This is depicted in figure (11b).

We now apply a (-X) pulse with the time development governed by the Hamiltonian (see equation (25))

$$H^* = \omega_Q \, S_{X,3} + 2\omega_1 \, S_{X,1} - \frac{1}{3}\,\omega_Q (S_{Y,3} - S_{Z,3})$$

$$H^{*\prime} = \sqrt{\omega_Q^2 + (2\omega_1)^2} \;\; S'_{X,3} - \frac{1}{3}\,\omega_Q (S'_{Y,3} - S_{Z,3})$$

and $\omega_e = \sqrt{\omega_Q^2 + (2\omega_1)^2}$ (111)

Figure 11. a) Double quantum ADRF cross polarization with direct detection with a magic pulse. b) Precession in x-spin space caused by a magic pulse of phase (-X). c) Schematic representation of the Fourier transform obtained after the magic pulse, for the ideal case $\omega_{1S} >> \omega_Q$. The angle of the effective field is (see equation 25)

$$\varepsilon = \tan^{-1} \frac{2\omega_1}{\omega_Q}$$

and the precession is described by equation (112).

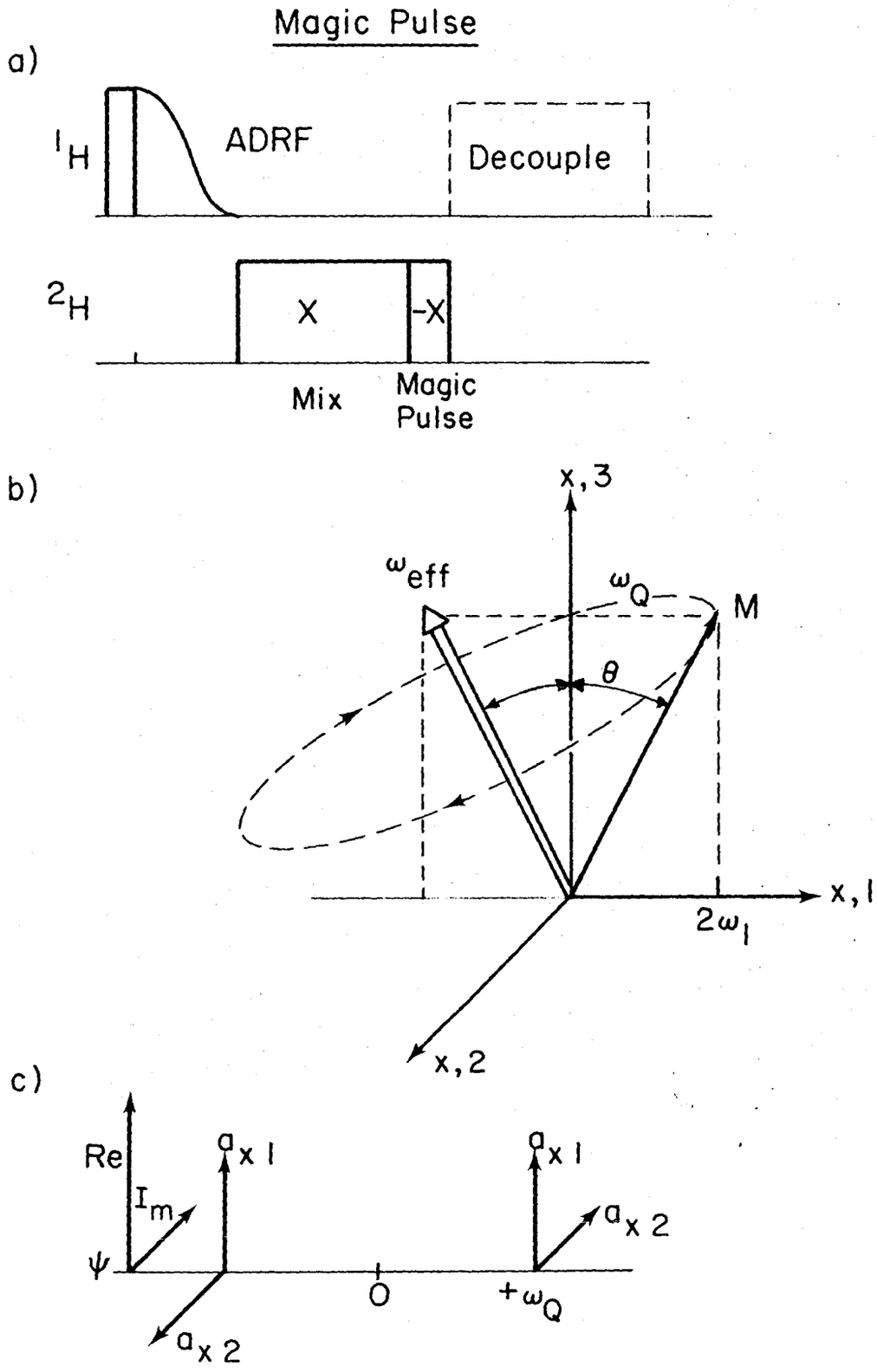
Magic Pulse
a)
^1H
ADRF
Decouple
^2H
X
-X
Mix
Magic Pulse
b)
x,3
ω_{eff}
ω_Q
M
θ
x,1
$2\omega_1$
x,2
c)
Re
I_m
a_{x1}
a_{x1}
a_{x2}
ψ
0
$+\omega_Q$
a_{x2}

XBL 766 8060

acting on the density matrix after cross polarization, equation (102) giving:

$$\sigma^*(t_M) = \beta_1 \frac{1}{2}\frac{\omega_1^2}{\omega_Q} [S_{X,3}(\cos\varepsilon \cos 2\varepsilon + \sin\varepsilon \sin 2\varepsilon \cos\omega_e t_M)$$

$$+ S_{X,1} (\sin 2\varepsilon \cos\varepsilon \cos\omega_e t_M - \sin\varepsilon \cos 2\varepsilon)$$

$$+ S_{X,2} (\sin 2\varepsilon \sin\omega_e t_M)] - \beta_1 \frac{1}{2}\frac{\omega_1^2}{\omega_Q} (S_{Y,3}-S_{Z,3}) \qquad (112)$$

This will give rise to a Fourier transformed signal which is shown in Figure 11. This indicates that both $a_{X,1}$ and $a_{X,2}$ can be detected, which will make the effects after the magic pulse look exactly like a magnetization precessing about an effective field at polar angle $-\varepsilon$. The maximum signal after an -X pulse will be only one-half of the total possible as in equation (103)

$$M_X = \frac{\beta_1}{2}\frac{\gamma_{eS}}{\gamma_{eS}} C_{eS\ 1S} \qquad (113)$$

4. Destruction Spectra

In an indirect cross polarization experiment, the destruction of proton order through cross polarization to deuterium is measured. The proton order is either the polarization in a spin locked state or the dipolar order for a demagnetized state in the rotating frame. Destruction spectra are an alternative to the method used in Chapter 1 for the determination of cross polarization dynamics. In Chapter 1 we determined the cross polarization time, T_{IS}, for a number of different r.f. field strengths and from that extracted correlation times. Here we show that correlation times may also be extracted by observing the destruction as a function of the deuterium offset frequency. The former has the

advantages of being more accurate and more direct while the destruction method is faster and more sensitive.

To derive the destruction of the proton order after a cross polarization time t with deuterium field strength ω_{1S} and frequency offset $\delta\omega$, we take the following form

$$\Delta I(t) = -\Delta I(\infty)(e^{-t/T_{IS}} - 1) \tag{114}$$

where ΔI is the destruction and $\Delta I(\infty)$ is the destruction after equilibrium has been reached between the two spin reservoirs. We neglect spin-lattice relaxation at this point, its effects will be discussed below. The limiting destruction is easily calculated from conservation of energy to be

$$\Delta I(\infty) = -\beta_I \; C_I \; H_{1,I} \; \left(\frac{\varepsilon\eta^2}{1+\varepsilon\eta^2}\right) \tag{115a}$$

where β_I is the initial spin temperature of the appropriate proton state, SL or ADRF, C_I and C_{eS} are the Curie constants for the protons and deuteriums respectively, given in equations (89). We note that equation (88a) gives:

$$\varepsilon = \frac{2}{3}\,\frac{N_S}{N_1}, \qquad \eta = \frac{\omega_{eS}}{\omega_{1I}} \tag{115b}$$

Here again $\varepsilon\eta^2$ is the ratio of the heat capacities, and

$$\omega_{eS} = \sqrt{\left(\frac{\omega_{1S}^2}{\omega_Q}\right)^2 + 4\delta\omega^2} \tag{115c}$$

The cross polarization time T_{IS} is given for the SL and ADRF case in equations (109) and (110) respectively. We must now assume functional forms for the spectral densities. Chapter 1 has shown that a Lorentzian correlation function, giving an exponential spectral density is quite reasonable for the ADRF case. Demco, Tegenfeld and Waugh[24] corroborate this and also show that for the SL case a Gaussian correlation function, giving a Gaussian spectral density are also very reasonable. Then for the ADRF experiment

$$C(\tau) = (1+\tau^2/\tau_c^2)^{-1}$$

giving for the spectral density

$$J(\omega) = \frac{\pi}{2}\,\tau_c\, e^{-\omega\tau_c} \tag{116}$$

and for SL the correlation function is

$$C(\tau) = e^{-\tau^2/\tau_c^2}$$

giving for the spectral density

$$J(\omega) = \frac{\sqrt{\pi}}{2}\,\tau_c\, e^{-\omega^2\,\tau_c^2/4} \tag{117}$$

giving finally

$$\Delta I(t) = \beta_I\, C_I\, H_{1I}\, \left(\frac{\varepsilon\eta^2}{1+\varepsilon\eta^2}\right)[\exp(-tM_{2,SI}\,\mu\,\frac{\pi}{2}\,\tau_c\,\exp(-\omega_{eS})\tau_c))-1] \tag{118}$$

for ADRF, and for SL

$$\Delta I(t) = \beta_I\, C_I\, H_{1I}\, \left(\frac{\varepsilon\eta^2}{1+\varepsilon\eta^2}\right)[\exp(-tM_{2,SI}\,\frac{M\sqrt{\pi}}{4}\,\tau_c\,\exp(-(\omega_{eS}-\omega_{1I})^2\,\frac{\tau_c^2}{4}))-1] \tag{119}$$

where

$$M = \cos^2 \frac{\theta_X}{2}$$

Note that we can in principle from one experiment (i.e., only one deuterium field strength) determine all of the necessary parameters, τ_c, $M_{2,IS}$ and γ_{eS} needed to describe the cross polarization process. We cannot, however, determine the actual shape of the spectral density function other than by trial and error, whereas the methods in Chapter 1 give the exact shape of the spectral density.

V. Chemical Shielding Tensors

The chemical shielding tensor is a second rank tensor which transforms under a rotation from X,Y,Z to X',Y',Z' as

$$\sigma_{ik} = \sum_{j,\ell} r_{ij}\, r_{k\ell}\, \sigma_{j\ell} \tag{120}$$

for the tensor in cartesian form and the r_{ij} are the direction cosines between the i unprimed axis and the j primed axis. We only observe the projection of σ along the external field direction which we call Z. The Hamiltonian is then:

$$H = H_0(1-\sigma_{ZZ})I_Z \tag{121}$$

Alternatively we can write the tensor in spherical form giving,

$$F_{00} = \frac{1}{\sqrt{3}}(\sigma_{11}+\sigma_{22}+\sigma_{33})$$

$$F_{1M} = 0$$

$$F_{22} = F_{2-2} = \frac{1}{2}(\sigma_{11}-\sigma_{22})$$

$$F_{21} = F_{2-1} = 0$$

$$F_{20} = \frac{1}{\sqrt{6}}(2\sigma_{33} - (\sigma_{11}+\sigma_{22})) \tag{122}$$

where σ_{ii} are the principal values of $\underset{\approx}{\sigma}$. The tensor then transforms as:

$$F'_{\ell\mu} = \sum_{m} D^{\ell}_{m\mu}(\Omega)\, F_{\ell m} \tag{123}$$

where the D's are the Wigner rotation matrices, and Ω is the set of Euler angles describing the X,Y,Z to X',Y',Z' axis rotation. The Hamiltonian can then be written:

$$H = \underset{\sim}{H} \cdot \underset{\approx}{\sigma} \cdot \underset{\sim}{I} = \sum_{\ell=0}^{2} \sum_{\mu=-\ell}^{\ell} (-)^{\mu} F_{\ell\mu} T_{\ell-\mu} \tag{124}$$

where the spin spherical tensors are defined as:

$$T_{00} = \frac{1}{\sqrt{3}} H I_Z$$

$$T_{22} = T_{2-2} = 0$$

$$T_{2\pm1} = \frac{1}{\sqrt{2}} H I_{\pm}$$

$$T_{20} = \sqrt{\frac{2}{3}} H I_Z \tag{125}$$

combining equation (125) and (124) and taking the form of the Wigner rotation matrices gives the result[37]

$$\sigma_{ZZ} = \sigma_i + \frac{2}{3} \Delta\sigma \left(\frac{3}{2} \cos^2\theta - \frac{1}{2}\right) + \frac{\eta}{2} \cos^2\phi \sin^2\theta \tag{126}$$

where

$$\Delta\sigma = \sigma_{33} - (\sigma_{11} + \sigma_{22}) \text{ and } \eta = \sigma_{11} - \sigma_{22} \tag{127}$$

Using equation (126) we can easily show that σ_{ZZ} transforms as $P_2(\cos\theta) = (\frac{3}{2} \cos^2\theta - \frac{1}{2})$ during a rotation of the crystal only if we rotate about one of the principal axis. This will be quite useful later on. In equation (126) we set $\phi = 0$ and θ equal to the rotation angle. This change of coordinates then corresponds to a rotation of the tensor about the σ_{22}

principal axis. This gives

$$\sigma_{ZZ} = \sigma_i' + \frac{2}{3}\Delta\sigma' \left(\frac{\theta}{2}\cos^2\theta - 1\right)$$

where the prime indicates

$$\sigma_i' = \frac{(\sigma_{33}+2\sigma_{11})}{3}, \quad \Delta\sigma' = (\sigma_{33}-\sigma_{11}) \tag{128}$$

To find the general rotation dependence we first transform the tensor from the molecular frame (with axes 1,2,3) to a set of crystal fixed axes (N,P,S) using equation (126) or its equivalent cartesian form (120). We then apply a second rotation about one of the crystal axes, the **axis** to find the tensor in the laboratory frame (Y,Z). The Z projection of the tensor is

$$\sigma_{ZZ} = \sigma_{PP}\sin^2\theta + \sigma_{NN}\cos^2\theta - 2\sigma_{NP}\sin\theta\cos\theta \tag{129}$$

where θ is the angle of the N axis relative to the Z laboratory axis, and the σ_{ij}, i,j=N,P,S are the elements of the tensor in the crystal frame,

$$\sigma_{NN} = r_{N1}^2\,\sigma_{11} + r_{N2}^2\,\sigma_{22} + r_{N3}^2\,\sigma_{33} + 2r_{N1}r_{N2}\,\sigma_{12} + 2r_{N1}r_{NS}\,\sigma_{13} + 2r_{N2}r_{N3}\,\sigma_{23}$$

$$\sigma_{PP} = r_{P1}^2\,\sigma_{11} + r_{P2}^2\,\sigma_{22} + r_{P3}^2\,\sigma_{33} + 2r_{P1}r_{P2}\,\sigma_{12} + 2r_{P1}r_{P3}\,\sigma_{13} + 2r_{P2}r_{P3}\,\sigma_{23}$$

$$\sigma_{NP} = r_{N1}r_{P1}\,\sigma_{11} + r_{N2}r_{P2}\,\sigma_{22} + r_{N3}r_{P3}\,\sigma_{33} + (r_{N1}r_{P2} + r_{P2}r_{N2})\sigma_{12} + (r_{N1}r_{P3} + r_{P1}r_{N3})\sigma_{13} + (r_{N2}r_{P3} + r_{P2}r_{N3})\sigma_{23} \tag{130}$$

If rotations about three crystal axes N,P,S are performed we obtain the full tensor in the crystal frame. This may be diagonalized to give the chemical shielding tensor in the molecular frame, thus completing the determination.

In the present case only one such rotation was performed, but we will find that it obeys equation (128), that is $\sigma_{NP} \approx 0$ in equation (129). We will then know only two of the principal elements(σ_3, σ_1) but we can also determine the complete orientation of the tensor.

VI. Experimental

A. Double Quantum Spectroscopy

1. Sample

The sample chosen was oxalic acid dihydrate. The short deuterium relaxation time, less than 1 sec., and large chemical shielding anisotropy of the carboxyl proton made it an ideal model material for this study. The short relaxation times are due to rapid flipping of the water molecules of hydration, about their C_2 axis. Commercial oxalic acid dihydrate (J. T. Baker and Sons) was dissolved in either 100% D_2O (99.8% D Biorad Laboratories) or 10% D_2O in H_2O and filtered then allowed to stand at room temperature to evaporate yielding large single crystals.

2. Double Quantum Pulse

A convenient orientation of the 100% deuterated oxalic acid dihydrate was chosen giving a quadrupolar splitting of 15.2 ± .1 kHz, where the splitting is taken from a satellite to zero frequency, i.e., $\frac{\omega_Q}{2\pi} = 15.2$ kHz. At this orientation of our crystal, the water lines are too broad to be observed due to exchange by 180° flips of the water molecules.[25] The chemical shift on the other hand, is expected to be completely averaged by this process. The spectrum is shown in Figure 12, on resonance, with the line width ≈ 82 ppm. Figure 13 shows the same orientation but 2000 ± 50 hz. In order to obtain the limiting linewidth another orientation was chosen, for which the satellites were well separated, see Figure 14. Note that the limiting linewidth is 54 ppm.

The strength of the first pulse was adjusted so that ω_{1S} satisfied the condition (54) with $\omega_1/\omega_Q \approx 1.9$. The length of the first pulse, P_1, was adjusted to be ≈ 270° pulse according to equation (50), to ensure that P_1

Figure 12. Deuterium spectrum of 100% deuterated -α-oxalic acid dihydrate (single crystal). The rf irradiation is near resonance. The spectrum is taken at 13 ± 3°C. The spectrum is "folded over" (see Figure 3) and only a small portion of the frequency axis is shown, i.e., 10 to 20 kHz, the spectrum center is at 0 kHz and the satellites are at ± 15.2 kHz.

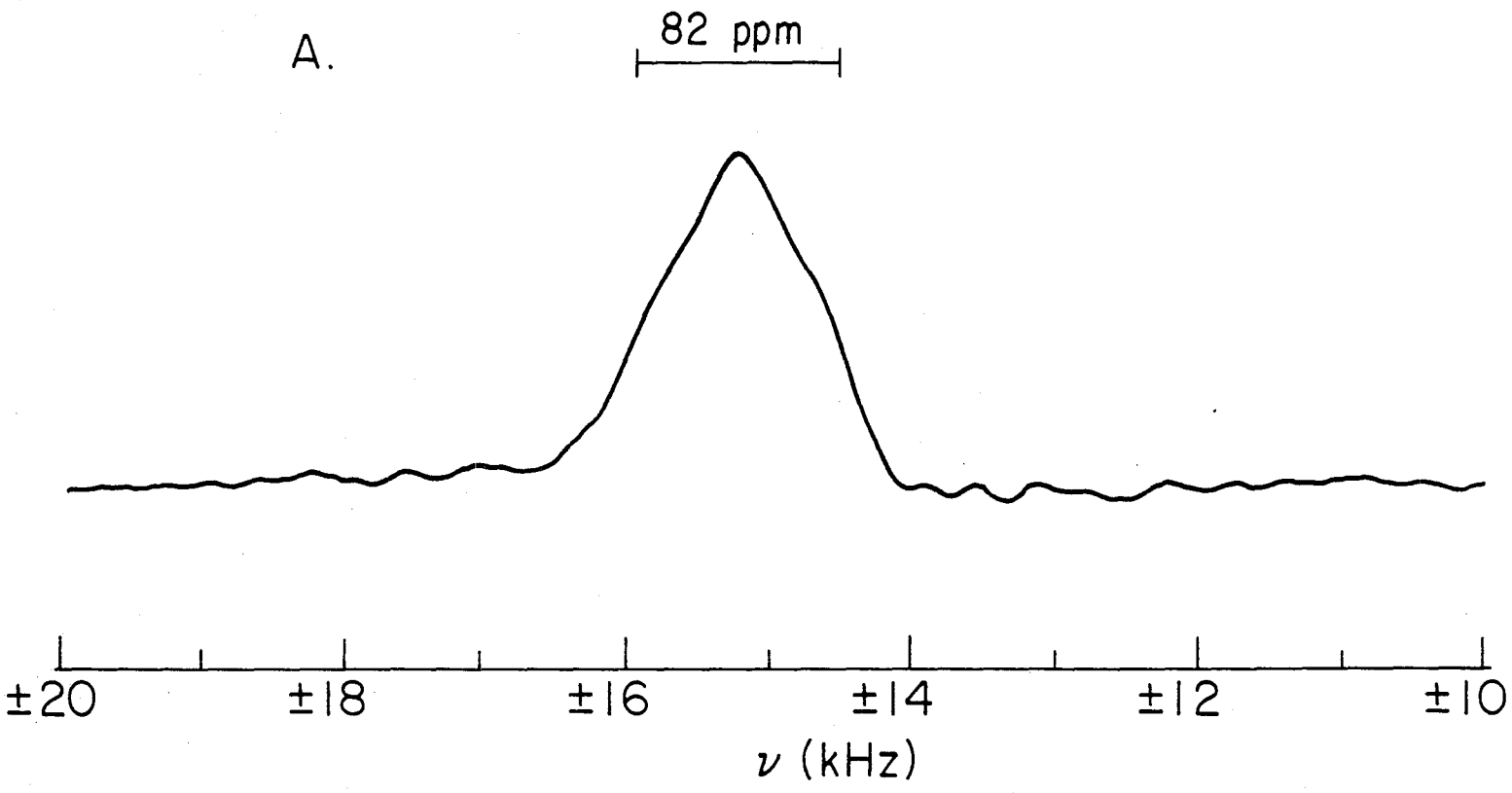

XBL 763-671

Figure 13. Deuterium spectrum of 100% deuterated -α-oxalic acid dihydrate (single crystal). The rf irradiation is off resonance with a frequency offset of 2.0 kHz, with other conditions the same as Figure 12. The structure on each of the satellites indicates that the spectra is from 2 inequivalent deuterons with slightly different quadrupole couplings. This spectrum is also "folded over", see Figure 12. Were there no fold over one of these peaks would appear at positive frequency and the other at negative frequency.

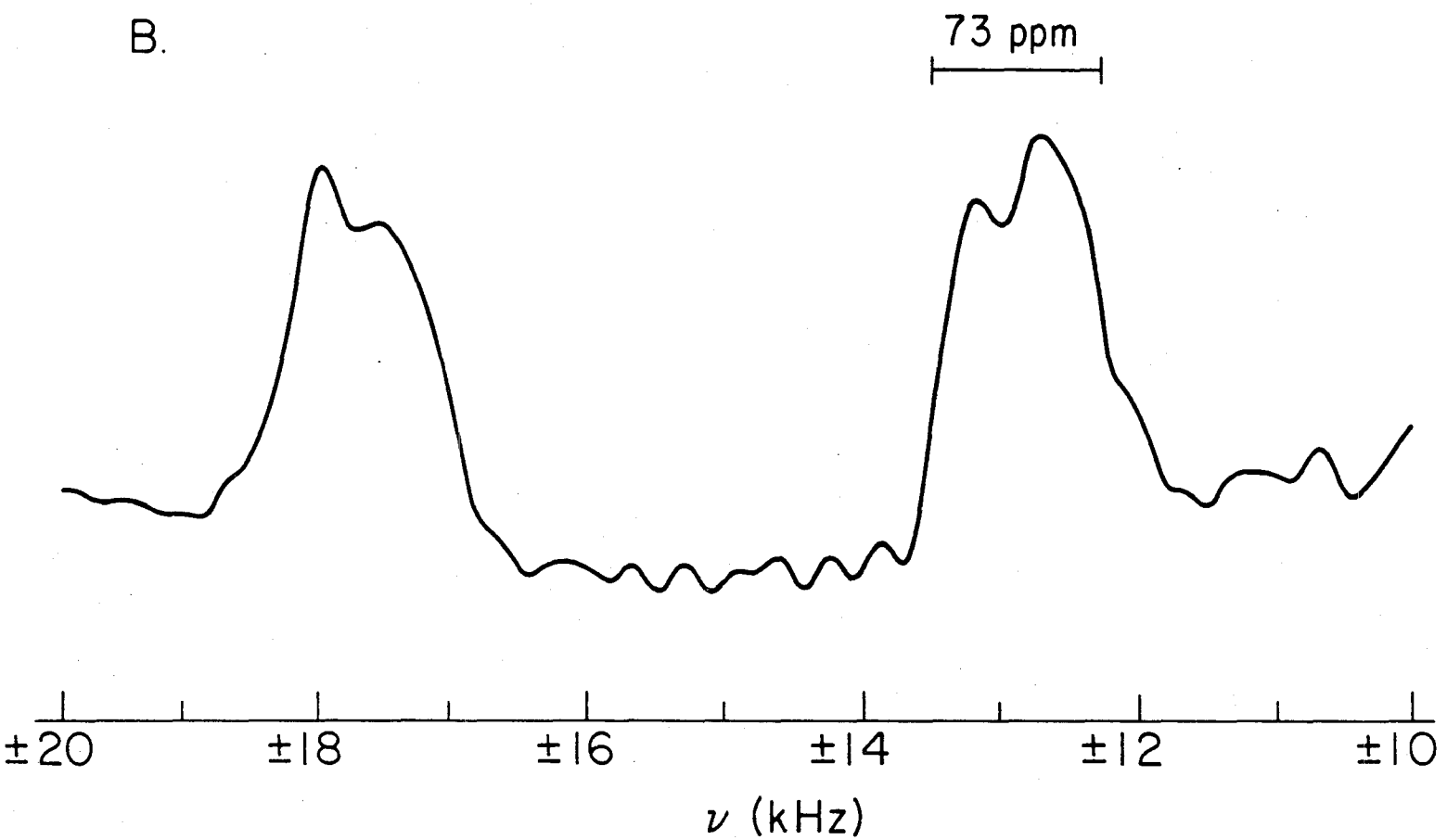

XBL 763-672

Figure 14. Deuterium spectrum of 100% deuterated α-oxalic acid dihydrate taken at a different orientation than that used in Figures 12 and 13, in order to show well resolved satellites. This was necessary to find the limiting line width of a single satellite.

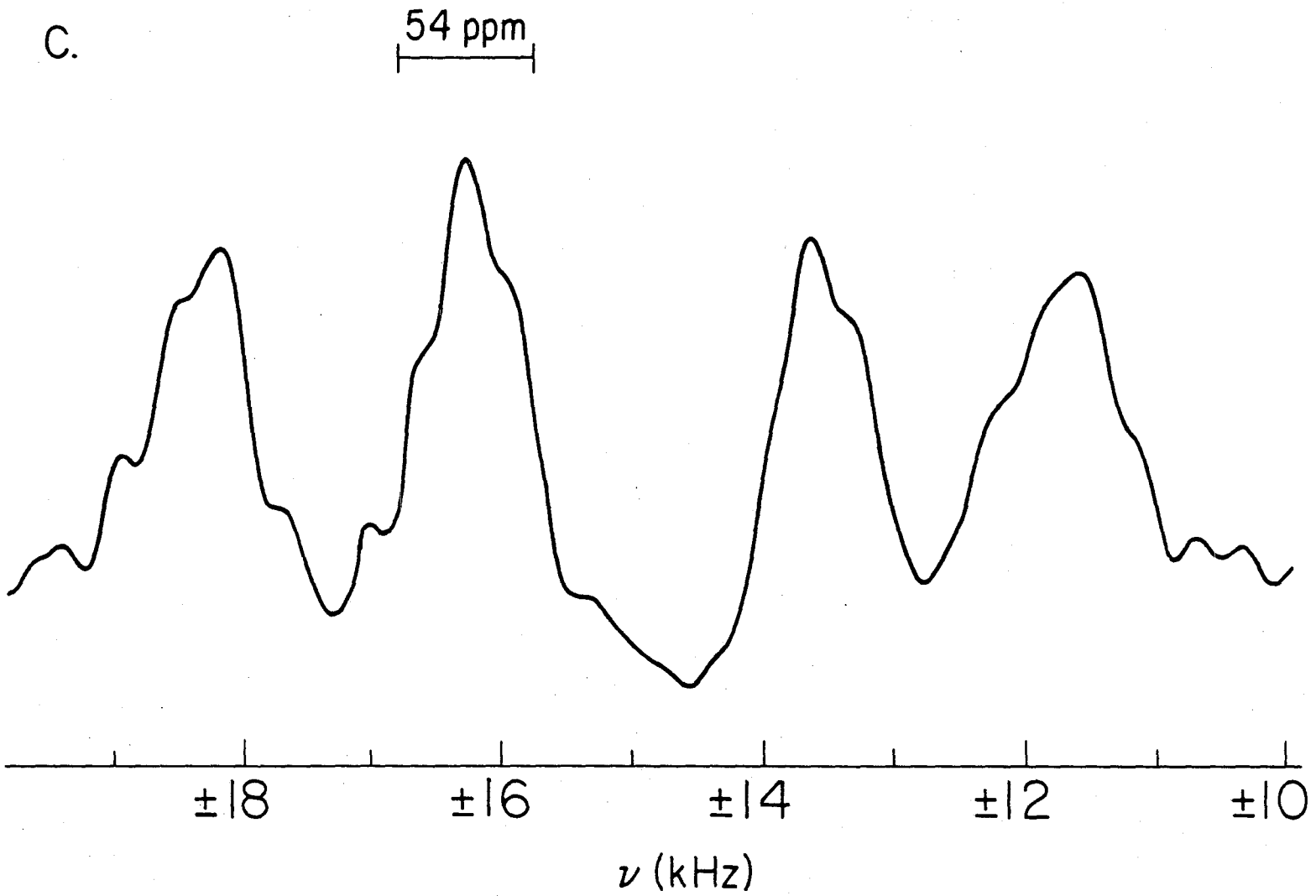

XBL 763-669

gave no signal. The phase detector was adjusted so that the FID after a

large pulse occured only in one channel, while on resonance, to align the phase detector $\bar{X}$ axis and the spin X axis. A rotary decay was then generated to check the prediction of equation (49). The rotary decay which measures the Z magnetization proportional to $a_{Z,1}$ and $a_{Z,2}$ was obtained simply by varying the length of the first pulse t_W with a fixed delay before P_2, t_1 - 5 msec, and fixed pulse length for P_2. The results are shown in Figure 15. The Fourier transform, Figure 16, shows two frequencies ν_Z and ν_Y, the difference of which should be the quadrupole splitting (see equations (49) and (50a)):

$$|\nu_Y| - \nu_Z = \nu_Q \tag{131}$$

Experimentally, ν_{1S} = 26.8 kHz and ν_Q = 15.2 kHz giving ν_Z = 20.3 kHz The peak positions in Figure 16 are 36.5 ± .5 kHz and 20.7 ± .5 Khz and 36.5 - 20.7 = 15.0 kHz. The agreement is quite satisfactory.

3. Double Quantum Decay

To obtain the double quantum decay the first pulse is set so that no signal is obtained. It is necessary to ensure that the phase of the double quantum FID after P_2 is 90° out of phase with the normal FID. Since with an X pulse the normal FID will be $\alpha\ S_{Y,1}$ while the D.Q.FID will be $\alpha\ S_{Y,2}$. This was done by Fourier transforming the FID's after the probe pulse, P_2, with and without P_1 with $t_1 = 0$. The length of the probe pulse was chosen to be approximately a 45° pulse for a liquid sample, that is

$$\sin \omega_1 \tau_P = \frac{1}{\sqrt{2}} \tag{132}$$

Figure 15. Rotary decay obtained with the two pulse sequence, Figure 8, for 100% deuterated oxalic acid dihydrate. The length of P_1 is varied, t_W with fixed delay between P_1 and P_2, t_1 = 5 msec, and fixed probing pulse length. The field strength of P_1 was ν_{1S} = 26.8 kHz and ν_Q = 15.2 kHz. The two frequencies come from the ω_Z and ω_Y terms in equation (49).

Rotary Decay

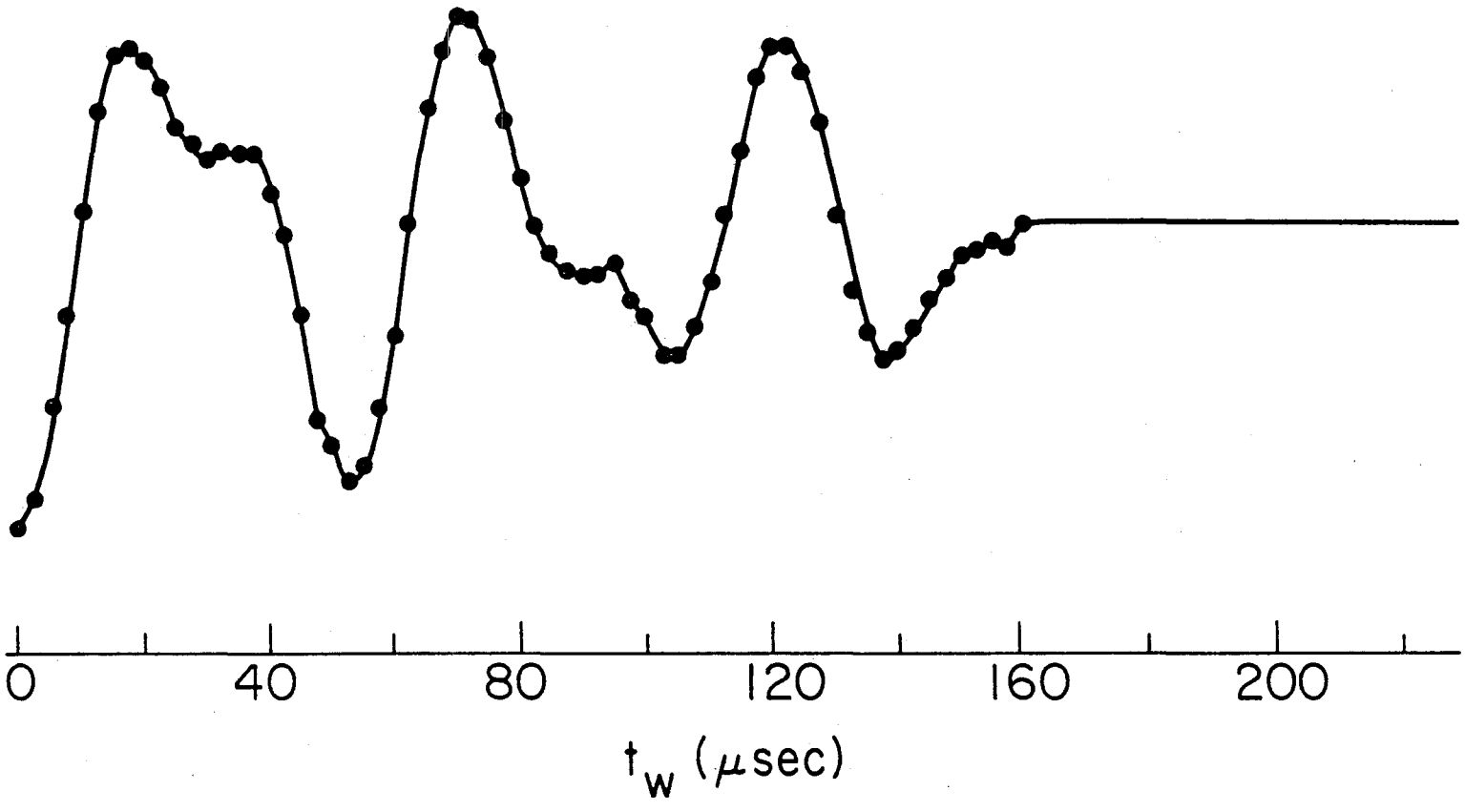

XBL 763-665

Figure 16. Fourier transform of the Rotary Decay (Figure 15). The frequencies are 20.7 ± .5 kHz and 36.5 ± .5 kHz, giving a difference of 15.8 kHz, where the peak at 36.5 corresponds to the frequency ν_Y and the peak at 20.7 kHz to ν_Z, see equations (48) and (49). The theoretical ν_Z taking ν_{1S} (see Figure 15) = 26.8 is

$$\nu_Z = \frac{1}{2} (\nu_Q{}^2 + (2\omega_1)^2 - \omega_Q) = 20.3 \text{ kHz}$$

in addition

$$\nu_Y - \nu_Z = \nu_Q = 15.2$$

The experimental numbers from the Fourier transform, ν_Z = 20.7 and ν_Q = 15.8 kHz are in quite good agreement with the theoretical predictions.

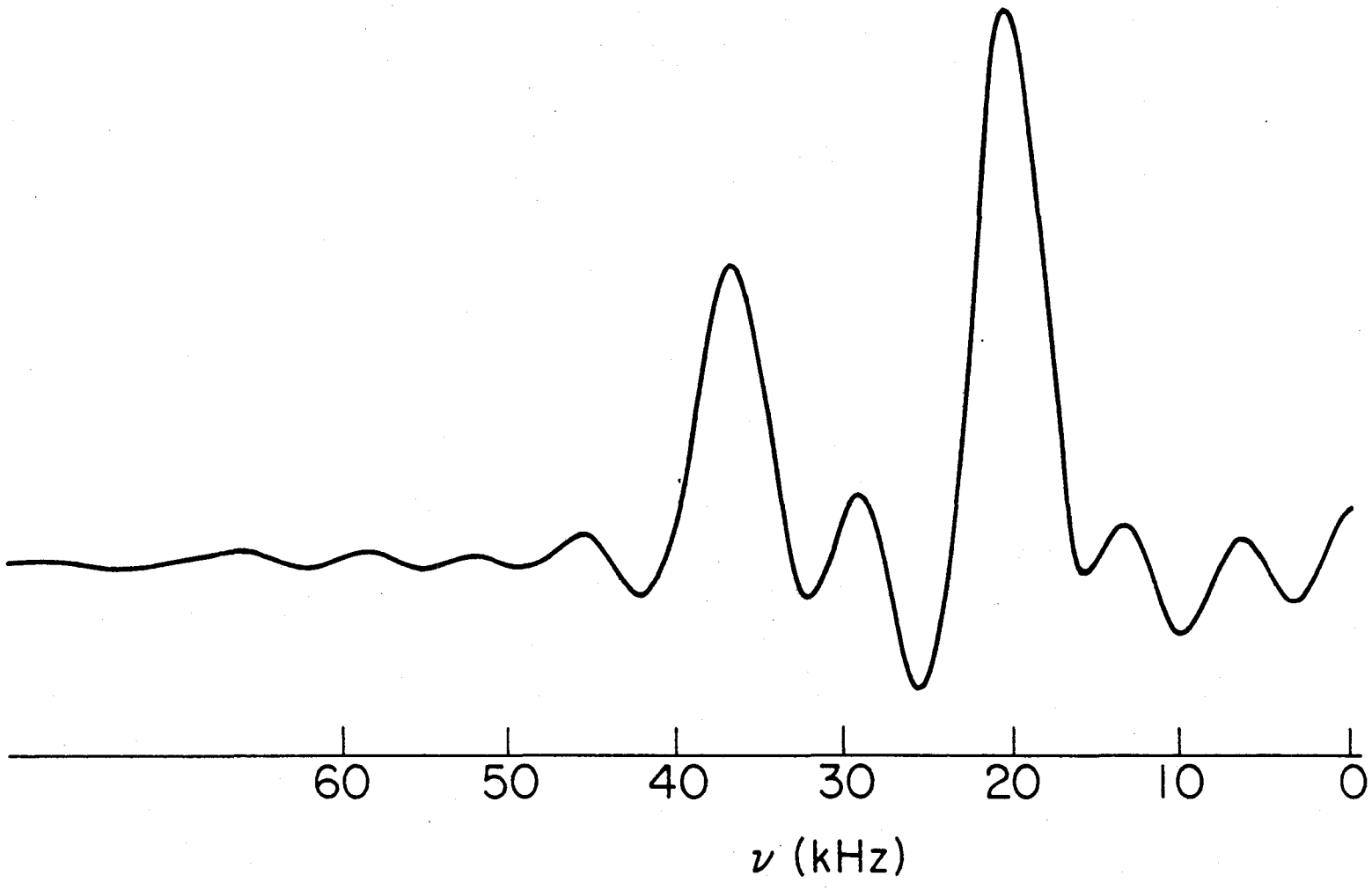

XBL 763-667

If $\omega_1 >> \omega_Q$ then from equation (25):

$$\omega_e \cong 2\omega_1 \tag{133}$$

and from equation (60),

$$a_{Y,2} \cong \cos 2\delta\omega t_1 \times 1$$

$$a_{X,2} \cong \sin 2\delta\omega t_1 \times 0 \tag{134}$$

giving the maximum signal for the term we wish to detect. The double quantum decay is obtained by varying t_1, Fourier transforming the resulting FID for each delay and plotting the resulting peak heights verses delay time, giving the double quantum FID (D.Q.FID). This is again transformed giving the double quantum spectrum. It is noticed however that there always persists a signal even for long t_1. This comes from a misadjustment in the length of P_1, by adding the constant term in $S_{Z,1}$ to the density matrix (see Section IIIE.2). It may be canceled out by adjusting the phase to the angle determined from a normal FID and then observing the double quantum signal 90° out of phase with it in the Fourier transform.

The double quantum FID's determined in this way for 100% deuterated oxalic acid dihydrate are shown in Figures 17 and 18 for offset frequencies 0 ± 50 hz and 2000 ± 50 hz, respectively. The Fourier transforms are shown in Figure (19). The on-resonance FID, (a), is seen to be actually slightly off-resonance, which is the reason for the larger linewidth between Figures 12 and 13. The shift between (a) and (b) should be $2\Delta\omega \approx 4$ kHz. Experimentally, they are 4.29 kHz apart.

Figure 17. Double Quantum FID obtained from the two pulse sequence (Figure 8) for 100% deuterated oxalic acid dihydrate. The irradiation frequency was near resonance corresponding to the deuterium spectrum in Figure 12. The deuterium field strength for the coherence pulse was ω_{1S} = 26.8 kHz giving $\omega_1/\omega_Q \approx 1.9$ and t_Z = 13.2 μsec, where t_Z is the theoretical 90° pulse for the double quantum transition, see equation (50). The pulse widths used were $P_1 \cong 36$ μsec (270° pulse) and $P_2 \cong$ 5 μsec (ω_{1S} = 50 kHz).

a. At Resonance

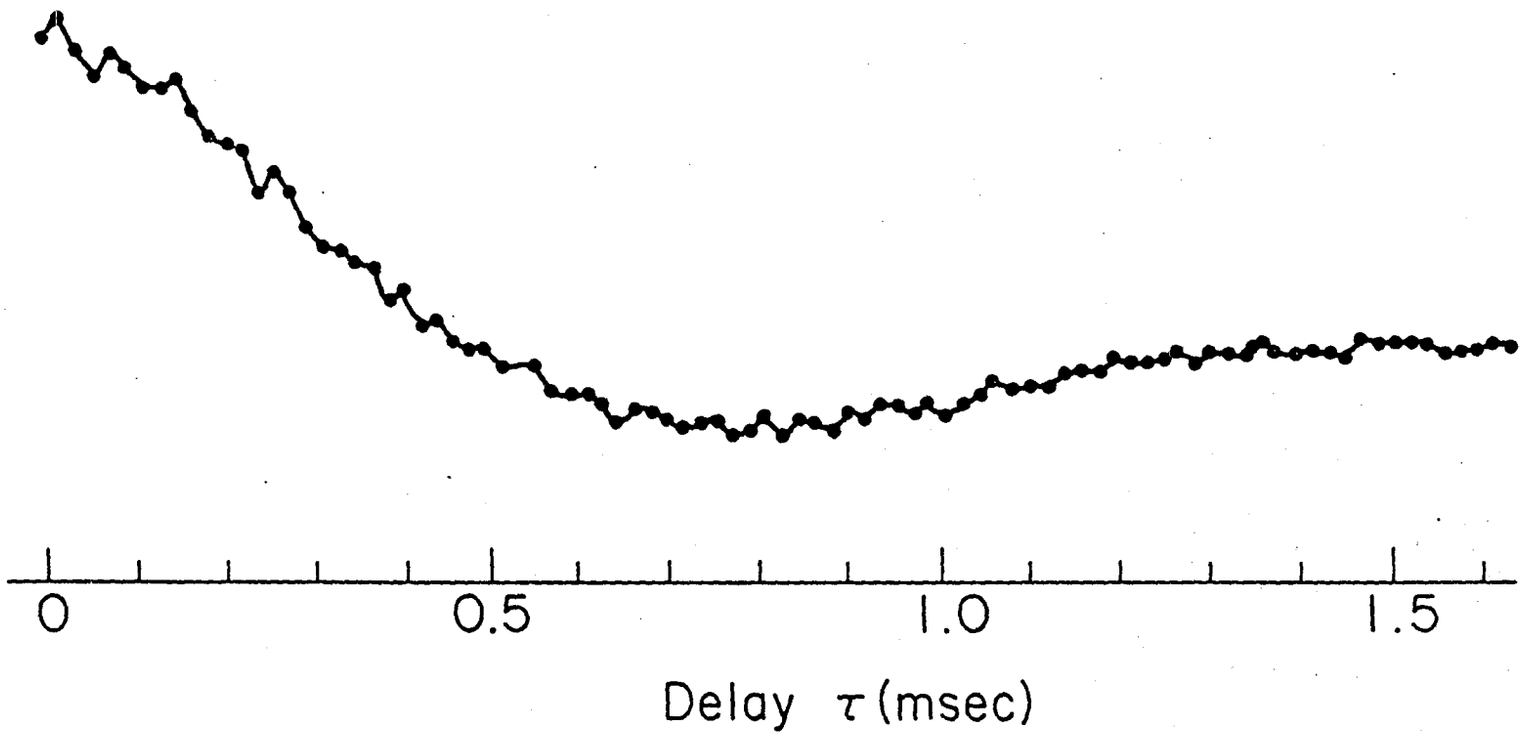

XBL 763-670

Figure 18. Double Quantum FID obtained from the two pulse sequence (Figure 8) for 100% deuterated oxalic acid dihydrate. The irradiation frequency was 2 kHz off resonance, corresponding to the deuterium spectrum in Figure 13. The deuterium field strength for the coherence pulse P_1 was ω_{1S} = 26.8 kHz giving $\omega_1/\omega_Q \approx 1.9$ and t_Z = 13.2 μsec, see Table 3 and Figure 16. The pulse widths used were $P_1 \cong 36$ μsec (270° pulse) and $P_2 \cong 5$ μsec (ω_{1S} = 50 kHz).

b. 2 kHz Off Resonance

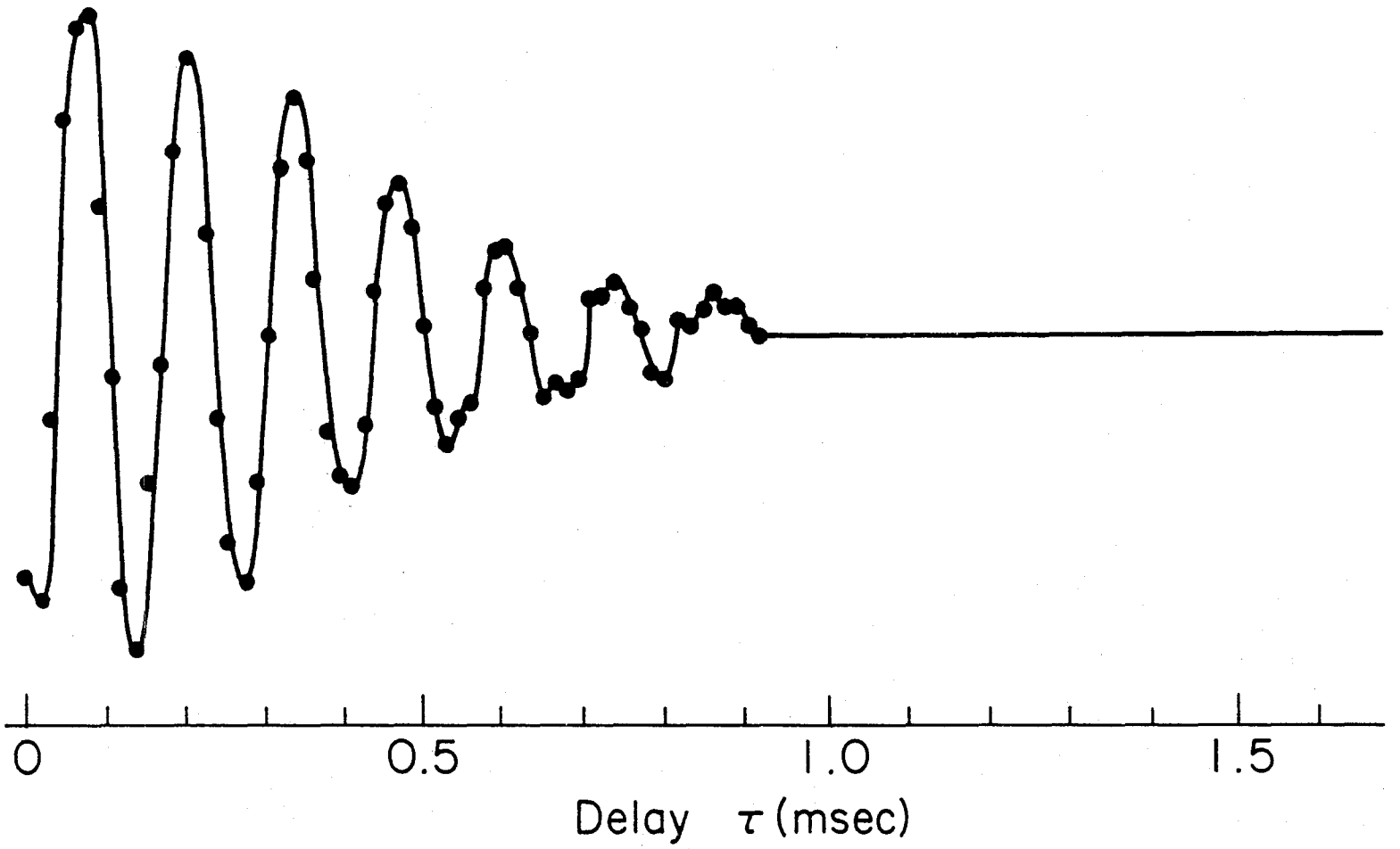

XBL 763-666

Figure 19. Fourier Transform Double Quantum Spectra of 100% oxalic acid dihydrate for the two offset frequencies given in Figure 17 (a) and 18 (b). The peak frequencies are a) 0.46 kHz and b) 4.75 kHz, for a difference of 4.29 kHz, the spacing should be 4.0 kHz.

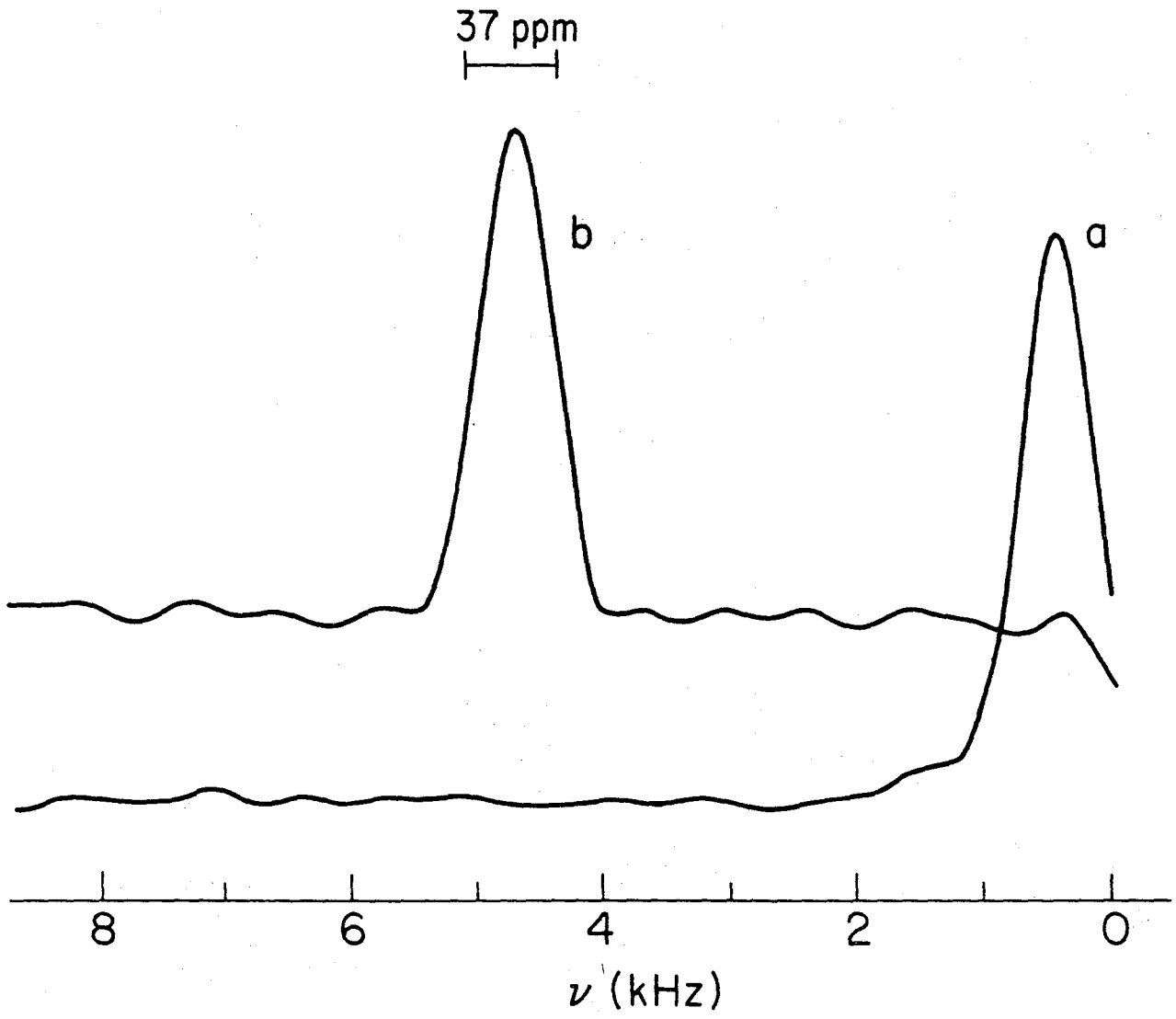

XBL 763-668

An alternative to choosing the phase of the observation channel as above and consistently correcting the phase of the Fourier transform was also attempted. We chose the Fourier transform phase which maximized the signal at each delay, t_1. The results of this treatment are shown in Figure 20. Note that this "best phase" result has been multiplied by 2. If the signal from the constant part of the density matrix is $a_{Y,1}$ and that from the double quantum $a_{Y,2}$ then the signal intensity is

$$I = a_{Y,1}^2 + a_{Y,2}^2$$

Fourier transforming the square of the double quantum decay obtained in this manner should then give the power spectrum of the double quantum transition.

The effect of the double quantum spectroscopy on the linewidths is shown by comparing Figure 19 to Figure 14. The limiting linewidth in Figure 14 is $\simeq$ 54 ppm for the quadrupolar satellites in the normal FID. The difference in linewidths is approximately 3. For the double quantum case, we would expect the relative linewidth to be identical between the two spectra, (see Section IIIE.1) if the broadening were dipolar. Then the factor of 3 is probably due to slight imperfections in the crystal giving rise to a distribution in quadrupolar frequencies.

We now summarize the phase adjustments necessary to create a double quantum spectrum.

1) Phase detector versus the spin axis-spectrometer phase adjustment. At resonance the deuterium FID, which is linearly polarized, will project onto the phase detector so that all of the deuterium FID occurs in one channel. This adjustment aligns the $\bar{X}$ axis of the phase detector with the X,1 axis of the spin system.

Figure 20. Double quantum FID under the same conditions as Figure 17, but derived from the "best phase" applied to the spectra from the first Fourier transformation, rather than the consistent phasing used to obtain Figure 17, see Section VI.3, equation (135). The FID has been scaled up by 2 in comparison with Figure 17.

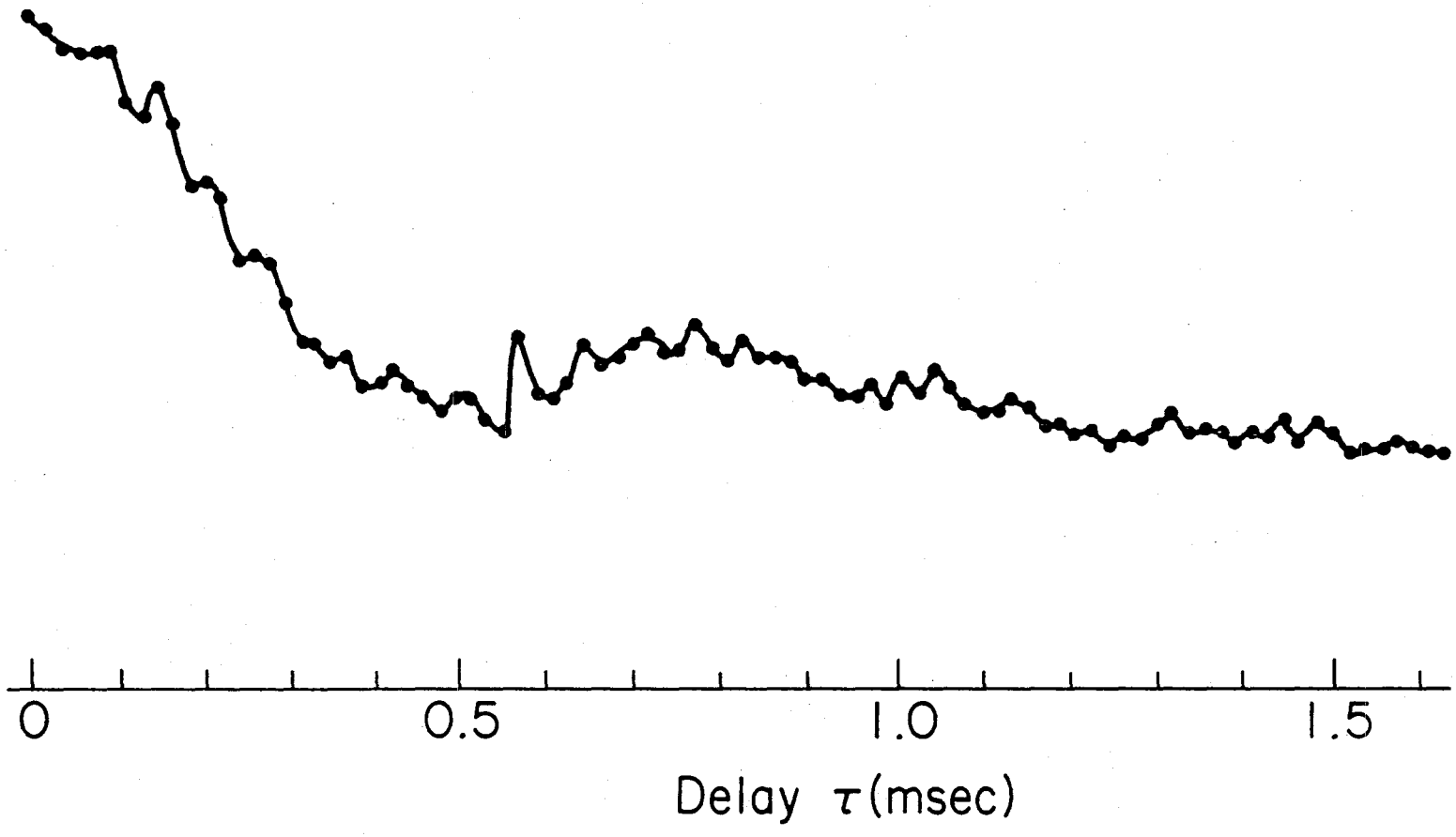

XBL 763-664

2) Double quantum coherence versus constant signal-Fourier transform phase. We wish to cancel out the constant signal and find the best Fourier transform phase to observe the double quantum coherence due to $a_{Y,2}$. The FID after P_2 without P_1 is transformed and phased so that it is purely absorptive in Imψ; this phase is then the reference with which all of the Fourier transforms from the two pulse sequence are phased. With this consistent phasing the term in $a_{Y,2}$ is always purely absorptive in Reψ.

3) Double quantum spectrum-Fourier transform phase. After the double quantum FID is synthesized another phase adjustment is necessary; this is shown by equation (72). The term from $a_{X,1}$ will add a dispersive part to the double quantum spectrum. A small phase adjustment to the Fourier transform is needed to correct for this.

B. High Resolution

1. Sample

These experiments were conducted on a sample of 10% deuterated oxalic acid dihydrate. The single crystal's morphology was well defined and was used to mount the crystal in a well defined orientation. There are two crystalline forms possible, α and β with space groups $P_{21/h}$ and $P_{21/a}$, respectively. There are two molecules per unit cell related by a C_2 axis, but not a center of inversion. Deuterons in the same molecule are related by a center of inversion. Chiba[25] has conducted deuterium magnetic resonance studies on the β form. His results are shown in Table 4.

Table 4. Deuterium Quadrupole parameters for perdeutero-β - oxalic acid dihydrate

species	temperature	eqQ/h(kHz)	η	q_{11}	q_{22}	q_{33} (kHz)
carboxyl		139.2 ± .8	.098 ± .005	-57.3	-47.1	104.4
water	-70°C	219.1 ± 2.	.016 ± .036	-91.7	-51.8	172.73
water	-70°C	230.3 ± 2.	.062 ± .006	-95.3	-69.0	164.3
water	67°C	121. ± 3.	.93 ± .02	-87.61	-45.4	90.8

The q values correspond to the elements of the EFG tensor in its principal axis system given as the frequencies that would actually be observed, calculated from equation (4). The powder spectrum of our sample is given in Figure 21. The peak positions are 48.8 ± .5 kHz and 39.4 ± .2 kHz with a small feature at ≈ 87 kHz. It is seen that our results do not agree with Chiba's. There are two possibilities for the line assignments

1) that our peak at 48.8 corresponds to Chiba's at 47.1 or

2) that our lower frequency peak corresponds to Chiba's peak at 47.1 kHz.

Possibility (2) might be expected if our samples were actually in the α modification. The difficulty with possibility (1) is that we cannot then assign the other peak at 39.4 kHz. It cannot be from the water since neither the low or the high temperature lines, as seen in Chiba's work, would appear there. On the other hand, if the peak at 48.8 corresponds to Chiba's high temperature water peak at 45.4 and the small feature at ≈ 87 corresponds to the shoulder expected at 87.61, we cannot understand why the carboxyl peak position is so low. Using data from Chiba's work (see Figure 5, reference 25) and Coppin's and Sabina's neutron diffraction study[26] we can roughly estimate the difference in the carboxyl eqQ/h

Figure 21. Deuterium powder spectrum of 10% deuterated α-oxalic acid dihydrate. The central peak with the dispersion lineshape is D_2O absorbed upon the surface of the crystal. The higher frequency satellite at 48.8 ± .5 kHz corresponds to the waters of hydration which are executing 180° jumps around their C_2 axis in the rapid exchange limit. The lower satellite, 39.4 ± .2 kHz, is due to the carboxyl deuterons. The temperature was 13 ± 3°C.

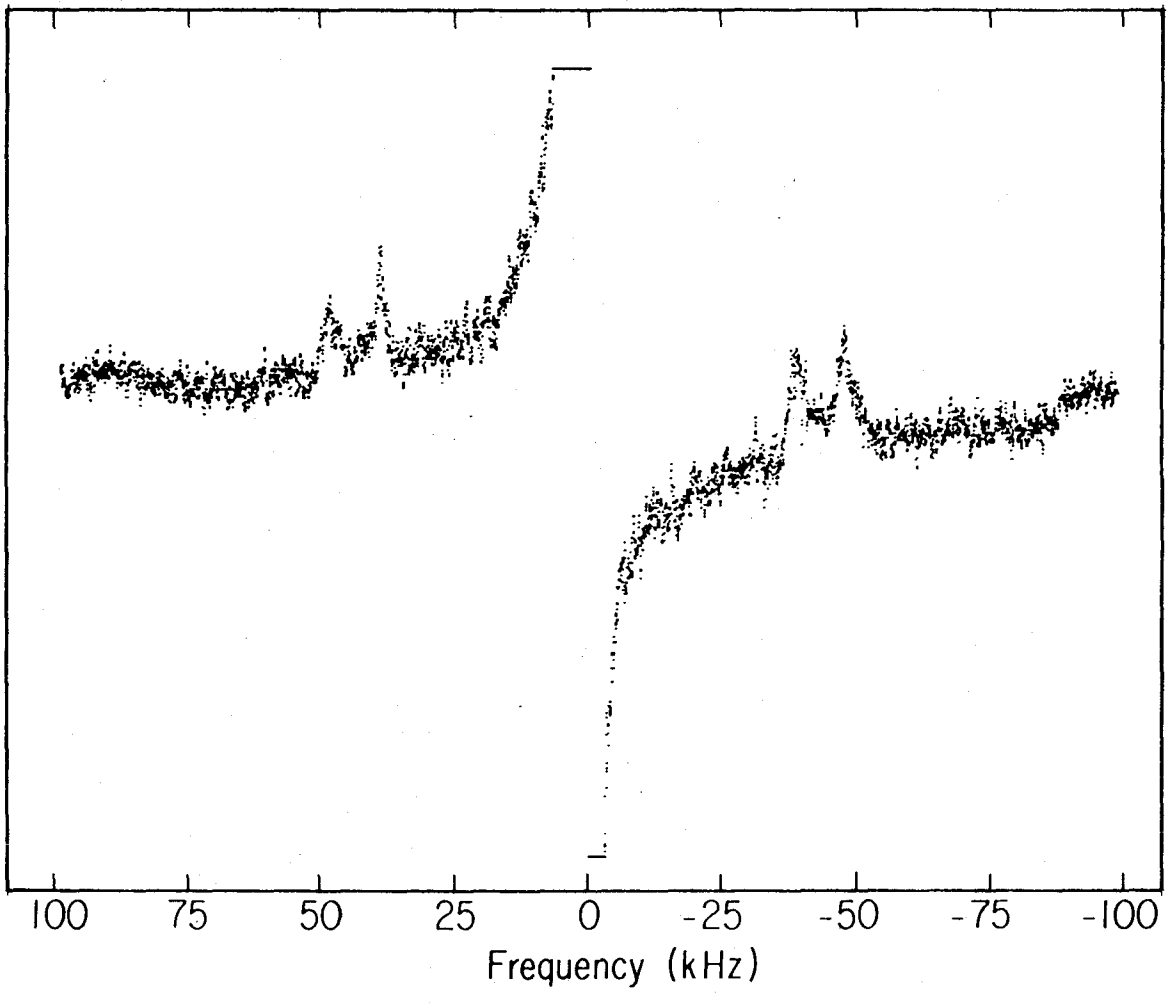

XBL 763-673

between the α and β forms. The oxygen-oxygen bond distance in the α form is 2.524 Å and in the β, 2.538 Å. Chiba's work describes a rough correlation between eqQ/h and this same distance, 42.5 kHz/Å, giving that eqQ/h for the α form should be ≈ 6 kHz less than the beta form. The difference between our line at 39.4 kHz and Chiba's carboxyl line is 7.6 kHz, our result being smaller. This all fits nicely with possiblity (2) and at the same time assigns our peak at 48.8 kHz to the waters. X-ray powder patterns of our samples were also taken by Dr. A. Zalkin and his colleagues at LBL and compared to a standard spectra of α-oxalic acid dihydrate.[28] All of the powder patterns are identical. As noted by Delaplane and Ibers[27] the lattice constants do not change much upon deuteration (≈ 0.5%), however the lattice constants differ significantly between the α and β forms. <u>These observations also support our conclusion that our crystals are in the α modification.</u> The bond distances for the deuterated α modification[26] are shown in Figure 22. The hydrogen bond is very short in this hydrated crystal.

There have been two previous studies on the shift tensors in oxalic acid dihydrate, one in a single crystal[34] and one in a powder.[35] These were of the multiple pulse type and as a consequence lacking in resolution, both because of the technique and also the overlap of the water lines with the carboxyl lines. These studies will serve as good comparisons to illustrate the advantages of our double quantum technique.

2. Quadrupole Satellite Spectroscopy

The deuterium spectrum of the single crystal, with simultaneous proton decoupling ($\frac{\omega_{1I}}{2\pi}$ = 30-35 kHz) is shown in Figure 23 for two orientations. The sharp lines arise from the carboxyl deuterons and the broad lines are from the water deuterons. The line near 0 kHz is due to

Figure 22. Bond lengths and angles of perdeutero-α-oxalic acid (from Coppens and Sabine, reference 26.)

Perdeutero-α-oxalic Acid Dihydrate

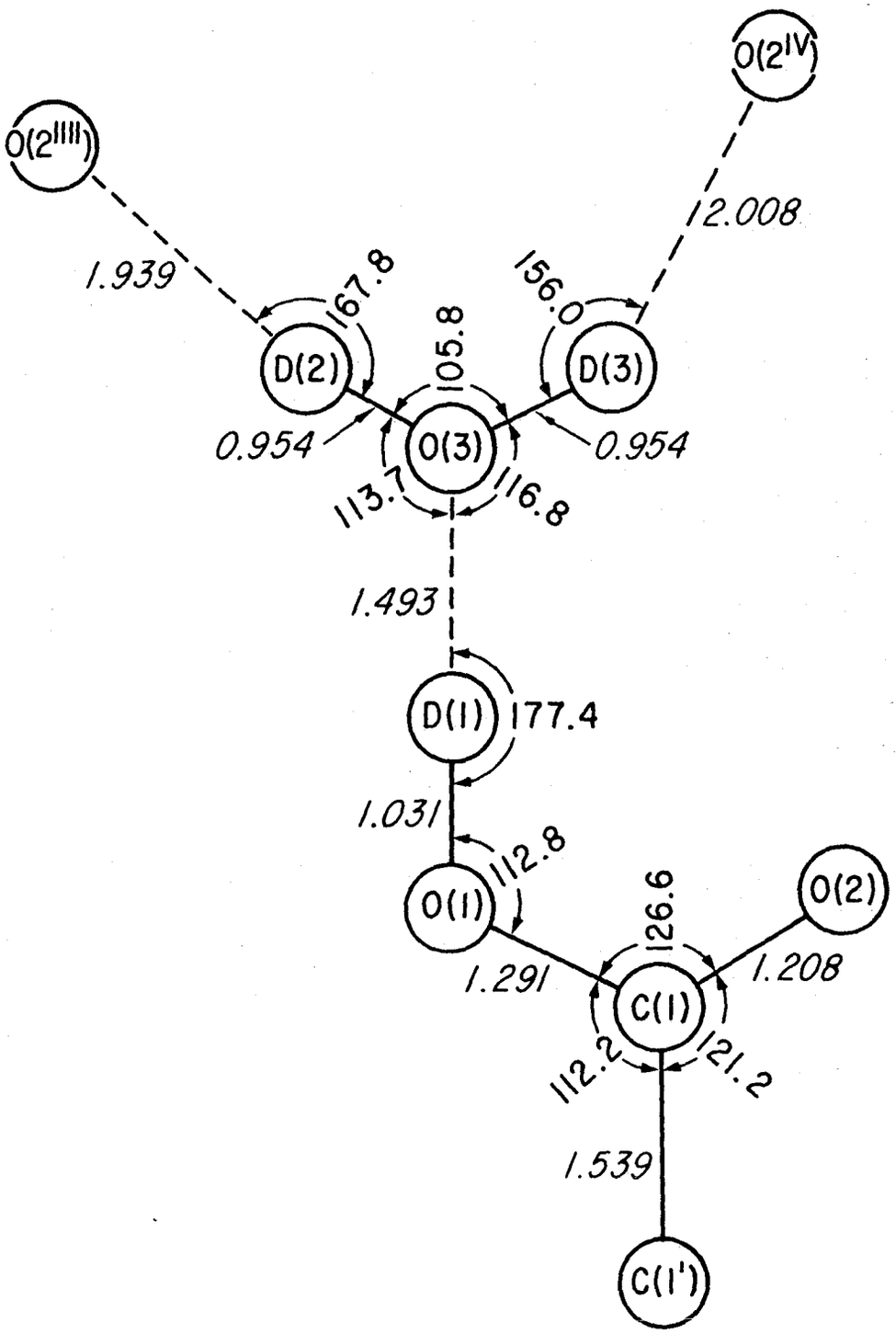

XBL 766 8061

Figure 23. Deuterium spectrum of 10% deuterated α-oxalic acid dihydrate for the orientations used in the high resolution double quantum experiments, Figures 26 and 29. The frequency offsets are 522.5 Hz for 57° and 576.2 Hz for 180°. The spectra were obtained while decoupling protons. The temperature was 13 ± 3°C.

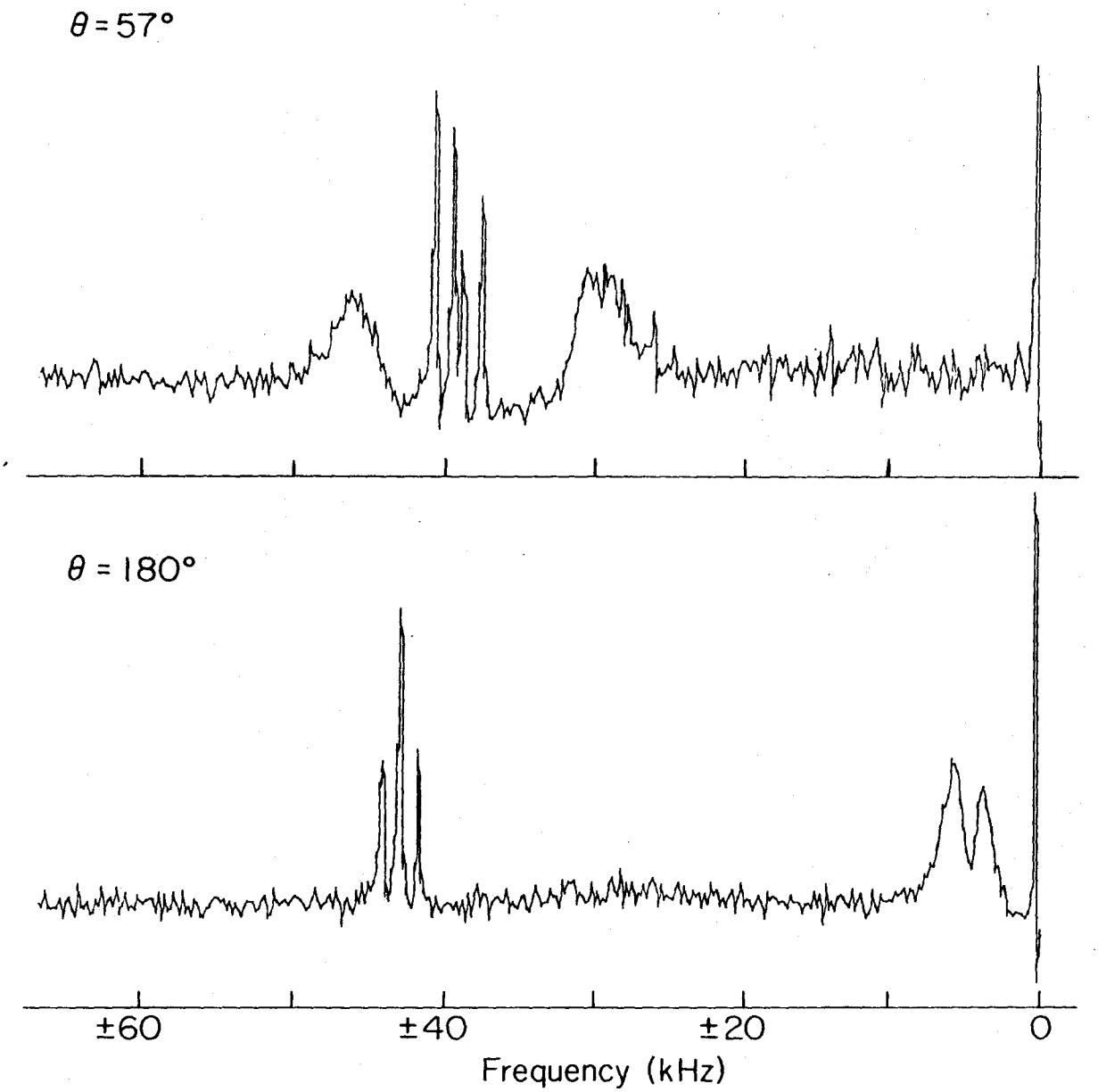

XBL 763-674

small amounts of absorbed isotropic water on the crystal and was used as the reference. The broadening of the water lines is caused by incomplete exchange narrowing as the water molecules flip about their C_2 axes[25] at room temperature.

The quadrupole rotation plot was obtained by averaging the positions of the carboxyl lines at each orientation. The result is shown in Figure 24. The solid line is the least squares fit to (equation 128)

$$\Delta\nu = \Delta\ P_2(\cos\theta) + X \qquad (128')$$

where

$$P_2(\cos\theta) = \frac{1}{2}\ (3\ \cos^2\theta - 1)$$

and Δ is the anisotropy of the EFG tensor and X is its isotropic value, $\frac{1}{3}(q_{11} + q_{22} + q_{33})$, which should be zero. The fitted parameters are $\Delta = -77.54$ kHz and $X = 0.068$ kHz. We can now ascertain the approximate orientation of the crystal. The powder spectrum before showed that $q_{22} = 39.45$ kHz, and q_{22} from the parameters Δ and X is 38.7 kHz or a factor of 1.02 smaller. The crystal is therefore very nearly aligned with one of its principle axis along the axis of rotation. If we assume that the EFG tensor is axial, as might be expected (see Table 4) we now know the complete tensor and its orientation. The fact that the rotation plot is well fit with $P_2(\cos\theta)$ also indicates that the alignment is excellent. The crystal gives four carboxyl lines, two lines for each of the two inequivalent deuterium sites, where the splitting is twice the offset and chemical shift (see equation (8)). The two inequivalent deuterium sites give the same chemical shift rotation plot, when extracted from the satellite splittings. The experiment was conducted with an offset

Figure 24. Quadrupole rotation plot for 10% oxalic acid. The data were obtained by averaging the carboxyl peak positions at each orientation, two of the orientations are shown in Figure 23. The least mean squares fit to $P_2(\cos\theta)$ is given as the solid line, giving the anisotropy, D = -77.54 kHz and the isotropic shift X = 0.068. The actual carboxyl peak positions vary in distance on either side of this average. This variance is due to the chemical shift, and is plotted in Figure 25.

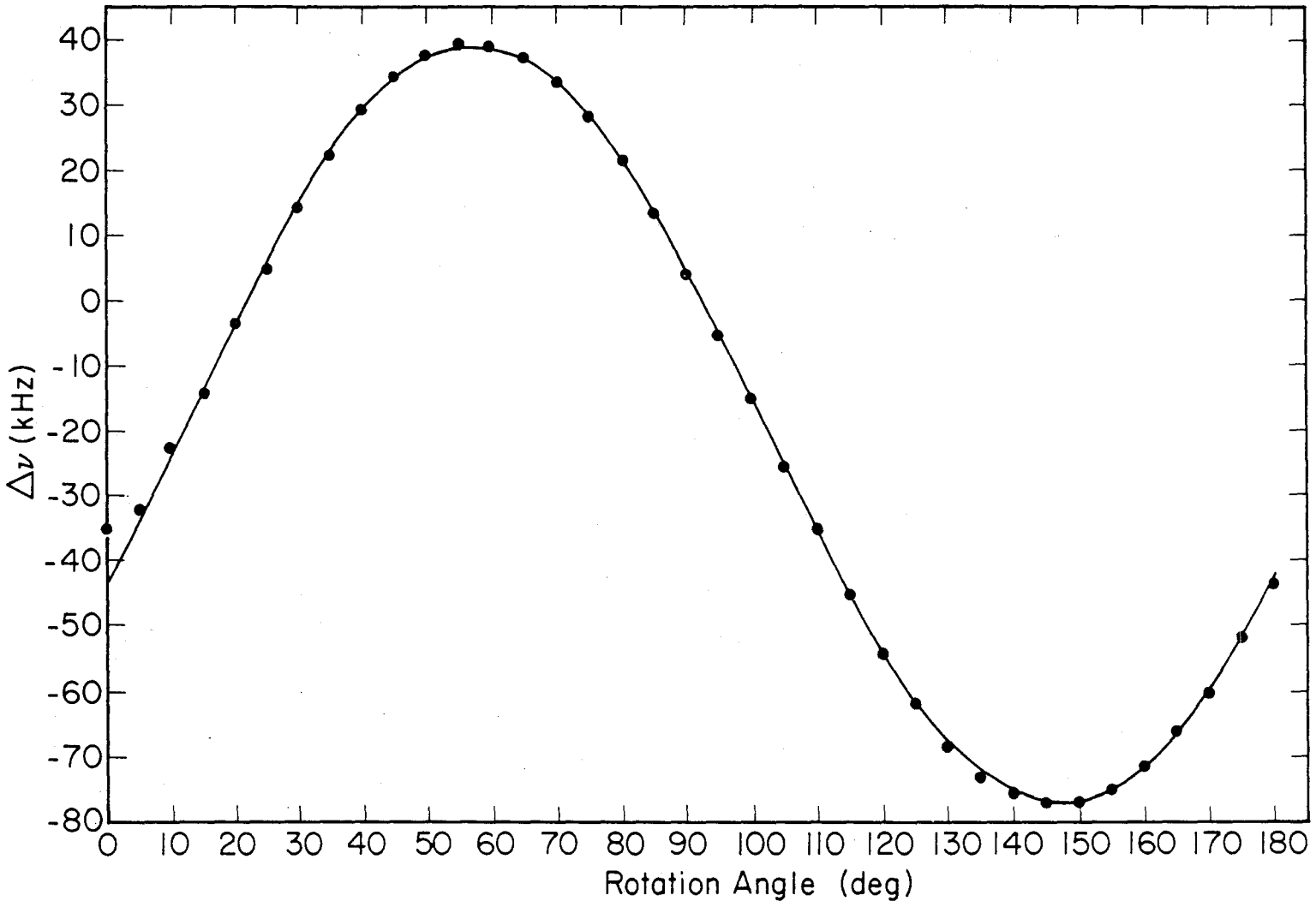
40
30
20
10
0
-10
-20
-30
-40
-50
-60
-70
-80
Δν (kHz)
0 10 20 30 40 50 60 70 80 90 100 110 120 130 140 150 160 170 180
Rotation Angle (deg)

XBL 763-678

frequency of 546.87 Hz below resonance and on resonance. The off resonance rotation plot is shown in Figure 25. The solid line is least squares fit to equation (129):

$$\sigma_{ZZ} = \sigma_{PP} \sin^2\alpha + \sigma_{NN} \cos^2\alpha - 2\sigma_{NP} \sin\alpha \cos\alpha \qquad (129)$$

giving $\sigma_{PP} = 125.6$, $\sigma_{NN} = 79.6$, $\sigma_{NP} = -.04$ kHz or to equation (128') giving $\Delta = -31.1 \pm 0.4$ kHz and $X = 110.4 \pm 0.2$ kHz. The on resonance rotation plot was fit to equation (121) giving $\Delta = -24.9$ and $X = 18.7$ kHz. Here σ_{NP} is found to be zero within experimental error, so we conclude that the chemical shielding tensor is aligned so that one of its principal axis is also along the axis of rotation. We may assume then that the principal axis of the EFG tensor and the chemical shielding tensor are approximately the same. However there is a $\approx 6°$ shift in the phase of the chemical shift plot relative to the quadrupole rotation plot. The signal to noise on the former is unfortunately not good enough to draw any significant conclusions from this observed shift; however, if it is true, the phase shift would indicate that the chemical shielding tensor is not exactly aligned with the EFG tensor. The results are given in Table 5 for the chemical shielding tensor in the crystal reference frame assuming the tensor to be axially symmetric.

We have shown, however, that the EFG tensor and the chemical shielding tensor are very closely aligned. Using the remarks in Section VI B.1, we have also shown that the EFG tensor is aligned withthe crystal axes, to within a factor of 1.02 in eqQ/h. Under these assumptions we may also consider the values in Table 5 as being the elements of the chemical shielding tensor in its own principal axis frame.

Figure 25. Chemical shift rotation plot obtained using QSS. The least means square fit to the general tensor rotation function (Equation (129)) is given as the solid line. The offset frequency is 546.87 Hz below resonance. The resulting anisotropy is D = -31.1 ± .4 kHz and the isotropic shift is X = 110.4 ± .2 kHz.

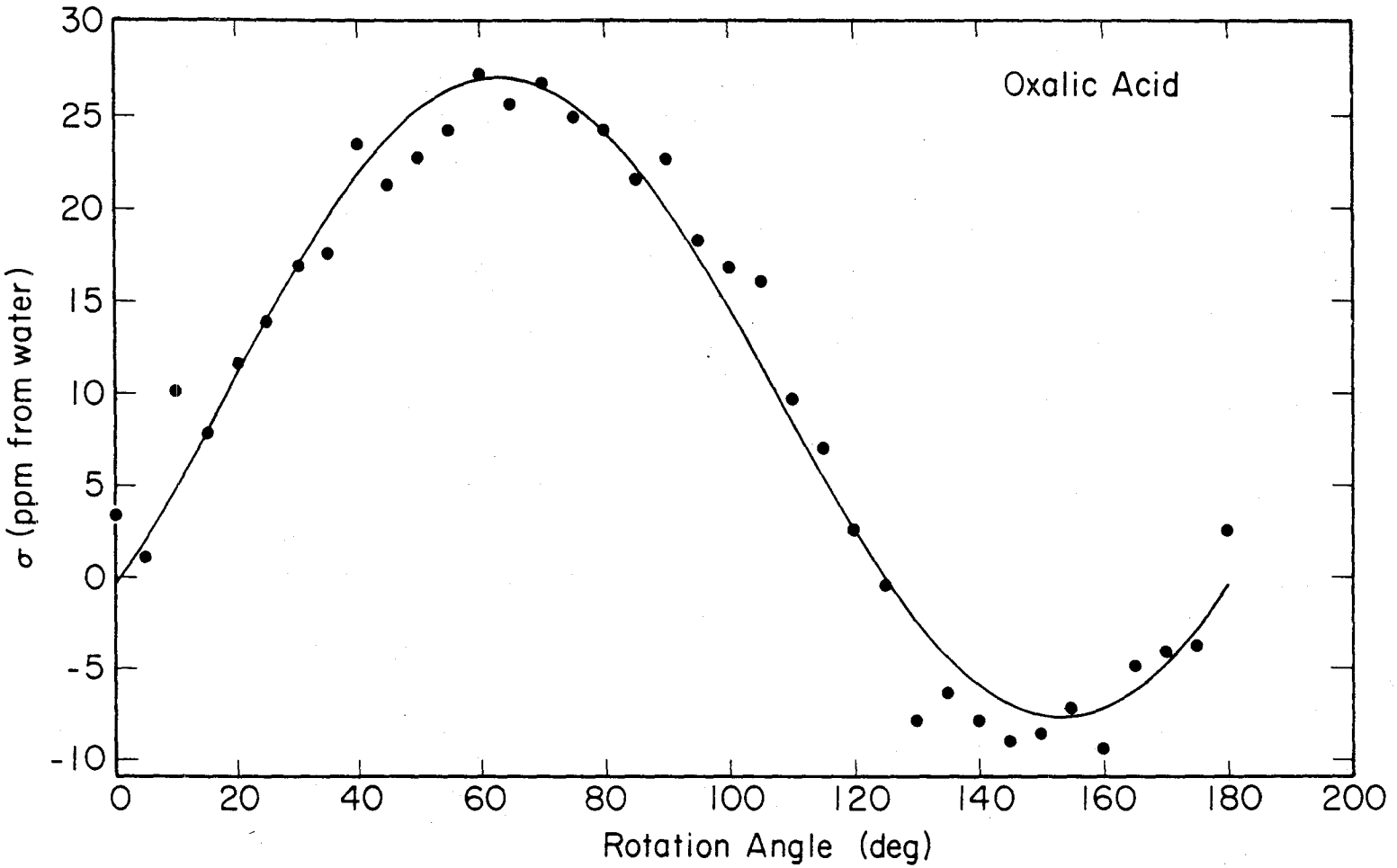
Oxalic Acid
σ (ppm from water)
30
25
20
15
10
5
0
-5
-10
0
20
40
60
80
100
120
140
160
180
200
Rotation Angle (deg)

XBL 763-679

Table 5. Carboxyl deuteron chemical shielding tensor.

Experiment	$\sigma_{\perp}$* (ppm)	σ_{11}	σ_i	D	X	$\Delta\sigma$(anisotropy)
on resonance	23.28	-4.65	13.97	-18.62	13.97	27.93
off fit to 128	26.95	-7.44	15.49	-22.93	15.49	34.38
off fit to 129	27.17	-7.69	15.56	-23.26	15.56	34.86
Double quantum	20.41	-9.33	10.49	-19.83	10.49	29.74

*ppm from adsorbed water reference; shift of water with respect to TMS is 4.76 ppm and of adamantane 1.81 ppm

3. Double Quantum Spectroscopy

The combined use of isotopic dilution and double quantum spectroscopy allows the extraction of high resolution spectra in another new way. The preceeding double quantum experiment (Section VI A.2) was repeated using the same crystal of 10% deuterated oxalic acid dihydrate. The double quantum spectrum was obtained for two different orientations, Figure 23, from which we may extract the full chemical shielding tensor, using the same assumptions as in QSS Section VI B.2. The same two pulse sequence was used as before (Figure 8) but with the following parameters:

$$\nu_Q = \frac{\omega_Q}{2\pi} \approx 40 \text{ kHz}, \ \omega_1/\omega_Q = 0.79 \Rightarrow \nu_1 = \frac{\omega_1}{2\pi} = 32 \text{ kHz} \tag{136}$$

$$\nu_Z = \frac{\omega_Z}{2\pi} = 18\text{kHz for which we find (see equation (49)):}$$

$$\omega_Z \tau = \frac{\pi}{2}$$

The phases were adjusted in the manner explained in Section VI A.2. In order to obtain high resolution spectra it was necessary to apply proton

decoupling during the delay between the pulses, t_1, as well as after the probing pulse, P_2. The strength of the decoupling field was $\frac{\omega_{1I}}{2\pi} \simeq$ 30-35 kHz. The decoupled double quantum FID's for the carboxyl deuteriums are shown for the two orientations in Figure 26. If no decoupling is used during t_1 the FID shown in Figure 27 is obtained. It is easily seen that decoupling the protons from the rare deuterons is a very significant part of the approach to high resolution. In Figure 28 we also show the double quantum FID obtained from the water peak (high frequency peak at 47 kHz in Figure 23). This shows that it is also possible to get high resolution spectra even from a quadrupole satellite which is very broad; that is, the chemical shift is fully narrowed by the water motion while the quadrupole coupling, being much larger, is not. It also illustrates that the range for which equation (51) is valid is relatively large. The water peaks in the 180° orientation were too far from 40 kHz, where the coherence preparation pulse, P_1 was matched, to obtain an FID. The Fourier transforms of the carboxyl FID's are shown in Figure 29.

The analysis to obtain the double quantum FID's was carried out automatically by computer,[29] as follows. The intensity was obtained at each delay, t_1, by integrating a region of the quadrupole spectrum containing the lines of interest and subtracting the integral of a region of the baseline. The resulting intensities were then plotted, automatically, versus the delay between the pulses. For the 57° orientation the area included in the integrals corresponds to the third carboxyl peak from the left in Figure 23. For the 180° orientation all three carboxyl lines were integrated. In addition, the water spectrum at 57° was obtained by integrating over a small region at the top of the peak, (± 400 Hz).

Figure 26. Double quantum FID for the two orientations given in figure (22). The quadrupole splitting for both orientations was $\omega_Q \cong 40$ kHz. The field strength was $\omega_{1S} = 32$ kHz giving $\omega_1^2/\omega_Q^2 = 0.63$. The pulse length of P_1 was 14 μsec (90° pulse) and of P_2 was again 5 μsec. The P_2 r.f. field strength was 47 ± 2 kHz.

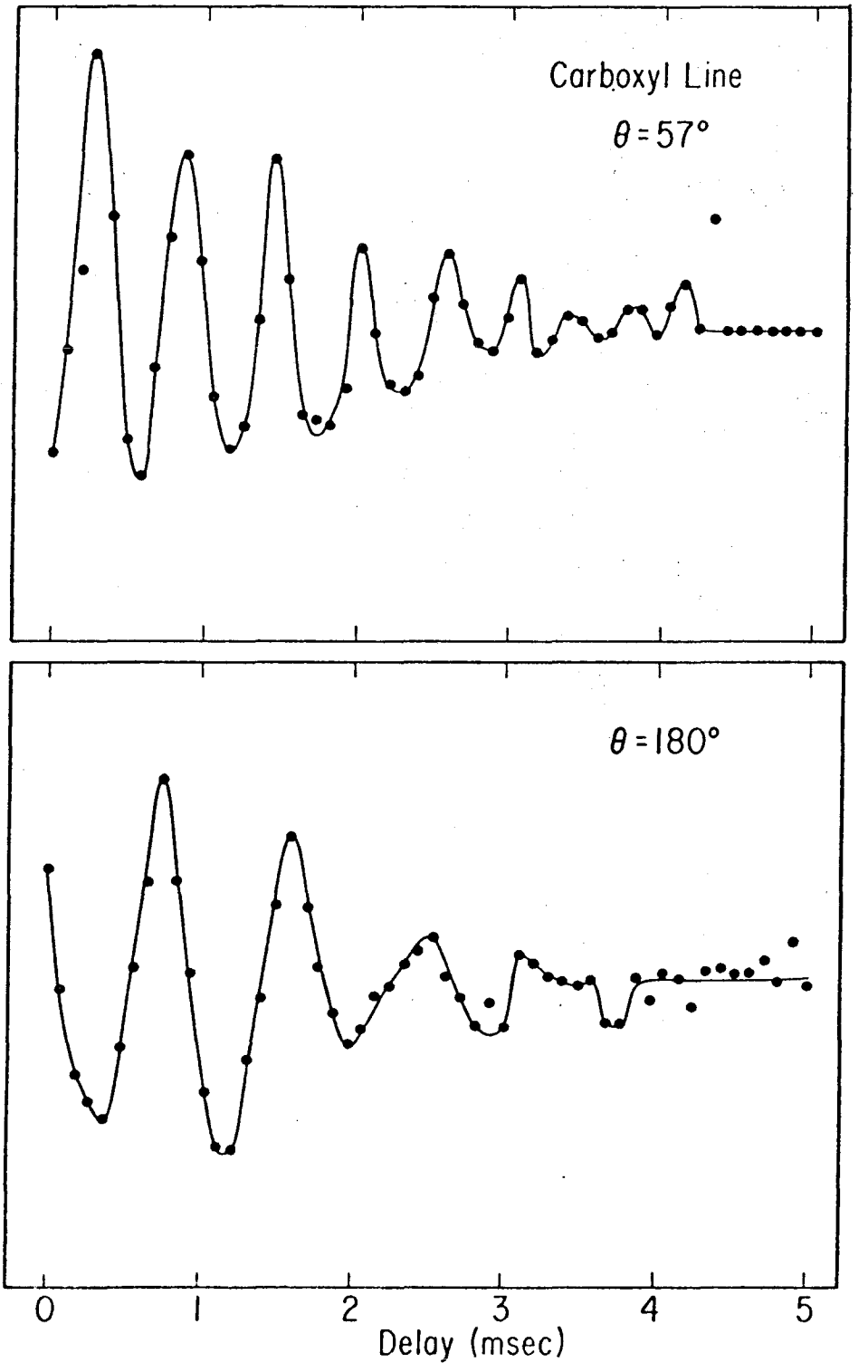

XBL 763-680

Figure 27. Same as Figure 26 but without proton decoupling.

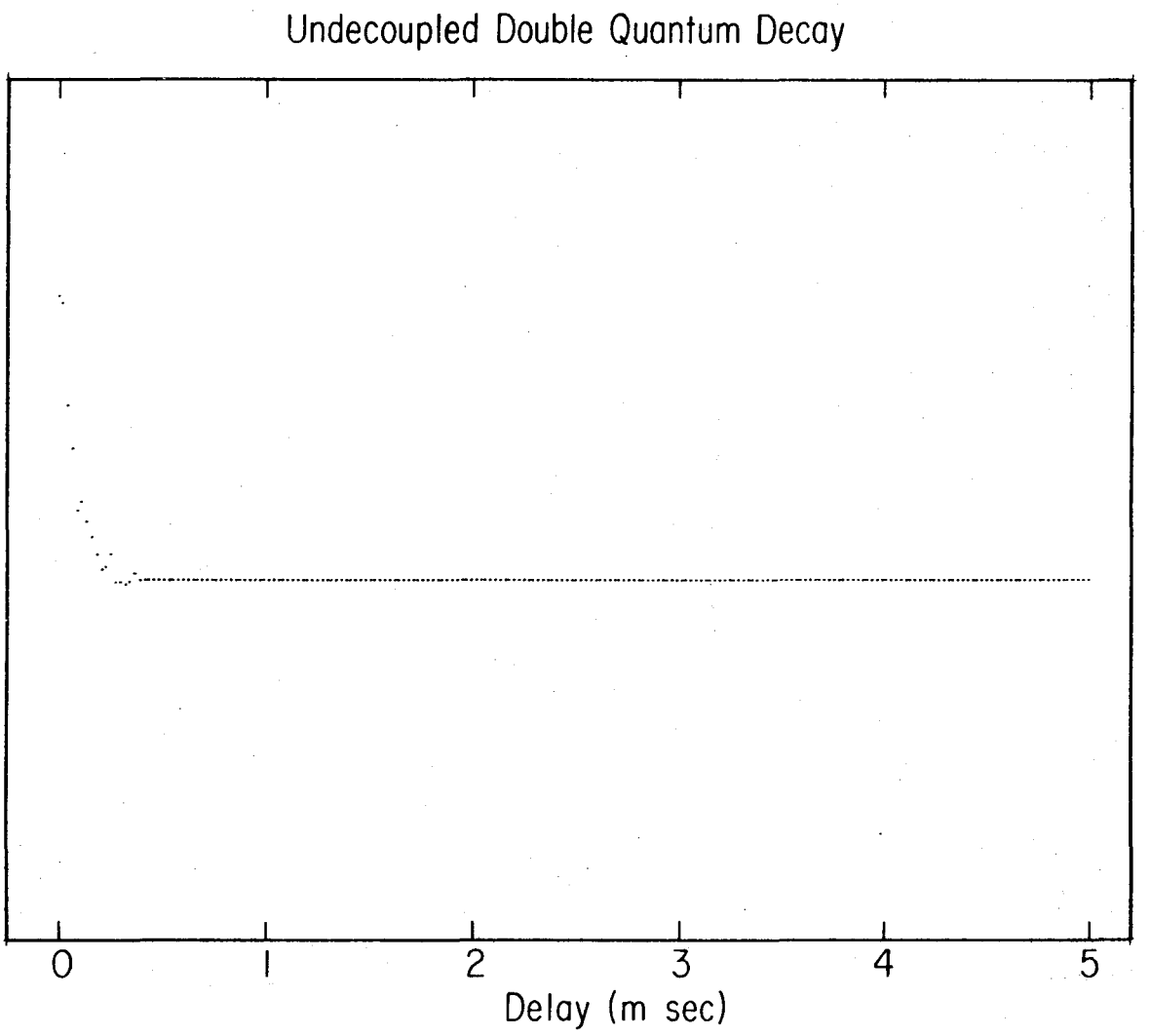

XBL 763-676

Figure 28. Double quantum FID for the water (D_2O) of hydration for the 57° orientation. This was obtained from the same spectra as in Figure 26 by integrating the broad water (D_2O) peaks at 47 kHz. Only the top of the peak was integrated, an area about the maximum of ± 500 Hz.

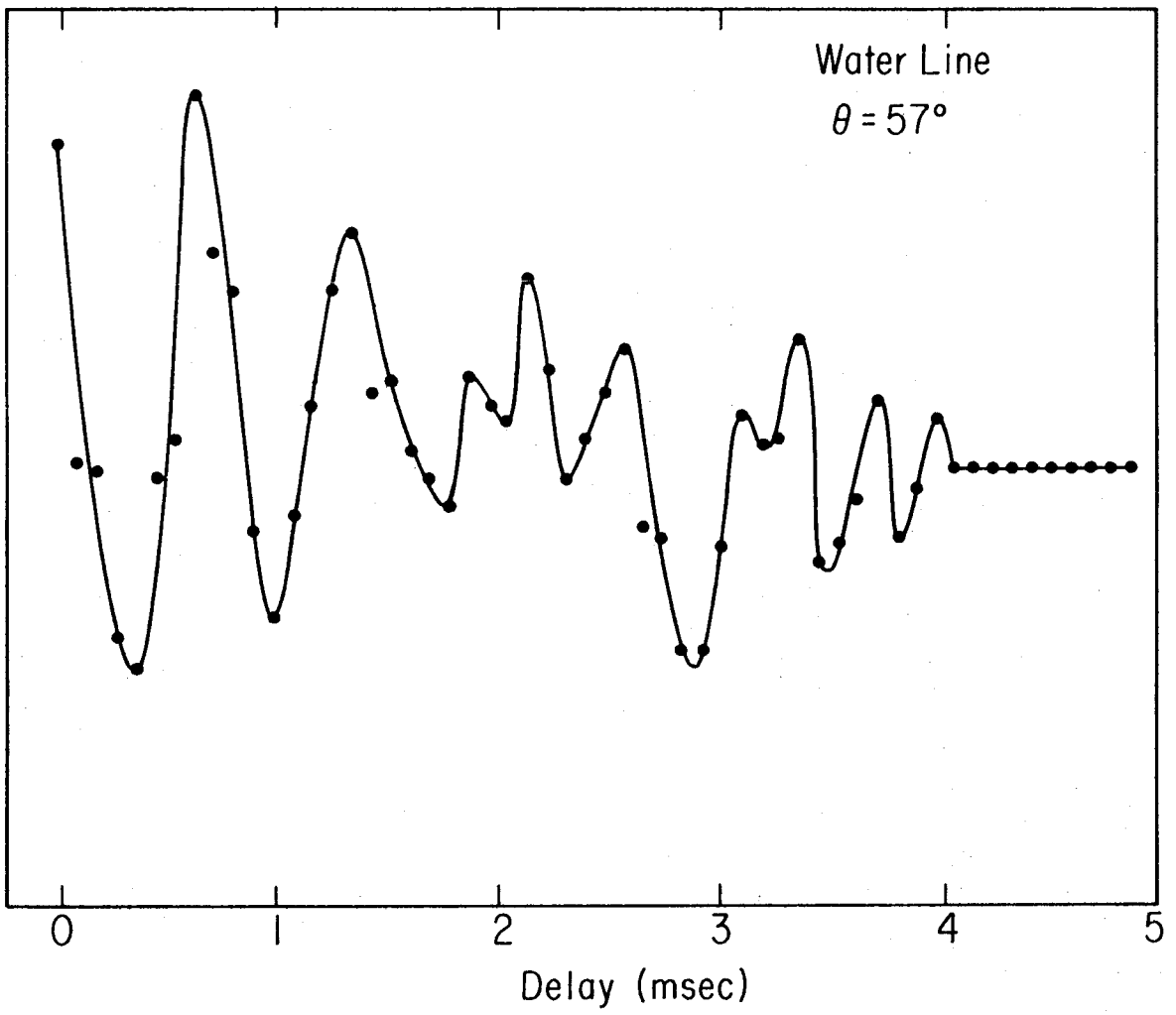

XBL 763-677

Figure 29. Fourier Transform Double Quantum Spectra obtained from the DQFID's in Figure 26. Spectrum a is from the 57° orientation and Spectrum b is from the 180° orientation. The raw line positions are for (a) 1711 Hz with an offset of 522.5 Hz and for (b) 1137 Hz with offset 576.2 Hz. The spectra are shown here plotted in ppm from an internal water reference. See Table 5 for the comparison of the QSS and FTDQS results.

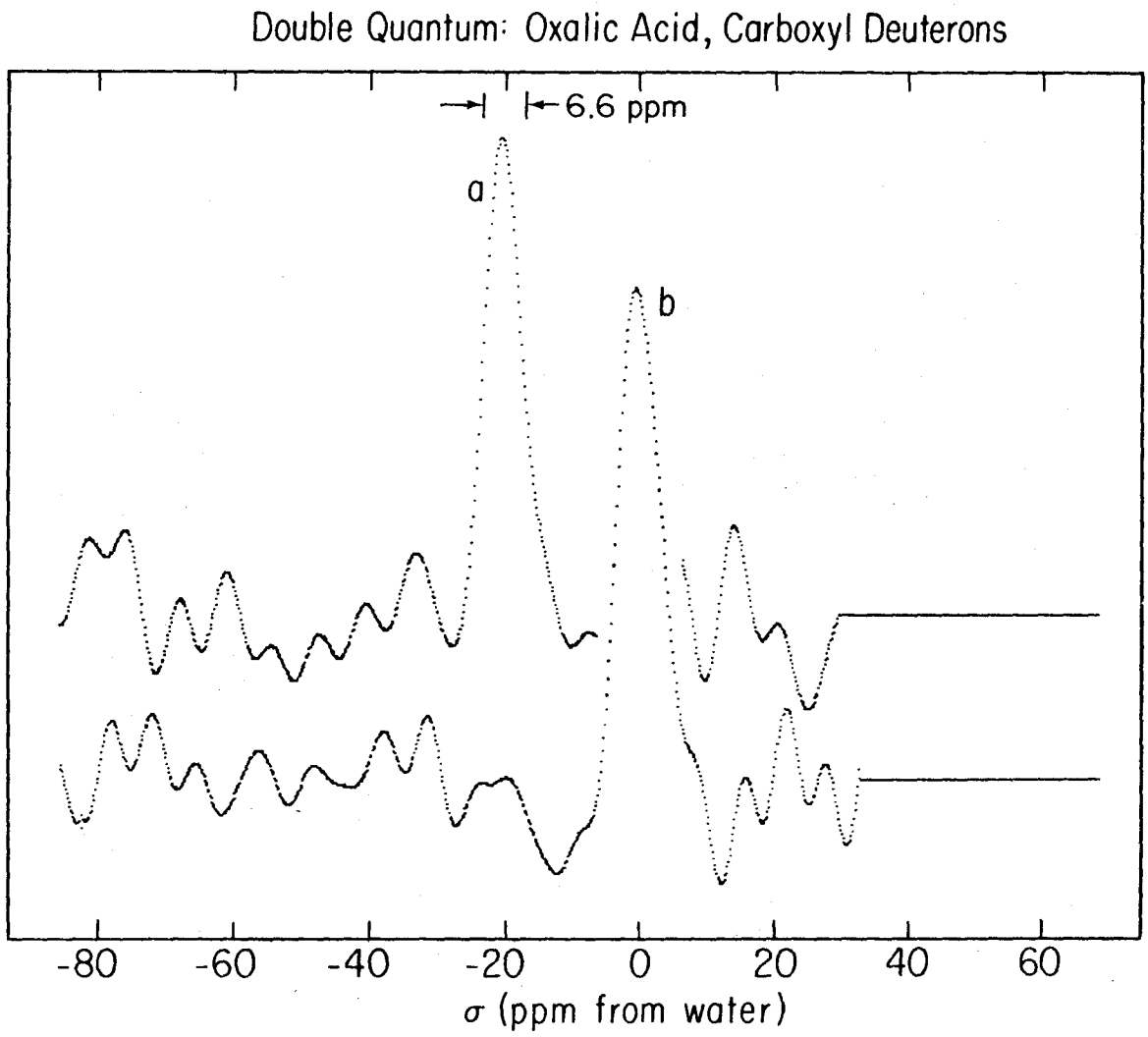
Double Quantum: Oxalic Acid, Carboxyl Deuterons
6.6 ppm
a
b
-80
-60
-40
-20
0
20
40
60
σ (ppm from water)

XBL 763-675 A

The exact orientation of the crystal was obtained by comparison of the frequencies of the lines with the quadrupole rotation plot using equation (128). Knowing these orientations and the corresponding chemical shifts, the chemical shift anisotropy may be calculated,

$$\theta_a = 57.0° ; \nu_a = 1711 \text{ Hz} ; \nu_{offset} = 522.5 \text{ Hz} ; \sigma_{ZZ} = 20.4 \text{ ppm}$$

$$\theta_b = 180.1° ; \nu_b = 1137 \text{ Hz} ; \nu_{offset} = 576.2 \text{ Hz} ; \sigma_{ZZ} = -.458 \text{ ppm}$$

The results for the chemical shielding tensor are given in Table 5, where the orientation dependence was assumed to follow equation (128). The chemical shift for the 180° orientation compares very well with the shift from QSS (see Figure 25) the value at 57° is however somewhat lower than that from QSS making the overall anisotropy smaller by ≈ 4 ppm.

Another approach to the analysis can be used which avoids the first Fourier transformation. The initial value of the FID after a pulse is the integral of the Fourier transform. Thus, following the initial value of the FID after the probing pulse P_2, should give the sum of all the double quantum FID's. Subsequent Fourier transformation then gives the spectrum for all of the chemical shifts at once. In practice the initial value of the FID cannot be obtained since it is obscured in the dead time of the spectrometer. The use of a value at a slightly later time will not produce a large effect, other than to distort the relative peak intensities in the double quantum spectrum. Another alternative which we are currently exploring, with successful preliminary results, employs an additional refocusing pulse to produce an echo. In Figure 30 we plot the initial value of the FID after P_2 versus the delay between P_1 and P_2, t_1. The pulse strengths are the same as used previously (see Figure 26).

Figure 30. Double quantum FID and the double quantum spectrum synthesized by obtaining the initial intensity of the FID. The two pulse sequence parameters are the same as for earlier experiments with $\omega_1^2/\omega_Q = .63$, see Figure 26.

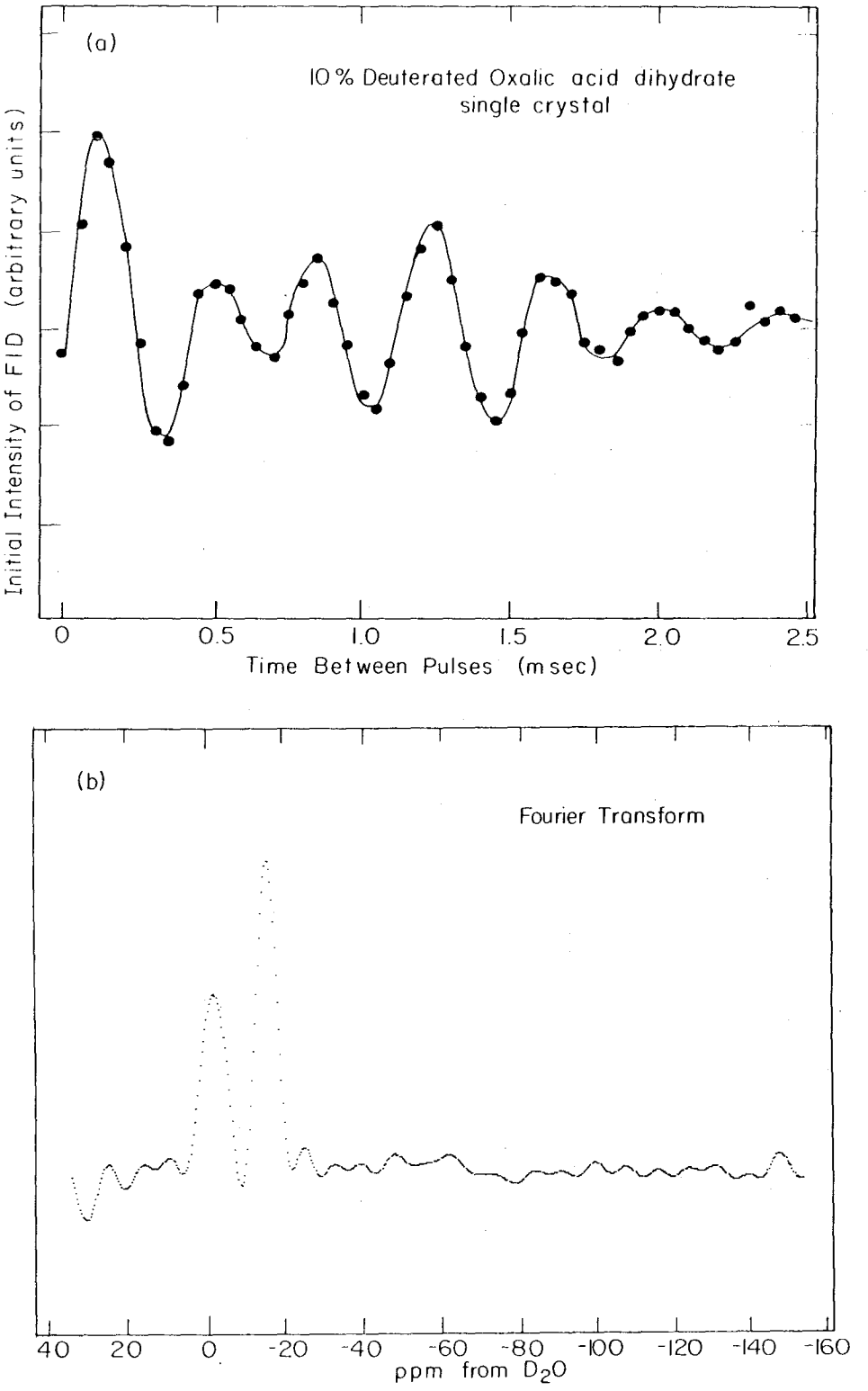
(a)
10 % Deuterated Oxalic acid dihydrate
single crystal
Initial Intensity of FID (arbitrary units)
0
0.5
1.0
1.5
2.0
2.5
Time Between Pulses (msec)
(b)
Fourier Transform
40
20
0
-20
-40
-60
-80
-100
-120
-140
-160
ppm from D_2O

XBL 762-6501

Figure 30b shows the Double Quantum Fourier Transform of the FID. The smaller peak is due to the water deuterons and the taller the carboxyl deuterons. For reference we have included the D.Q.FID and its Fourier transform taken by integrating just the carboxyl lines after a second Fourier transformation from the same experimental results used for Figure 30. These are shown in Figure 31a and b. Notice that the signal to noise ratio is actually better when the initial point is taken, rather than Fourier transforming a second time and integrating.

The effects of the finiteness of the probing pulse is easily observed by analyzing each of the carboxyl lines in the 57° orientation separately, from both parts of the first Fourier transform, Reψ and Imψ. This is shown in Figure 32. The signal from the imaginary part of the Fourier transform after the probe pulse must come from the non-zero $S_{X,2}$ or $S_{Y,1}$ terms. Equation (73) estimates this effect. The probe pulse used had:

$$\frac{\omega_{1S}}{2\pi} = 47 \pm 2 \text{ kHz}, \quad \tau_P = 4.25 \ \mu\text{sec} \tag{137}$$

making ω_e, with the quadrupole coupling range for this orientation of $\sim$ 40 kHz to $\sim$ 37 kHz,

$$\omega_e = \sqrt{\omega_Q^2 + 4\omega_{1S}^2} = 103 \text{ to } 102 \text{ kHz}$$

$$\sin \omega_e \tau_P = 0.37 \text{ to } 0.40 \tag{138}$$

This decrease in ω_e only accounts for a 10% increase in the signal height in the imaginary buffer. This is not surprising considering we derived equation (73) for the condition $\omega_1 >> \omega_Q$. Here ω_1 and ω_Q are approximately equal, so that the full Hamiltonian must be taken into

Figure 31. Double quantum FID and the double quantum spectrum obtained by integrating the carboxyl lines for comparison with Figure 30. The raw data used for both was the same, for Figure 30 the initial point was taken and for 31 the carboxyl lines (all 4) were integrated.

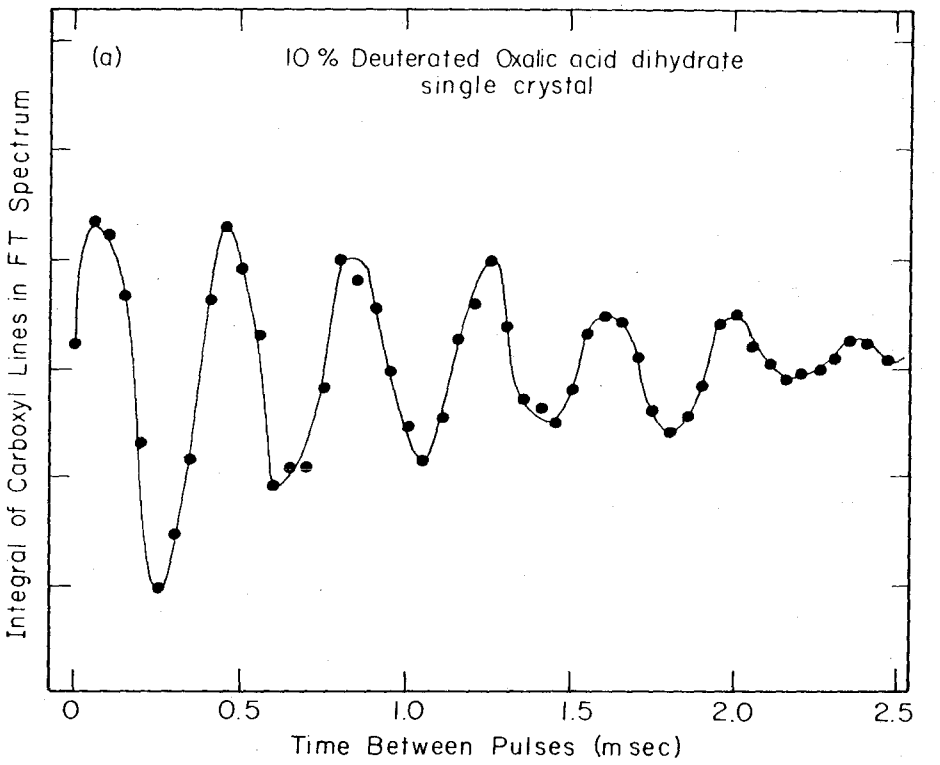
(a)
10 % Deuterated Oxalic acid dihydrate
single crystal
Integral of Carboxyl Lines in F T Spectrum
0
0.5
1.0
1.5
2.0
2.5
Time Between Pulses (m sec)

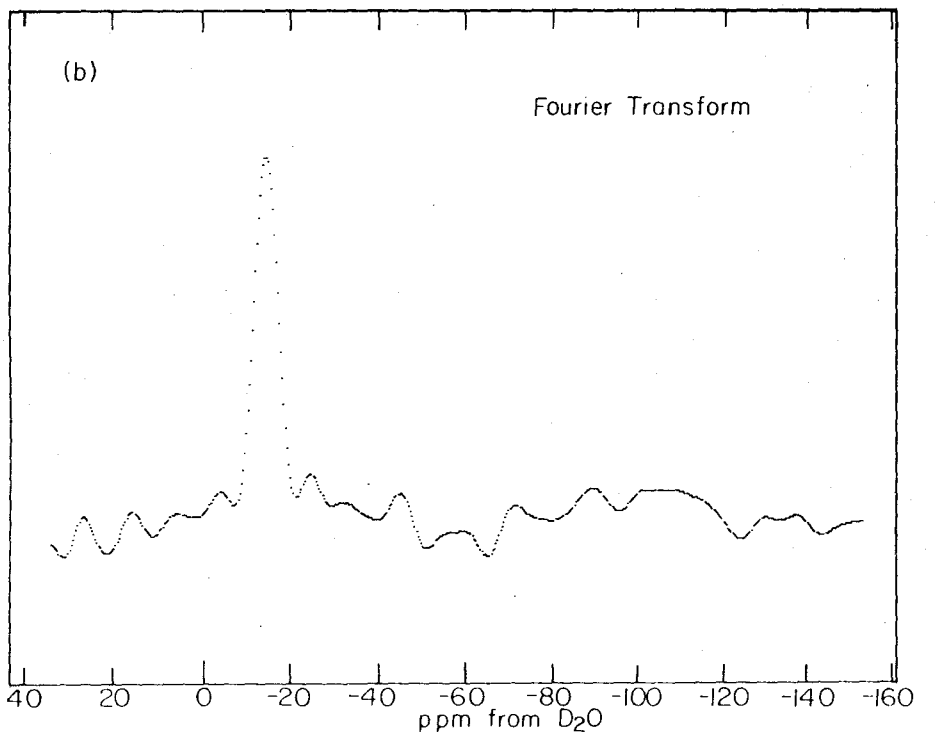
(b)
Fourier Transform
40
20
0
-20
-40
-60
-80
-100
-120
-140
-160
ppm from D_2O

XBL 762-6502

Figure 32. Imperfections caused by the finiteness of the probing pulse P_2. Line 1 is the highest frequency carboxyl satellite in Figure 23 for the 57° orientation, and line 4 is the lowest carboxyl line. These double quantum FID's were synthesized from the initial Fourier transforms used in Figure 26, but this time integrating line by line from both components of the Fourier transform, real and imaginary. The double quantum FID's for each of the lines has been derived from the component 90° out of phase with the reference phase of the initial Fourier transform.

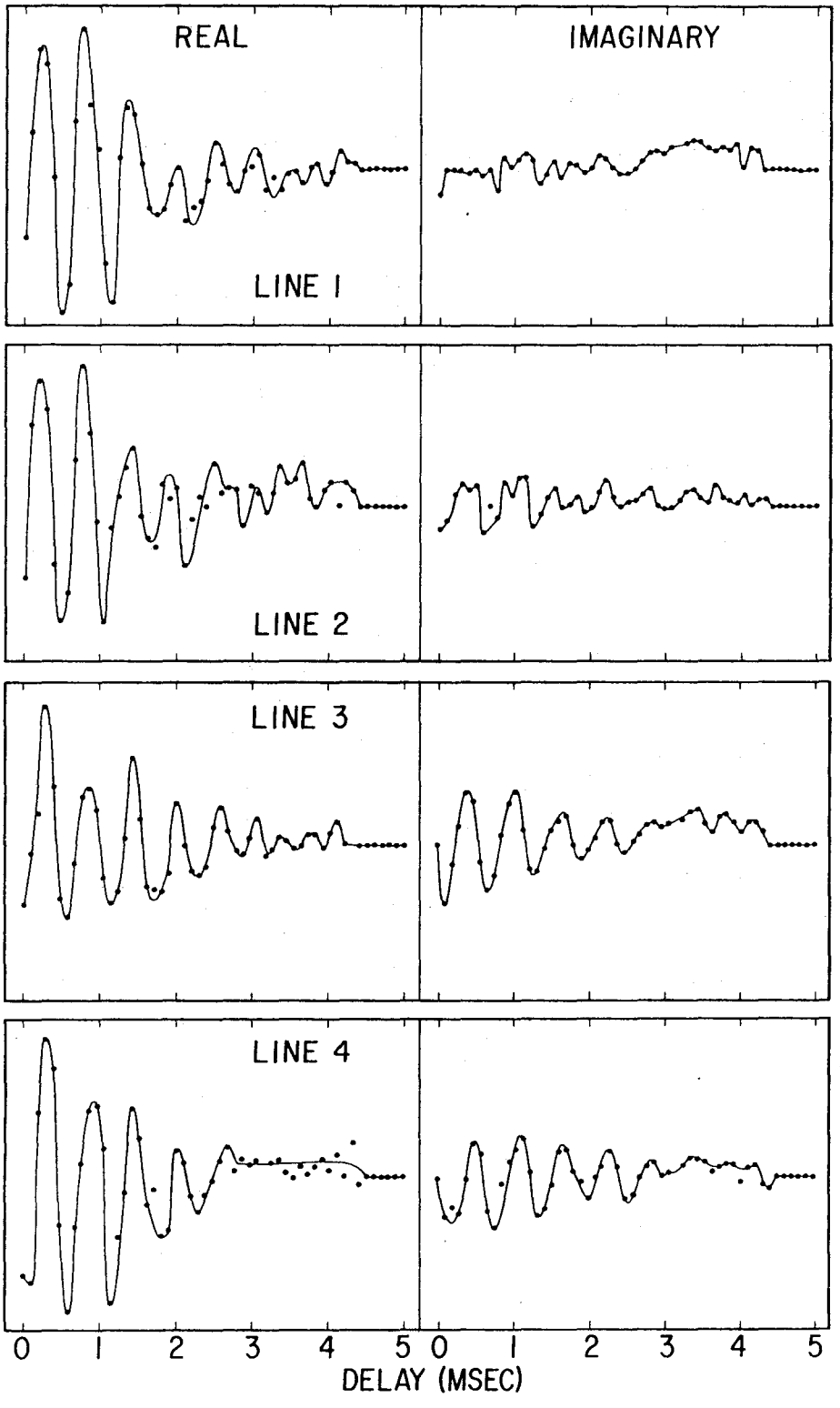
REAL
IMAGINARY
LINE 1
LINE 2
LINE 3
LINE 4
0
1
2
3
4
5
0
1
2
3
4
5
DELAY (MSEC)

account during the pulse. In addition there was also a relatively large frequency offset used which means that an exact analysis should include the offset terms in the Hamiltonian governing the time evolution during the pulse.

C. Cross Polarization

1. Sample

Monodeutero-benzene (99% D) obtained from Merck, Sharpe and Dohme. was used without further treatment. Benzene-D1 was chosen because its relaxation parameters all fall in the intermediate range of about 0.5 sec. The relatively high abundance of deuterium was also necessary for good signal to noise ratios for these preliminary experiments.

2. Indirect Detection

The cross polarization process was first[23] observed through the destruction of the proton order in the standard double resonance experiments (see Hartmann and Hahn). The pulse sequences of the indirect spin locking (SL) and adiabatic demagnetization (ADRF) double resonance experiments are shown in Figure 33. The proton signal was observed after the cross polarization spin locking pulse for the SL case. For the ADRF experiments the proton order, which is dipolar in nature, was monitored, after cross polarization, with a 45° pulse.[30]

The sample was cooled by nitrogen gas to ≈ -35°C. The demagnetization time for ADRF was optimal at 2 msec, the same time as used in the carbon-13-proton experiments in Chapter 1. The quadrupole splitting between the intense satellite regions of the powder spectrum and zero was $\frac{\omega_Q}{2\pi} = \nu_Q =$ 35.2 kHz. Since this was a powder the total range from zero freqency of $(\frac{\omega_Q}{2\pi})$ was then $\pm$70.4 kHz. <u>However most of the experiments were done with</u>

Figure 33. Pulse sequence for indirect detection of the cross polarization. (Note that a derivative signal of the FID is obtained after the 45° pulse[30,32]). Cross polarization is detected by the destruction of the proton FID. Indirect detection affords higher sensitivity but much lower resolution than direct detection.

Indirect Detection

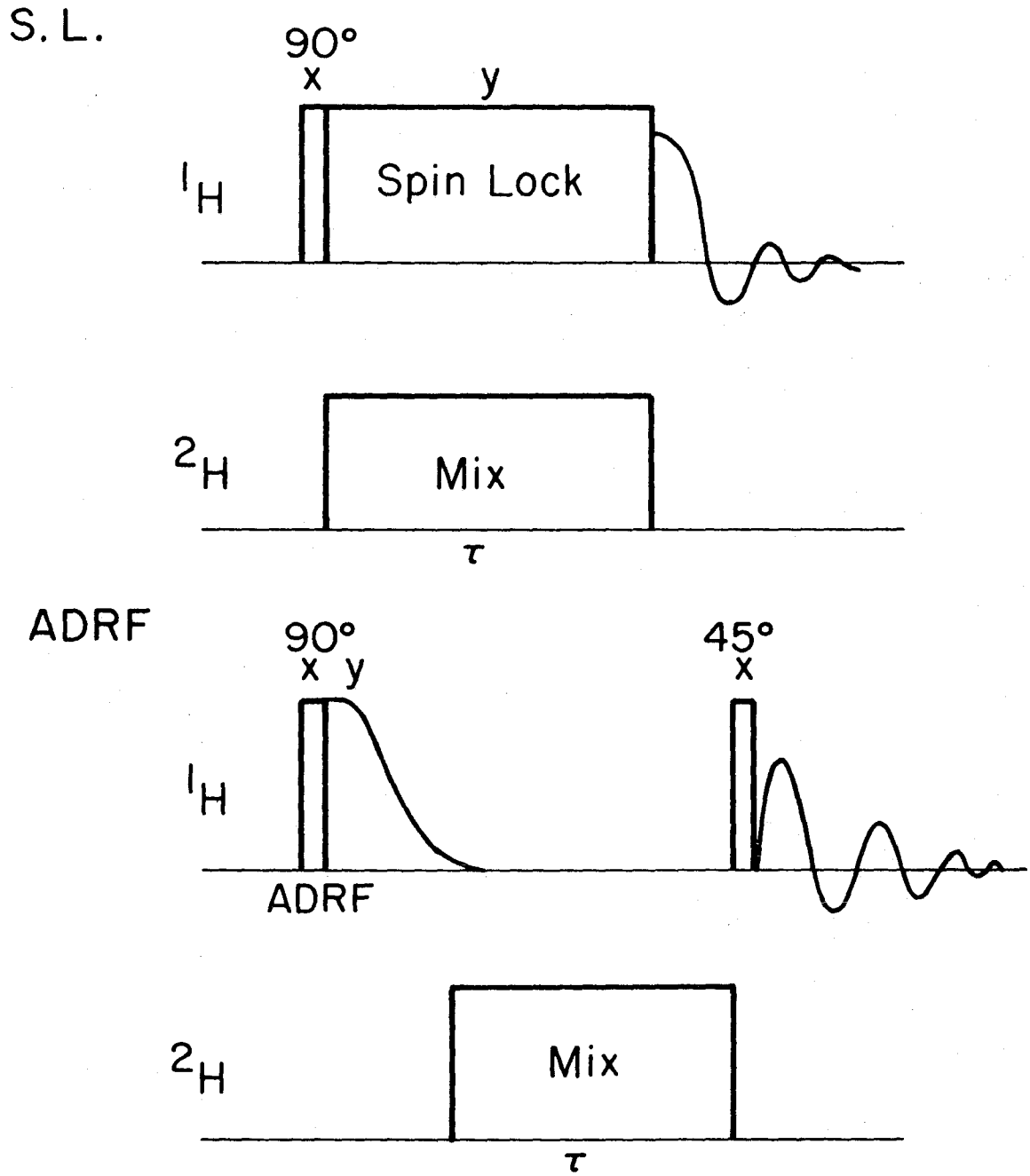

XBL 765-1980

philosophy that most of the area, as far as the actual cross polarization experiment is concerned, is within a small bandwidth (few kHz) about 35.2 kHz, and this area acts as if it were from a single crystal.

The cross polarization experiments were carried out at two different deuterium frequencies a) at or near the frequency of the high frequency satellite at 35.2 kHz and b) at or near the center frequency (double quantum). The proton destruction for both the single and double quantum experiments as a function of deuterium power is shown in Figures 34 for the SL case and Figure 35 for the ADRF case.

For the single quantum SL experiment the maximum destruction experimentally occurs at 7 kHz. The matching condition is predicted to be as in equation (85)

$$\sqrt{2}\ \omega_{1S} = \omega_{1I} \tag{139}$$

For our case $\frac{\omega_{1I}}{2\pi}$ = 10 kHz and $\sqrt{2}$ x 7 kHz = 9.9 kHz. Thus, the results are in good agreement with the theoretical prediction. The double quantum matching condition is, for $\delta\omega = 0$, given by equation (99):

$$\frac{\omega_{1S}^2}{\omega_Q} = \omega_{1I} \tag{140}$$

Here the experimental maximum destruction is at $\frac{\omega_{1S}}{2\pi}$ = 19 kHz. Then

$$\frac{\omega_{1S}^2}{2\pi\omega_Q} = \frac{19^2}{35.2} = 103 \text{ kHz} \tag{141}$$

Indeed, the proton rf field used was $\frac{\omega_{1I}}{2\pi}$ = 10.5 kHz, again showing good agreement with the theoretical prediction. The proton frequency was at

Figure 34. Indirectly detected SL cross polarization for D-1-benzene as a function of deuterium field strength. For the single quantum case a) ω_{1I} = 10 kHz, the mixing time was 15 msec and $\frac{\Delta\omega}{2\pi}$ = 35.2 kHz. For the double quantum case b) ω_{1I} = 10.5 kHz, the mixing time was 15 msec and $\frac{\delta\omega}{\pi}$ = 0. The temperature was ≈ -35°C.

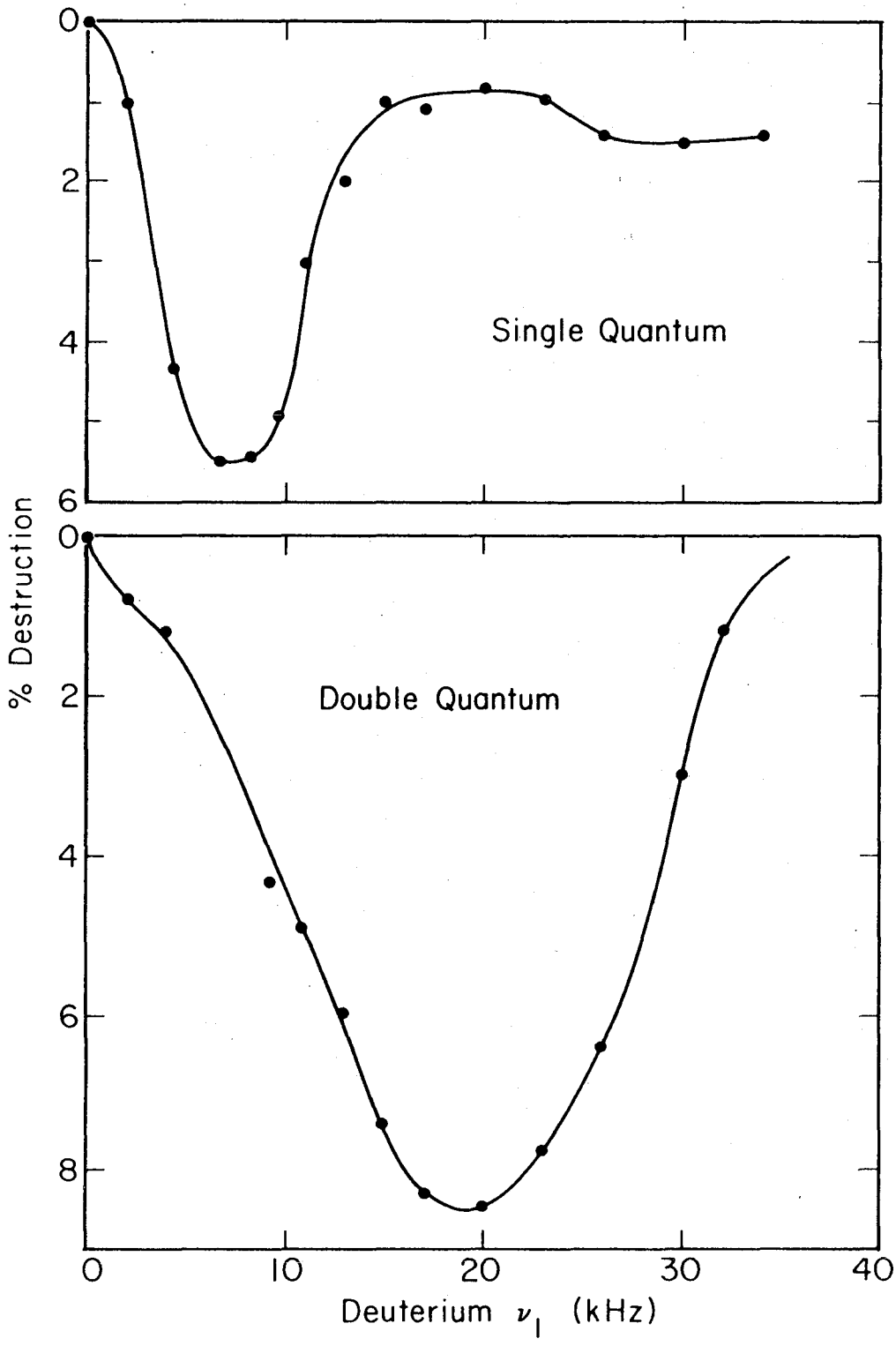
0
2
4
6
Single Quantum
0
2
4
6
8
Double Quantum
% Destruction
0
10
20
30
40
Deuterium ν_1 (kHz)

XBL 764-1531

Figure 35. Indirectly detected ADRF cross polarization for D-1-benzene. For the single quantum case, a), $\frac{\Delta\omega}{2\pi}$ = 35.2 kHz and for the double quantum, b), $\frac{\delta\omega}{2\pi}$ = 0. The mixing time for both was 50 msec. The temperature was -35°C.

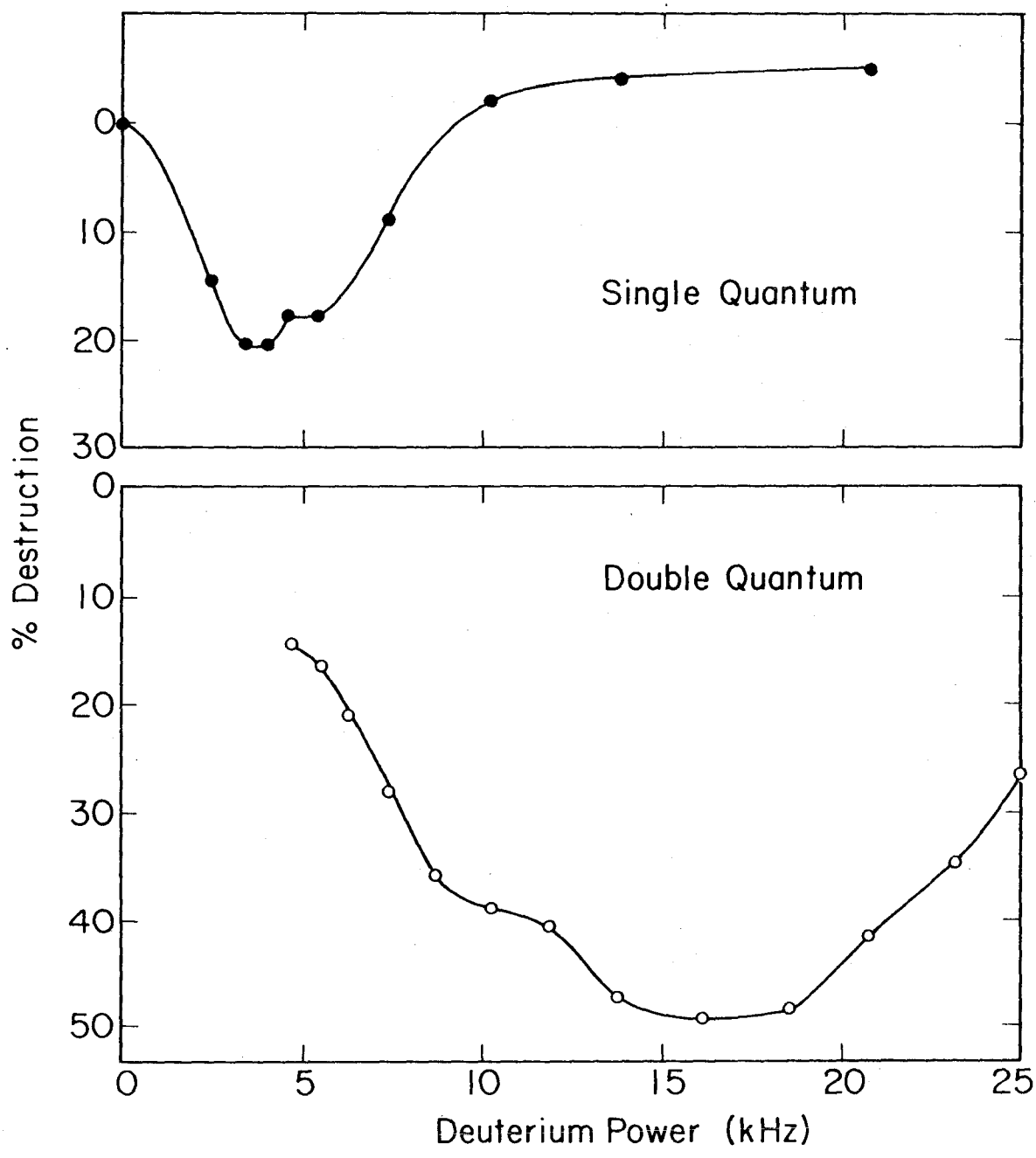
Single Quantum
Double Quantum
% Destruction
0
10
20
30
0
10
20
30
40
50
0
5
10
15
20
25
Deuterium Power (kHz)

XBL 764-1529

resonance, while the deuterium frequency was either at resonance $\delta\omega = 0$ double quantum or $\Delta\omega = 35.2$ kHz single quantum. We note also that the double quantum destruction peaks are much broader than the single quantum.

The destruction as a function of deuterium offset frequency is shown in Figure 36 for the SL case and Figure 37 for the ADRF experiment. The solid line in each destruction spectrum is included only to guide the eye. The mixing times are 15 msec for SL and 50 msec for ADRF. The irradiation fields were $\frac{\omega_{1S}}{2\pi} = 8$ kHz and $\frac{\omega_{1I}}{2\pi} = 11$ kHz for the SL case and $\frac{\omega_{1S}}{2\pi} = 14.7$ kHz for the ADRF case. The broad background for the SL case comes from single quantum cross polarization to the side peaks and from the distribution of ω_Q's in the powdered sample. The two dips occur when the offset frequency is large enough to match equation (99),

$$\frac{\omega_e}{2\pi} = \sqrt{\frac{8^4}{35.2^2} + 4(5.5)^2} = 11.1 \text{ kHz} = \frac{\omega_{1I}}{2\pi} \tag{142}$$

<u>the double quantum Hartmann-Hahn condition.</u> The difference in the destruction at the two minima is not predicted by the dynamics. Note also that there is an asymmetry in the destruction peak positions.

The difference in the minima may at least be partially explained by realizing that at the beginning of cross polarization there is some of the room temperature deuterium magnetization present. The amount which is left at the beginning of cross polarization will be the projection of the equilibrium magnetization on the effective field axis. That is

$$M_S(0) = \sin\theta_Z \, \beta_L \, C_S \, H_{0S} \tag{143}$$

Conservation of energy then gives:

Figure 36. Indirectly detected SL cross polarization for D-1-benzene as a function of deuterium offset frequency. The rf field strengths were $\frac{1}{2\pi}\omega_{1S} = 8$ kHz and $\frac{1}{2\pi}\omega_{1I} = 11$ kHz, the mixing time was 15 msec. The solid line is included only to guide the eye. The asymmetry in the peak positions and heights is not predicted by equation (117).

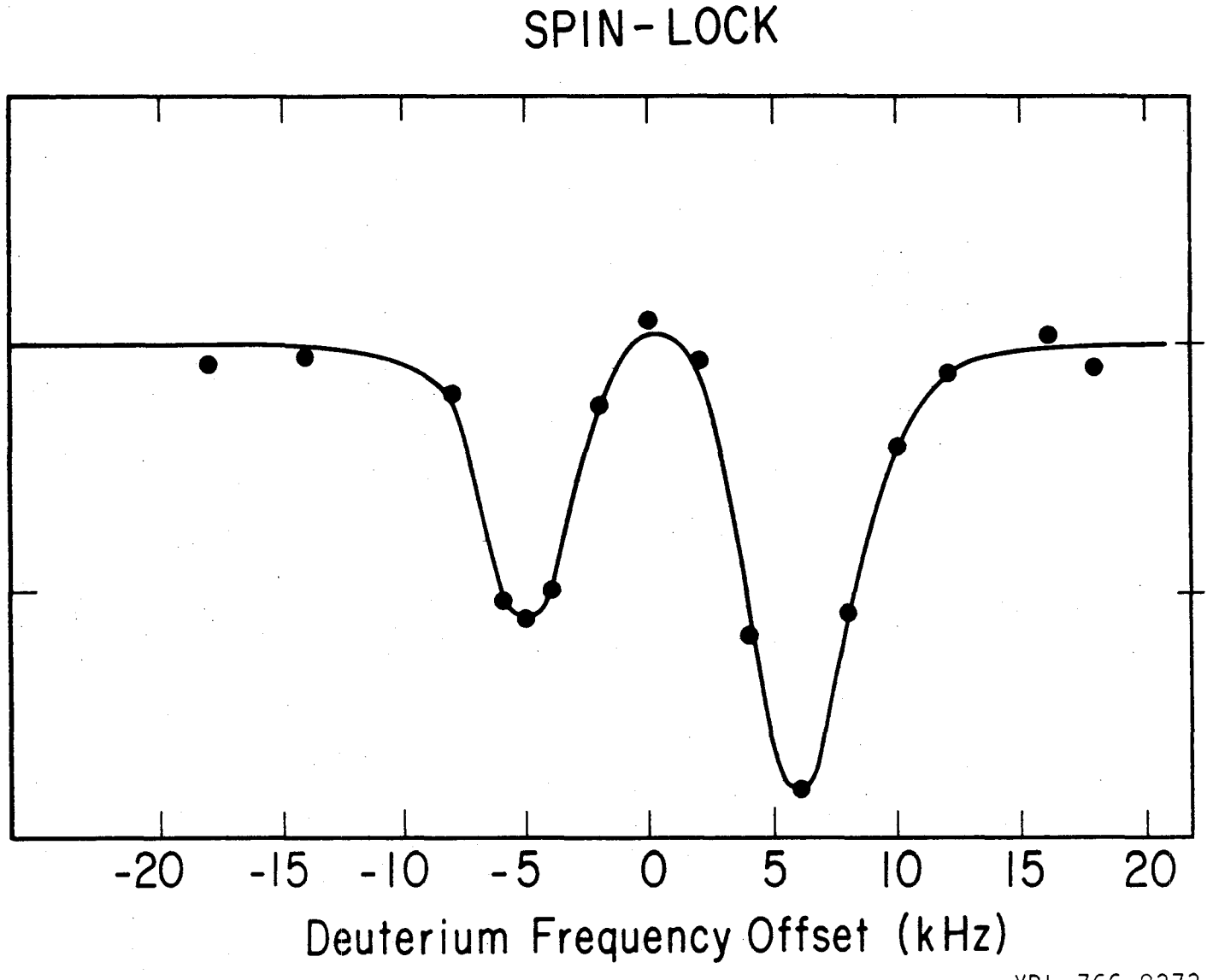
SPIN-LOCK
-20
-15
-10
-5
0
5
10
15
20
Deuterium Frequency Offset (kHz)

XBL 766-8373

Figure 37. Indirectly detected ADRF cross polarization for D-1-benzene as a function of the deuterium offset frequency. The deuterium field strength was ω_{1S} = 14.7 kHz and the mixing time was 50 msec. The solid line is included to guide the eye. The asymmetry in the peak position and heights is not predicted by equation (116).

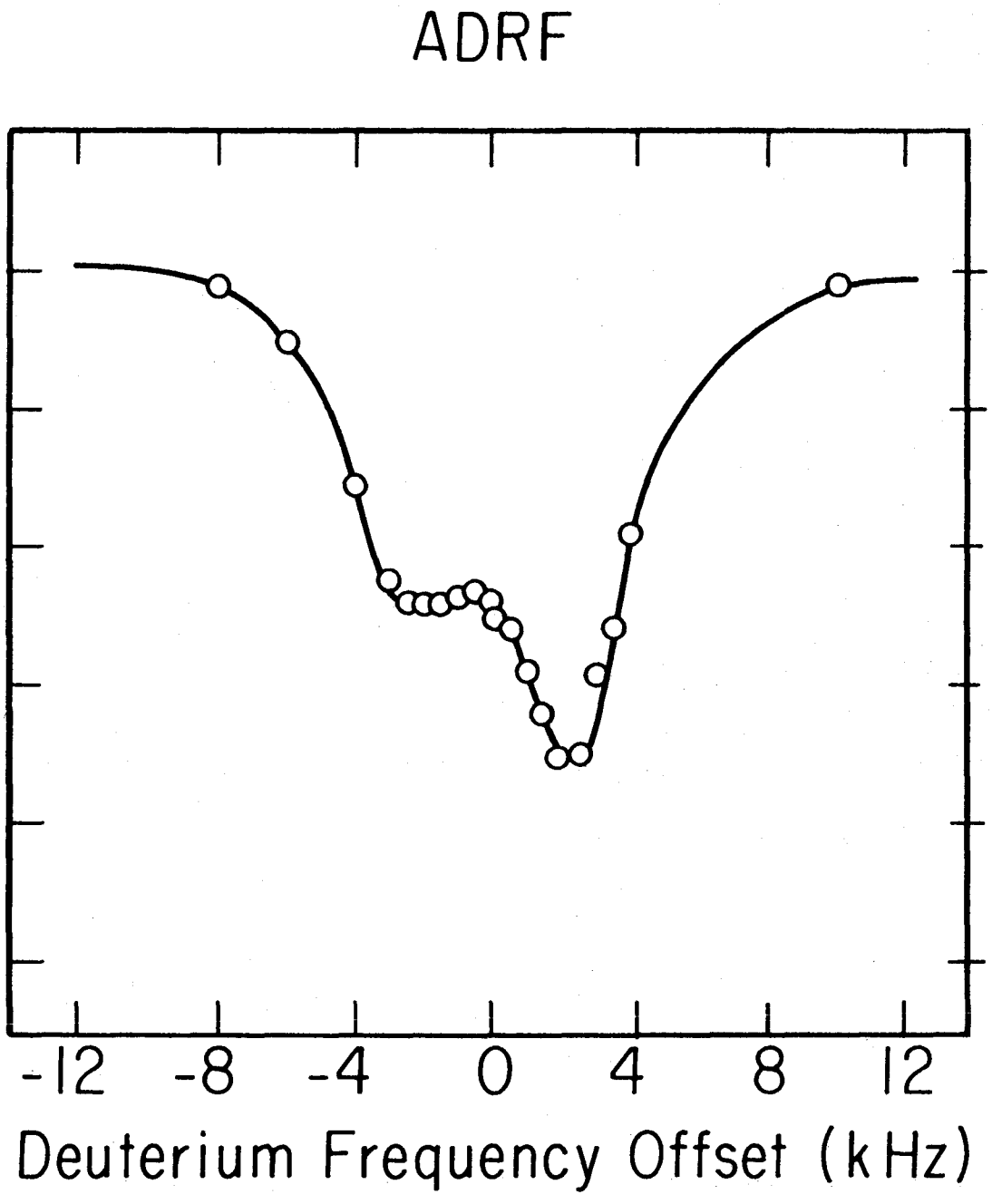

XBL 766-8372

$$\beta_I\ C_I\ H_{1I}^2 + \beta_L\ C_S\ H_{0S}\left(\frac{\omega_{eS}}{\gamma_{eS}}\right)^2 \sin\theta_Z = \beta_1 [C_I\ H_{1I}^2 + C_S\left(\frac{\omega_{eS}}{\gamma_{eS}}\right)^2] \tag{144}$$

and

$$\beta_1 = \beta_L\ \frac{\omega_{0I}}{\omega_{1I}}\ (\frac{1}{1+\varepsilon\eta^2}) + \beta_L\ \frac{\omega_{0S}}{\omega_{eS}}\ \sin\theta_Z\ (\frac{\varepsilon\eta^2}{1+\varepsilon\eta^2})$$

<u>This gives the asymmetry in the destruction minima as</u>

$$\text{asymmetry} = 1 + \frac{\gamma_S}{\gamma_I}\ \frac{\omega_{1I}}{\omega_{eS}}\ \sin\theta_Z \tag{145}$$

However this factor does not account sufficiently for the difference. It also does not predict the asymmetry in the minima positions.

The width of the destruction peaks is a measure of the breadth (in frequency space) of the correlation functions. In order to extract correlation times for the two cases (SL and ADRF) equations (118) and (119) were used to fit the experimental data. The second moments $M_{2,IS}$ could also be obtained in principal from this procedure but the asymmetries mentioned above make these figures very unreliable. The curve fitting of the destruction spectra was carried out with C, β and τ_c as variable parameters where (see equations (118) and (119))

$$C = \beta_I\ C_I\ H_{1,I} \tag{146}$$

and $\beta = \frac{\pi}{2}\ M_{2,IS}{}^t$ for ADRF

and $\beta = \sqrt{\frac{\pi}{2}}\ \frac{M_{2,IS}}{2} t$ for SL.

The ratio of the heat capacites which was used was

$$\varepsilon\eta^2 = \frac{N_S \frac{1}{2}/(2S+1)}{N_I \frac{1}{2}/(2I+1)} \frac{\omega_{eS}^2}{\omega_{1I}^2} \quad . \tag{147}$$

This form will be experimentally validated later in this chapter. The details of the computer programs for the nonlinear least squares analysis are given in Appendix 2.4. The fitting gives

$$\tau_{c,SL} = 418 \ \mu\text{sec} \quad \text{for SL} \tag{148}$$

and

$$\tau_{c,ADRF} = 577 \ \mu\text{sec} \quad \text{for ADRF.}$$

For the ADRF case H_L was taken to be $H_L = 0.646$ Gauss. This value was calculated from the proton line width in benzene, as will be discussed later in this chapter.

It should be noted that the correlation times are approximate because of the asymmetries and because only one value of ω_Q was used, treating the quadrupolar spectrum as a single crystal as discussed before. Undoubtably there is a range of ω_Q's which contribute measurably to the cross polarization. Also the effect of relaxation was not included, however when it is these results do not change significantly.

3. Direct Detection

These experiments are the immediate extension to deuterium of the proton-carbon-13 cross polarization discussed in the first chapter. But again we have taken two choices for the frequency of the deuterium irradiation, near the high frequency satellite or near the center of the spectrum. The following results were obtained without proton decoupling, since the linewidth of the satellites did not change significantly. The

single quantum experiment is straight-forward since the polarized state which is prepared is directly observable. The double quantum state must be probed with a magic pulse, which we discuss first after the single quantum experiments followed by the results of the standard experiment on cross polarization dynamics. The results of the dynamics have already been used in the preceeding section to discuss the destruction spectra.

The density matrix for the single quantum cross polarization is given in equation (90), the only observable term is $(S_{X,1}-S_{Y,2})$ which indicates that only the satellite nearest the irradiation is polarized. This is shown to be the case experimentally in Figure 38. The spectrum in (a) is the normal FID. In (b) is the result after cross polarization from a SL state with a cross polarization time of 15 msec. The deuterium frequency offset was ≈ 43 kHz above resonance. The enhancement from the cross polarization was only 1.5, while the theoretical value is 4.6. (Note that 36a has been multiplied by 1.5).

The effect of a magic pulse (see Figure 11) is shown in Figure 39, after ADRF cross polarization with the deuterium frequency exactly at resonance. The cross polarization time was 50 msec which was immediately followed by a magic pulse 180° out of phase and of variable length. A-X pulse, which is 180° out of phase with the X mixing pulse, was chosen since (see Section IV B.3) it should only transform the X coordinate space. The intensity follows the approximate shape expected from equation (112) up to about a 180° precession of the magnetization, that is t_M = 10.5 μsec, however the pattern should be symmetrical about 180°. Figure 40 shows the evolution of the intensity (0) and the phase (0) of the signal. The component along the $\bar{X}$ axis of the phase detector was extracted by multiplying the intensity by the cosine of the experimental phase angle (shown as 0), the theoretical

Figure 38. Normal single pulse FID compared with the result of a SL cross polarization for the single quantum transition. The frequency offset was $\frac{\Delta\omega}{2\pi}$ = 43 kHz above resonance and the mixing time was 15 msec. The normal FID, a), has been multiplied by 1.5. The temperature was -35°C. These spectra accumulated for ≈ 10 hours.

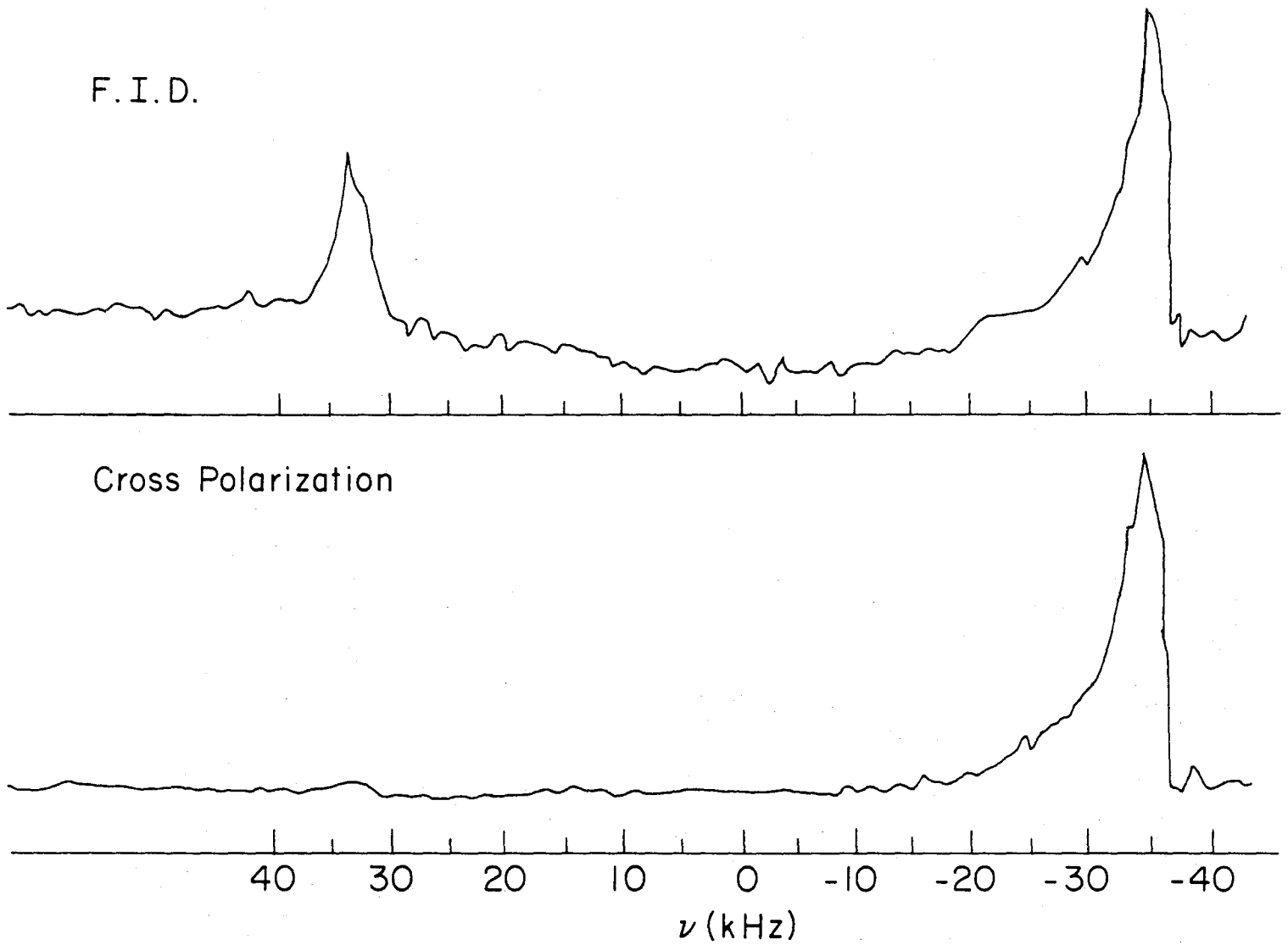

XBL 764-1516

Figure 39. Magic pulse cross polarization. The signal intensity is shown as a function of the magic pulse width, for the magic pulse 180° out of phase with the mixing pulse. The demagnetization time was 2 msec and the mixing time was 50 msec. The solid line is included only to guide the eye. The magic pulse intensity is ω_{1S} = 16.1 kHz and ω_Q = 35.2 kHz giving θ = 42° and ω_e = 47.7 kHz. The 180° pulse time should be 10.5 μsec.

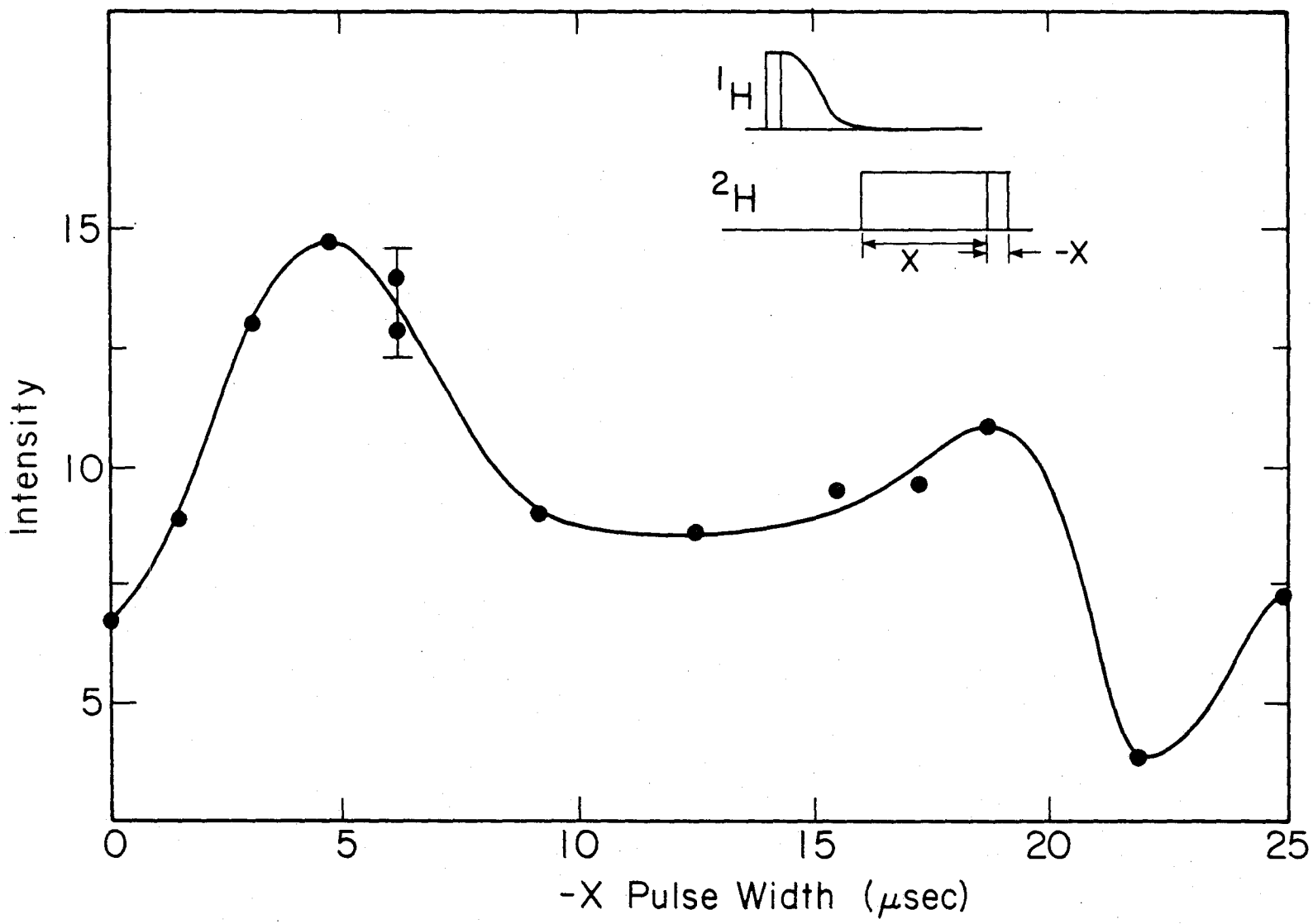

XBL 764-1511

Figure 40. Magic pulse cross polarization. Figure 38 is redrawn (··) along with its phase angle with respect to the fixed phase detector. The intensity multiplied by the cosine of the phase angle gives the projection of the initial amplitude of the FID along the $\bar{X}$ phase detector axis (oo). The solid line through these points is the theoretical pulse width dependence (equation (112)) for ω_Q = 35.2, ω_e = 47.7 kHz and the constant ρ found by fitting the curve to the first point.

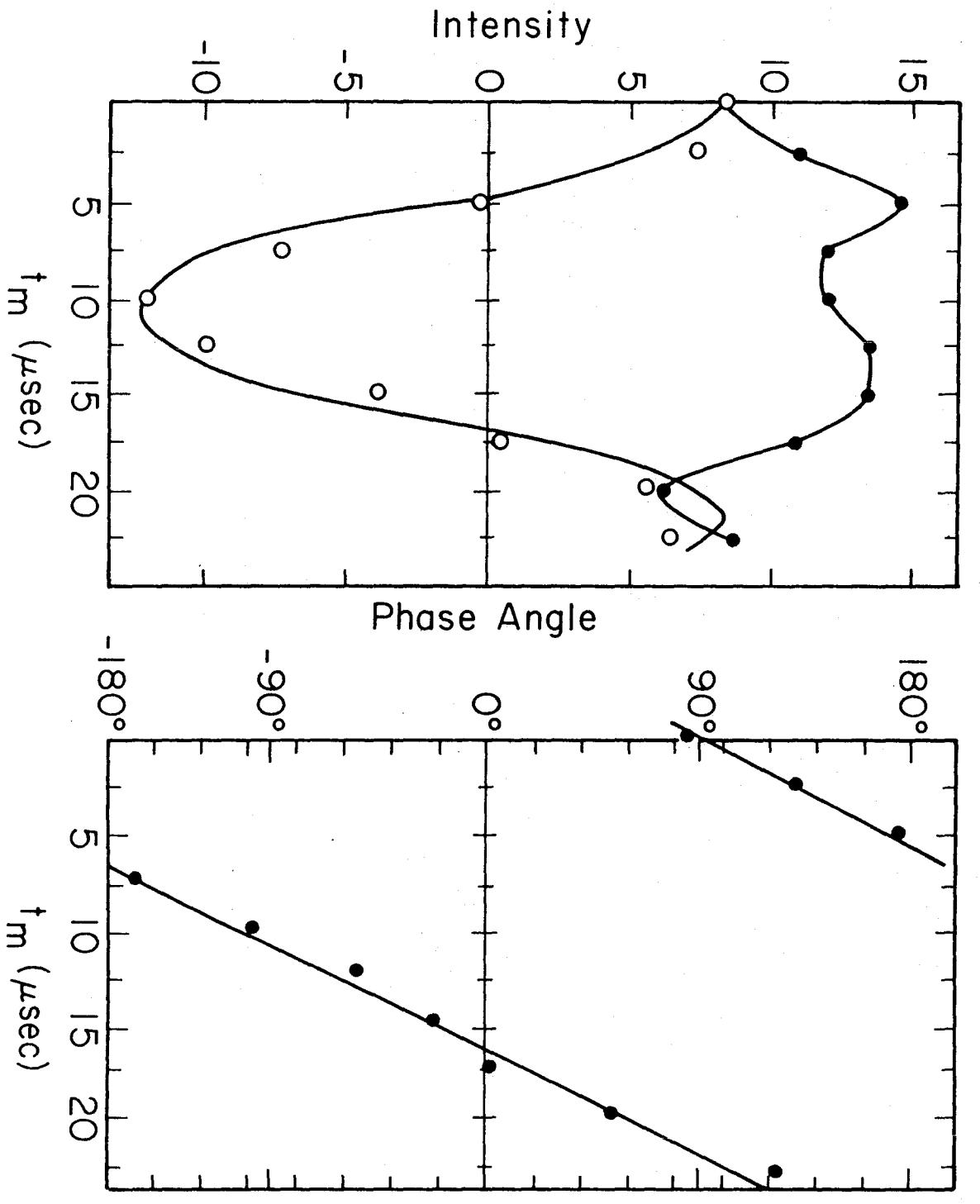
Intensity
15
10
5
0
-5
-10
Phase Angle
180°
90°
0°
-90°
-180°
5
10
15
20
t_m (μsec)

XBL 764-1514

value

$$X = \rho \sin 2\varepsilon \cos\varepsilon \cos\omega t - \rho \cos 2\varepsilon \sin\varepsilon \tag{149}$$

where

$$\rho = \beta_1 \frac{1}{2} \frac{\omega_1^2}{\omega_Q} \gamma_S \, tr(S^2_{X,1}) \tag{150}$$

from equation (112) is shown as the solid line with ε calculated from the experimental parameters, $\varepsilon = 42°$, $\frac{\omega_Q}{2\pi} = 35.2$, $\frac{\omega_e}{2\pi} = 47.7$ kHz, τ for 180° pulse = 10.5 μsec and ρ was calculated by fitting the curve to the initial point. As can be seen the behavior of the phase and the X component are quite in line with the theory. The total intensity on the other hand is very sensitive in its shape to imperfections. These imperfections are generated by the finiteness of the magic pulse in that the term from the density matrix in $(S_{Y,3}-S_{Z,3})$ will also be affected.

Another cause of the discrepancy may be the simultaneous cross polarization due to off resonance irradiation, that is, a Provotorov type cross relaxation. In an attempt to judge the magnitude of other cross polarization mechanisms the following preliminary experiment was performed. The magic pulse experiment was repeated but without the X phase mixing pulse. That is the thermal mixing was between the dipolar reservoir of the protons and the quadrupolar and dipolar reservoirs of the deuteriums. A signal was obtained, with a significant intensity, which was 90° out of phase with the signal derived from the experiment with the mixing pulse. Further work is needed in this area to fully characterize these mechanisms for cross polarization.

4. Double Quantum Cross Polarization Dynamics

We wish to verify that the rotating frame heat capacity of the double quantum transition is simply that of the equivalent spin ½ system where

$$C_{eS} = N_S \frac{1}{2} (2S+1) \gamma_{eS}^2 \qquad \text{and } \gamma_{eS}^2 = \frac{\omega_1}{\omega_Q} \gamma_S \tag{151}$$

The experiment was performed on resonance for both the protons and deuteriums so that,

$$\omega_{eS} = \omega_{1S} \tag{152}$$

the deuterium magnetization was measured directly in an ADRF cross polarization. We must be very careful at this point to know exactly how much of the polarization we are measuring. We therefore use a -X magic pulse to transform all of the polarization in the X-spin frame so that it is directly observable. This is accomplished by adjusting -X pulse length and phase detector for a maximum signal. Reference to equation (112) and (113) shows that we can only recover one half of the polarization in this way.

The cross polarization curve obtained with this magic pulse is shown in Figure 41. The experimental parameters are

$$\frac{\omega_{1S}}{2\pi} = 17.2 \text{ kHz}, \qquad T_L = -35 \pm 1°C, \qquad t_M(-X) = 12.5 \ \mu\text{sec} \tag{153}$$

In order to extract the heat capacity and cross polarization time all of the relaxation parameters and H_L, the proton local field, must be measured. The proton relaxation time T_{1D} was measured in the standard manner, ADRF

Figure 41. Cross polarization curve for D-1-benzene at 35 ± 1° C. The parameters used were $\frac{\omega_{1S}}{2\pi}$ = 17.2 kHz, T_L = 35 ± 1°C, and the magic pulse time was $t_M(-X)$ = 12.5 μsec. The solid curve is the fit to the general cross relaxation equation, equation (156).

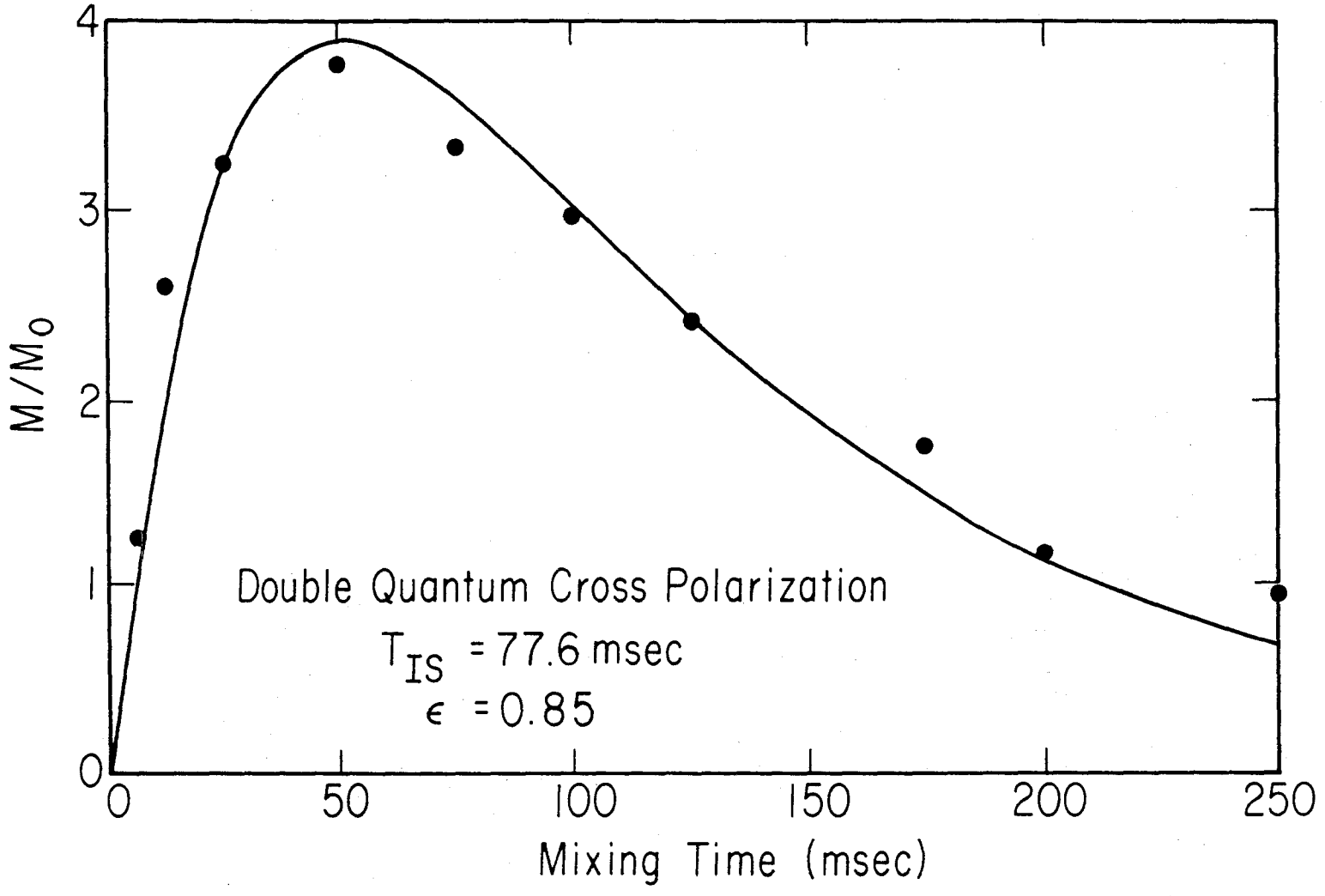

XBL 7511-9417

followed at time τ by a 45° probing pulse. These results are shown in Figure 42. The experiment was done at -35 ± 1°C. Since the relaxation times are quite sensitive to temperature it was necessary to control the temperature fairly precisely. Linear least squares gives T_{1D} = 0.30 ± .01 sec. The equivalent of $T_{1\rho}$ for the double quantum transition was measured using the pulse sequence in Figure 43. The deuteriums are cross polarized for a time t, the proton 45° pulse then destroys the dipolar order of the proton reservoir after which the deuterium order decays for a time τ before it is directly monitored. The results of the experiment at -35 ± 1°C are shown in Figure 44 for $H_{1S} \cong 14.7$ kHz $\cong$ 26.3 Gauss. The cross polarization time was 50 msec. Linear least squares gave

$$T_{1\rho} = 4.3 \pm 1. \text{ msec.} \tag{154}$$

The proton local field H_L, was determined from the proton line width, which was assumed to be Gaussian, through the formulas,[31,32]

$$\delta = 1.18 \quad M_2 \quad , \qquad H_L^2 = \frac{1}{3} M_2 \tag{155}$$

where δ is the halfwidth at half maximum, and M_2 is the second moment of a Gaussian line. The local field derived in this way is the local field in the rotating frame. We can now fit the cross polarization curve to equation (41) of Chapter 1 to extract ε, the ratio of the heat capacities, and T_{IS}, the cross polarization time. Since T_{1D} for the protons is so short for benzene we must solve equation (41) in its full form. A closed form expression was not derived, but instead the system of equations was solved exactly (not by interpolation or integration) by computer. The solution of the equation

Figure 42. Proton dipolar relaxation time T_{1D} for D-1-benzene at 35 ± 1°C. The pulse sequence used was ADRF (for 2 msec) followed after a time τ with a 45° pulse. The solid line is the linear least squares fit to the data.

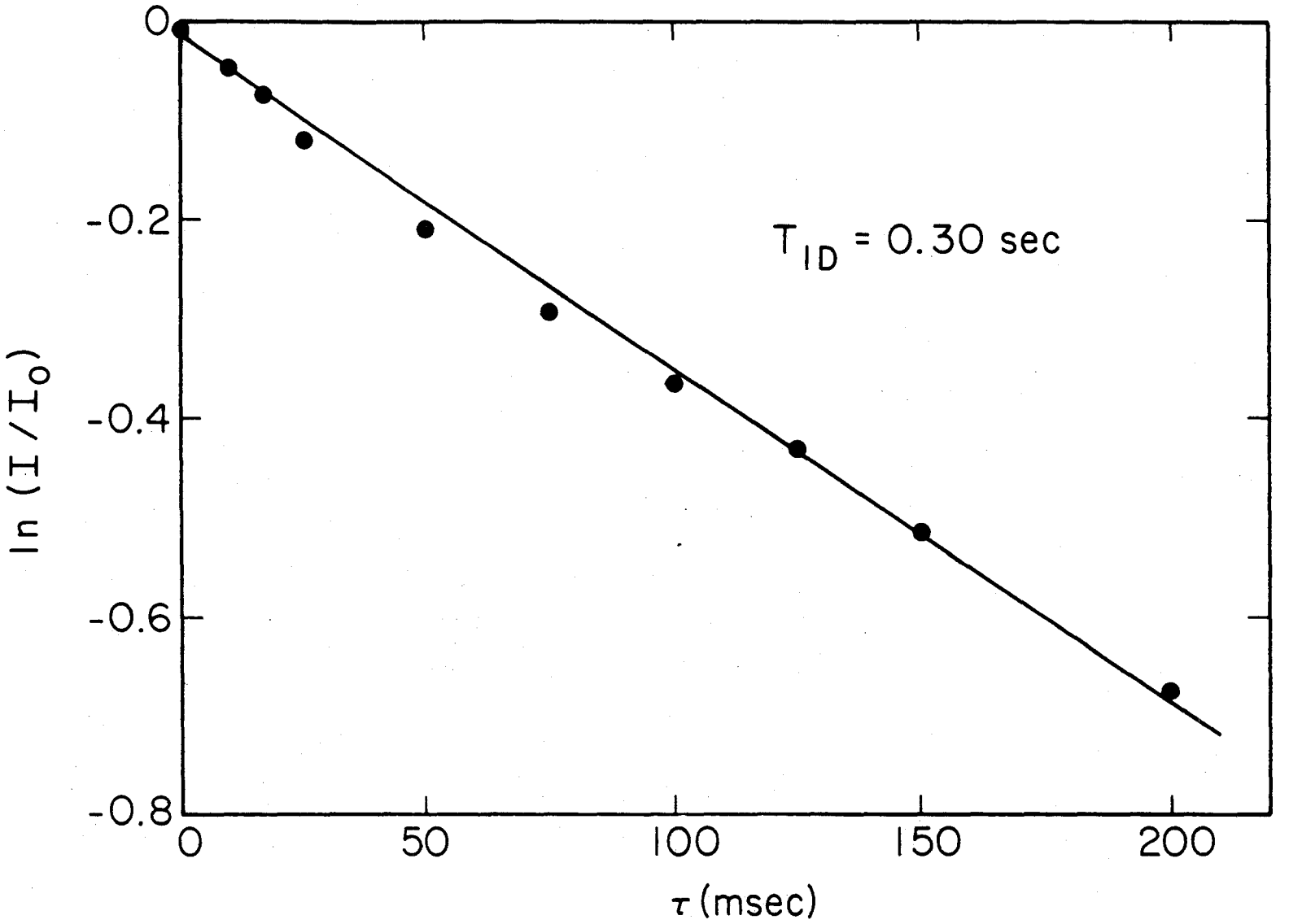

XBL 764-1512

Figure 43. Deuterium rotating frame relaxation time, $T_{1\rho}$, pulse sequence. The double quantum coherence is prepared by a normal cross polarization for time t after which the proton dipolar order is destroyed with a 45° pulse. The spin locked deuteriums are allowed to evolve for a time t before monitoring the polarization.

Double Quantum $T_{1\rho}$

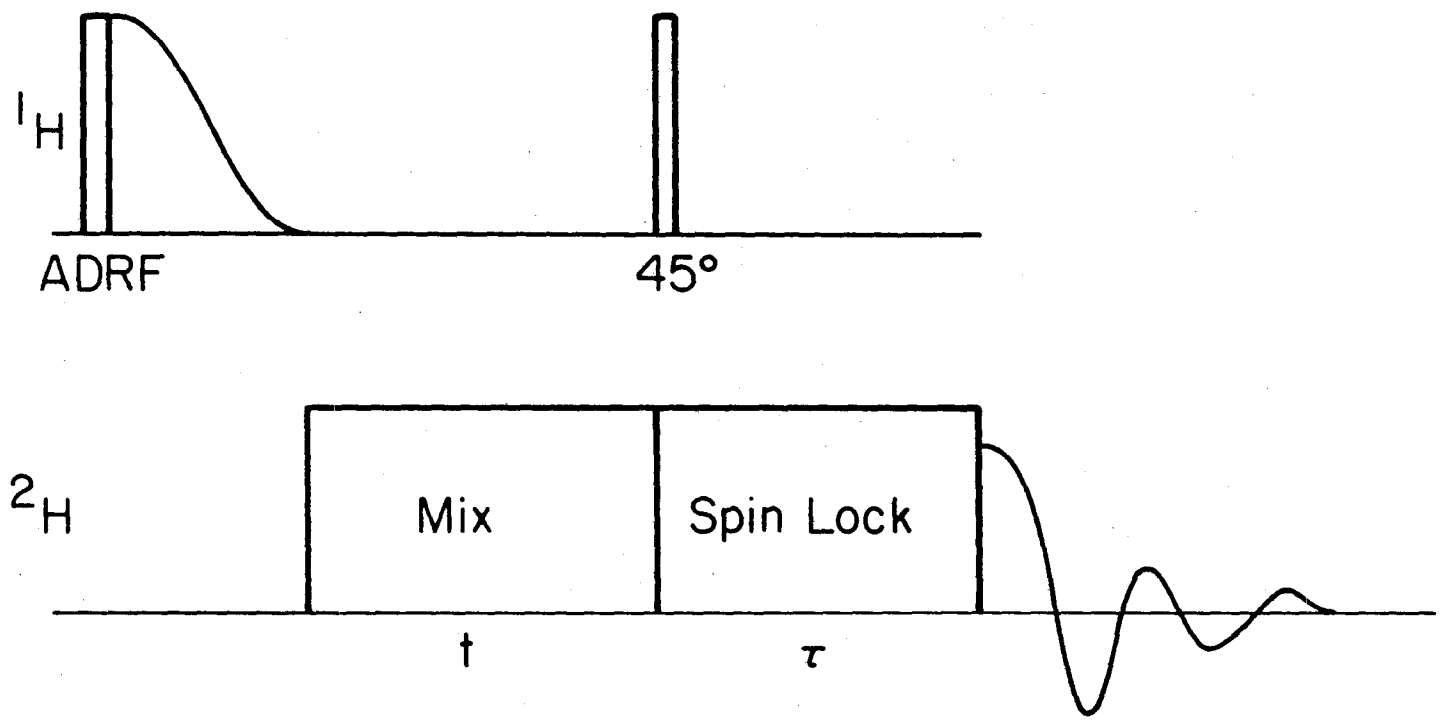

XBL 765-1979

Figure 44. Deuterium double quantum $T_{1\rho}$ using the pulse sequence in Figure 43. The deuterium field strength was ω_{1S} = 17.2 kHz the cross polarization time was 50 msec. The temperature was 35 ± 1°C. The solid line is the linear least squares fit to the data.

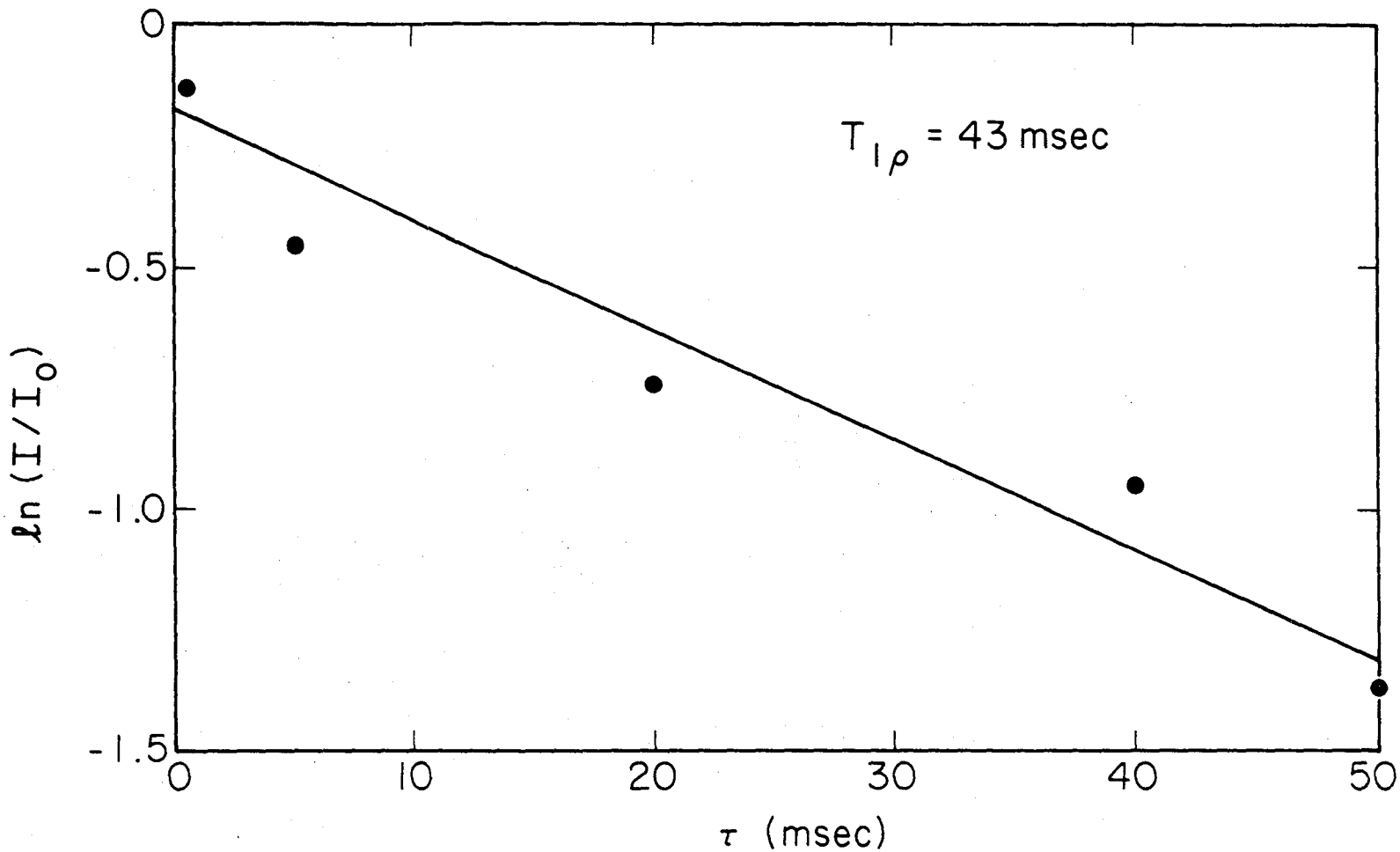

NBL 764-1510

$$\frac{d}{dt}\,\underset{\sim}{v} = \underset{\sim}{a} + \rho \underset{\sim}{v} \tag{156}$$

where

$$\underset{\sim}{v} = \begin{pmatrix} \beta_I \\ \beta_S \end{pmatrix} \qquad \underset{\sim}{a} = \begin{pmatrix} \beta_L/T_{1D} \\ \beta_L/T_{1\rho} \end{pmatrix}$$

$$\rho = \begin{pmatrix} -(\varepsilon/T_{IS} + \frac{1}{T_{1D}} & \varepsilon/T_{IS} \\ \frac{1}{T_{IS}} & -(\frac{1}{T_{IS}} + \frac{1}{T_{1\rho}}) \end{pmatrix}$$

with boundary conditions $\underset{\sim}{v}(0) = \begin{pmatrix} \beta_L \; \mu_0 \frac{H_0}{H_L} \\ 33 \end{pmatrix}$ where μ is the efficiency of the demagnetization, is given by,

$$\underset{\sim}{v} = De^{\Lambda t}\, D^{-1}\, \underset{\sim 0}{v} + D(-1-e^{\Lambda t})D^{-1}\, D\Lambda^{-1}\, D^{-1}\, \underset{\sim}{a} \tag{157}$$

Λ is obtained by diagonalizing ρ,

$$\Lambda = D^{-1}\, \rho\, D, \qquad \Lambda = \begin{pmatrix} \lambda_- & 0 \\ 0 & \lambda_+ \end{pmatrix}$$

where D is found explicitly to be

$$D = \begin{pmatrix} 1 & 1 \\ \frac{-\rho_{21}}{\rho_{22}-\lambda_-} & \frac{-\rho_2}{\rho_{22}-\lambda_+} \end{pmatrix}$$

and

$$\lambda_- = \frac{1}{2}(\rho_{11}+\rho_{22} - \sqrt{(\rho_{11}+\rho_{22})^2 - 4(\rho_{11}\rho_{22} - \rho_{21}\rho_{12})}$$

$$\lambda_+ = \frac{1}{2}(\rho_{11}+\rho_{22} + \sqrt{(\rho_{11}+\rho_{22})^2 - 4(\rho_{11}\rho_{22} - \rho_{21}\rho_{12})}$$

The deuterium magnetization is normalized to the FID for this experiment, and it is related to these solutions by

$$\frac{2M(t)}{M^{(o)}} = \frac{\beta_S \quad C_S^{DQ} \quad H_{1S}}{\beta_L \quad C_S^{SB} \quad H_0} \tag{158}$$

where $M^{(o)}$ is the magnetization for a normal FID and

where the superscripts remind us that the Curie constants contain the γ_{eS} which is appropriate for the experiment performed, and

$$\frac{C_S^{DQ}}{C_S^{S}} = \frac{\omega_1}{\omega_Q} \tag{159}$$

giving:

$$\frac{2M(t)}{M^{(o)}} = \frac{\beta_S}{\beta_L} \frac{\omega_1^2/\omega_Q}{\omega_0} \tag{160}$$

The factor of 2 is introduced to take into account that we observe only ½ of the total polarization. The cross polarization curve is then fit, knowing T_{1D}, $T_{1\rho}$, β_L, H_{1S}, H_L and H_0 and assuming $\mu = 0.95$ which was obtained in the same way as in the carbon-13 cross polarization experiments (see Chapter 1, Section IV C.1). The values of ε and T_{IS} were varied so as to minimize the deviations by trial and error. The results are for the ratio of the heat capacities:

$$\varepsilon\eta^2 = \varepsilon \left(\frac{H_{1S}}{H_2}\right)^2 = \frac{N_S}{N_I} \frac{2}{3} \frac{\gamma_{eS}^2}{\gamma_I^2} \left(\frac{H_{1S}}{H_2}\right)^2 = 0.85 \pm .05 \tag{161}$$

and T_{IS} = 77.6 msec.

Using $\gamma_{eS} = (\omega_1/\omega_Q)\gamma_S$, we derive the theoretical value $\varepsilon\eta^2 = 1.18$. These results are in good agreement, and we note that there were only 2

variable parameters used to produce the fit. Note that if $\gamma_{eS} = \sqrt{2}\,\gamma_S$ then ε would have been 10.3. So as expected the rotating frame heat capacity is smaller than for the single quantum case.

VII Discussion

A. Spectroscopy

We must be somewhat careful, and point out that the normal Fourier transform relation does not hold for our form of double quantum spectroscopy. That is, the time responses given by the double quantum decay is not the Fourier transform of the continuous wave absorption experiment, this is easily seen since the double quantum decay is at frequency $2\delta\omega$ while the continuous wave absorption occurs at $\omega_0 + \delta\omega$. However the double quantum decay is related to the absorption spectrum, which would be obtained if $\omega_Q = 0$, in the rotating frame by the Fourier transform relation, This is easily shown since in the rotating frame the double quantum transition behaves exactly as if it were a normal spin ½ transition.

The inclusion of second order effects for the quadrupole coupling must be discussed since they can shift the m = 1 and -1 levels differently. This will effect the accuracy of both double quantum spectroscopy and QSS. A rough calculation of the second order shift for the oxalic acid experiment indicates that it is less than the uncertainty, i.e., $\simeq$ 1.5 ppm. This is true because the quadrupole coupling for the two orientations was relatively small. However for more accurate work, and for cases with the maximum quadrupole couplings the second order shifts must be calculated explicitly. This requires no new information. The second order correction is given as[31]

$$E_m^{(2)} = -\hbar \left(\frac{\omega_Q^2}{12\,\omega_0}\right) m \left[\frac{3}{2}\mu^2(1-\mu^2)(8m^2-4I(I+1)+1) + \frac{3}{8}(1-\mu^2)^2(-2m^2+2m(I(I+1))-1)\right. \tag{162}$$

where $\mu = \cos\theta_Q$

QSS and double quantum spectroscopy are seen to give a great advantage in that they can actually separate the spectra of species with very similar or equal chemical shifts. This can occur in a number of ways. The most general is that the quadrupole coupling is much greater than the chemical shift in magnitude in comparison with the line width, which is the same for both cases. For example if two species have slightly different chemical shifts which are not resolvable because of the linewidth we may still be able to separate the quadrupole satellites of the two species because their quadrupole splittings will be much larger and then we can apply one of the new spectroscopic techniques to the satellites individually. This increase in discrimination can also come about through (a) differences in quadrupole coupling size between the two species, (b) differences in orientation dependence or (c) differences in motional averaging. A case in point for the latter is seen in our oxalic acid experiments where the water satellites disappear completely in some orientations leaving only the carboxyl satellites.

For single crystals it may be preferable to carry out any experiment with QSS rather than double quantum spectroscopy, since it is easier and faster, with the time savings perhaps an order of magnitude or more. For powders there is little choice and work is proceeding towards developing better double quantum pulse sequences to handle them. The water of hydration in oxalic acid is an interesting case though in that FTDQS achieves much better resolution; this comes about because the chemical shielding is totally averaged while the quadrupole interaction is not. A dramatic illustraction of this is the fact that the linewidth of the water peak in Figure 28 is the same as for the carboxyl line. The water

satellites in the normal FID Figure 23 for this same orientation are approximately an order of magnitude larger than the carboxyl satellites. DQS yields then an order of magnitude increase in resolution, indicating its usefulness for special cases.

An exciting extension of this work would be the observation of oxygen 17 and nitrogen 14 chemical shifts. Nitrogen 14 is spin 1 and the extension of our theory is immediate. It's quadrupole moment is 10 times bigger than deuterium's however, necessitating a different detection technique, perhaps that of Hatanaka *et al.* Oxygen 17, spin $\frac{5}{2}$, has a quadrupole coupling also of the same order as nitrogen, but the electric field gradients may be somewhat smaller than deuterium's for some classes of compounds.

B. Cross Polarization

Many of the inconsistencies between theory and experiment are basically the result of the finite size of the deuterium rf field strength. One way to overcome these inconsistencies is of course to use more deuterium power, but more satisfying will be the development of more complete solution for the time evolution for arbitrary rf strength, by calculations on a computer. Such a program has been written and is now being used to fill in the details missing from our more ideal closed form solutions. This should clear up the difficulties with the observed response to a magic pulse.

The simultaneous occurence of other cross polarization mechanisms, which may be a difficulty for the magic pulse experiments, needs to be pursued further also. The preliminary experiment performed, ADRF cross polarization without a deuterium rf field, should be expanded upon. However

we judge these effects to be somewhat minor in their importance.

More problematic is our attempt to explain the asymmetry for the indirect cross polarization experiments for a variable deuterium rf frequency. The effect of the room temperature equilibrium magnetization can easily be avoided by it's destruction before the cross polarization is begun. This is a simple measure and it will be pursued shortly.

Taken in total, however, the experimental results seem to agree quite well with our theory. They corroborate well our idea of the satellites and double quantum transitions as fictitious spin ½ systems with effective γ's. In addition, the indirect detection methods are seen to provide a new way to find correlation times for the dipolar state fluctuations. To judge the accuracy of our determinations we note that the SL and ADRF correaltion times are relatively close to each other, as expected. In particular,[23] (see Chapter 1 for definitions, equations (61) and (61c)):

$$\frac{\tau^2_{c,SL}}{\tau^2_{c,ADRF}} = \frac{4}{5}\,\frac{S_1S_2-S_4}{S_1S_2+\frac{8}{5}S_4} \tag{163}$$

If $S_1S_2 >> S_4$ then

$$\frac{\tau_{c,SL}}{\tau_{c,ADRF}} = 0.894 \tag{164}$$

Experimentally we find

$$\frac{\tau_{c,SL}}{\tau_{c,ADRF}} = \frac{418\ \mu\text{sec}}{577\ \mu\text{sec}} = 0.724 \tag{165}$$

From Table 1, Chapter 1, S_1S_2/S_4 ranges from ≈ 5-10. With this under

consideration $\tau_{c,SL}/\tau_{c,ADRF}$ ranges from .696 to .788. Our experimental result is then seen to be quite reasonable.

C. Chemical Shielding Tensor

We find a value for the total anisotropy of the carboxyl deuteron in α-oxalic acid dihydrate to be

$$\Delta\sigma = 32 \pm 3 \text{ ppm} \tag{166}$$

The most shielded direction is along the hydrogen bond direction, as found by virtue of the alignment with the EFG tensor. The large size of this anisotropy is undoubtably due to the extremely short hydrogen bond $r_{O-O} = 2.5$ Å. Our anisotropy is somewhat larger than Yeung's,[34] of 25 ppm. Our $\sigma_{\perp} = 27$ ppm with respect to adamantane agrees quite well with Haeberlen's estimate of ≈ 28 ppm.[35] In Table 6 are a number of other carboxyl anisotropies from other studies for comparison.

At this point we should exercise a little caution, in that we must realize that the substitution of a deuterium for a proton in a hydrogen bond may have a large effect. (Note added in proof: It is difficult to grow a mouse which is more than 30% deuterated, presumably due to hydrogen bond perturbations). But this information is in itself very useful and can now be studied using NMR. We note however that the agreement between our work and Haeberlen's proton study argue against any large effect for the sample we studied. The effect of substitution of deuterium in other types of bonds can be expected to be much less critical, that being a very small effect due to the change in the vibrational averaging.

Table 6. Carboxyl chemical shielding tensor anisotropies

Compound	Ref	anisotropy	hydrogen bond partner	bond distance
butynedoic acid	36	20 ± 2	dimer	2.668[46]
squaric	36	22 ± 2	dimer	2.55[44]
oxalic acid dihydrate	35	≈ 28	water	2.52
oxalic acid anhydrous	35	17.8	dimer	2.71[43]
malonic	35	18	dimer	2.71 and 2.68[40]
succinic	35	19	dimer	2.64[41]
fumaric	35	16.8	dimer	2.684 ± .002[45]
maleic	35	25.8	itself	2.46 inter. 2.75[42]
phthalic	35	22	dimer	2.67 ± .05 [39]
oxalic acid dihydrate	34	25	water	2.52

Appendix 2.1 Transformation Properties of the Fictitious Spin ½ Operators

In this section all of the possible transformations generated by the fictitious spin ½ operators are given. Using these relations we calculate the effect of an r.f. pulse upon the density matrix for several special cases.

Given an operator ρ, we may in general expand it in terms of the 9 fictitious spin ½ operators which are used as a basis set.

$$\rho = \sum_{p,i} a_{p,i} S_{p,i} \tag{A2.1-1}$$

A rotation about any axis defined by one of the operators in the basis set is given by

$$R_p(\theta,i) \quad S'_{p,i} = U_{p,i} S_{p,i} U^{+}_{p,i} = \sum_{ip} G_{p,i} S_{p,i} \tag{A2.1-2}$$

The knowledge of all of the transformations of this form then completely describes the transformation properties of any operator ρ.

In Table 7 we repeat the definitions of the fictitious spin operators and the important commutation relations for easy reference. In Table 8 are listed all of the unitary transformation matrices generated by the 9 operators. Their action upon the complete set of "basis operators", the 9 operators themselves is listed in Table 9. Table 10 gives the transformations for some specific angles.

The utility of these transformations are easily shown by the following examples. We wish to calculate the effect of an r.f. pulse upon a density matrix for two extremes $\Delta\omega = \omega_Q + \delta\omega$ and $\Delta\omega = 0$. Consider an initial density matrix

$$\sigma_S^* = C\ S_{Z,1} \tag{A2.1-3}$$

which corresponds to equilibrium in the laboratory frame. We now apply a pulse of strength $\omega_1 (\omega_1 << \omega_Q)$ at frequency $\Delta\omega = \omega_Q + \delta\omega$ and duration t. The Hamiltonian which governs the time dependence is,

$$H_S^* = -2(\delta\omega + \omega_Q)S_{Z,1} + \frac{2}{3}\omega_Q(S_{X,3} - S_{Y,3}) - 2\omega_1\ S_{X,1} \tag{A2.1-4}$$

We now apply the rotations $R_Z(90,2)$ and $R_X(\phi,2)$ and rearrange using equation (2-10) in analogy to the derivation of equation (2-83), giving

$$H_S^* = -\omega_e\ S''_{X,3} - \frac{4}{3}\omega_Q(S''_{y,3} - S''_{Z,3}) \tag{A2.1-5}$$

with ϕ defined by $\tan\phi = \frac{\sqrt{2}\ \omega_1}{\delta\omega}$.

We have assumed $\omega_1 << \omega_Q$ and $\delta\omega << \omega_Q$, in order to ignore the term in $S_{Y,2}$ in comparison with the term in $S_{Y,3}$ (see equations (18) and (19)), and in order to approximate the quadrupolar term by ignoring $\delta\omega$ (see equation (24)). The effective field is

$$\omega_e = (\delta\omega^2 + 2\omega_1^2)^{1/2}$$

and we note that

$$\sin\phi = \frac{\sqrt{2}\ \omega_1}{\omega_e} \quad \text{and} \quad \cos\phi = \frac{\delta\omega}{\omega_e}$$

Transforming the density matrix into the same frame gives,

$$\sigma^*_{(o)} = -c\ S''_{Z,3} + \frac{c}{2}\sin\phi\ \ S''_{X,1} - c\ \sin^2\phi/2\ S''_{X,3} \tag{A2.1-6}$$

We must now solve

$$\sigma^*(t) = e^{-i H_S^* t} \sigma^{*''}(o) e^{iH_S^{*''} t} \tag{A2.1-7}$$

This is solved using Table 9 yielding

$$\sigma^{*''}(t) = - c S''_{Z,3} - c \sin^2\phi/2 S''_{X,3} + \frac{c}{2} \sin\phi \{S''_{x,1} \cos\omega_e t + S''_{X,2} \sin\omega_e t\} \quad . \tag{A2.1-8}$$

The rotations $R_X(-\phi,2)$ and $R_Z(-90,2)$ are now applied to bring σ back into the untilted rotating frame. The results are given in Table 11. The effect of a pulse at frequency $\Delta\omega = 0$ for arbitrary strength ω_1 is solved in an analogous way, and the density matrix immediately following such a pulse is given in Table 12. We include for completeness the effect of such a pulse on all possible density matrices.

Table 7. Fictitious spin ½ operators

Basis set: $|X\rangle = \frac{}{2}(|+1\rangle - |-1\rangle)$

$|Y\rangle = \frac{}{2}(|+1\rangle + |-1\rangle$

$|Z\rangle = |0\rangle$

Matrix Representation of Operators:

$$S_{Z,1} = \frac{1}{2}\begin{pmatrix} 0 & i & 0 \\ -i & 0 & 0 \\ 0 & 0 & 0 \end{pmatrix} \quad S_{Z,2} = \frac{1}{2}\begin{pmatrix} 0 & 1 & 0 \\ 1 & 0 & 0 \\ 0 & 0 & 0 \end{pmatrix}. \quad S_{Z,3} = \frac{1}{2}\begin{pmatrix} 1 & 0 & 0 \\ 0 & -1 & 0 \\ 0 & 0 & 0 \end{pmatrix}$$

$$S_{Y,1} = \frac{1}{2}\begin{pmatrix} 0 & 0 & 1 \\ 0 & 0 & 0 \\ 1 & 0 & 0 \end{pmatrix} \quad S_{Y,2} = \frac{1}{2}\begin{pmatrix} 0 & 0 & i \\ 0 & 0 & 0 \\ -i & 0 & 0 \end{pmatrix} \quad S_{Y,3} = \frac{1}{2}\begin{pmatrix} -1 & 0 & 0 \\ 0 & 0 & 0 \\ 0 & 0 & 1 \end{pmatrix}$$

$$S_{X,1} = \frac{1}{2}\begin{pmatrix} 0 & 0 & 0 \\ 0 & 0 & 1 \\ 0 & 1 & 0 \end{pmatrix} \quad S_{X,2} = \frac{1}{2}\begin{pmatrix} 0 & 0 & 0 \\ 0 & 0 & -i \\ 0 & i & 0 \end{pmatrix} \quad S_{X,3} = \frac{1}{2}\begin{pmatrix} 0 & 0 & 0 \\ 0 & 1 & 0 \\ 0 & 0 & -1 \end{pmatrix}$$

Quadrupole Hamiltonian:

$$H^*_S = -2\Delta\omega\, S_{Z,1} - 2\omega_1 S_{X,1} + \omega_r S_{r,3} - Er(S_{p,3} - S_{q,3})$$

with $\omega_X = -\omega_Y = \omega_Q$, $\omega_Z = 0$, $E_X = E_Y = \frac{1}{3}\omega_Q$, $E_Z = -\frac{2}{3}\omega_Q$

Table 7 continued

Commutation relations:

$$[S_{p,i}, S_{p,j}] = i\, S_{p,k} \qquad i;\ j,k \text{ cyclic}$$

$$[S_{p,3}, S_{q,3}] = 0 \qquad \text{all } p,q$$

$$[\{S_{p,3} - S_{q,3}\}, S_{r,i}] = 0 \qquad \text{all } i,\ p \neq q \neq r\ .$$

Table 8. Transformations generated by the fictitious spin ½ operators

$$U_{X,1} = \begin{pmatrix} 1 & 0 & 0 \\ 0 & \cos\theta/2 & -i\sin\theta/2 \\ 0 & -\sin\theta/2 & \cos\theta/2 \end{pmatrix} \qquad U_{X,2} = \begin{pmatrix} 1 & 0 & 0 \\ 0 & \cos\theta/2 & -\sin\theta/2 \\ 0 & \sin\theta/2 & \cos\theta/2 \end{pmatrix}$$

$$U_{X,3} = \begin{pmatrix} 1 & 0 & 0 \\ 0 & e^{-i\theta/2} & 0 \\ 0 & 0 & e^{i\theta/2} \end{pmatrix}$$

$$U_{Y,1} = \begin{pmatrix} \cos\theta/2 & 0 & -i\sin\theta/2 \\ 0 & 1 & 0 \\ -i\sin\theta/2 & 0 & \cos\theta/2 \end{pmatrix} \qquad U_{Y,2} = \begin{pmatrix} \cos\theta/2 & 0 & \sin\theta/2 \\ 0 & 1 & 0 \\ -\sin\theta/2 & 0 & \cos\theta/2 \end{pmatrix}$$

$$U_{Y,3} = \begin{pmatrix} e^{i\theta/2} & 0 & 0 \\ 0 & 1 & 0 \\ 0 & 0 & e^{-i\theta/2} \end{pmatrix}$$

$$U_{Z,1} = \begin{pmatrix} \cos\theta/2 & \sin\theta/2 & 0 \\ -\sin\theta/2 & \cos\theta/2 & 0 \\ 0 & 0 & 1 \end{pmatrix} \qquad U_{Z,2} = \begin{pmatrix} \cos\theta/2 & -i\sin\theta/2 & 0 \\ -i\sin\theta/2 & \cos\theta/2 & 0 \\ 0 & 0 & 1 \end{pmatrix}$$

$$U_{Z,3} = \begin{pmatrix} e^{-i\theta/2} & 0 & 0 \\ 0 & e^{i\theta/2} & 0 \\ 0 & 0 & 1 \end{pmatrix}$$

$$U_{X,3-Y,3} = \begin{pmatrix} e^{-i\theta/2} & 0 & 0 \\ 0 & e^{-i\theta/2} & 0 \\ 0 & 0 & e^{i\theta} \end{pmatrix} \qquad U_{Y,3-Z,3} = \begin{pmatrix} e^{i\theta} & 0 & 0 \\ 0 & e^{-i\theta/2} & 0 \\ 0 & 0 & e^{-i\theta/2} \end{pmatrix}$$

$$U_{Z,3-X,3} = \begin{pmatrix} e^{-i\theta/2} & 0 & 0 \\ 0 & e^{i\theta} & 0 \\ 0 & 0 & e^{-i\theta/2} \end{pmatrix}$$

Table 9. Rotations generated by Fictitious spin ½ operators $R_p(\theta,i)$ is given by $U_{p,i}\ S\ U^+_{p,i}$

$R_X(\theta,1)$

$$S_{X,1} \to S_{X,1}$$

$$S_{X,2} \to \cos\theta\ S_{X,2} + \sin\theta\ S_{X,3}$$

$$S_{X,3} \to -\sin\theta\ S_{X,2} + \cos\theta\ S_{X,3}$$

$$S_{Y,1} \to \cos\theta/2\ S_{Y,1} + \sin\theta/2\ S_{Z,1}$$

$$S_{Y,2} \to \cos\theta/2\ S_{Y,2} - \sin\theta/2\ S_{Z,2}$$

$$S_{Y,3} \to S_{Y,3} + 1/2\ \sin\theta\ S_{X,2} + \sin^2\theta/2\ S_{X,3}$$

$$= \frac{1}{2}\ (S_{X,2}\ \sin\theta - S_{X,3}\ \cos\theta) + \frac{1}{2}\ (S_{Y,3} - S_{Z,3})$$

$$S_{Z,1} \to \cos\theta/2\ S_{Z,1} - \sin\theta/2\ S_{Y,1}$$

$$S_{Z,2} \to \cos\theta/2\ S_{Z,2} + \sin\theta/2\ S_{Y,2}$$

$$S_{Z,3} \to S_{Z,3} + \frac{1}{2}\ \sin\theta\ S_{X,2} + \sin^2\theta/2\ S_{X,3}$$

$$= \frac{1}{2}\ (S_{X,2}\ \sin\theta - S_{X,3}\ \cos\theta) - \frac{1}{2}\ (S_{Y,3} - S_{Z,3})$$

$R_X(\theta,2)$

$$S_{X,1} \to \cos\theta\ S_{X,1} - \sin\theta\ S_{X,3}$$

$$S_{X,2} \to S_{X,2}$$

$$S_{X,3} \to \sin\theta\ S_{X,1} + \cos\theta\ S_{X,3}$$

$$S_{Y,1} \to \cos\theta/2\ S_{Y,1} - \sin\theta/2\ S_{Z,2}$$

$$S_{Y,2} \to \cos\theta/2\ S_{Y,2} - \sin\theta/2\ S_{Z,1}$$

$$S_{Y,3} \to S_{Y,3} - \frac{1}{2}\ \sin\theta\ S_{i,1} + \sin^2\theta/2\ S_{X,3}$$

$$= -\frac{1}{2}\ (S_{X,1}\ \sin\theta + S_{X,3}\ \cos\theta) + \frac{1}{2}\ (S_{Y,3} - S_{Z,3})$$

Table 9 continued

$$S_{Z,1} \rightarrow \cos\theta/2\ S_{Z,1} + \sin\theta/2\ S_{Y,2}$$

$$S_{Z,2} \rightarrow \cos\theta/2\ S_{Z,2} + \sin\theta/2\ S_{Y,1}$$

$$S_{Z,3} \rightarrow S_{Z,3} - \frac{1}{2}\sin\theta\ S_{X,} + \sin^2\theta/2\ S_{X,3}$$

$$= -\frac{1}{2}(S_{X,}\ \sin\theta + S_{X,3}\cos\theta) - \frac{1}{2}(S_{Y,3} - S_{Z,3})$$

$R_X(\theta,3)$

$$S_{X,1} \rightarrow \cos\theta\ S_{X,1} + \sin\theta\ S_{X,2}$$

$$S_{X,2} \rightarrow -\sin\theta\ S_{X,1} + \cos\theta\ S_{X,2}$$

$$S_{X,3} \rightarrow S_{X,3}$$

$$S_{Y,1} \rightarrow \cos\theta/2\ S_{Y,1} - \sin\theta/2\ S_{Y,2}$$

$$S_{Y,2} \rightarrow \cos\theta/2\ S_{Y,2} + \sin\theta/2\ S_{Y,1}$$

$$S_{Y,3} \rightarrow S_{Y,3}$$

$$S_{Z,1} \rightarrow \cos\theta/2\ S_{Z,1} - \sin\theta/2\ S_{Z,2}$$

$$S_{Z,2} \rightarrow \cos\theta/2\ S_{Z,2} + \sin\theta/2\ S_{Z,1}$$

$$S_{Z,3} \rightarrow S_{Z,3}$$

$R_Y(0,1)$

$$S_{X,1} \rightarrow \cos\theta/2\ S_{X,1} - \sin\theta/2\ S_{Z,1}$$

$$S_{X,2} \rightarrow \cos\theta/2\ S_{X,2} + \sin\theta/2\ S_{Z,2}$$

$$S_{X,3} \rightarrow S_{X,3} + \frac{1}{2}\sin\theta\ S_{Y,2} + \sin^2\theta/2\ S_{Y,3}$$

$$= \frac{1}{2}(S_{Y,2}\ \sin\theta - S_{Y,3}\cos\theta) - \frac{1}{2}(S_{Z,3} - S_{X,3})$$

Table 9 continued

$$S_{Y,1} \rightarrow S_{Y,1}$$

$$S_{Y,2} \rightarrow \cos\theta\ S_{Y,2} + \sin\theta\ S_{Y,3}$$

$$S_{Y,3} \rightarrow -\sin\theta\ S_{Y,2} + \cos\theta\ S_{Y,3}$$

$$S_{Z,1} \rightarrow \cos\theta/2\ S_{Z,1} + \sin\theta/2\ S_{X,1}$$

$$S_{Z,2} \rightarrow \cos\theta/2\ S_{Z,2} - \sin\theta/2\ S_{X,2}$$

$$S_{Z,3} \rightarrow S_{Z,3} + \frac{1}{2}\sin\theta\ S_{Y,2} + \sin^2\theta/2\ S_{Y,3}$$

$$= \frac{1}{2}(S_{Y,2}\sin\theta - S_{Y,3}\cos\theta) + \frac{1}{2}(S_{Z,3} - S_{X,3})$$

$R_Y(\theta,2)$

$$S_{X,1} \rightarrow \cos\theta/2\ S_{X,1} + \sin\theta/2\ S_{Z,2}$$

$$S_{X,2} \rightarrow \cos\theta/2\ S_{X,2} + \sin\theta/2\ S_{Z,1}$$

$$S_{X,3} \rightarrow S_{X,3} - \frac{1}{2}\sin\theta\ S_{Y,1} + \sin^2\theta/2\ S_{Y,3}$$

$$= -\frac{1}{2}(S_{Y,1}\sin\theta + S_{Y,3}\cos\theta) - \frac{1}{2}(S_{Z,3} - S_{X,3})$$

$$S_{Y,1} \rightarrow \cos\theta S_{Y,1} - \sin\theta\ S_{Y,3}$$

$$S_{Y,2} \rightarrow S_{Y,2}$$

$$S_{Y,3} \rightarrow \sin\theta\ S_{Y,1} + \cos\theta\ S_{Y,3}$$

$$S_{Z,1} \rightarrow \cos\theta/2\ S_{Z,1} - \sin\theta/2\ S_{X,2}$$

$$S_{Z,2} \rightarrow \cos\theta/2\ S_{Z,2} - \sin\theta/2\ S_{X,1}$$

$$S_{Z,3} \rightarrow S_{Z,3} - \frac{1}{2}\sin\theta\ S_{Y,1} - \sin^2\theta/2\ S_{Y,3}$$

$$= -\frac{1}{2}(S_{Y,1}\sin\theta + S_{Y,3}\cos\theta) + \frac{1}{2}(S_{Z,3} - S_{X,3})$$

Table 9 continued

$R_Y(\theta,3)$

$$S_{X,1} \rightarrow \cos\theta/2\ S_{X,1} - \sin\theta/2\ S_{X,2}$$

$$S_{X,2} \rightarrow \cos\theta/2\ S_{X,2} + \sin\theta/2\ S_{X,1}$$

$$S_{X,3} \rightarrow S_{X,3}$$

$$S_{Y,1} \rightarrow \cos\theta\ S_{Y,1} + \sin\theta\ S_{Y,2}$$

$$S_{Y,2} \rightarrow -\sin\theta\ S_{Y,1} + \cos\theta\ S_{Y,2}$$

$$S_{Y,3} \rightarrow S_{Y,3}$$

$$S_{Z,1} \rightarrow \cos\theta/2\ S_{Z,1} - \sin\theta/2\ S_{Z,2}$$

$$S_{Z,2} \rightarrow \cos\theta/2\ S_{Z,2} + \sin\theta/2\ S_{Z,1}$$

$$S_{Z,3} \rightarrow S_{Z,3}$$

$R_Z(\theta,1)$

$$S_{X,1} \rightarrow \cos\theta/2\ S_{X,1} + \sin\theta/2\ S_{Y,1}$$

$$S_{X,2} \rightarrow \cos\theta/2\ S_{X,2} - \sin\theta/2\ S_{Y,2}$$

$$S_{X,3} \rightarrow S_{X,3} + \frac{1}{2}\sin\theta\ S_{Z,2} + \sin^2\theta/2\ S_{Z,3}$$

$$= \frac{1}{2}(S_{Z,2}\sin\theta - S_{Z,3}\cos\theta) + \frac{1}{2}(S_{X,3} - S_{Y,3})$$

$$S_{Y,1} \rightarrow \cos\theta/2\ S_{Y,1} - \sin\theta/2\ S_{X,1}$$

$$S_{Y,2} \rightarrow \cos\theta/2\ S_{Y,2} + \sin\theta/2\ S_{X,2}$$

$$S_{Y,3} \rightarrow S_{Y,3} + \frac{1}{2}\sin\theta\ S_{Z,2} + \sin^2\theta/2\ S_{Z,3}$$

$$= \frac{1}{2}(S_{Z,2}\sin\theta - S_{Z,3}\cos\theta) - \frac{1}{2}(S_{X,3} - S_{Y,3})$$

Table 9 continued

$$S_{Z,1} \rightarrow S_{Z,1}$$

$$S_{Z,2} \rightarrow \cos\theta\ S_{Z,2} + \sin\theta\ S_{Z,3}$$

$$S_{Z,3} \rightarrow -\sin\theta\ S_{Z,2} + \cos\theta\ S_{Z,3}$$

$R_Z(\theta,2)$

$$S_{X,1} \rightarrow \cos\theta/2\ S_{X,1} - \sin\theta/2\ S_{Y,2}$$

$$S_{X,2} \rightarrow \cos\theta/2\ S_{X,2} - \sin\theta/2\ S_{Y,1}$$

$$S_{X,3} \rightarrow S_{X,3} - \frac{1}{2}\sin\theta\ S_{Z,1} + \sin^2\theta/2\ S_{Z,3}$$

$$= -\frac{1}{2}(S_{Z,1}\sin\theta + S_{Z,3}\cos\theta) + \frac{1}{2}(S_{X,3} - S_{Y,3})$$

$$S_{Y,1} \rightarrow \cos\theta/2\ S_{Y,1} + \sin\theta/2\ S_{X,2}$$

$$S_{Y,2} \rightarrow \cos\theta/2\ S_{Y,2} + \sin\theta/2\ S_{X,1}$$

$$S_{Y,3} \rightarrow S_{Y,3} - \frac{1}{2}\sin\theta\ S_{Z,1} + \sin^2\theta/2\ S_{Z,3}$$

$$= -\frac{1}{2}(S_{Z,1}\sin\theta + S_{Z,3}\cos\theta) - \frac{1}{2}(S_{X,3} - S_{Y,3})$$

$$S_{Z,1} \rightarrow \cos\theta\ S_{Z,1} - \sin\theta\ S_{Z,3}$$

$$S_{Z,2} \rightarrow S_{Z,2}$$

$$S_{Z,3} \rightarrow +\sin\theta\ S_{Z,1} + \cos\theta\ S_{Z,3}$$

$R_Z(\theta,3)$

$$S_{X,1} \rightarrow \cos\theta/2\ S_{X,1} - \sin\theta/2\ S_{X,2}$$

$$S_{X,2} \rightarrow \cos\theta/2\ S_{X,2} + \sin\theta/2\ S_{X,1}$$

Table 9 continued

$S_{X,3} \rightarrow S_{X,3}$

$S_{Y,1} \rightarrow \cos\theta/2\ S_{Y,1} - \sin\theta/2\ S_{Y,2}$

$S_{Y,2} \rightarrow \cos\theta/2\ S_{Y,2} + \sin\theta/2\ S_{Y,1}$

$S_{Y,3} \rightarrow S_{Y,3}$

$S_{Z,1} \rightarrow \sin\theta\ S_{Z,2} + \cos\theta\ S_{Z,1}$

$S_{Z,2} \rightarrow \cos\theta\ S_{Z,2} - \sin\theta\ S_{Z,1}$

$S_{Z,3} \rightarrow S_{Z,3}$

$R_{X-Y}(\theta,3)$

$S_{X,1} \rightarrow \cos\ 3/2\theta\ S_{X,1} + \sin\ 3/2\theta\ S_{X,2}$

$S_{X,2} \rightarrow \cos\ 3/2\theta\ S_{X,2} - \sin\ 3/2\theta\ S_{X,1}$

$S_{Y,1} \rightarrow \cos\ 3/2\theta\ S_{Y,1} - \sin\ 3/2\theta\ S_{Y,2}$

$S_{Y,2} \rightarrow \cos\ 3/2\theta\ S_{Y,2} + \sin\ 3/2\theta\ S_{Y,1}$

$R_{Y-Z}(\theta,3)$

$S_{Y,1} \rightarrow \cos\ 3/2\theta\ S_{Y,1} + \sin\ 3/2\theta\ S_{Y,2}$

$S_{Y,2} \rightarrow \cos\ 3/2\theta\ S_{Y,2} - \sin\ 3/2\theta\ S_{Y,1}$

$S_{Z,1} \rightarrow \cos\ 3/2\theta\ S_{Z,1} - \sin\ 3/2\theta\ S_{Z,2}$

$S_{Z,2} \rightarrow \cos\ 3/2\theta\ S_{Z,2} + \sin\ 3/2\theta\ S_{Z,1}$

Table 9 continued

$R_{Z-X}(\theta,3)$

$$S_{X,1} \rightarrow \cos 3/2\theta\ S_{X,1} - \sin 3/2\theta\ S_{X,2}$$

$$S_{X,2} \rightarrow \cos 3/2\theta\ S_{X,2} + \sin 3/2\theta\ S_{X,1}$$

$$S_{Z,1} \rightarrow \cos 3/2\theta\ S_{Z,1} + \sin 3/2\theta\ S_{Z,2}$$

$$S_{Z,2} \rightarrow \cos 3/2\theta\ S_{Z,2} - \sin 3/2\theta\ S_{Z,1}$$

Table 10 Special Rotations

	90°	180°	270°
$R_X(\theta,1)$			
$S_{X,1}$	$S_{X,1}$	$S_{X,1}$	$S_{X,1}$
$S_{X,2}$	$S_{X,3}$	$-S_{X,2}$	$-S_{X,3}$
$S_{X,3}$	$-S_{X,2}$	$-S_{X,3}$	$S_{X,2}$
$S_{Y,1}$	$1/\sqrt{2}\ S_{Y,1} + 1/\sqrt{2}\ S_{Z,1}$	$S_{Z,1}$	$-1/\sqrt{2}\ S_{Y,1} + 1/\sqrt{2}\ S_{Z,1}$
$S_{Y,2}$	$1/\sqrt{2}\ S_{Y,2} - 1/\sqrt{2}\ S_{Z,2}$	$-S_{Z,2}$	$-1/\sqrt{2}\ S_{Y,2} - 1/\sqrt{2}\ S_{Z,2}$
$S_{Y,3}$	$S_{Y,3} + \frac{1}{2} S_{X,2} + \frac{1}{2} S_{X,3}$	$-S_{Z,3}$	$S_{Y,3} - \frac{1}{2} S_{X,2} + \frac{1}{2} S_{X,3}$
$S_{Z,1}$	$1/\sqrt{2}\ S_{Z,1} - 1/\sqrt{2}\ S_{Y,1}$	$-S_{Y,1}$	$-1/\sqrt{2}\ S_{Z,1} - 1/\sqrt{2}\ S_{Y,1}$
$S_{Z,2}$	$1/\sqrt{2}\ S_{Z,2} + 1/\sqrt{2}\ S_{Y,2}$	$S_{Y,2}$	$-1/\sqrt{2}\ S_{Z,2} + 1/\sqrt{2}\ S_{Y,2}$
$S_{Z,3}$	$S_{Z,3} + \frac{1}{2} S_{X,2} + \frac{1}{2} S_{X,3}$	$-S_{Y,3}$	$S_{Z,3} - \frac{1}{2} S_{X,2} + \frac{1}{2} S_{X,3}$
$R_X(\theta,2)$			
$S_{X,1}$	$-S_{X,3}$	$-S_{X,1}$	$S_{X,3}$
$S_{X,2}$	$S_{X,2}$	$S_{X,2}$	$S_{X,2}$
$S_{X,3}$	$S_{X,1}$	$-S_{X,3}$	$-S_{X,1}$
$S_{Y,1}$	$1/\sqrt{2}\ S_{Y,1} - 1/\sqrt{2}\ S_{Z,2}$	$-S_{Z,2}$	$-1/\sqrt{2}\ S_{Y,1} - 1/\sqrt{2}\ S_{Z,2}$
$S_{Y,2}$	$1/\sqrt{2}\ S_{Y,2} - 1/\sqrt{2}\ S_{Z,1}$	$-S_{Z,1}$	$-1/\sqrt{2}\ S_{Y,2} - 1/\sqrt{2}\ S_{Z,1}$
$S_{Y,3}$	$S_{Y,3} - \frac{1}{2} S_{X,1} + \frac{1}{2} S_{X,3}$	$-S_{Z,3}$	$S_{Y,3} + \frac{1}{2} S_{X,1} - \frac{1}{2} S_{X,3}$
$S_{Z,1}$	$1/\sqrt{2}\ S_{Z,1} + 1/\sqrt{2}\ S_{Y,2}$	$S_{Y,2}$	$-1/\sqrt{2}\ S_{Z,1} + 1/\sqrt{2}\ S_{Y,2}$
$S_{Z,2}$	$1/\sqrt{2}\ S_{Z,2} + 1/\sqrt{2}\ S_{Y,1}$	$S_{Y,1}$	$-1/\sqrt{2}\ S_{Z,2} + 1/\sqrt{2}\ S_{Y,1}$
$S_{Z,3}$	$S_{Z,3} - \frac{1}{2} S_{X,1} + \frac{1}{2} S_{X,3}$	$-S_{Y,3}$	$S_{Z,3} + \frac{1}{2} S_{X,1} - \frac{1}{2} S_{X,3}$

Table 10 continued

$R_X(\theta,3)$

$S_{X,1}$	$S_{X,2}$	$-S_{X,1}$	$-S_{X,2}$
$S_{X,2}$	$-S_{X,1}$	$-S_{X,2}$	$S_{X,1}$
$S_{X,3}$	$S_{X,3}$	$S_{X,3}$	$S_{X,3}$
$S_{Y,1}$	$1/\sqrt{2}\ S_{Y,1} - 1/\sqrt{2}\ S_{Y,2}$	$-S_{Y,2}$	$-1/\sqrt{2}\ S_{Y,1} - 1/\sqrt{2}\ S_{Y,2}$
$S_{Y,2}$	$1/\sqrt{2}\ S_{Y,2} + 1/\sqrt{2}\ S_{Y,1}$	$+S_{Y,1}$	$-1/\sqrt{2}\ S_{Y,2} + 1/\sqrt{2}\ S_{Y,1}$
$S_{Y,3}$	$S_{Y,3}$	$S_{Y,3}$	$S_{Y,3}$
$S_{Z,1}$	$1/\sqrt{2}\ S_{Z,1} - 1/\sqrt{2}\ S_{Z,2}$	$-S_{Z,2}$	$-1/\sqrt{2}\ S_{Z,1} - 1/\sqrt{2}\ S_{Z,2}$
$S_{Z,2}$	$1/\sqrt{2}\ S_{Z,2} + 1/\sqrt{2}\ S_{Z,1}$	$+S_{Z,1}$	$-1/\sqrt{2}\ S_{Z,2} + 1/\sqrt{2}\ S_{Z,1}$
$S_{Z,3}$	$S_{Z,3}$	$S_{Z,3}$	$S_{Z,3}$

$R_Y(\theta,1)$

$S_{X,1}$	$1/\sqrt{2}\ S_{X,1} - 1/\sqrt{2}\ S_{Z,1}$	$-S_{Z,1}$
$S_{X,2}$	$1/\sqrt{2}\ S_{X,2} + 1/\sqrt{2}\ S_{Z,2}$	$S_{Z,2}$
$S_{X,3}$	$S_{X,3} + \frac{1}{2}\ S_{Y.2} + \frac{1}{2}\ S_{Y,3}$	$-S_{Z,3}$
$S_{Y,1}$	$S_{Y,1}$	$S_{Y,1}$
$S_{Y,2}$	$S_{Y,3}$	$-S_{Y,2}$
$S_{Y,3}$	$-S_{Y,2}$	$-S_{Y,3}$
$S_{Z,1}$	$1/\sqrt{2}\ S_{Z,1} + 1/\sqrt{2}\ S_{X,1}$	$S_{X,1}$
$S_{Z,2}$	$1/\sqrt{2}\ S_{Z,2} - 1/\sqrt{2}\ S_{X,2}$	$-S_{X,2}$
$S_{Z,3}$	$S_{Z,3} + \frac{1}{2}\ S_{Y,2} + \frac{1}{2}\ S_{Y,3}$	$-S_{X,3}$

Table 10 continued

$R_Y(\theta,2)$

$S_{X,1}$	$1/\sqrt{2}\ S_{X,1} + 1/\sqrt{2}\ S_{Z,2}$	$S_{Z,2}$
$S_{X,2}$	$1/\sqrt{2}\ S_{X,2} + 1/\sqrt{2}\ S_{Z,1}$	$S_{Z,1}$
$S_{X,3}$	$S_{X,3} - \frac{1}{2}\ S_{Y,1} + \frac{1}{2}\ S_{Y,3}$	$-S_{Z,3}$
$S_{Y,1}$	$-S_{Y,3}$	$-S_{Y,1}$
$S_{Y,2}$	$S_{Y,2}$	$S_{Y,2}$
$S_{Y,3}$	$S_{Y,1}$	$-S_{Y,3}$
$S_{Z,1}$	$1/\sqrt{2}\ S_{Z,1} - 1/\sqrt{2}\ S_{X,2}$	$-S_{X,2}$
$S_{Z,2}$	$1/\sqrt{2}\ S_{X,2} - 1/\sqrt{2}\ S_{X,1}$	$-S_{X,1}$
$S_{Z,3}$	$S_{Z,3} - \frac{1}{2}\ S_{Y,1} + \frac{1}{2}\ S_{Y.3}$	$-S_{X,3}$

$R_Y(\theta,3)$

$S_{X,1}$	$1/\sqrt{2}\ S_{X,1} - 1/\sqrt{2}\ S_{X,2}$	$-S_{X,2}$
$S_{X,2}$	$1/\sqrt{2}\ S_{X,2} + 1/\sqrt{2}\ S_{X,1}$	$+S_{X,1}$
$S_{X,3}$	$S_{X,3}$	$S_{X,3}$
$S_{Y,1}$	$S_{Y,2}$	$-S_{Y,1}$
$S_{Y,2}$	$-S_{Y,1}$	$-S_{Y,2}$
$S_{Y,3}$	$S_{Y,3}$	$S_{Y,3}$
$S_{Z,1}$	$1/\sqrt{2}\ S_{Z,1} - 1/\sqrt{2}\ S_{Z,2}$	$-S_{Z,2}$
$S_{Z,2}$	$1/\sqrt{2}\ S_{Z,2} + 1/\sqrt{2}\ S_{Z,1}$	$+S_{Z,1}$
$S_{X,3}$	$S_{Z,3}$	$S_{Z,3}$

Table 10 continued

$R_Z(\theta,1)$

$S_{X,1}$	$1/\sqrt{2}\ S_{X,1} + 1/\sqrt{2}\ S_{Y,1}$	$S_{Y,1}$
$S_{X,2}$	$1/\sqrt{2}\ S_{X,2} - 1/\sqrt{2}\ S_{Y,2}$	$-S_{Y,2}$
$S_{X,3}$	$S_{X,3} + \frac{1}{2}\ S_{Z,2} + \frac{1}{2}\ S_{Z,3}$	$-S_{Y,3}$
$S_{Y,1}$	$1/\sqrt{2}\ S_{Y,1} - 1/\sqrt{2}\ S_{X,1}$	$-S_{X,1}$
$S_{Y,2}$	$1/\sqrt{2}\ S_{Y,2} + 1/\sqrt{2}\ S_{X,2}$	$S_{X,2}$
$S_{Y,3}$	$S_{Y,3} + \frac{1}{2}\ S_{Z,2} + \frac{1}{2}\ S_{Z,3}$	$-S_{X,3}$
$S_{Z,1}$	$S_{Z,1}$	$S_{Z,1}$
$S_{Z,2}$	$S_{Z,3}$	$-S_{Z,2}$
$S_{Z,3}$	$-S_{Z,2}$	$-S_{Z,3}$

$R_Z(\theta,2)$

$S_{X,1}$	$1/\sqrt{2}\ S_{X,1} - 1/\sqrt{2}\ S_{Y,2}$	$-S_{Y,2}$
$S_{X,2}$	$1/\sqrt{2}\ S_{X,2} - 1/\sqrt{2}\ S_{Y,1}$	$-S_{Y,1}$
$S_{X,3}$	$S_{X,3} - \frac{1}{2}\ S_{Z,1} + \frac{1}{2}\ S_{Z,3}$	$-S_{Y,3}$
$S_{Y,1}$	$1/\sqrt{2}\ S_{Y,1} + 1/\sqrt{2}\ S_{X,2}$	$S_{X,2}$
$S_{Y,2}$	$1/\sqrt{2}\ S_{Y,2} + 1/\sqrt{2}\ S_{X,1}$	$S_{X,1}$
$S_{Y,3}$	$S_{Y,3} - \frac{1}{2}\ S_{Z,1} + \frac{1}{2}\ S_{Z,3}$	$-S_{X,3}$
$S_{Z,1}$	$-S_{Z,3}$	$-S_{Z,1}$
$S_{Z,2}$	$S_{Z,2}$	$S_{Z,2}$
$S_{Z,3}$	$S_{Z,1}$	$-S_{Z,3}$

Table 10 continued

$R_Z(\theta,3)$

$S_{X,1}$	$1/\sqrt{2}\ S_{X,1} - 1/\sqrt{2}\ S_{X,2}$		$-S_{X,2}$
$S_{X,2}$	$1/\sqrt{2}\ S_{X,2} + 1/\sqrt{2}\ S_{X,1}$		$+S_{X,1}$
$S_{X,3}$		$S_{X,3}$	$S_{X,3}$
$S_{Y,1}$	$1/\sqrt{2}\ S_{Y,1} - 1/\sqrt{2}\ S_{Y,2}$		$-S_{Y,2}$
$S_{Y,2}$	$1/\sqrt{2}\ S_{Y,2} + 1/\sqrt{2}\ S_{Y,1}$		$+S_{Y,1}$
$S_{Y,3}$		$S_{Y,3}$	$S_{Y,3}$
$S_{Z,1}$		$S_{Z,2}$	$-S_{Z,1}$
$S_{Z,2}$		$-S_{Z,1}$	$-S_{Z,2}$
$S_{Z,3}$		$S_{Z,3}$	$S_{Z,3}$

Table 11. The effect of a pulse of frequency $\Delta\omega = \omega_Q + \delta\omega$ upon an initial density matrix at equilibrium with the lattice for $\omega_1 \ll \omega_Q$ and $\delta\omega \ll \omega_Q$, $\omega_e = (\delta\omega^2 + 2\omega_1^2)^{\frac{1}{2}}$.

$$\sigma^*(0) = S_{Z,1}$$

$$a_{X,1} = \frac{1}{2}\,\omega_1\delta\omega/\omega_e^2\,(1-\cos\omega_e t)$$

$$a_{X,2} = \frac{1}{2}\,\omega_1/\omega_e\,\sin\omega_e t$$

$$a_{X,3} = -\,\omega_1^2/\omega_e^2\,(1-\cos\omega_e t)$$

$$a_{Y,1} = \frac{1}{2}\,\omega_1/\omega_e\,\sin\omega_e t$$

$$a_{Y,2} = \frac{1}{2}\,\omega_1\delta\omega/\omega_e^2\,(1-\cos\omega_e t)$$

$$a_{Z,1} = 1 - \frac{1}{2}\,\omega_1^2/\omega_e^2\,(1-\cos\omega_e t)$$

$$a_{Z,3} = -\,\frac{1}{2}\,\omega_1^2/\omega_e^2\,(1-\cos\omega_e t\,)$$

Table 12. The effect of a pulse of frequency $\Delta\omega = 0$ upon an initial density matrix $S_{p,i}$ for $\omega_1 \ll \omega_Q$, $\nu_e = \frac{\omega_e}{2\pi} = \frac{1}{2\pi}\sqrt{4\omega_1^2 + \omega_Q^2}$

$\sigma^*(0) = S_{Z,1}$

$$a_{Z,1} = \frac{1}{2}\left(1 + \frac{\nu_Q}{\nu_e}\right)\{\cos[(\nu_e-\nu_Q)\pi t]\} + \frac{1}{2}\left(1 - \frac{\nu_Q}{\nu_e}\right)\{\cos[\nu_e+\nu_Q)\pi t]\}$$

$$= (\cos\nu_e\pi t)(\cos\nu_Q\pi t) + \frac{\nu_Q}{\nu_e}(\sin\nu_e\pi t)(\sin\nu_Q\pi t)$$

$$a_{Z,2} = -\frac{1}{2}\left(1 + \frac{\nu_Q}{\nu_e}\right)\{\sin[\nu_e-\nu_Q)\pi t]\} + \frac{1}{2}\left(1 - \frac{\nu_Q}{\nu_e}\right)\{\sin[(\nu_e+\nu_Q)\pi t]\}$$

$$= (\cos\nu_e\pi t)(\sin\nu_Q\pi t) - \frac{\nu_Q}{\nu_e}(\sin\nu_e\pi t)(\cos\nu_Q\pi t)$$

$$a_{Y,1} = \frac{1}{2}\left(\frac{2\nu_1}{\nu_e}\right)\{\sin[(\nu_e+\nu_Q)\pi t] + \sin[(\nu_e-\nu_Q)\pi t]\}$$

$$= \left(\frac{2\nu_1}{\nu_e}\right)(\sin\nu_e\pi t)(\cos\nu_Q\pi t)$$

$$a_{Y,2} = \frac{1}{2}\left(\frac{2\nu_1}{\nu_e}\right)\{\cos[(\nu_e+\nu_Q)\pi t] - \cos[(\nu_e-\nu_Q)\pi t]\}$$

$$= -\left(\frac{2\nu_1}{\nu_e}\right)(\sin\nu_e\pi t)(\sin\nu_Q\pi t)$$

$\sigma^*(0) = S_{Z,2}$

$$a_{Z,1} = \frac{1}{2}\left(1 + \frac{\nu_Q}{\nu_e}\right)\{\sin[\nu_e-\nu_Q)\pi t]\} - \frac{1}{2}\left(1 - \frac{\nu_Q}{\nu_e}\right)\{\sin[\nu_e+\nu_Q)\pi t]\}$$

$$= -(\cos\nu_e\pi t)(\sin\nu_Q\pi t) + \frac{\nu_Q}{\nu_e}(\sin\nu_e\pi t)(\cos\nu_Q\pi t)$$

$$a_{Z,2} = \frac{1}{2}\left(1 + \frac{\nu_Q}{\nu_e}\right)\{\cos[(\nu_e-\nu_Q)\pi t]\} + \frac{1}{2}\left(1 - \frac{\nu_Q}{\nu_e}\right)\{\cos[(\nu_e+\nu_Q)\pi t]\}$$

$$= (\cos\nu_e\pi t)(\cos\nu_Q\pi t) + \frac{\nu_Q}{\nu_e}(\sin\nu_e\pi t)(\sin\nu_Q\pi t)$$

$$a_{Y,1} = \frac{1}{2}\left(\frac{2\nu_1}{\nu_e}\right)\{\cos[(\nu_e+\nu_Q)\pi t] - \cos[(\nu_e-\nu_Q)\pi t]\}$$

$$= -\left(\frac{2\nu_1}{\nu_e}\right)(\sin\nu_e\pi t)(\sin\nu_Q\pi t)$$

Table 12 continued

$$a_{Y,2} = -\frac{1}{2}\left(\frac{2\nu_1}{\nu_e}\right)\{\sin[\nu_e-\nu_Q)\pi t] + \sin[(\nu_e+\nu_Q)\pi t]\}$$

$$= -\left(\frac{2\nu_1}{\nu_e}\right)(\sin\nu_e\pi t)(\cos\nu_Q\pi t)$$

$\sigma^*(0) = S_{Y,1}$

$$a_{Y,1} = \frac{1}{2}\left(1 + \frac{\nu_Q}{\nu_e}\right)\{\cos[(\nu_e+\nu_Q)\pi t]\} + \frac{1}{2}\left(1 - \frac{\nu_Q}{\nu_e}\right)\{\cos[(\nu_e-\nu_Q)\pi t]\}$$

$$= (\cos\nu_e\pi t)(\cos\nu_Q\pi t) - \frac{\nu_Q}{\nu_e}(\sin\nu_e\pi t)(\sin\nu_Q\pi t)$$

$$a_{Y,2} = -\frac{1}{2}\left(1 + \frac{\nu_Q}{\nu_e}\right)\{\sin[(\nu_e+\nu_Q)\pi t]\} + \frac{1}{2}\left(1 - \frac{\nu_Q}{\nu_e}\right)\{\sin[(\nu_e-\nu_Q)\pi t]\}$$

$$= -(\cos\nu_e\pi t)(\sin\nu_Q\pi t) - \frac{\nu_Q}{\nu_e}(\sin\nu_e\pi t)(\cos\nu_Q\pi t)$$

$$a_{Z,1} = -\frac{1}{2}\left(\frac{2\nu_1}{\nu_e}\right)\{\sin[(\nu_e+\nu_Q)\pi t] + \sin[(\nu_e-\nu_Q)\pi t]\}$$

$$= -\left(\frac{2\nu_1}{\nu_e}\right)(\sin\nu_e\pi t)(\cos\nu_Q\pi t)$$

$$a_{Z,2} = \frac{1}{2}\left(\frac{2\nu_1}{\nu_e}\right)\{\cos[(\nu_e+\nu_Q)\pi t] - \cos[(\nu_e-\nu_Q)\pi t]\}$$

$$= -\left(\frac{2\nu_1}{\nu_e}\right)(\sin\nu_e\pi t)(\sin\nu_Q\pi t)$$

$\sigma^*(0) = S_{Y,2}$

$$a_{Y,1} = \frac{1}{2}\left(1 + \frac{\nu_Q}{\nu_e}\right)\{\sin[(\nu_e+\nu_Q)\pi t]\} - \frac{1}{2}\left(1 - \frac{\nu_Q}{\nu_e}\right)\{\sin[(\nu_e-\nu_Q)\pi t]\}$$

$$= (\cos\nu_e\pi t)(\sin\nu_Q\pi t) + \frac{\nu_Q}{\nu_e}(\sin\nu_e\pi t)(\cos\nu_Q\pi t)$$

$$a_{Y,2} = \frac{1}{2}\left(1 + \frac{\nu_Q}{\nu_e}\right)\{\cos[(\nu_e+\nu_Q]\pi t]\} + \frac{1}{2}\left(1 - \frac{\nu_Q}{\nu_e}\right)\{\cos[(\nu_e-\nu_Q)\pi t]\}$$

$$= (\cos\nu_e\pi t)(\cos\nu_Q\pi t) - \frac{\nu_Q}{\nu_e}(\sin\nu_e\pi t)(\sin\nu_Q\pi t)$$

Table 12 continued

$$a_{Z,1} = \frac{1}{2}\left(\frac{2\nu_1}{\nu_e}\right)\{\cos[(\nu_e+\nu_Q)\pi t] - \cos[(\nu_e-\nu_Q)\pi t]\}$$

$$= -\left(\frac{2\nu_1}{\nu_e}\right)(\sin\nu_e\pi t)(\sin\nu_Q\pi t)$$

$$a_{Z,2} = \frac{1}{2}\left(\frac{2\nu_1}{\nu_e}\right)\{\sin[(\nu_e+\nu_Q)\pi t] + \sin[(\nu_e-\nu_Q)\pi t]\}$$

$$= \left(\frac{2\nu_1}{\nu_e}\right)(\sin\nu_e\pi t)(\cos\nu_Q\pi t)$$

$$\sigma^*(0) = S_{Z,3}$$

$$a_{Z,3} = 1$$

$$a_{X,1} = \frac{\nu_1\nu_Q}{\nu_e^2}[1 - \cos(2\pi\ \nu_e t)]$$

$$a_{X,2} = -\frac{\nu_1}{\nu_e}\sin(2\pi\ \nu_e t)$$

$$a_{X,3} = \frac{2\nu_1^2}{\nu_e^2}[1 - \cos(2\pi\ \nu_e t)]$$

$$\sigma^*(0) = S_{Y,3}$$

$$a_{Y,3} = 1$$

$$a_{X,1} = \frac{\nu_1\nu_Q}{\nu_e^2}[1 - \cos(2\pi\ \nu_e t)]$$

$$a_{X,2} = -\frac{\nu_1}{\nu_e}\sin(2\pi\ \nu_e t)$$

$$a_{X,3} = \frac{2\nu_1^2}{\nu_e^2}[1 - \cos(2\pi\ \nu_e t)]$$

$$\sigma^*(0) = S_{X,1}$$

$$a_{X,1} = \frac{\nu_Q^2}{\nu_e^2}\cos(2\pi\ \nu_e t) + \frac{4\nu_1^2}{\nu_e^2}$$

Table 12 continued

$$a_{X,2} = \cos(2\pi\ \nu_e t)$$

$$a_{X,3} = \frac{2\nu_1}{\nu_e}\ \sin(2\pi\ \nu_e t)$$

$$\sigma^*(0) = S_{X,2}$$

$$a_{X,1} = -\frac{\nu_Q}{\nu_e}\ \sin(2\pi\ \nu_e t)$$

$$a_{X,2} = \cos(2\pi\ \nu_e t)$$

$$a_{X,3} = -\frac{2\nu_1}{\nu_e}\ \sin(2\pi\ \nu_e t)$$

$$\sigma^*(0) = S_{X,3}$$

$$a_{X,1} = -\frac{2\nu_1\nu_Q}{\nu_e^{\ 2}}\ [1 - \cos(2\pi\ \nu_e t)]$$

$$a_{X,2} = \frac{2\nu_1}{\nu_e}\ \sin(2\pi\ \nu_e t)$$

$$a_{X,3} = \frac{4\nu_1^{\ 2}}{\nu_e^{\ 2}}\ \cos(2\pi\ \nu_e t) + \frac{\nu_Q^{\ 2}}{\nu_e^{\ 2}}$$

Appendix 2.2 Fictitious Spin ½ Operators and Group Theory

The utility and significance of the fictitious spin ½ operators goes much deeper than is evident so far. The name chosen for them is in fact quite inapropos, since these 9 operators plus the identity are in fact a complete basis set which spans the space of operators which describe the properties of a spin 1 system, in exactly the same manner as I_X, I_Y, I_Z and 1 span spin ½ space. These operators provide us with a rigorous representation of the complete quantum mechanical problem, so in fact there is nothing fictitious about them. We have persisted in using the term "fictitious spin ½" to underscore their analogy with two level systems and to remind us of their original construction as generalized Pauli spin matrics. We therefore present in this appendix a slightly more rigorous and general presentation of their properties. We first discuss their relationship to the more familiar spherical tensor operators and then we discuss the formal basis for our approach. Finally, we relate the operators to their matrix elements and the methods of solution used for other non-spin multi-level systems.

Let us begin by obtaining a complete set of linear unitary operators for a spin ½ system. We begin with the operators I_X, I_Y and I_Z as represented by the Pauli spin matrices and then obtain all necessary quadratic combinations made from them, to complete the set.

$$I_X = \frac{1}{2}\begin{pmatrix} 0 & 1 \\ 1 & 0 \end{pmatrix} \quad I_Y = \frac{1}{2}\begin{pmatrix} 0 & -i \\ i & 0 \end{pmatrix} \quad I_Z = \begin{pmatrix} \frac{1}{2} & 0 \\ 0 & -\frac{1}{2} \end{pmatrix}$$

$$I_X^2 + I_Y^2 = I_Z^2 = \frac{1}{4}\begin{pmatrix} 1 & 0 \\ 0 & 1 \end{pmatrix} = \frac{1}{4}\ 1$$

$$I_X I_Y = \frac{1}{4}\begin{pmatrix} i & 0 \\ 0 & -i \end{pmatrix} = \frac{i}{4}\ I_Z$$

$$I_X I_Y = I_Y I_Z = 0 \qquad \text{(A2.2-1)}$$

It is obvious that no other forms are possible and that the set of I_X, I_Y, I_Z and span the operator space for $S = \frac{1}{2}$. We could have predicted this from the beginning since we know that the Pauli matrices are a complete set of 2 x 2 matrices. For S = 1, however, quadratic combinations of I_X, I_Y and I_Z generate <u>new</u> operators, for example in the $|1\rangle$, $|0\rangle$, $|-1\rangle$ basis set we find:

$$I_Z = \begin{pmatrix} 1 & 0 & 0 \\ 0 & 0 & 0 \\ 0 & 0 & -1 \end{pmatrix} = A_1 \qquad I_X = \begin{pmatrix} 0 & 1 & 0 \\ 1 & 0 & 1 \\ 0 & 1 & 0 \end{pmatrix} = A_2 \qquad I_Y = \begin{pmatrix} 0 & -i & 0 \\ i & 0 & -i \\ 0 & i & 0 \end{pmatrix} = A_3$$

giving

$$I_Z^2 \propto \begin{pmatrix} 1 & 0 & 0 \\ 0 & 0 & 0 \\ 0 & 0 & -1 \end{pmatrix}^2 = \begin{pmatrix} 1 & 0 & 0 \\ 0 & 0 & 0 \\ 0 & 0 & 1 \end{pmatrix} = A_4$$

$$I_X^2 \propto \begin{pmatrix} 0 & 1 & 0 \\ 1 & 0 & 1 \\ 0 & 1 & 0 \end{pmatrix}^2 = \begin{pmatrix} 1 & 0 & 1 \\ 0 & 2 & 0 \\ 1 & 0 & 1 \end{pmatrix} = A_5 \qquad \text{(A2.2-2)}$$

plus others, where A_4, A_5, etc., are the <u>new</u> operators. For this case, S = 1, we find we must use $(2I + 1)^2 - 1 = 8$ traceless independent operators in addition to the unity to span the necessary operator space.

Convenience dictates that some linear combinations of these operators (A_1-A_8) are more appropriate than others. For $S = \frac{1}{2}$, for instance, we choose the operators I_X, I_Y and I_Z or I_Z, I_+ (= $IX_{+1}\ I_Y$) and I_- (= $IX_{-1}\ I_Y$) depending on the problem to be solved. For S = 1, we use the Hamiltonian

of interest, the Quadrupole Hamiltonian, to generate the most convenient basis operators. This is most easily done by building the set up using all of the possible commutation relations. For example assume I_X is a good choice for one of the basis operators, then commuting this with H_Q gives:

$$[I_Z^2 - \frac{1}{3} I(I+1),\ I_X] = i\ (I_Y I_Z + I_Z I_Y)$$

and

$$[I_Z^2 - \frac{1}{3} I(I+1),\ (I_Y I_Z + I_Z I_Y)] = -iI_X \qquad (A2.2\text{-}3)$$

Thus I_X and $(I_Y I_Z + I_Z I_Y)$ are seen to be good basis operators. The fictitious spin ½ operators are generated in exactly this way, considering all of the possible commutation relations of H_Q, I_X, I_Y, I_Z and each of the new operators in turn. And, of course when the operators are represented as 3 x 3 matrices, this process generates a complete set. The results of the process are listed in Table 13B. Any general operator for spin 1 may now be expanded in terms of these operators giving

$$Q = \sum_{p,i} a_{p,i}\ I_{p,i} \qquad (A2.2\text{-}4)$$

This brings us to the connection between the set of spherical tensor operators and the fictitious spin operators. A spherical spin tensor operator of rank k transfers according to the kth irreducible representation of O(3). It is found by reducing the product of a tensor of rank m and rank n where $m + n \geq k$. For spin ½ we form all combinations I_p, I_q for p, q = X, Y, Z which can be reduced according to; $D^{(\frac{1}{2})} \otimes D^{(\frac{1}{2})} = D^{(1)} \oplus D^{(0)}$ giving the spin tensors as

$$T_{1,+1} = \frac{1}{\sqrt{2}} I^{+} = \frac{1}{\sqrt{2}} (I_X + iI_Y)$$

$$T_{1,-1} = \frac{1}{\sqrt{2}} I^{-} = \frac{1}{\sqrt{2}} (I_X - iI_Y)$$

$$T_{1,0} = I_Z$$

$$T_{0,0} = 1 \qquad \text{(A2.2-5)}$$

For S = 1 the spin operator products are reduced as $D^{(1)} \otimes D^{(1)} = D^{(2)} \oplus D^{(1)} \oplus D^{(0)}$ and the spin tensors are given in Table 13A, for an operator $T_{L,M}$. We may now fully relate the two sets of operators, spin tensor operators and fictitious spin operators by combining Tables 13A and B. The results of this algebra is given in Tables 13C and D.

We now note that in order to solve a dynamics problem we must find the transformation properties of the basis operators of the form

$$I_{p,i}(t) = e^{-iH_Q t} I_{p,i} e^{+iH_Q t} \qquad \text{(A2.2-6)}$$

this will involve terms like

$$I_{p,i}(t) = e^{-iI^2_{p,i} t} I_{p,i} e^{+iI^2_{p,i} t} \qquad \text{(A2.2-7)}$$

which we wish very much to avoid, since we must involve nonlinear algebra.

For example we know the form for the transformations $e^{-iI_Z t}$, $e^{-iI_X t}$ and $e^{-iI_Y t}$, since these are the transformations which comprise the group O(3). We know that any such transformation may be put into terms of Euler angles. Then the transformation is given by $D^{\frac{1}{2}}(\alpha,\beta,\gamma)$

for $S = \frac{1}{2}$ ($D^{\frac{1}{2}}$ is the basic representation, i.e., the representation is given by the generators of the corresponding unitary group). For $S = 1$ we would use $D^{(1)}(\alpha,\beta,\gamma)$. But for $e^{-i(I_Y I_Z + I_Z I_Y)t}$ there is no such easy form. Therefore we have defined a new operator $I_{X,2}$, and have found its matrix representation and then calculated $e^{-iI_{X,2}t}$ explicitly. This was done in Table 8. In group theory terms we go to a higher symmetry group (we have added 5 new transformations giving SU(3)) and use a new representation (the octet representation of the higher group) for our transformation properties.

There is in principle no advantage in doing this, that is the transformations are actually the same. However we do gain in that we may consider all of the transformations in the new group (SU(3)) in a much simpler algebraic form, that is as simple rotations about a specified axis. And in addition we have shown that in certain instances we may rigorously draw analogies between two level systems and our spin 1 system. This allows a much better visualization of the dynamics. And it is for this last reason that we maintain the name "fictitious spin ½" as was originally proposed by Abragam.[8]

We can ascribe another meaning to our description using the fictitious spin ½ operators. As was mentioned before we can expand any function in the $I_{p,i}$. In particular the density matrix is given as,

$$\rho = \sum_{p,i} a_{p,i} I_{p,i} \qquad \text{(A2.2-8)}$$

We have also shown the correspondence of the $I_{p,i}$ and the spherical spin tensor operators (Table 13). So, what we realize by the expansion in equation (8) is in effect a tensor expansion or a multipole expansion of

the density matrix. This treatment was first suggested by Fano,[37] and it is also implicit in the distinctions made by de Boer (see Section III D) between vector polarization and alignment, when put into terms of the density matrix. But instead of the standard expansion in spherical harmonics, our expansion is seen to be the most convenient one for such a description for our system given the symmetry and form of the Hamiltonian. As an example of this concept's utility we note that it has been shown that without an external perturbation, the tensor rank of the density matrix will be conserved during time development. For our system this implies that once the density matrix has been prepared in a state which corresponds to pure alignment ($I_{Z,3}$) that no vector polarization will spontaneously develop and conversely once the density matrix has been prepared in a state which corresponds to pure polarization, no alignment will spontaneously develop.

We conclude with a reminder of the relationship of our operators to the actual matrix elements which would be obtained in a particular basis set. This then indicates the coincidence of our method with the normal matrix element methods of treating multilevel systems as used in for example ENDOR,[2b] microwave,[2e], pulsed optical studies,[2a] and the approach of Hatanaka *et al.* for multiple quantum coherence.[6] We wish to find the matrix elements of the operators $S_{p,i}$ for the following two basis sets,

$$
\begin{array}{lll}
|+1\rangle \quad \text{and} & |X\rangle = 1/\sqrt{2}\,(|+1\rangle - |-1\rangle) & \\
|0\rangle & |Y\rangle = i/\sqrt{2}\,(|+1\rangle + |-1\rangle) & \\
|-1\rangle & |Z\rangle = |0\rangle & \qquad \text{(A2.2-9)}
\end{array}
$$

with which a general wavefunction ψ may be denoted as,

$$\psi = a|X\rangle + b|Y\rangle + c|Z\rangle$$

or

$$\psi = \alpha|+1\rangle + \beta|0\rangle + \gamma|-1\rangle \qquad \text{(A2.2-10)}$$

The appropriate matrix elements are given in Table 14.

Table 13. The relationships between the Fictitious spin ½ operators and the normal Cartesian operators (I_X, I_Y, I_Z) and the spherical spin tensors.

a Normalized Spherical Tensors

	-2	-1	0	1	2
0	0	0	$I \cdot I = I(I+1)$	0	0
1	0	$-\frac{1}{\sqrt{2}} I_-$	I_Z	$\frac{1}{\sqrt{2}} I_+$	0
2	$\frac{1}{2} I_-^2$	$-\frac{1}{2}(I_Z I_- + I_- I_Z)$	$\frac{1}{\sqrt{6}} (3I_Z^2 - I \cdot I)$	$\frac{1}{2} (I_Z I_X + I_X I_Z)$	$\frac{1}{2} I_X^2$

b Fictitious Spin Operators vs. Cartesian Operators

$I_{p,i}$	1	2	3
X	$\frac{1}{2} I_X$	$\frac{1}{2} (I_Y I_Z + I_Z I_Y)$	$\frac{1}{2} (I_Z^2 - I_Y^2)$
Y	$\frac{1}{2} I_Y$	$\frac{1}{2} (I_X I_Z + I_Z I_X)$	$\frac{1}{2} (I_X^2 - I_Z^2)$
Z	$\frac{1}{2} I_Z$	$\frac{1}{2} (I_X I_Y + I_Y I_X)$	$\frac{1}{2} (I_Y^2 - I_X^2)$

c Spherical Tensors vs. Fictitious Spin Operators

$T_{\ell m}$	-2	-1	0	1	2
0	0	0	$\pm I$	0	0
1	0	$\frac{2}{\sqrt{2}} (-)(I_{X,1} - I_{Y,1})$	$2 I_{Z,1}$	$\frac{2}{\sqrt{2}} (I_{X,1} + iI_{Y,1})$	0
2	$-iI_{Z,2} - I_{Z,3}$	$I_{Y,2} - iI_{X,2}$	$\frac{2}{\sqrt{6}} (I_{X,3} - I_{Y,3})$	$I_{Y,2} + iI_{X,2}$	$I_{Z,3} - iI_{Z,2}$
	$-(I_{Z,3} + iI_{Z,2})$				

Table 13 continued

d Fictitious Spin Operators vs. Spherical Tensors

$I_{p,i}$	1	2	3
X	$\frac{\sqrt{2}}{4}(T_{11}-T_{1-1})$	$-\frac{i}{2}(T_{21}-T_{2-1})$	$\frac{\sqrt{6}}{4}T_{20}+\frac{1}{4}(T_{22}+T_{2\bar{2}})$
Y	$-\frac{\sqrt{2}}{4}i(T_{11}+T_{1-1})$	$\frac{1}{2}(T_{21}+T_{2-1})$	$-\frac{\sqrt{6}}{4}T_{20}+\frac{1}{4}(T_{22}+T_{2\bar{2}})$
Z	$\frac{1}{2}T_{10}$	$-\frac{i}{2}(T_{22}-T_{2\bar{2}})$	$-\frac{1}{2}(T_{22}+T_{2\bar{2}})$

Table 14. Relationship of the fictitious spin operators to final matrix elements.

Basis sets:

$|-1\rangle \qquad |X\rangle = -1/\sqrt{2} \quad (|+1\rangle - |-1\rangle)$

$|0\rangle \qquad |Y\rangle = i/\sqrt{2} \quad (|+1\rangle + |-1\rangle)$

$|+1\rangle \qquad |Z\rangle = |0\rangle$

Wave functions:

$$\psi = a|X\rangle + b|Y\rangle + c|Z\rangle$$

$$= \alpha|+1\rangle + \beta|0\rangle + \gamma|-1\rangle$$

$$\alpha = \frac{b-ia}{\sqrt{2}}, \quad \gamma = \frac{b+ia}{\sqrt{2}}, \quad \beta = C, \quad b = \frac{\alpha+\gamma}{\sqrt{2}}, \quad a = i\,\frac{\alpha-\gamma}{\sqrt{2}}$$

Matrix elements:

$$\langle S_{Z,1}\rangle_\psi = -\,i/2\ (a^*b - b^*a) = 1/2\ (|\alpha|^2 - |\gamma|^2)$$

$$\langle S_{Z,2}\rangle_\psi = -\,1/2\ (a^*b + b^*a) = -i/2\ (\alpha^*\gamma - \gamma^*\alpha)$$

$$\langle S_{Z,3}\rangle_\psi = 1/2\ (|a|^2 - |b|^2) = -1/2\ (\alpha^*\gamma + \gamma^*\alpha)$$

$$\langle S_{Y,1}\rangle_\psi = 1/2\ (a^*c - c^*a) = i/_{2\sqrt{2}}\ (\alpha^*\beta - \beta^*\alpha) + -i/_{2\sqrt{2}}\ (\beta^*\gamma - \gamma^*\beta)$$

$$\langle S_{Y,2}\rangle_\psi = -1/2\ (a^*c + c^*a) = 1/_{2\sqrt{2}}\ (\alpha^*\beta + \beta^*\alpha) - 1/_{2\sqrt{2}}\ (\beta^*\gamma + \gamma^*\beta)$$

$$\langle S_{Y,3}\rangle_\psi = -1/2\ (|a|^2 - |c^2|) = 1/2\ |\beta|^2 - 1/4(|\alpha|^2 - \alpha^*\gamma - \gamma^*\alpha + |\gamma|^2)$$

$$\langle S_{X,1}\rangle_\psi = i/2\ (-b^*c + c^*b) = 1/_{2\sqrt{2}}\ (\alpha^*\beta + \beta^*\alpha) + i/_{2\sqrt{2}}\ (\beta^*\gamma + \gamma^*\beta)$$

$$\langle S_{X,2}\rangle_\psi = -i/2\ (b^*c + c^*b) = -i/_{2\sqrt{2}}\ (\alpha^*\beta - \beta^*\alpha) + i/_{2\sqrt{2}}(\beta^*\gamma - \gamma^*\beta)$$

$$\langle S_{X,3}\rangle_\psi = 1/2\ (|b|^2 - |c|^2) = -1/2|\beta|^2 + 1/4(|\alpha|^2 + \alpha^*\gamma + \gamma^*\alpha + |\gamma|^2)$$

Appendix 2.3 Derivation of the cross polarization time

The details of the derivation of the cross polarization time T_{IS} are given below for the S = 1 single quantum case. The calculation for the double quantum case is straight forward once equations (2-98a, 2-108), are derived. The commutator in equation (94) is calculated using equations (2-83 and 2-95) giving

$$[H^{o}_{IS}{}', H_{SL}{}'] = \omega_{eS} \cos\theta_X \sum_i b_i I_{ip} S_{X2}{}'' \qquad \text{(A2.3-1)}$$

where p = X for SL and Z for ADRF (as in all that follows). Substituting 1 back into equation (2-94) gives for ADRF

$$T_{IS}^{-1} = \frac{\cos^2 \theta_X}{tr\{S''_{X1}\}^2} \int_0^{\infty} d\tau \; g(\tau) \qquad \text{(A2.3-2)}$$

$$g(\tau) = tr\{(\sum_i 2b_i I_{ip} S''_{X2})(S''_{X2} \cos\omega_{eS}\tau + S''_{X3} \sin\omega_{eS}\tau) \exp(i H^*_{IP})$$

$$\tau \sum_i b_i I_{ip} \exp(-i H^*_{IP}\tau)\} \quad .$$

The traces can be taken over the I and S spins separately since $tr = tr_I tr_S$. However instead of evaluating the traces over the S-spins explicitly we choose to multiply by:

$$\frac{tr(\sum_i b_i I_{ip})^2}{tr(\sum_i b_i I_{ip})^2}$$

and rearrange using equation (1) to give:

$$T_{IS}^{-1} = \cos^2\theta_X \; \frac{tr[\sum_i 2b_i I_{ip} \; S''_{Z3}, \; S''_{X1}]^2}{tr(S_{X1})^2} \int_0^\infty \cos\omega_{eS}\tau \; c(\tau) \; d\tau$$

$$c(\tau) = \frac{tr_S\{(\sum_i b_i I_{ip}) \; \exp(i \; H^*_{IP}\tau)(\sum_i b_i I_{ip}) \; \exp(-i \; H^*_{IP}\tau)\}}{tr(\;\; b_i I_{ip})^2} \qquad (A2.3\text{-}4)$$

The forms for H^*_{IP} are exactly as that given in Chapter One where for SL:

$$H^*_{IX} = \omega_{eI} \; I_X + P_2(\cos\theta_I) \; H^{(o)}_{II} = \omega_{eI} I_X - \frac{1}{2} \; H^{(o)}_{II}$$

and for ADRF

$$H^*_{IZ} = P_2(\cos\theta_I) \; H^{(o)}_{II} = H^{(o)}_{II}$$

The commutator is in exactly the same form as the Van Vleck second moment in the reference frame for the appropriate transition, which for this case is a single quantum reference frame (see Section III B-1).

$$M''_{2,IS} = \frac{tr[\sum_i 2b_i I_{iZ} S''_{Z3}, \; S''_{X1}]^2}{tr(S''_{X1})^2} \qquad (A2.3\text{-}5)$$

If we apply a $R_Z(-90,2)$ rotation to get back to the normal rotating frame (see equation (2-95)) we obtain:

$$M'_{2,IS} = \frac{tr[\sum_i b_i I_{iZ} \; S_{Z1}, S_{X1} - S_{Y2}]^2}{tr(S_{X1} - S_{Y2})^2} \qquad (A2.3\text{-}6)$$

The linear combination of operators $S_{X1} - S_{\;2}$ is the operator for the sideband nearest the irradiation frequency, $|+1\rangle \rightarrow |0\rangle$ (see Section III-B1)

To complete the calculation for the SL case we simply use the form

for the correlation function derived by Demco et al.[24] Since we have shown by equation (4) the correspondence to the normal spin ½ case given in Chapter One. That is, the time development governed by H^*_{IX} generates spectral density functions at frequencies; $\omega_{eS}-\omega_{eI}$, $\omega_{eS}+\omega_{eI}$ and ω_{eS}. However in high field only one of these $\omega_{eS}-\omega_{eI}$ is important since it involves the lowest frequencies for which the spectral density is still high. Taking this into account gives the final result.

$$T_{IS}^{-1} = \frac{1}{2}\cos^2\theta_X \quad M_{2IS}\ J_X(\omega_{eS}-\omega_{eI})$$

where the factor of ½ reflects the neglect of the other spectral density terms. For ADRF we conclude

$$T_{IS}^{-1} = \cos^2\theta_X\ M_{2,IS}\ J_Z(\omega_{eS}) \quad \text{where } \theta_X = \tan^{-1}\frac{\delta\omega}{2\omega_{1s}}$$

To calculate the cross polarization time for the double quantum case we need only repeat the above calculation with the new perturbation Hamiltonian. This only involves a change in the geometrical factor (see equation (2-108) so that we may write the results directly in correspondence with the single quantum case:

$$T_{IS}^{-1} = \frac{1}{2}\cos^2\theta_X\ M_{2,IS}\ J_X(\omega_{eS}-\omega_{1I}) \tag{109}$$

for SL and for ADRF:

$$T_{IS}^{-1} = \cos^2\theta_X\ M_{2,IS}\ J_Z(\omega_{eS}) \tag{110}$$

with $\theta_X = \tan^{-1}\dfrac{2\omega_{1S}}{\omega_Q}$. (105)

Appendix 2.4 Computer Programs

The programs to fit rotation data to equations (2-128) and (2-129) are given in Tables 15 and 16 respectively (see Section V). Linear least mean squares is used for the two parameters Δ and X for (128) and the three parameters σ_{PP}, σ_{NN} and σ_{NP} for (129). In addition a phase angle is required which is simply a reference angle between the initial data point and the maximum of the rotation curve. The programs are written in Basic and are quite specific to the particular equation fitted.

The indirect detection experiment, Section VI-C2, must again be fitted with nonlinear least mean squares. The program for the ADRF case is given in Table 17. The matrix of derivatives with respect to the three parameters c, β, and τ_c (τ_c = G) is inverted explicitly for speed. For the SL case the program is modified according to equation (2-119), after allowing the proton field strength ω_{1I} to be read into the program.

The program to fit the cross polarization dynamics for the case in which neither T_{1D} or $T_{1\rho}$ is negligible is given in Table 18. The formulas are given in VI-C4. Because of the difficulty of obtaining the derivatives of the simultaneous solutions with respect to the parameters needed for a least squares analysis, a general search algorithm was implemented for the parameters T_{IS} and ε. The subroutine DIFEQ2 generates a completely general solution for two simultaneous differential equations at a single time t. This solution is not based on the normal integration techniques but instead is the exact solution. The factor for the effective field which enter into the calculation of the final normalized magnetization is added as a parameter (see equation (159)). Then $M^{ag}, C^{st} = \omega_1/\omega_Q$ for the double quantum case and = 1 for the normal spin ½ case.

Table 15. Program to fit crystal rotation data to the function $y = D\ P_2(\cos\theta) + X$, using linear least mean squares.

```
P2FIT   BA    1.0

1 DIM A(40),S(40),S1(40)
3 LET P=3.1415926
6 PRINT "INPUT I,ORIENTATION AND SHIFT"
8 INPUT I,A,S
10 IF I=0 GO TO 18
12 LET A(I)=A*P/180.
14 LET S(I)=S
16 GO TO 8
18 PRINT "GUESS ISOTROPIC SHIFT AND ANISOTROPY AND PHASE"
20 INPUT X,D,P6
21 LET Y=0
22 PRINT "NUMBER OF POINTS TO FIT"
23 INPUT J
24 FOR I=1 TO J
25 LET A6=A(I)-P6*P/180.
26 LET P2=1.5*COS(A6)*COS(A6)-.5
28 LET S1(I)=D*P2+X
30 LET Y=Y+(S1(I)-S(I))*(S1(I)-S(I))
32 NEXT I
34 PRINT "STANDARD DEVIATION"
36 PRINT Y
37 GOSUB 300
38 PRINT "PLOT?"
40 INPUT Y$
42 IF Y$="Y" GOTO 50
44 GO TO 18
50 PRINT "ORIENTATION ,EXPERIMENTAL , FIT"
51 FOR I=1 TO J
52 PRINT A(I),S(I),S1(I)
54 NEXT I
56 PRINT
57 PRINT
60 FOR I=1 TO 36
61 LET U=40./D
62 LET V=25.-40.*X/D
63 LET J=S(I)*U+V+0.5
64 LET A6=A(I)-P6*P/180.
66 LET P2=1.5*COS(A6)*COS(A6)-.5
68 LET S1(I)=D*P2+X
70 LET K=S1(I)*U+V+0.5
72 IF INT(J)>INT(K) GO TO 100
74 IF INT(J)=INT(K) GO TO 90
76 IF INT(J)>0 GO TO80
78 PRINT "N";TAB(K);"*"
79 GO TO 110
80 PRINT TAB(J);"+";TAB(K);"*"
82 GO TO 110
90 PRINT TAB(J);"*"
92 GO TO 110
100 PRINT TAB(K);"*";TAB(J);"+"
110 NEXT I
111 PRINT PNT(10),PNT(10);PNT(10);PNT(10);PNT(10)
112 PRINT "NEW GUESS?"
114 INPUT Y$
116 IF Y$="Y" GOTO 18
118 PRINT "NEW DATA?"
120 INPUT Y$
122 IF Y$="Y" GO TO 6
300 LET X1=0
302 LET Y1=0
```

```
304 LET X2=0
306 LET Y2=0
308 FOR I=1 TO J
310 LET A6=A(I)-P6*P/180.
312 LET P2=1.5*COS(A6)*COS(A6)-.5
314 LET X1=X1+P2
316 LET Y1=Y1+S(I)
318 LET X2=X2+P2*P2
320 LET Y2=Y2+P2*S(I)
322 NEXT I
324 LET X6=(Y1*X2-X1*Y2)/(J*X2-X1*X1)
326 LET D6=(J*Y2-X1*Y1)/(J*X2-X1*X1)
328 PRINT "LMS ISO AND ANISO SHFT=";X6;D6
330 RETURN
380 END

READY
```

Table 16. Program to fit crystal rotation data to the general tensor transformation equation (2-129) using linear least mean squares.

```
TENSFI  T     1.0

1 DIM  A(40),S(40),S1(40)
3 P=3.14158
6 PRINT "INPUT I,ORIENTATION AND SHIFT"
8 INPUT I,A,S
10 IF I=0 GO TO 18
12 LET A(I)=A*P/180
14 S(I)=S
16 GO TO 8
18 PRINT "GUESS SNN,SPP,SNPAND PHASE"
20 INPUT P2,N2,P3,P9
22 PRINT "LIMITS FOR FIT"
24 INPUT M,O
25 Y9=1000
26 A3=0
27 B3=0
28 C3=0
29 E3=0
30 F3=0
31 I3=0
32 J3=0
33 K3=0
34 L3=0
35 Y4=0
40 FOR N=MTO O
42 X2=A(N)-P9*P/180
44 S2=SIN(X2)*SIN(X2)
46 C2=COS(X2)*COS(X2)
48 S3=-2.*SIN(X2)*COS(X2)
50 Y8=P2*S2+N2*C2+P3*S3
52 A3=A3+S2*S2
54 B3=B3+S2*C2
55 C3=C3+S2*S3
56 E3=E3+C2*C2
57 F3=F3+C2*S3
58 I3=I3+S3*S3
60 Y7=S(N)-Y8
62 J3=J3+S2*Y7
63 K3=K3+C2*Y7
64 L3=L3+S3*Y7
65 Y4=Y4+Y7*Y7
70 NEXT N
71 D=A3*E3*I3+B3*F3*C3+B3*F3*C3-C3*E3*C3-F3*F3*A3-B3*B3*I3
72 Q1=(E3*I3-F3*F3)/D
74 Q2=(-B3*I3+C3*F3)/D
75 Q3=(B3*F3-E3*C3)/D
76 Q4=(A3*I3-C3*C3)/D
77 Q5=(-A3*F3+C3*B3)/D
78 Q6= (A3*E3-B3*B3)/D
80 P4=Q1*J3+Q2*K3+Q3*L3
81 N4=Q2*J3+Q4*K3+Q5*L3
82 P5=Q3*J3+Q5*K3+Q6*L3
85 P2=P2+P4
86 N2=N2+N4
87 P3=P3+P5
88 PRINT P2,N2,P3,Y4
89 IF ABS(Y4-Y9)/Y9< 001 GO TO 94
91 Y9=Y4
92 GO TO 26
94 PRINT "SNN.SPP,SNP=";P2,N2,P3."SSDEV=";Y4
100 PRINT "PLOT?"
101 INPUT Y$
```

```
102 IF Y$="Y" GO TO 104
103 GO TO 18
104 PRINT "ORIENTAION, EXPERIMENTAL, FIT"
105 FOR I=1 TO 37
106 X2=A(I)-P9*P/180.
107 S1(I)=P2*SIN(X2)**2+N2*COS(X2)**2-P3*2*SIN(X2)*COS(X2)
109 PRINT A(I),S(I),S1(I)
110 NEXT I
111 PRINT
112 PRINT
113 FOR I=1 TO 37
114 U=40./(2/3*(P2-N2))
115 V=25.-40.*(P2/(2/3*(P2-N2))-1.)
116 J=S(I)*U+V+0.5
117 K=S1(I)*U+V+0.5
118 IF INT(J)>INT(K) GO TO127
119 IF INT(J)=INT(K) GO TO 125
120 IF INT (J)>0 GO TO 123
121 PRINT "N";TAB(K);"*"
122 GO TO 128
123 PRINT TAB(J);"+";TAB(K);"*"
124 GO TO 128
125 PRINT TAB(J);"*"
126 GO TO 128
127 PRINT TAB(K);"*";TAB(J);"+"
128 NEXT I
129 PRINT PNT(10);PNT(10);PNT(10);PNT(10);PNT(10)
130 PRINT "NEW GUESS?"
131 INPUT Y$
132 IF Y$="Y" GO TO 18
133 PRINT "NEW DATA?"
134 INPUT Y$
135 IF Y$="Y" GO TO 6
300 END

READY
```

Table 17. Program to fit the destruction spectra from the cross polarization experiments, using nonlinear least mean squares. DISFIT is for the ADRF case and DISSL is for SL case.

```
DISFIT  BA    1.0

1 DIM A(24),S(24),S1(24)
2 PRINT "INPUT OMEGA1S,OMEGA Q, OMEGA I AND CONVERGENCE FACTOR"
3 INPUT O1,O2,O8,F5
4 T8=100
5 E8=4.6666E-03/(O8*O8)
6 T3=ATN(SQR(2)*O1/O2)
8 PRINT "INPUT I,OFFSET AND % DIST"
9 INPUT I,A(I),S(I)
10 IF I=0 GO TO 18
```

```
12 IF T8<ABS(A(I)-A(I-1)) GO TO 16
14 T8=ABS(A(I)-A(I-1))
16 GO TO 9
18 PRINT "GUESS C,BETA,GAMMA"
19 INPUT C,B,G
21 PRINT "LIMITS FOR FIT"
23 INPUT M,O
25 Y9=1000
26 A3=0
27 B3=0
28 C3=0
29 E3=0
30 F3=0
31 I3=0
32 J3=0
33 K3=0
34 L3=0
35 Y4=0
40 FOR I=M TO O
42 GO SUB 500
46 A3=A3+R1*R1
47 B3=B3+R1*R2
48 C3=C3+R1*R3
49 E3=E3+R2*R2
50 F3=F3+R2*R3
51 I3=I3+R3*R3
52 Y7=S(I)-I7
53 J3=J3+R1*Y7
54 K3=K3+R2*Y7
55 L3=L3+R3*Y7
58 Y4=Y4+Y7*Y7
60 NEXT I
62 D=A3*E3*I3+B3*F3*C3+B3*F3*C3-C3*E3*C3-F3*F3*A3-B3*B3*I3
63 Q1=(E3*I3-F3*F3)/D
64 Q2=(-B3*I3+C3*F3)/D
65 Q3=(B3*F3-E3*C3)/D
66 Q4=(A3*I3-C3*C3)/D
67 Q5=(-A3*F3+C3*B3)/D
68 Q6=(A3*E3-B3*B3)/D
70 C4=Q1*J3+Q2*K3+Q3*L3
71 B4=Q2*J3+Q4*K3+Q5*L3
72 G4=Q3*J3+Q5*K3+Q6*L3
73 GO SUB 700
74 C=C+C4
75 B=B+B4
76 G=G+G4
78 PRINT C,B,G,Y4
79 IF ABS(Y4-Y9)/Y9<0.01 GO TO 93
81 Y9=Y4
82 INPUT G$
83 IF G$="G" GO TO 26
93 PRINT PNT(10);PNT(10);PNT(10)
94 PRINT "C,BETA,GAMMA=";C,B,G,"S2DEV=";Y4
95 GO SUB 600
96 T9=.0001
97 PRINT "OFFSET , % DISTRUCTION, FIT"
98 Y4=0
99 FOR I=1 TO O
100 GO SUB 500
101 S1(I)=I7
102 IF T9>I7 GO TO 104
103 T9=I7
104 PRINT A(I),S(I),S1(I)
105 Y4=Y4+(S(I)-S1(I))**2
106 NEXT I
107 PRINT PNT(10);"S2DEV=",Y4;PNT(10);PNT(10)
```

```
108 PRINT "PLOT"
109 INPUT Y$
110 IF Y$="N" GO TO 95
112 PRINT PNT(10);PNT(10);PNT(10)
113 V=-1
114 FOR I=1 TO 24
116 U=68/T9
118 V=V+1
119 IF A(I) >T8*V-A(1)+.005 GO TO 121
120 GO TO 123
121 PRINT
122 GO TO 118
123 J=S(I)*U+2.5
124 K=S1(I)*U+2.5
126 IF INT(J)>INT(K) GO TO 137
127 IF INT (J)=INT(K) GO TO 135
128 IF INT (J)>0 GO TO 133
130 PRINT "N";TAB(K);"*"
131 GOTO 138
133 PRINT TAB(J);"+";TAB(K);"*"
134 GO TO 138
135 PRINT TAB(J);"*"
136 GO TO 138
137 PRINT TAB(K);"*";TAB(J);"+"
138 NEXT I
140 PRINT PNT(10);PNT(10);PNT(10);PNT(10)
142 PRINT "NEW GUESS?"
143 INPUT Y$
144 IF Y$="Y" GO TO 18
145 PRINT "NEW DATA?"
146 INPUT Y$
147 IF Y$="Y" GO TO 2
160 REM SUB ROUTINE TO CALCULATE FUNCTION
500 T2=ATN(2*A(I)/(O1*O1/O2))
502 O5=SQR(O1**4/(O2*O2)+4*A(I)*A(I))
504 M5=(COS(T2/2)**2+COS(T2)+SIN(T2)+SIN(T2/2)*SIN(T2))**2 =1
506 I4=C*(E8*O5*O5/(1.+E8*O5*O5))
508 I5=EXP(-O5*G)
510 I6=EXP(-B*M5*G*I5)
512 I7=I4*(I6-1.)
514 R1=I7/C
516 R2=-I7*I5*M5*G
518 R3=I7*B*M5*I5*(G*O5-1.)
530 RETURN
600 REM  FINAL INPUT ROOUTINE
601 PRINT "FINAL PARAMETERS?"
603 INPUT C2,B2,G2
605 IF C2=0 GO TO 611
607 C=C2
608 B=B2
609 G=G2
611 RETURN
700 REM CONVERGENCE FUDGE
702 IF ABS(C4/C)<0.01 GO TO 706
704 C4=C4/F5
706 IF ABS(B4/B)<0.01 GO TO 710
708 B4=B4/F5
710 IF ABS(G4/G)<0.01 GO TO 714
712 G4=G4/F5
714 RETURN
800 END

READY
```

```
DISSL   BA    1.0

1 DIM A(24),S(24),S1(24)
2 PRINT "INPUT OMEGA1S,OMEGA Q, OMEGA I AND CONVERGENCE FACTOR"
3 INPUT O1,O2,O8,F5
4 T8=100
5 E8=4.66667E-03/(O8*O8*.1535*.1535)
6 T3=ATN(SQR(2)*O1/O2)
8 PRINT "INPUT I,OFFSET AND % DIST"
9 INPUT I,A(I),S(I)
10 IF I=0 GO TO 18
12 IF T8<ABS(A(I)-A(I-1)) GO TO 16
14 T8=ABS(A(I)-A(I-1))
16 GO TO 9
18 PRINT "GUESS C,BETA,GAMMA"
19 INPUT C,B,G
21 PRINT "LIMITS FOR FIT"
23 INPUT M,O
25 Y9=1000
26 A3=0
27 B3=0
28 C3=0
29 E3=0
30 F3=0
31 I3=0
32 J3=0
33 K3=0
34 L3=0
35 Y4=0
40 FOR I=M TO O
42 GO SUB 500
46 A3=A3+R1*R1
47 B3=B3+R1*R2
48 C3=C3+R1*R3
49 E3=E3+R2*R2
50 F3=F3+R2*R3
51 I3=I3+R3*R3
52 Y7=S(I)-I7
53 J3=J3+R1*Y7
54 K3=K3+R2*Y7
55 L3=L3+R3*Y7
58 Y4=Y4+Y7*Y7
60 NEXT I
62 D=A3*E3*I3+B3*F3*C3+B3*F3*C3-C3*E3*C3-F3*F3*A3-B3*B3*I3
63 Q1=(E3*I3-F3*F3)/D
64 Q2=(-B3*I3+C3*F3)/D
65 Q3=(B3*F3-E3*C3)/D
66 Q4=(A3*I3-C3*C3)/D
67 Q5=(-A3*F3+C3*B3)/D
68 Q6=(A3*E3-B3*B3)/D
```

```
70 C4=Q1*J3+Q2*K3+Q3*L3
71 B4=Q2*J3+Q4*K3+Q5*L3
72 G4=Q3*J3+Q5*K3+Q6*L3
73 GO SUB 700
74 C=C+C4
75 B=B+B4
76 G=G+G4
78 PRINT C,B,G,Y4
79 IF ABS(Y4-Y9)/Y9<0.01 GO TO 93
81 Y9=Y4
82 INPUT G$
83 IF G$="G" GO TO 26
93 PRINT PNT(10);PNT(10);PNT(10)
94 PRINT "C,BETA,GAMMA=";C,B,G,"S2DEV=";Y4
95 GO SUB 600
96 T9=.0001
97 PRINT "OFFSET , % DISTRUCTION, FIT"
98 Y4=0
99 FOR I=1 TO 0
100 GO SUB 500
101 S1(I)=I7
102 IF T9>I7 GO TO 104
103 T9=I7
104 PRINT A(I),S(I),S1(I)
105 Y4=Y4+(S(I)-S1(I))**2
106 NEXT I
107 PRINT PNT(10);"S2DEV=",Y4;PNT(10);PNT(10)
108 PRINT "PLOT"
109 INPUT Y$
110 IF Y$="N" GO TO 95
112 PRINT PNT(10);PNT(10);PNT(10)
113 V=-1
114 FOR I=1 TO 24
116 U=68/T9
118 V=V+1
119 IF A(I) >T8*V-A(1)+.005 GO TO 121
120 GO TO 123
121 PRINT
122 GO TO 118
123 J=S(I)*U+2.5
124 K=S1(I)*U+2.5
126 IF INT(J)>INT(K) GO TO 137
127 IF INT (J)=INT(K) GO TO 135
128 IF INT (J)>0 GO TO 133
130 PRINT "N";TAB(K);"*"
131 GOTO 138
133 PRINT TAB(J);"+";TAB(K);"*"
134 GO TO 138
135 PRINT TAB(J);"*"
136 GO TO 138
137 PRINT TAB(K);"*";TAB(J);"+"
138 NEXT I
140 PRINT PNT(10);PNT(10);PNT(10);PNT(10)
142 PRINT "NEW GUESS?"
143 INPUT Y$
144 IF Y$="Y" GO TO 18
145 PRINT "NEW DATA?"
146 INPUT Y$
147 IF Y$="Y" GO TO 2
160 REM SUB ROUTINE TO CALCULATE SL FUNCTION
500 T2=ATN(2*A(I)/(Q1*Q1/Q2))
502 Q5=SQR(Q1**4/(Q2*Q2)+4*A(I)*A(I))
504  M5=(COS(T2/2)**2*COS(T2)+SIN(T2/2)**2*SIN(T2))**2
506 I4=C*(E8*Q5*Q5/(1.+E8*Q5*Q5))
508 I5=EXP(-(Q5-Q8)*(Q5-Q8)*G)
510 I6=EXP(-B*M5*G*I5)
```

```
512 I7=I4*(I6-1.)
514 R1=I7/C
516 R2=-I7*I5*M5*G
518 R3=I7*B*M5*I5*(G*(O5-O8)*(O5-O8)-1)
530 RETURN
600 REM  FINAL INPUT ROOUTINE
601 PRINT "FINAL PARAMETERS?"
603 INPUT C2,B2,G2
605 IF C2=0 GO TO 611
607 C=C2
608 B=B2
609 G=G2
611 RETURN
700 REM CONVERGENCE FUDGE
702 IF ABS(C4/C)<0.01 GO TO 706
704 C4=C4/F5
706 IF ABS(B4/B)<0.01 GO TO 710
708 B4=B4/F5
710 IF ABS(G4/G)<0.01 GO TO 714
712 G4=G4/F5
714 RETURN
800 END
```

Table 18. Program to implement a search for the parameters to fit a general cross polarization experiment.

```
C PROGRAM TO SOLVE CROSS RELAXATION DIFEQ FOR GENERAL CASE.
C THEN IT COMPARES RESULT TO EXPERIMENTAL NUMBERS TYPED IN
C FROM THE KEYBOARD.THE RESULT IS PRINTED OUT IN A MATRIX OF
C  STANDARD DEVIATIONS, VARING TIS AND EPS AROUND CHOSEN VALUES.
      DIMENSION VO(2),A(2),RO(2,2),VT(2),TIME(14),PT(14),ERROR(5),
     1 TIS(5),BETAB(14)
      ACCEPT ,"NUMBER OF DATA POINTS=",N
      DO 5 I=1,N
      ACCEPT ," TIME(I)=",TIME(I),"PT(I)=",PT(I),
5     CONTINUE
100   ACCEPT ,"NORMALIZE TO I=",NORM,
      ACCEPT ," TIR,TID,BETAL,H1,XMU,H0,HL, MAG CNST=",
      ACCEPT ,TIR,TID,BETAL,H1,XMU,H0,HL,CSTMG
      COOL=H0/HL
      VO(1)=COOL*BETAL*XMU
      VO(2)=0.
      A(1)=BETAL/TID
      A(2)=BETAL/TIR
      TYPE ,"TIR=",TIR,"TID=",TID,"  BETAL=",BETAL,"  BETA AI=",VO(1),
10    CONTINUE
      ACCEPT ,"EPS=",TESEPS,"TIS=",TESTIS,
      ACCEPT ,"EPS STEP=",ESTEP,"TIS STEP=",TSTEP,
      DO 20 I=1,5
      EPS=(TESEPS-2.5*ESTEP)+FLOAT(I)*ESTEP
      EPS=(EPS*H1*H1)/(HL*HL)
      DO 30 J=1,5
      TIS(J)=(TESTIS-2.5*TSTEP)+FLOAT(J)*TSTEP
      RO(1,1)=-(EPS/TIS(J)+1./TID)
      RO(1,2)=EPS/TIS(J)
      RO(2,1)=1./TIS(J)
      RO(2,2)=-(1./TIS(J)+1./TIR)
      ERROR(J)=0.
      DO 25 K=1,N
      T=TIME(K)
      CALL DIFEQ2(VO,A,RO,T,VT)
      BETAB(K)=VT(2)
25    CONTINUE
      DO 40 IK=1,N
      BETAB(IK)=BETAB(IK)*(CSTMG*H1/(H0*BETAL))
40    CONTINUE
      IF(NORM .EQ. 0) GO TO 150
      BETNM=BETAB(NORM)/PT(NORM)
150   IF(NORM .EQ. 0) BETNM=1.
      DO 50 IK=1,N
      BETAB(IK)=BETAB(IK)/BETNM
      ERROR(J)=ERROR(J)+(BETAB(IK)-PT(IK))**2
50    CONTINUE
30    CONTINUE
      WRITE(10,1) EPS,(ERROR(KK),KK=1,5)
1     FORMAT(E13.5,"I",5E13.5)
20    CONTINUE
      WRITE(10,3)
3     FORMAT(13X,65(" "))
      WRITE(10,2) (TIS(KK),KK=1,5)
2     FORMAT(13X,5E13.5)
C TRY AGAIN?
      ACCEPT ,"AGAIN?",NYES,
      IF (NYES .EQ. 1) GO TO 10
      ACCEPT ,"FINAL EPS=",EPS,"FINAL TAU=",TAU
      RO(1,1)=-(EPS/TAU+1./TID)
      RO(1,2)=EPS/TAU
      RO(2,1)=1./TAU
      RO(2,2)=-(1./TAU+1./TIR)
      WRITE(10,4)
4     FORMAT(6X,"TIME",10X,"BA",11X,"BB",11X,"MB",10X,"EXPER")
      DO 90 K=1,N
```

```
      T=TIME(K)
      CALL DIFEQ2(VO,A,RO,T,VT)
      XMB=CSTMG*HI/HU*VT(2)/BETAL
      WRITE(10,1) T,VT(1),VT(2),XMB,PT(K)
90    CONTINUE
      ACCEPT ,"AGAIN?",NYES,
      IF(NYES .EQ. 1) GO TO 10
      ACCEPT ,"NEW PARAMETERS?", NYES,
      IF(NYES .EQ. 1) GO TO 100
      END
*
```

```
      SUBROUTINE DIFEQ2(VO,A,RO,T,VT)
C ROUTINE TO SOLVE 2ND ORDER SIMULTANEOUS DIFFERINTIAL EQUATION
C BY MATRIX METHOD. DV(T)=A+RO*V(T) WHERE V,AAND VO ARE VECTORS AND RO IS A MATIX.
C VO=V(Ø) THE INITIAL CONDITIONS
C A=VECTOR OF CONSTANTS.
C RO =MATRIX OF COEFFICIENTS
C VT=V(T) THE SOLUTION AT TIME =T
      REAL LAMDP,LAMDM
      DIMENSION VO(2),A(2),RO(2,2),VT(2),D(2,2),DI(2,2),CAPLAMI(2,2),
     1 EX(2,2),TEMP(2,2),VTEMP(2),SECPT(2)
C FIND EIGENVALUES
      ROOT=SQRT((RO(1,1)+RO(2,2))*(RO(1,1)+RO(2,2))-4.*(RO(1,1)*RO(2,2)-
     1 RO(2,1)*RO(1,2)))
      LAMDP=Ø.5*(RO(1,1)+RO(2,2)+ROOT)
      LAMDM=Ø.5*(RO(1,1)+RO(2,2)-ROOT)
C FIND ROTATION MATRICES
      D(1,1)=1.
      D(1,2)=1.
      D(2,1)=-RO(2,1)/(RO(2,2)-LAMDM)
      D(2,2)=-RO(2,1)/(RO(2,2)-LAMDP)
      FACTOR=D(1,1)*D(2,2)-D(2,1)*D(1,2)
      DI(1,1)=1./FACTOR*D(2,2)
      DI(1,2)=1./FACTOR*(-D(1,2))
      DI(2,1)=1./FACTOR*(-D(2,1))
      DI(2,2)=1./FACTOR*D(1,1)
C FIND EIGEN VALUE MATRICES
      CAPLAMI(1,1)=1./LAMDM
      CAPLAMI(1,2)=Ø.
      CAPLAMI(2,1)=Ø.
      CAPLAMI(2,2)=1./LAMDP
C AND EXPONENTIAL MATRICES
      EX(1,1)=EXP(LAMDM*T)
      EX(1,2)=Ø.
      EX(2,1)=Ø.
      EX(2,2)=EXP(LAMDP*T)
C CALCULATE SOLUTION VECTOR VT=D EXP(LAM*T) D-1 VO +
C   D (-1-EXP(LAM*T)) D-1 D LAM-1 D-1 A.
      CALL MATRIX(2,D,EX,TEMP)
      CALL MATRIX(2,TEMP,DI,EX)
      CALL VECTOR(2,EX,VO,VTEMP)
      VT(1)=VTEMP(1)
      VT(2)=VTEMP(2)
      EX(1,1)=-1.+EX(1,1)
      EX(1,2)=EX(1,2)
      EX(2,1)=EX(2,1)
      EX(2,2)=-1.+EX(2,2)
      CALL MATRIX(2,D,CAPLAMI,TEMP)
      CALL MATRIX(2,TEMP,DI,CAPLAMI)
      CALL VECTOR(2,CAPLAMI,A,VTEMP)
      CALL VECTOR(2,EX,VTEMP,SECPT)
      VT(1)=VT(1)+SECPT(1)
      VT(2)=VT(2)+SECPT(2)
      RETURN
      END
```

Chapter Two References

1. A. Pines, M. G. Gibby and J. S. Waugh, J. Chem. Phys. 59 (2) 569 (1973); H. E. Bleich and A. G. Redfield, J. Chem. Phys. 55, (11) 5405 (1971).
2. a) R. G. Brewer and E. L. Hahn, Phys. Rev. A 11, 1641 (1975).
   b) W. G. Breiland, H. C. Brenner and C. B. Harris, J. Chem. Phys. 62 (4) 3458 (1974).
   c) L. Mandel and E. Wolf, Coherence and Quantum Optics (Plenum Press, New York, 1973).
3. T. Chiba, J. Chem. Phys. 39 (4) 947 (1963).
4. T. Chiba, J. Chem. Phys. 41 (5) 1352 (1964).
5. S. Ketudat and R. V. Pound, J. Chem. Phys. 26, 708 (1957).
6. a) H. Hatanaka, T. Terao and T. Hashi, J. Phys. Soc. Japan, 39, 835 (1975).
   b) A. Pines, S. Vega and T. W. Shattuck, Lawrence Berkeley Laboratory Report No. 4550, Annual Review, 1975. See also Reference 49.
   c) J. Jeener, private communication to Professor A. Pines.
   d) W. P. Aue, E. Bartholdi and R. R. Ernst, J. Chem. Phys. 64, 2229 (1976).
7. J. S. Waugh, L. M. Huber, U. Haeberlin, Phys. Rev. Lett. 20, 180 (1968).
8. A. Abragam, The Principles of Nuclear Magnetism, (Oxford University Press, Oxford, 1961) pp. 36.
9. S. Vega, J. Chem. Phys. 63 (9) 3769, (1975).
10. W. A. Anderson, Phys. Rev. 104, 850 (1956).
11. J. I. Kaplan and S. Meiboom, Phys. Rev. 106, 499 (1957).
12. S. Yatsiuv, Phys. Rev. 113, 1522 (1959).
13. a) M. M. Yves Ayant, P. Ducros, X. Pare and M. Soutif, J. Acad. des. Sciences (France) 252, 550 (1961).

b) M. M. Yves Ayant, J. de Physique 24 (4) 225 (1963).

14. a) H. Wennerstrom, N. O. Persson, and B. Lindman, J. Mag. Res. 13 348 (1974).

b) J. Charvolin and P. Rigny, Chem. Phys. Lett. 18, 575 (1973).

c) K. D. Lawson and T. J. Flautt, J. Phys. Chem. 72, 2066 (1968).

15. a) P. C. Hewitt, S. Meiboom and L. C. Snyder, J. Chem. Phys. 58 (11) 5089 (1972).

b) L. C. Snyder and S. Meiboom, J. Chem. Phys. 58 (11) 5096 (1972).

16. a) H. Hatanaka and T. Hashi, J. Phys. Soc. Japan 39 (4) 1139 (1975).

b) H. Hatanaka, T. Terao and T. Hashi, J. Phys. Soc. Japan 39 (9) 835 (1975).

17. a) S. Vega, J. Chem. Phys. 63 (9) 3769 (1975).

b) S. Vega, Advances in Magnetic Resonance (J. S. Waugh Editor, Academic Press, New York, 1973). Volume 6, page 259.

18. A. G. Anderson and S. R. Hartmann, Phys. Rev. 128, 2029 (1962).

19. M. Schwab and E. L. Hahn, J. Chem. Phys. 52, 3152 (1970).

20. M. Goldman and A. Landesman, Phys. Rev. 132, 610 (1963).

21. W. de Boer, Phys. Review B, 12, 828 (1975).

22. W. S. Veeman and C. S. Yannoni, Chem. Phys. Lett. 32, 499 (1975).

23. a) D. A. McArthur and E. L. Hahn and R. E. Walstedt, Phys. Rev. 188, 609 (1969).

b) S. R. Hartman and E. L. Hahn, Phys. Rev. 128, 2042 (1962).

24. D. E. Demco, J. Tegenfeld and J. S. Waugh, Phys. Review B, 11 (11) 4133 (1975).

25. T. Chiba, J. Chem. Phys., 41, 1352 (1964).

26. P. Coppens and T. M. Sabine, Acta Cryst. B25, 2442 (1969).

27. R. G. Delaplane and J. A. Ibers, Acta. Cryst. B25, 2423 (1969).

28. H. Ruben and A. Zalkin, private communication.

29. The details of this system are published elsewhere. D. Ruben, A. Pines, Lawrence Berkeley Laboratory Report, to be published.

30. J. Jeener and P. Broekaert, Phys. Rev. 157 (2) 232 (1967).

31. A. Abragam, The Principles of Nuclear Magnetism (Oxford University Press, Oxford, 1961) page 107.

32. M. Goldman, Spin Temperature and Nuclear Magnetic Resonance in Solids (Oxford University Press, Oxford, 1970) page 29.

33. H. Levanon and S. Vega, J. Chem. Phys. 61 (6) 2265 (1974).

34. H. N. Yeung, Ph.D. thesis, M.I.T. (1972).

35. U. Haeberlin and U. Kohlschütter, Chem. Phys. 2, 76 (1973).

36. H. Raber, G. Brünger and M. Mehring, Chem. Phys. Letters, 23 (3), 400 (1973).

37. a) U. Fano, Phys. Rev. 90, 577 (1953).

b) For a general discussion see D. M. Brink and G. R. Satchler, Angular Momentum (Oxford University Press, Oxford, 1962).

38. D. E. Demco, S. Kaplan, S. Pausak and J. S. Waugh, Chem. Phys. Lett., 30 (1), 77 (1975).

39. T. G. D. van Schalkwyk, Acta. Cryst. 7, 775 (1954).

40. J. A. Goedkoop, C. H. Mac Gillavry, Acta. Crystl. 10, 125 (1957).

41. J. M. H. Robertson and J. S. Morrison, J. Chem. Soc. 987 (1949).

42. M. Shahat, Acta. Cryst. 5, 763 (1952).

43. E. G. Cox, M. W. Dougill and G. A. Jeffrey, J. Chem. Soc., 4854 (1952).

44. D. Semmingsen, Acta. Chem. Scand. 27 (10), 3961 (1973).

45. C. J. Brown, Acta. Cryst. 21 (1), 1-5 (1966).

46. V. Benghiat, L. Leiserowitz, G. M. J. Schmidt, J. Chem. Soc. Perkin Trans. II, 1769 (1972).

47. C. P. Slichter, Principles of Magnetic Resonance (Harper and Row, New York, 1963) page 53.

48. E. Hahn, Magnetic Resonance and Relaxation, Proceedings of the 14th Colloque Ampere, Ljubljana, 1966 (North-Holland Amsterdam, 1967).

49. S. Vega, T. W. Shattuck, A. Pines, Phys. Rev. Letters, 37, 43 (1976).